

ISSN 2367-7570

Workshop
**"Solar Influences on the Magnetosphere,
Ionosphere and Atmosphere"**

Book
of
Proceedings

Ninth Workshop
Sunny Beach, Bulgaria, May 30 - June 3, 2017

Organized by:
**Space Research and Technologies Institute
Bulgarian Academy of Sciences**

The workshop is partly supported by the **National Science Fund of Bulgaria**



No. ДПМНФ 01/16 (29 May 2017)

Scientific Organizing Committee

Katya Georgieva (Space Research and Technologies Institute, Bulgaria) - *Chair*
Crisan Demetrescu (Institute of Geodynamics, Romanian Academy)
Ümit Deniz Göker (Istanbul Gelisim University, Turkey)
Petra Koucka-Knizova (Institute of Atmospheric Physics, Czech Republic)
Vladimir Obridko (IZMIRAN, Moscow, Russian Federation)
Atila Özgüc (Kandilli Observatory, Turkey)
Jean-Pierre Rozelot (OCA-Lagrange, CNRS, Nice University, France)
Olga Malandraki (IAASARS, National Observatory of Athens, Greece)
Irina Mironova (Institute of Physics, St. Petersburg State University, Russia)

Editors: Katya Georgieva, Boian Kirov, Dimitar Danov

CONTENT

Sun and Solar Activity

| | |
|--|----|
| <i>Podgorny I.M., Podgorny A.I.</i> Diagnostics of Solar Flares by Analyzing the Spectral Line Emission of Highly Ionized Iron | 01 |
| <i>Kalinichenko N., Olyak M., Konovalenko A., Brazhenko A., Ivantishin O., Lytvynenko O., Bubnov I., Yerin S., Kuhai N., Romanchuk O.</i> A method for reconstructing the solar-wind stream structure beyond Earths orbit | 07 |
| <i>Melnik V., Brazhenko A., Dorovskyy V., Rucker H., Panchenko M., Frantsuzenko A., Shevchuk M.</i> Decameter type IV burst associated with behind-limb CME observed on November 7, 2013 | 13 |
| <i>Miteva R., Samwel S.W., Krupar V.</i> Solar radio burst emission from proton-producing flares and coronal mass ejections | 19 |
| <i>Veselovsky I., Kaportseva K., Lukashenko A.</i> Eight types of the solar wind and their origins | 24 |
| <i>Stanislavsky A.A., Konovalenko A.A., Koval A.A., Volvach Ya.S.</i> An upgrade of the UTR-2 radio telescope to a multifrequency radio heliograph | 29 |
| <i>Popova E., Zharkova V., Shepherd S., Zharkov S.</i> On a role of quadruple component of magnetic field in defining solar activity in grand cycles | 34 |
| <i>Dorovskyy V., Melnik V., Konovalenko A., Brazhenko A., Rucker H.</i> Spatial properties of the complex decameter type II burst observed on 31 May 2013 | 40 |
| <i>Ishkov V.N., Zabarinskaya L.P., Sergeeva N.A.</i> The collection and compile data on SPE for the period 19th-23rd cycles of solar activity | 46 |
| <i>Bojilova R., Mukhtarov P.</i> Influence of solar and geomagnetic activity on the ionosphere over Bulgaria | 54 |
| <i>Boychev B., Belyaev G., Kostin V., Ovcharenko O., Trushkina E.</i> Features of upper ionosphere modification by interactive tropical cyclons based on Cosmos-1809 and Interkosmos Bulgaria-1300 Satellite Data | 58 |
| <i>Miteva R., Danov D.</i> On-line catalogues of solar energetic protons at SRTI-BAS | 66 |
| <i>Rozelot J.- P., Kosovichev Al., Kilcik A.</i> A Look on the Solar Diameter Data Analysis over the Centuries | 70 |
| <i>Yankova Kr.</i> Unified model of the AGN | 77 |

Solar Wind-Magnetosphere-Ionosphere Interactions

| | |
|---|-----|
| <i>Yaşar M., Canyilmaz M.</i> The Energy Barrier and Collision Number of O+ + H₂(v=0, j=0) Reaction in the Earth Ionosphere | 83 |
| <i>Shagimuratov I., Chernouss S., Despirak I., Filatov M., Efishov I., Tepenitsyna N.</i> Occurrence of TEC fluctuations and GPS positioning errors at different longitudes during auroral disturbance | 86 |
| <i>Manninen J., Turunen T., Kleimenova N., Rycroft M., Gromova L.</i> Recently revealed new type of daytime VLF emissions observed under quiet space weather conditions | 91 |
| <i>Ishkova L., Ruzhin Yu., Bershadszkaya I.</i> The large-scale ionosphere TEC disturbances before two power Chilean earthquakes | 97 |
| <i>Gromova L.I., Gromov S.V., Kleimenova N.G., Dremukhina L.A.</i> Role of the IMF Bz / By in the appearance of the daytime high-latitude magnetic bays | 103 |

CONTENT

| | |
|--|-----|
| Solar Influences on the Lower Atmosphere and Climate | |
| <i>Kleimenova N., Michnowski S., Odzimek A., Kubicki M.</i> Space Weather Effects in Atmospheric Electric Field Variations | 109 |
| <i>Tonev P.</i> Transient variations in global electrical circuit caused by different factors and their relation to cloud formation | 115 |
| Data Processing and Modeling | |
| <i>Skokić I., Brajša R., Sudar D., Kuhar M., Benz A.O.</i> Identification of features in solar ALMA images and comparison with solar atmospheric models | 121 |
| Instrumentation for Space Weather Monitoring | |
| <i>Bárta M., Skokić I., Brajša R. & the Czech ARC Node Team.</i> Solar research with ALMA: Czech node of European ARC as your user-support infrastructure | 127 |
| Author index | 133 |

Diagnostics of Solar Flares by Analyzing the Spectral Lines Emission of Highly Ionized Irons

*I. M. Podgorny*¹, *A. I. Podgorny*²

¹ Institute for Astronomy RAS, Moscow, Russia

² Lebedev Physical Institute RAS, Moscow, Russia

E-mail: podgorny@inasan.ru

Abstract.

The photos of the pre-flare development observed in the spectral lines of highly ionized iron (SDO AIA apparatus) indicate the energy accumulation for a flare in the corona in the pre-flare local (about 1010 cm) high temperature structure. The pre-flare structures in the corona are observed in UV spectral lines of ions FeXXIV, FeXXIII, FeXVIII several hours before big solar flares. During a flare the emission of the UV spectral lines in the corona are increased explosively. These phenomena can be used for prediction of solar cosmic rays. Information obtained from the worldwide neutron monitor network and measurements on GOES spacecraft demonstrates unambiguously that solar cosmic rays are generated in solar flares. These phenomena are well described by the solar flare electrodynamic model, created on the basis of the observational data and the numerical magnetohydrodynamic simulation using the initial and boundary conditions, taken from the active regions observation before the flare. It is impossible to exclude that the similar mechanism of particle acceleration is responsible for galactic cosmic rays generation. Now all published mechanisms of cosmic ray generation are based on unproven assumptions. These assumptions are not confirmed by long-term observations. With the modern concept of cosmic rays, a fundamentally important question arises: can the mechanism of proton acceleration in solar flares explain the acceleration of particles of galactic cosmic rays.

Introduction

One of the most interesting properties of solar activity is the solar flare. The energy pulse about 10^{32} erg can be realized. The numerical MHD simulation [Podgorny and Podgorny, 2013] shows that the flare appears at a current sheet decay in the solar corona above an active region. This current sheet is created at a singular line due to magnetic disturbance focusing that arrived from the photosphere before the flare. During this current sheet creation the magnetic energy accumulation takes place. Some of big flares are accompanied by a proton event. The most popular acceleration mechanisms considered in many publications are associated with shock waves. However, the possible mechanisms for accelerating cosmic rays in shock waves remain only hypotheses. Protons with the energy of ~ 20 GeV accelerated by a solar flare is demonstrated with neutron monitors [Balabin *et al.*, 2005; Podgorny *et al.*, 2010a, 2010b]. It is shown that proton acceleration takes part in the flare current sheet. The similar mechanism is observed in the laboratory [Artsimovich, 1974]. This result gives us hope to get the new information about the mechanism of galactic cosmic rays generation because the possibility of the same mechanism for the acceleration of galactic and solar cosmic rays cannot be ruled out. This circumstance makes research of solar flares especially urgent. A number of phenomena related to the acceleration and propagation of protons accelerated on the Sun are available for observation by modern methods. In the work of Podgorny and Podgorny, 2015 the analysis of GOES measurements of proton with the energy ~ 100 MeV is carried out. The flare appears above the active regions after the magnetic flux becomes bigger than 10^{22} Max [Podgorny *et al.*, 2015]. The magnetic field distribution in the active region remains practically unchanged during the flare [Podgorny and Podgorny, 2011]. This means that magnetic energy dissipation occurs in the corona. It is also proven that the protons of solar cosmic rays are accelerated in the electric field appeared due to magnetic

reconnection in the coronal current sheet. The characteristics of the pulses of accelerated protons recorded at the Earth's orbit strongly depend on the interplanetary magnetic field [Podgorny and Podgorny, 2015]. The protons accelerated in the western solar flares arrive to the Earth along the Archimedes magnetic line without collision, but protons from the eastern flares arrive across the interplanetary magnetic lines with the delay of several hours. Apparently these protons propagate due to collisionless diffusion. Not all flares are accompanied by proton acceleration. In this paper we analyze ultraviolet photographs of pre-flare states and flares observed by the Solar Dynamics Observatory Atmospheric Imaging Assembly (SDO AIA) in the emission of high-ionized iron spectral lines, which allow us to judge about the place of energy accumulation before the flare and energy release during the flare.

Results

According to the flare electrodynamical model [Podgorny and Podgorny, 2006], the magnetic energy accumulates above the active region at a temperature exceeding the corona temperature $T > 1\text{MK}$, and then the magnetic energy rapidly dissipates in the corona, causing a strong local heating of the coronal plasma. Observational evidence for such flare development has been obtained for the first time for the X4.8 flare in 2002, observed at the eastern limb of the solar disk [Lin *et al.*, 2003] at measurements of thermal X-ray radiation. These processes can be observed in spectral lines of many times ionized iron, characteristic for the solar corona temperature. However, such data was then absent. At present time, the photographs of the pre-flare states and flares obtained in the lines of highly ionized iron are contained in the SDO data archive (sdo.gsfc.nasa.gov). The most convenient for the analysis of the flares are the short-wave UV emission lines 94\AA and 193\AA . The first of which belongs to the FeXVIII ion, and the second to the FeXII and FeXXIV ions. The maximum brightness of the 94\AA line emission is reached at the temperature of 6.3MK . The emission of the 193\AA line contains radiation of the FeXXVI ion from the very hot region ($\sim 20\text{MK}$). If a solar flare occurred in the corona at very high temperature, then the photographs in these lines must show fast radiation increase at a flare appearance.

The all solar disk photo taken in the spectral line 94\AA 60 min before the X1.6 flare and during this flare and the magnetogram are presented in Fig. 1. The solar X1.6 flare is produced by the AR12158 active region. Two days prior to this flare appearance the bright UV pre-flare structure unlike other bright UV emissions has appeared over AR12158 active region. Only this bright structure, which is shown in a white square, has accompanied by a flare. Brightness of this pre-flare structure gradually increased (Fig. 2) within two days. The structure is brightly flashed during the solar flare. The flare is produced near the center of the solar disk. It is followed by the pulse of solar cosmic rays with the very flat (about a day) front, which is delayed in more than three hours. Protons could reach Earth only moving across the magnetic field. The time of flare and proton flow appearing are shown in right panels of the Fig. 2. In Fig. 2 one can see a typical very hot pre-flare structure and the flare which cannot exist in rather cold plasma of chromospheres. This bright UV pre-flare structure is situated in the corona above the AR12158 active region. The hot pre-flare structure must exist in the corona, if the flare energy is accumulated in the magnetic field of a coronal current sheet, but not supplied from the Sun surface.

The dynamics of the pre-flare structure measured by the SDO AIA apparatus in the highly ionized iron lines UV 94\AA , 131\AA , and 193\AA is demonstrated in Fig. 2. The data are obtained by processing the results obtained on SDO and presented in the Internet (sdo.gsfc.nasa.gov). The photographs show the pre-flare dynamics above the active region and the X1.6 flare, which occurred on September 10, 2014 at 17:21.

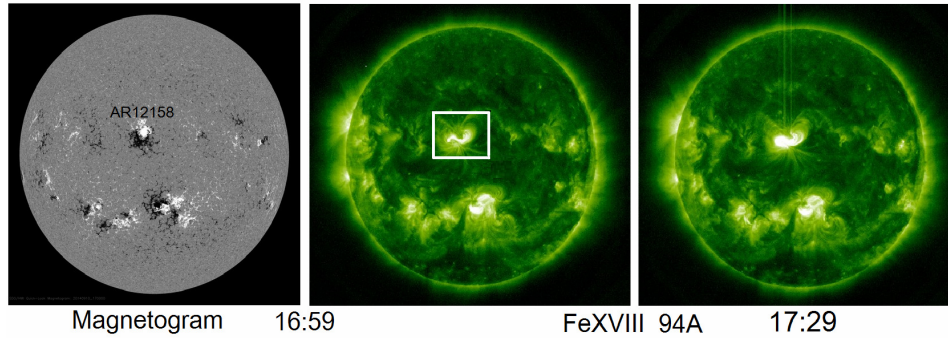


Fig. 1. The solar disk magnetogram, pre-flare and flare emissions. The pre-flare structure is marked by the white.

The increasing of the luminous structure takes place before the flare. The shape of the structure does not correspond to the shape of the magnetic lines, which is clearly seen in the photographs. The temperature of these local pre-flare emissions is much higher than the temperature of the chromosphere, hence the pre-flare process develops in the corona over the active region. Very sharp increase of UV emissions during the flare is demonstrated by spectral lines 131\AA and 193\AA , which are radiated by ions ionized 23 and 24 times. The typical size of the structure of local pre-flare emission is about 10^{10} cm. The clearest and brightest image of the flare corresponds to the high temperature line 193\AA , but this line is not very bright at earlier time. The fast increasing of the spectral line 193\AA brightness during the flare demonstrates explosive energy release during the flare.

The graph in the Fig. 2, shows that protons recorded on the Earth's orbit are clearly lagging in comparison with the time of proton direct flight from the flare to the Earth, when the protons propagate along a magnetic line without collisions, but in this event the propagation of protons from the disk center occurs across the lines of the magnetic field. The delay relative to the flare is almost 10 hours.

The arrow in Fig. 2 below shows the time of the first frame taken before the flare, when the X-ray has been almost constant and is not exceed C1. The frame shots taken before the flare clearly show the slowly changing luminous structure of the heated plasma, which does not have a form of magnetic field lines. Only a current system in the corona can produce such shape of luminous configuration, but it is not the shape of the magnetic field line with the field aligned current. Such current system must heat up the plasma in the pre-flare state, when magnetic energy accumulation takes place. The UV emission of the pre-flare current system can be observed for more than ten hours before the flare.

The decay of the current system should lead to a fast dissipation of the energy that has been accumulated in the magnetic field before the released during a flare. The current dynamics is observed over the active region in spectral lines of the highly ionized iron. The UV spectral line emissions of highly ionized FeXVIII iron revealed in Fig. 2 and 3 can not belong to the chromosphere or photosphere. Thus, the previously conclusions about the accumulation of energy for a flare in the corona and flare production above an active region (the coronal origin of flares) are confirmed by the independent way.

The pre-flare current structure presented in Fig. 2 and 3 is observed for ~50 per cent of big flares appeared in the eastern or central part of the solar disk, where the protons propagate to the Earth across magnetic field lines. The image in one projection does not make it possible to draw an accurate conclusion about the spatial form of pre-flare structures. There is every reason to assert that the hot plasma structures can not belong to the cold plasma of the chromosphere. They situate above the active region in the corona. We can confidently assert that these pre-flare structures are not a field aligned configurations. The pre-flare structure has the form of a tape with the length about 10^{10} cm. However, there are every reasons to assert

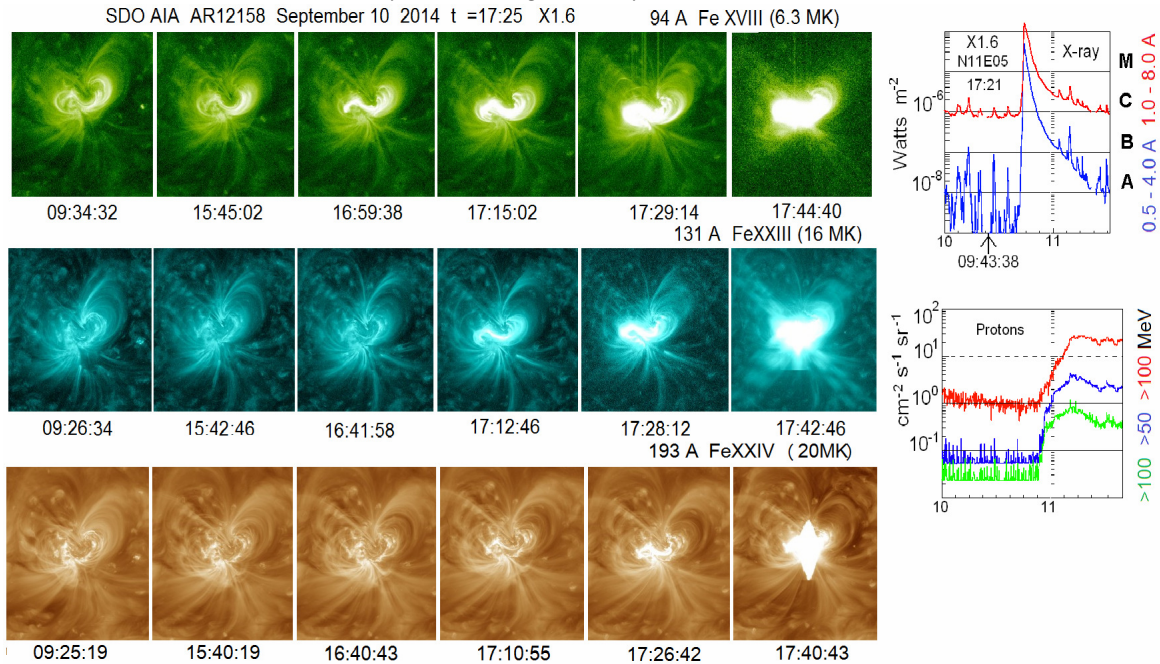


Fig. 2. Photos of the active region AR12158 before the flare and during the X1.6 flare from SDO data in the emission of three spectral lines of highly ionized iron. The 17:21 flare onset is recorded by thermal X-ray radiation on GOES devices.

that a hot plasma configurations can not belong to the cold plasma of the chromospheres. The pre-flare structure are located above the active region in the corona as it follows from Fig. 1 and 2. Apparently, it is caused by the current generation in the current sheet.

The analysis of the available SDO data shows that the pre-flare structures are appeared before all big flares, but the typical shape of structure that can be used for flare prognosis is observed only for half of considered flares. The other pre-flare structures cannot be distinguished from UV structures on the solar disk that are not accompanied by a flare. The pre-flare structures appeared before different flares are shown in Fig. 3.

The flare appeared on the limb of the solar disk makes it possible to observe the accumulation of energy and energy release in the corona outside the solar disk, when the influence of the solar disk radiation is completely ruled out. The flare on July 23, 2002 that is very convenient for observing in the corona has been investigated [Lin *et al.*, 2003], when it is clearly shown that the thermal X-ray source of the X4.8 flare had been located in the coronal plasma cloud with a concentration of $10^{11} cm^{-3}$ and the number of particles order of $\sim 10^{37}$.

The rare event is shown in Fig. 4, where the flare had been observed in the corona outside the eastern limb, as the flare appeared on July 23, 2002 [Lin *et al.*, 2003]. This flare is accompanied by a flux of solar cosmic rays with the delay about 20 h, because the protons could come to the GOES devices only after drift across the lines of the interplanetary magnetic field. In the upper line the photos are presented that obtained in the spectral line of the ionized helium HeI 304Å (temperature $\sim 50\ 000$ K.). The pre-flare image in this "cold" line is barely noticeable before the flare. 304Å line emission appears during the flare on the solar disk boundary.

Otherwise, the emission the high-ionized iron FeXVIII 94Å line of hot plasma with the temperature of ~ 6.3 MK, considerably exceeding the usual corona temperature, is appeared in the corona. The high temperature emission is appeared in the pre-flare state, when the magnetic energy is accumulated for the flare. During the flare, the brightness of 94Å image is increased. This image is situated in the corona beyond the boundaries of the solar disk. The release of the flare energy is occurred in the corona over the active region. These photos leave no doubt about the coronal origin of the flare.

PREFLARE STRUCTURES (94 Å)

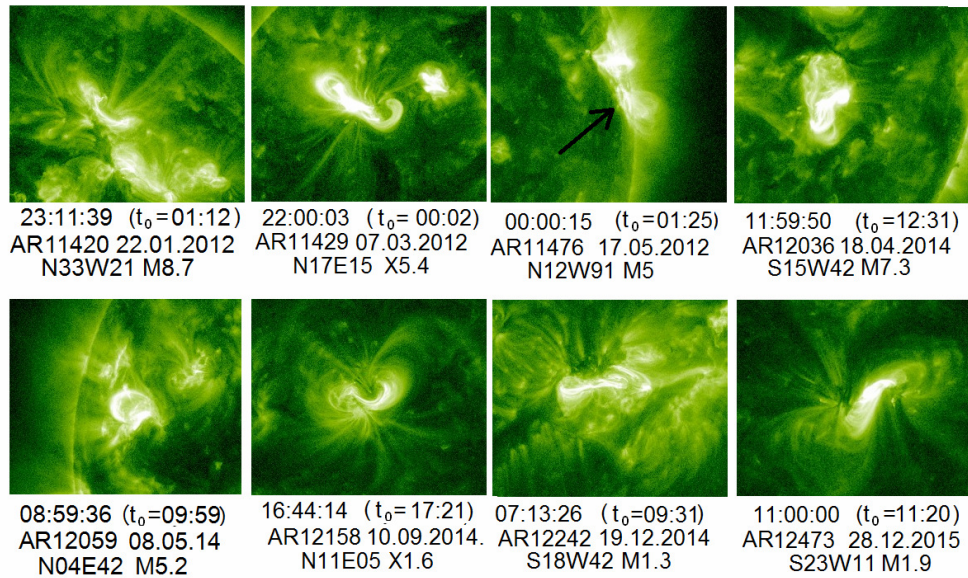


Fig. 3. Photos obtained before the different flares in the 94\AA spectral line.

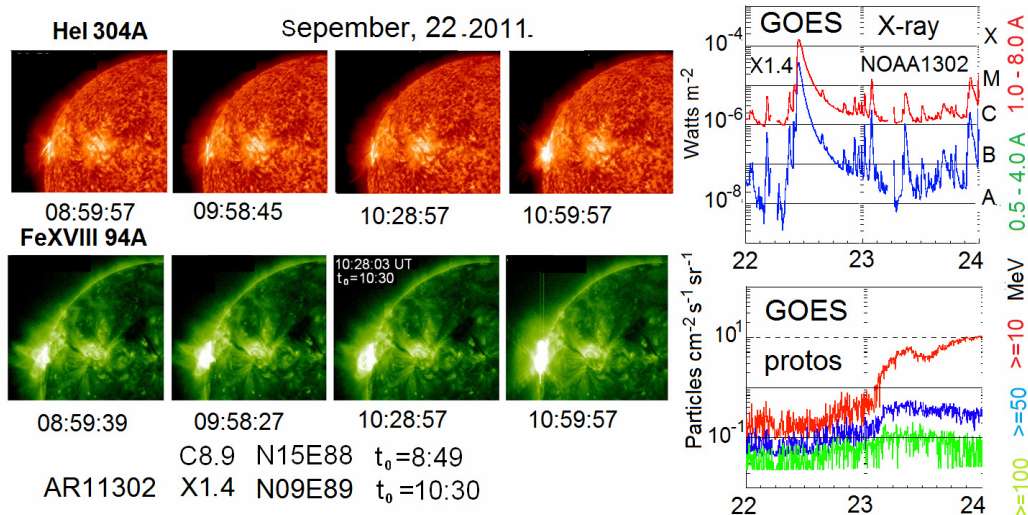


Fig. 4. Pre-flare state and limb flare in the spectral lines emission of cold chromosphere plasma and hot coronal plasma.

Fig. 5 shows M5 flare development of on the western limb. Apparently, a significant portion of the active region AR11476 is realized on the back side of Sun during this flare. At frame 02:00:20 one can clearly see the appearance of the hot plasma cloud in the solar corona outside the western boundary of the solar disk. The picture clearly indicates that the flare energy release takes part in the solar corona (black arrow). The flare was accompanied by the flow of solar cosmic rays with a sharp front, arrived with a delay relative to the front of the flare not more than 20 min. This means that the flow front of the protons arrive the Earth's orbit without collision along the magnetic field lines of the Archimedes spiral. The delay of arrival to GOES ~ 20 min is typical for protons coming from the West.

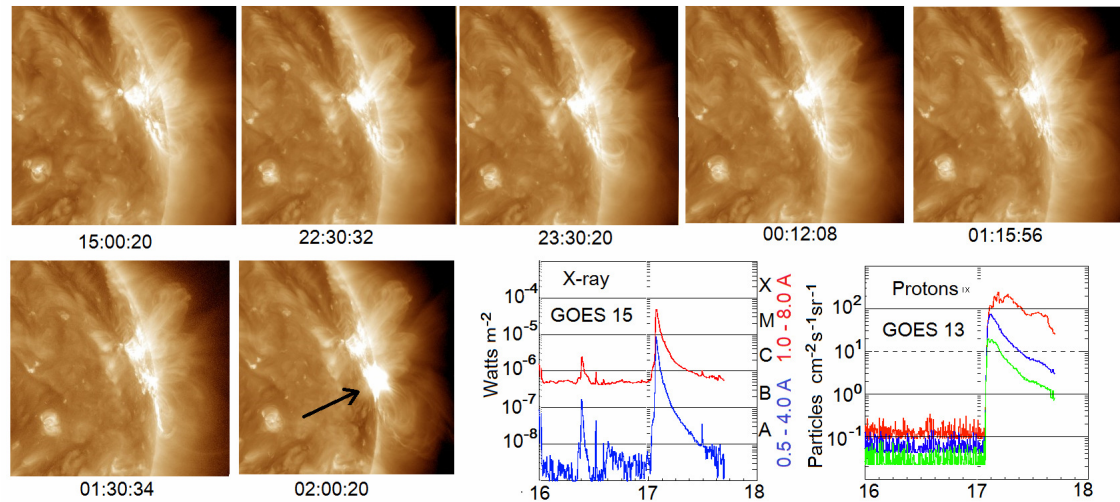


Fig. 5. Pre-flare condition and the X5 flare in 193Å spectral line from SDO data. The graphs show the flare thermal X-ray radiation and solar cosmic rays according to GOES data.

Conclusions

The appearance of a local source of UV emission in the corona above an active region before the flare and during the flare is investigated. The systematically recorded data of on the SDO spacecraft are used. The UV spectral line emission usually appears about 2 days before a flare due to accumulation of the magnetic energy for this flare. The flare can be predicted by the appearance of a high-temperature plasma structure with the length $\sim 10^{10}$ cm. The brightness of the UV emission sharply (within ~ 20 min) increases during the flare. The plasma structure above the active region reaches the temperature ~ 20 MK during the flare. At the same time, the temperature of the Sun surface also increases, but much less.

The rapid arrival of protons and the steep front of the proton flow from the western flare are created due to the particle propagation along the magnetic field lines of the Archimedes spiral without collisions. The delayed flow of protons from the eastern flare has a gently sloping front. Solar cosmic rays from the eastern flares propagate diffusing across the magnetic field. For the solar flare a sharp (several minutes) increase of the UV spectral lines emission localized above the Sun surface is observed. The strong heating of the plasma above the active region cannot be explained by the flare energy release on the surface of the Sun in the chromosphere. The flare energy release takes part in the corona.

References

- Artsimovich L.A. (1974). Controlled thermonuclear reaction. Gordon and Breach. New York.
- Balabin Yu.V., Vashenyuk E.V., Mingalev O.V., Podgorny A.I. Podgorny I.M. (2005). The spectrum of solar cosmic rays: data of observations and numerical simulation. Astronomy Reports, 49, 837–846.
- Lin R.P., Krucker S., Hurford, G.J. et al. (2003). RHESSI observations of particles acceleration and energy release in an intense gamma-ray line flare. Astrophys. J. 595, L69_L76.
- Podgorny A.I., Podgorny, I.M.: (2006). Astronomy Reports. 50, 842–850.
- Podgorny I.M., Balabin Yu.V., Vashenuk E.M., Podgorny A.I.: (2010a). The generation of hard X-rays and relativistic protons observed during solar flares. Astronomy Reports. 54, 645–656.
- Podgorny I.M., Balabin Yu.V., Podgorny A.I., Vashenyuk E.V. (2010b). Spectrum of solar flare protons. JASTP. 72, 988–991.
- Podgorny A.I., Podgorny I.M. (2011). Magnetic flux in an active solar region and its correlation with flares. Astronomy Reports. 55, 629–636.
- Podgorny A.I., Podgorny I.M. (2015). Acceleration of solar cosmic rays in a flare current sheet and their propagation in interplanetary space. Astronomy Reports. 59, 888–897.
- Podgorny I.M., Podgorny A.I., Meshalkina N. S. (2015). Dynamics of magnetic fields of active regions in pre-flare states and during solar flares. Astronomy Reports. 59, 795–805.

A method for reconstructing the solar wind stream structure beyond Earth's orbit

M.M. Kalinichenko¹, M.R. Olyak¹, O.O. Konovalenko¹, A.I. Brazhenko²,
O.L. Ivantishin³, O.O. Lytvynenko¹, I.M. Bubnov¹, S.M. Yerin¹, N.V. Kuhai⁴,
O.I. Romanchuk⁵

¹ Institute of Radio Astronomy of NASU, Kharkiv, Ukraine;

² Gravimetrical observatory of Geophysical institute of NASU, Poltava, Ukraine;

³ Institute of physics and mechanics of NASU, Lviv, Ukraine;

⁴ National Pedagogical Dragomanov University, Kyiv, Ukraine

⁵ Hlukhiv national pedagogical university, Hlukhiv, Ukraine

E-mail: kalinich@rian.kharkov.ua

Abstract.

The paper describes a new method for reconstructing the solar wind stream structure beyond Earth's orbit. The method is based on the use of two-station interplanetary scintillation data obtained at decameter wavelengths. Solar wind stream structure is reconstructed by fitting model characteristics to the experimental ones. The model characteristics were obtained by using Feynman path-integral technique. Authors use multi-flow model of the solar wind.

Introduction

The solar corona is non-uniform, so it is not surprising that the solar wind also is highly structured. For example the recurrent high-speed streams from coronal holes are clearly seen in in-situ spacecraft data (Figure 1). Ulysses spacecraft measurements show that the solar wind has a "fast" component and a "slow" component [Lang K.R., 1996]. There are some compositional differences in the two wind streams in addition to differences in their speeds [Ulysses Web page]. Consequently, the solar wind observed anywhere in the heliosphere is a collection of streams with different parameters.

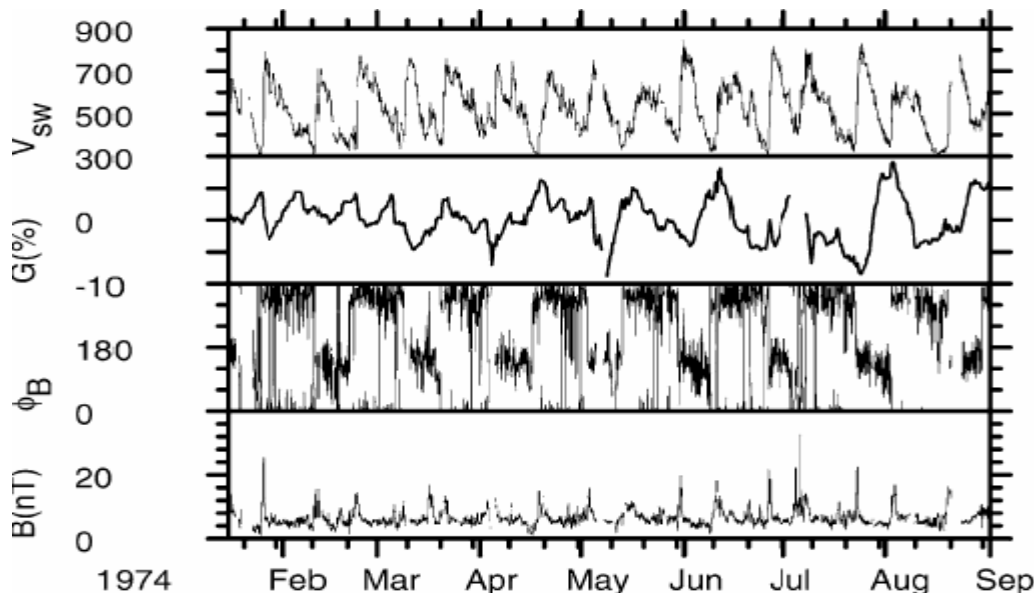


Fig. 1 Solar wind according to IMP-8 space craft observations during January - August, 1974

Also, there is another possibility for the investigations of solar wind stream structure then spacecraft measurements. This is observations of the interplanetary scintillations (IPS)

[Hewish A. et al, 1964]. Interplanetary scintillations of the radio waves from distant compact cosmic radio sources (such as quasars, pulsars, galaxies) are produced by density irregularities in the solar wind. Observations of IPS phenomenon allow conclusions to be made on the parameters and the stream structure of the solar wind [Dennison P.A. and Hewish A, 1967; Coles W.A., 1996]. Decameter radio waves provide a possibility to study effectively the solar wind parameters at large distances from the Sun [Falkovich I.S. et al., 2010, Kalinichenko M.M., 2012] where high frequencies are only slightly scattered by the rarefied interplanetary plasma.

The aim of this paper is to describe a new method for reconstructing the solar wind stream structure beyond Earth’s orbit by using two-station interplanetary scintillation data obtained at decameter wavelengths.

Observations

We carry out IPS observations with UTR-2 (8÷32 MHz) and URAN system (8÷32 MHz) radio telescopes [Braude S.Ya et. al, 1978, Megn A.V. et. al, 2003] (Figure 2) since 2006.

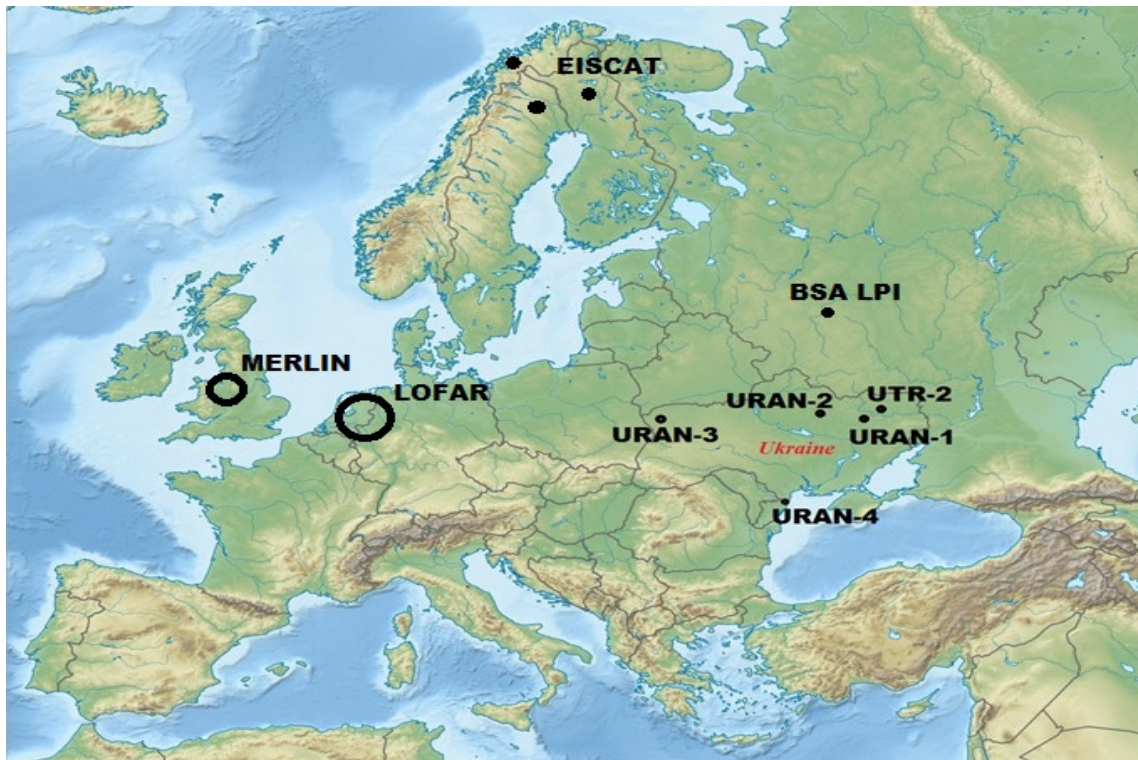


Fig.2 Ukrainian decameter radio telescopes for IPS observations UTR-2 and URAN-1-4 on the map

The data used in this investigation were obtained by using UTR-2 (Grakove) and URAN-2 (Poltava) radio telescopes (base 152 km) during the period from January 12 to January 17, 2016. The use of the high linearity wideband receivers and records from several radio telescopes allow us to apply a special technique for selecting data, which are not corrupted by Earth's ionosphere and interferences, and to achieve sensitivity that is close to maximal. Figure 3 shows an example of IPS records obtained with UTR-2 radio telescope.

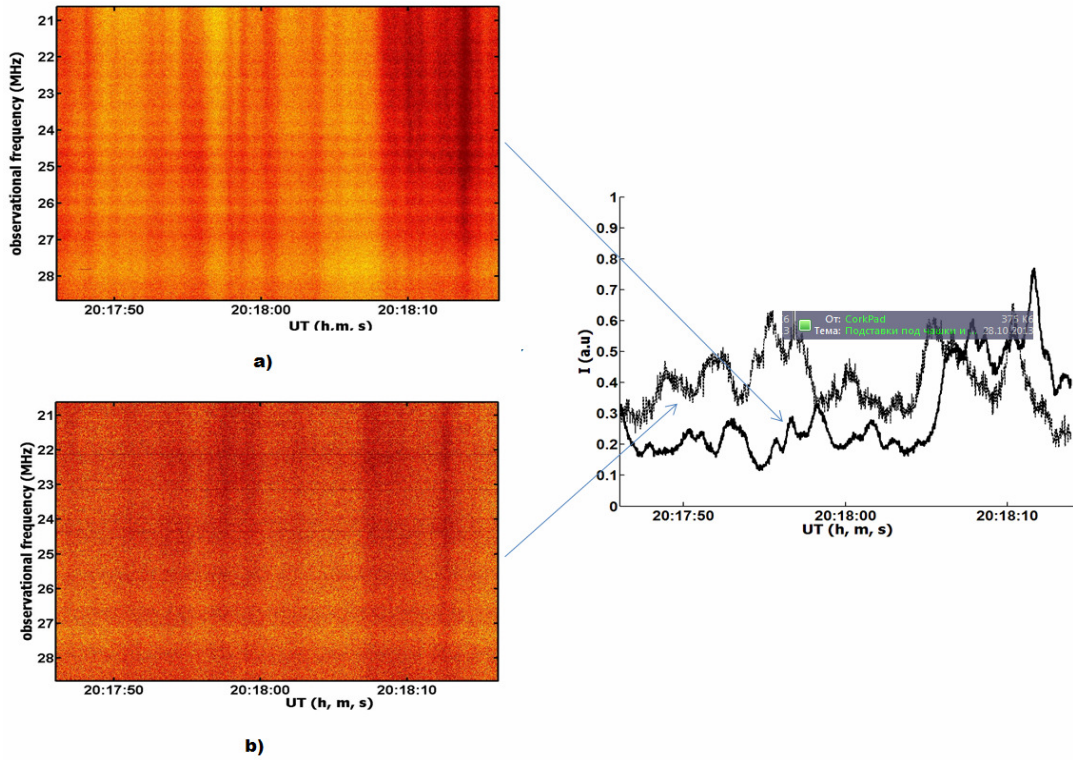


Fig.3 Dynamic spectra which were synchronously obtained by using the radio telescopes UTR-2 (a) and URAN-2 (b). January 12, 2016.

The processing of experimental IPS data consisted in estimation of the experimental spectra and experimental cross-correlation functions between records in two sites. If more than one stream presented on the line of sight to the radio source, the additional knees appeared on experimental spectrum and asymmetric cross-correlation functions were observed.

The model

The solar wind stream structure is obtained by fitting the model theoretical characteristics to the experimental ones as you see in Figure 4. For model fitting we obtain equations for theoretical spectrum (1) and cross-spectrum (2) by using Feinman path integral technique [Frehlich R.G., 1987]. These equations give better results than equations obtained by using phase screen model and allow us to estimate the width of the solar wind stream. We consider spectrum and cross-correlation function as a sum of contribution from each flow.

$$W(f) = \sum_{m=1}^M W_m(v_m, f)$$

$$W_m(v_m, f) \approx 2\pi l_0^2 l_m \left(\frac{4\pi r_e^2}{k} \right)^2 \int_0^1 d\zeta \int_{2\pi/v_{m\perp}(\zeta)}^{\infty} \sin^2 \left(\frac{\kappa_{m\perp}^2 l_m \zeta}{2k} \right) \times \frac{\kappa_{m\perp} \Phi_{Nm}(\kappa_{m\perp}, 0, \zeta)}{\sqrt{\zeta(\kappa_{m\perp}^2 v_{m\perp}^2(\zeta) - 4\pi^2 f^2)}} \exp \left(-\frac{1}{2} \kappa_{m\perp}^2 L^2 \zeta^2 \theta_0^2 \right) d\kappa_{m\perp} \quad (1)$$

$$W(b, f) = \sum_{m=1}^M W_m(b, v_m, f) \quad (2)$$

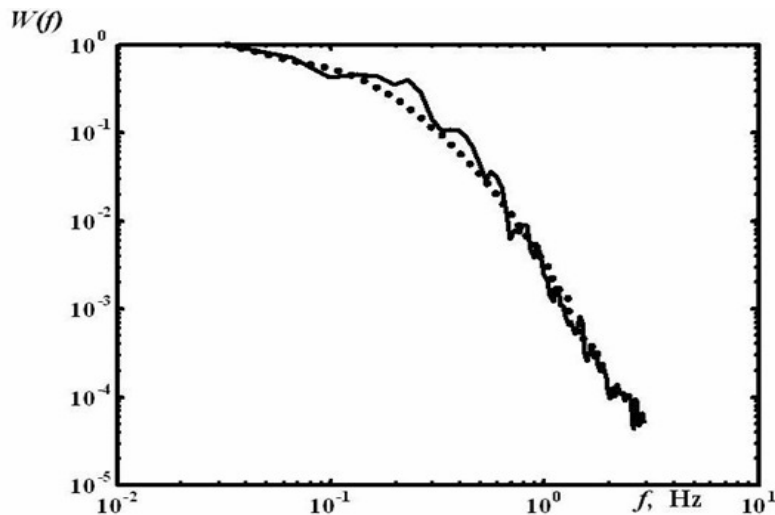
$$W_m(b, v_m, f) \approx$$

$$\approx 2\pi I_0^2 l_m \left(\frac{4\pi r_e^2}{k} \right)^2 \int_0^1 d\zeta \int_{2\pi f/v_{m\perp}(\zeta)}^{\infty} \sin^2 \left(\frac{\kappa_{m\perp}^2 l_m \zeta}{2k} \right) \exp \left(\frac{2\pi i f b \cos \beta_m}{v_{m\perp}(\zeta)} \right) \times$$

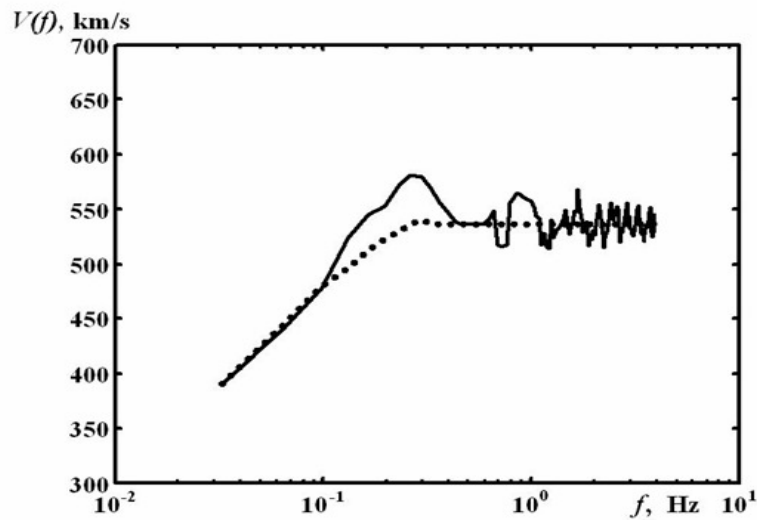
$$\times \frac{\kappa_{m\perp} \Phi_{Nm}(\kappa_{m\perp}, 0, \zeta)}{\sqrt{\zeta(\kappa_{m\perp}^2 v_{m\perp}^2(\zeta) - 4\pi^2 f^2)}} \exp \left(-\frac{1}{2} \kappa_{m\perp}^2 L^2 \zeta^2 \theta_0^2 \right) d\kappa_{m\perp}$$

Dispersion dependence can be written as:

$$V_f(f) = 2\pi f b \cos \beta / \Delta\Psi, \text{ where } \Delta\Psi = \arccos(\text{Re} W(b, f) / |W(b, f)|)$$



a)



b)

Fig. 4 Model fitting procedure. Experimental (solid lines) and model (dotted lines) spectra (a) and dispersion dependences (b)

Reconstructed stream structure of solar wind

Figure 5 shows an example of the reconstruction of the solar wind stream structure for January 13, 2016. The different streams are marked by the different colors - the higher

velocity, the deeper red color is used. There are two streams of the solar wind on the line of sight to the radio source 3C144: the fast flow with parameters: speed $v_1=530$ km/c, spectral index of the interplanetary turbulence spectrum $n_1=3.9$, the width $l_1=0.4$ a.e., and the slow flow with $v_2=400$ km/c, $n_2=3.9$, $a_2=2.2$, $l_2=2$ a.e. The estimated solar wind speed on the line of sight to the radio source 3C144 is in agreement with one measured by spacecraft (during 12÷15 we see speed about 500 km/s and then it becomes lower).

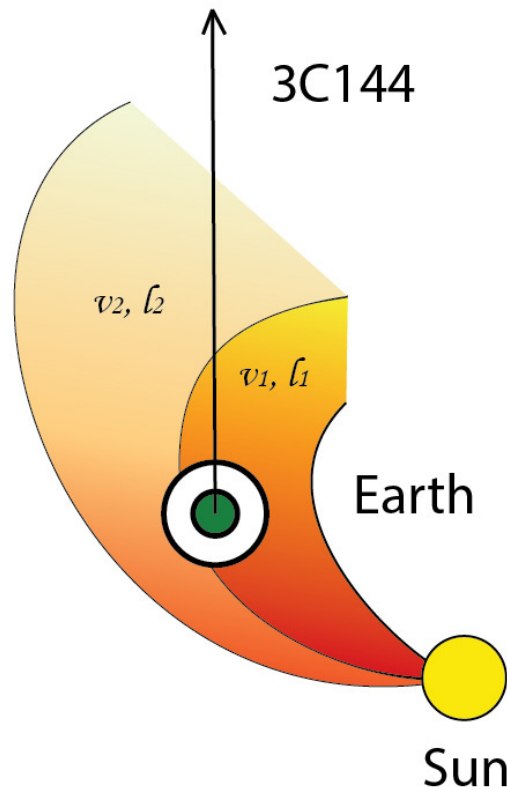


Fig. 5 The reconstructed stream structure of the solar wind for January 13, 2016

Conclusions

IPS observations at decameter wavelengths allow us to obtain the solar wind parameters and to reconstruct the stream structure of the solar wind beyond Earth's orbit. The future progress in this investigation is connected with using more scintillating radio sources. As the resolving ability of the IPS observations is improved due to the much larger baselines, the use of other European radio telescopes for synchronic observations of the same radio sources is desirable. Such approach is good from the standpoint of the different ionospheric effect and interference immunity.

Acknowledgment

This study was supported by Target Complex Program of the NAS of Ukraine for Scientific Space Studies for 2012-2017 "Synchronous investigations of solar system objects by methods of ground-space low-frequency radio astronomy. Complex studies of manifestations of solar activity"

References

- Braude S.J., A.V. Meg, L.G. Sodin (1978), Radio telescope of decameter wave range UTR-2, Antennas, Moscow, 28.
- Coles W. A. (1996), A bimodal model of the solar wind speed. *Astrophysics and Space Science*, 243, no. 1, 87–96.
- Dennison P.A., A. Hewish (1967), The solar wind outside the plane of the ecliptic. *Nature*, 213, 343-346.
- Falkovich I.S., A.A. Konovalenko, N.N. Kalinichenko, M.R. Olyak, A.A. Gridin, I.N. Bubnov, A.I. Brazhenko, A. Lecacheux, H. Rucker (2010), Dispersion Analysis of Interplanetary Scintillations at Decameter Wavelengths: First Results. *Radio Physics and Radio Astronomy*, 1, no. 1, 3-9.
- Frehlich R.G., 1987. Space-time fourth moment of waves propagating in random media. *Radio Science* 358, 481-492.
- Hewish A., P.F. Scott, D. Wills (1964), Interplanetary Scintillation of Small Diameter Radio Sources. *Nature*, 203, no. 4951, 1214-1217.
- Kalinichenko N.N. (2012), Scintillations of Radio Source 4C21.53 at decameter wavelengths and elongations 43o-138o. *Radio Physics and Radio Astronomy*, 3, no. 2, 131-138.
- Lang K.R. (1996), Unsolved Mysteries of the Sun. *Sky and Telescope*, 92, no. 2, 38.
- Megn A.V., N.K. Sharykin, V.V. Zakharenko, V.G. Bulatsen, A.V. Brazhenko, R.V. Vashishin (2003), *Radiofizika i radioastronomia*, no. 8, 345-361.

Decameter type IV burst associated with behind-limb CME observed on November 7, 2013

*Melnik V.*¹, *Brazhenko A.*², *Konovalenko A.*¹, *Dorovskyy V.*¹, *Rucker H.*³,
*Panchenko M.*⁴, *Frantsuzenko A.*², *Shevchuk*¹

¹ Institute of Radio Astronomy, Kharkiv, Ukraine

² Institute of Geophysics, Gravimetrical Observatory, Poltava, Ukraine

³ Commission for Astronomy, Graz, Austria

⁴ Catholic University of Leuven, Leuven, Belgium

E-mail: melnik@rian.kharkov.ua

ABSTRACT

We report the results of observations of type IV burst by URAN-2 in the frequency range 22÷33 MHz, which is associated with the CME initiated by behind-limb active region (1500E). This burst was observed also by the radio telescope NDA in the frequency band 30÷60 MHz. CME's core was situated at the distance about 3Rs at the moment, when type IV burst registered at frequencies 22÷60 MHz. We conclude that the radio emission escape from the center of CME's core at frequency 60 MHz and comes from the periphery of the core at frequency 30 MHz due to occultation by the solar corona at corresponding frequencies. We find densities in these regions supposing plasma mechanism of radio emission. We show that the frequency drift of the leading edge of type IV burst is governed by expansion of CME's core. Type III bursts, which were observed against type IV burst, are shown to be generated by fast electrons propagating through the CME core plasma. Type II burst registered at frequencies 40÷50 MHz and 5÷16 MHz was radiated by a shock with velocity about 1000 km/s.

INTRODUCTION

Type IV burst were classified in the separate type of solar phenomenon by Boishot in 1957 [*Boishot A.*, 1957]. They distinguish stationary and moving type IV bursts [*Stuart R.T.*, 1985]. Coronal arches and CMEs are considered to be responsible for the former and latter correspondingly. For a long time type IV bursts observed only in the decimeter and meter range [*Stuart, R.T.*, 1985]. Regular observations of these bursts at the decameter frequencies 8-32 MHz were began during 23 cycle at the radio telescopes UTR-2 and URAN-2 due to wide frequency range 60-channel spectrometers and DSPs (digital spectral polarimeters) [*Melnik, V.N., et al.*, 2008]. With launching WIND and later STEREO A and B a possibility to observe type IV bursts in the hectometer range was appeared [*Gopalswamy, N., et al.*, 2016], [*Hillaris, A. et al.*, 2016].

There are some points concerning to mechanism of type IV bursts radio emission, the places from which radio emission at different frequencies escape, beaming of radiation of these bursts, their connections with type II bursts and SEPs, and others [*Stuart, R.T.*, 1985], [*Aschwanden, M.J.*, 2004], [*Gopalswamy, N.*, 2011], which remain under the question.

Recently appeared the paper [*Gopalswamy, N., et al.*, 2016], in which the event on November 7, 2013 was discussed. This day CME was ejected in behind limb region. It was accompanied by type IV burst observed by STEREO A and B from 10:40 UT to 11:50 UT and did not registered by WIND. The authors concluded that the directivity of type IV radio emission was narrow, about 60⁰, along its movement and that observed type IV burst was stationary not moving.

This day the radio telescope URAN-2 (Poltava, Ukraine) carried out observation from 06:00 UT to 13:30 UT in the frequency band 17÷33 MHz. Beginning from 10:22 UT and up to 10:44 UT this type IV burst was registered. At approximately this time the burst also was observed by NDA (Nancay, France) in the frequency band 30÷60 MHz. In this report we

discuss a possible source of this type IV radio emission basing on results of observations of telescopes URAN-2, NDA, STEREO A and B and SOHO.

RESULTS and DISCUSSION

The radio telescope URAN-2 is situated near Poltava (Ukraine) [Brazhenko, A.I., et al., 2005]. Its effective area is about 28 000 sq.m that gives a very good sensitivity. The working frequency band is 8÷33 MHz but this day observations were carried out from 17 to 33 MHz because of ionosphere interferences. Registration was produced with DSPz, which allowed to have frequency – time resolutions 4kHz - 100ms. The radio telescope also measured polarization of registered radio emission.

In fig.1 the dynamic spectrum of solar radio emission from 10:17 UT to 11:01 UT in the frequency band 17÷33 MHz is shown. It is seen that type IV burst began at approximately at 10:22 UT and finished at 10:44 UT. There are also type III bursts against type IV burst. The fluxes of the type IV burst and type III burst achieved 30-40 s.f.u. and 100 s.f.u. Polarizations of these bursts were high, a little smaller than 40% for type IV burst and up to 50% for type III bursts. Type III bursts were diffusive with sub-bursts with positive and negative frequency drift rates 2-6 MHz/s. At the same time the drift rate of type IV burst forehead was about 30 kHz/s.

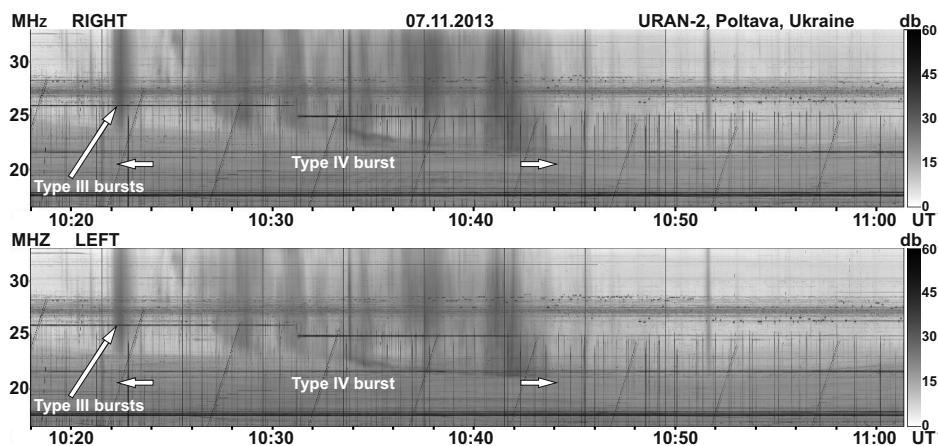


Fig.1. Type IV burst and type III bursts according to URAN-2 on November 7, 2013.

The radio telescope NDA observed the Sun (fig.2) this time also. We see that the type IV burst and the same type III bursts were also registered at approximately those time as at radio telescope URAN-2 but at frequencies 30-60 MHz. Besides a weak type II burst with drift rate about 250kHz/s was observed at frequencies 44-64 MHz from 10:16 UT to 10:17 UT.

As reported in [Gopalswamy, N., et al., 2016] STEREO A and B registered type IV burst, type III bursts and type II burst approximately at those time (fig.3) as radio telescopes URAN-2 and NDA but a little later. Authors of [Gopalswamy, N., et al., 2016] associated this event with CME, which initiated by active region with longitude 150° in the Earth view. This CME propagated practically in the direction of STEREO B (fig.4b) so it was registered by STEREO B as halo-CME. At the same time STEREO A registered this CME as a compact object with bright core and envelope (fig.4a). The velocity of this CME was high, up to 2000 km/s [Gopalswamy, N., et al., 2016].

The fact, that both type IV burst and type III bursts associated with behind-limb CME are seen at frequencies 22-60 MHz at ground-based radio telescopes, raises a question about the places of sources of these bursts and their connection with CME. The locations of CME core and its sizes (obtained from STEREO A data) at 10:22 UT and 10:28 UT, when the type IV burst was observed in frequencies ranges 30-60 MHz and 23-30 MHz, are shown in fig.5.

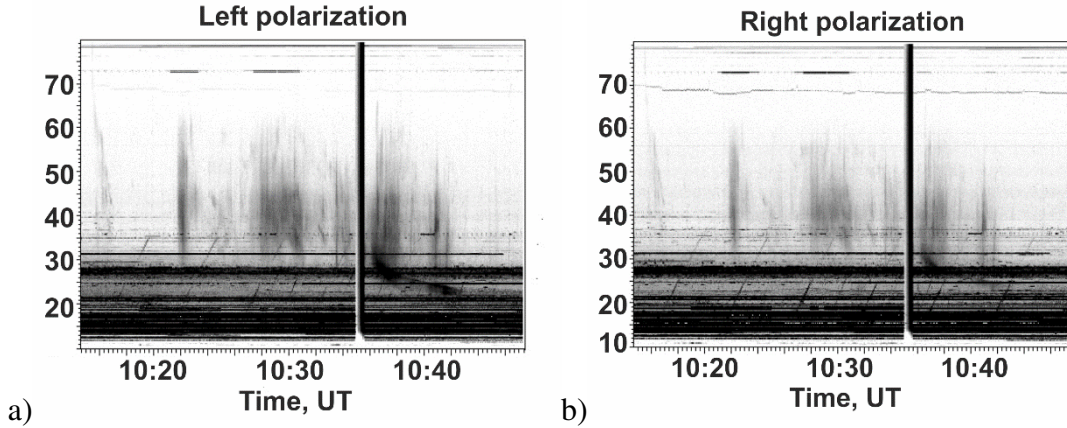


Fig.2. Type IV burst, type III bursts and type II burst observed by radio telescope NDA on November 7, 2013 – left (a) and right (b) polarizations.

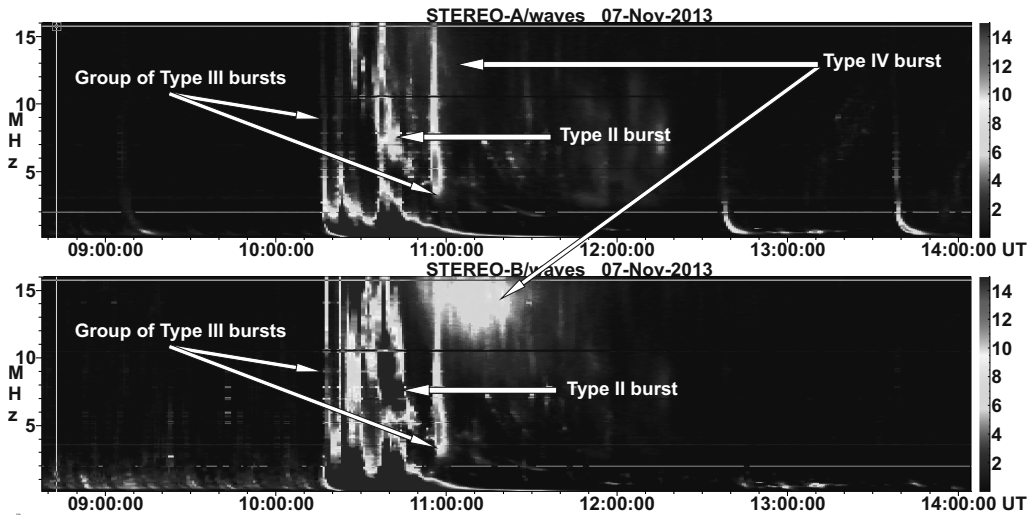


Fig.3. Type IV burst, type III bursts and type II burst according to STEREO A and B.

Also levels of local plasma frequencies 23, 30 and 60 MHz and the regions of occultation by Newkirk’s solar corona are given. From the fig.5 we see that radio emissions at 23, 30 and 60 MHz escape from the regions to the left from lines $f_{NK} = 23, 30, 60$ MHz correspondingly. If we suppose that the source of type IV burst is the CME core then radio emissions at frequencies 23 and 30 MHz escape from the periphery regions of core and at frequency 60 MHz from its center. Assuming plasma mechanism of radio emission, we find densities in the center ($n_c = 4.5 \cdot 10^7 \text{ cm}^{-3}$) and in periphery regions ($n_c = 1.3 \cdot 10^7 \text{ cm}^{-3}$) of CME core. If the density distribution in the core is exponential

$$n(r) = n_c \exp(-\alpha r) \quad (1)$$

where r is the distance from the core center, then $\alpha = 2.5/R_s$ taking into account that at $r = 0.5R_s$ (the core radius at 10:22 UT) density equals $n(r=R_s/2) = n_p = 1.3 \cdot 10^7 \text{ cm}^{-3}$. For compensation of gas kinetic pressure $p = nkT$ at core surface by magnetic pressure $p_B = B^2/8\pi$ it needs magnetic field $6 \cdot 10^{-2} G$ at plasma temperature in the core $T = 10^5 K$ and $0.6 G$ at temperature $T = 10^6 K$. The density of surrounding coronal plasma at distance $R = 2.8R_s$ equals only $n_p = 1.2 \cdot 10^6 \text{ cm}^{-3}$ that is essentially smaller than the density in the core at this distance.

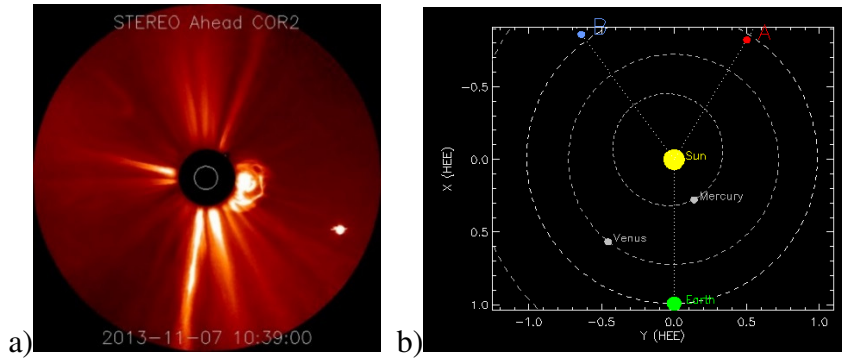


Fig.4. CME according to STEREO A (a) and STEREO A and B on the Earth orbit on November 7, 2013 (b).

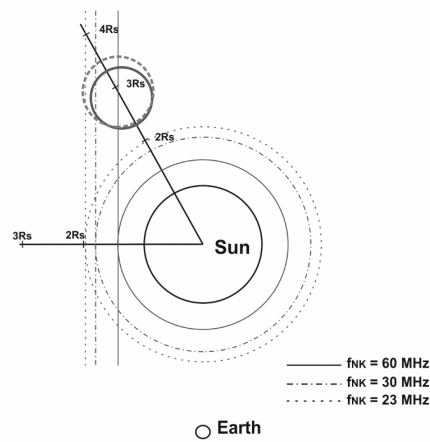


Fig.5. Schematic positions of CME core at 10:22 UT and 10:28 UT, the Sun and the Earth and levels in the solar corona, which corresponds local plasma frequencies 23, 30 and 60 MHz.

The mass of the CME core at density distribution (1) can be estimated as

$$M_{CME} = 4\pi \int_0^{R_c/2} m_p \cdot n(r) \cdot r^2 dr \approx 10^{16} g \quad (2)$$

This value is in agreement with SOHO data (https://cdaw.gsfc.nasa.gov/CME_list/UNIVERSAL/2013_11/univ2013_11.html).

Due to expansion of core the periphery density decreases and this leads to the frequency drift of forehead of type IV burst whose drift rate is defined by the equation

$$df/dt = f/2 \cdot dn/ndr \cdot dr/dt \quad (3)$$

where dr/dt is the velocity of core expansion which is equaled to 300 km/s according to STEREO A data.

Taking into account the inhomogeneity size the drift rate is about 27 kHz/s in the frequency range 22÷33 MHz that is in good agreement with observations. As we see in fig.1÷fig.3 the single type III bursts and their groups at 10:22 UT, 10:29 UT, 10:32 UT, 10:35 UT, 10:37 UT и 10:42 UT were registered by NDA, URAN-2, STEREO A and STEREO B. But it is worth to notice that if type III bursts at frequencies 22÷60 MHz were observed against type IV burst, these bursts at frequencies lower 16 MHz went before the type IV burst. At the same time rather powerful type III bursts at 10:18 UT and 10:58 UT observed by STEREO A and B were absent on the dynamic spectrum of URAN-2 and NDA. Such specific feature of appearance of type III bursts can be understood if to suppose that

visible with all radio telescopes bursts escape from the CME core, when they radiated at frequencies 22÷60 MHz and out of the core, when they radiated at frequencies lower 16 MHz. If only these bursts generated radio emission at frequencies 22-60 MHz from the coronal plasma the ground based radio telescopes could not registered them because of occultation by solar corona (fig.5). Consequently, we conclude that we observed fast electrons which propagate through plasma of CME core at first and after that these electrons go out of core and propagate in the coronal plasma before CME core. Moreover, we see that these electrons pass the front of shock, which is responsible for type II burst seen on the dynamic spectrum of STEREO A and B. The fact that radio emission at frequencies 22-60 MHz escape from the CME core confirmed by diffuse character of type III bursts at these frequencies, which is manifested in a large number of sub-bursts with different positive and negative drift rates. This reflects the complex structure of core plasma with different inhomogeneities. Type III burst at 10:18 UT (Fig.3) escaped from the coronal plasma before CME and as a result the ground-based radio telescopes could not observe this burst due to occultation, but STEREO A and B registered it. Analogically the type III burst at 10:58 UT (fig.3) could not be observed by the radio telescopes UTR-2 and URAN-2 because type III electrons passed the distances $1.4\div 2R_s$ (fig.5) in the solar corona, from which radio emissions at frequencies 22÷60 MHz are generated, in 30 minutes later after passage these altitudes by CME.

The velocity of shocks, which were responsible for Type II bursts observed at frequencies 44÷64 MHz and 3÷16 MHz, can be derived from the Equation (3), where dr/dt is the required velocity and it can be estimated as 1000 km/s and 800 km/s correspondingly. Taking into account that the velocity of CME was 2000km/s [Gopalswamy, N., et al., 2016] we conclude that type II bursts were radio emissions of flank shocks.

CONCLUSIONS

We report the results of observations of type IV burst associated with behind-limb CME (E 150⁰) by ground-based radio telescopes URAN-2 and NDA in the frequency range 22÷60 MHz. This burst can be belonged to moving type IV bursts with frequency drift rate about 30 kHz/s at frequencies 22÷33 MHz. The registration of this burst at the Earth was possible if to suppose that radio emission leaves the CME core with the density in the center $n_c = 4.5 \cdot 10^7 \text{ cm}^{-3}$ and the density in the core periphery $n_p = 1.3 \cdot 10^7 \text{ cm}^{-3}$. The expansion of the core provides the observed frequency drift rate of type IV forehand.

The observed type III bursts and their groups against type IV burst in the frequency band 23÷60 MHz were generated by fast electrons propagating through the core plasma. After leaving the core these electrons got out into the coronal plasma, where generated radio emission at lower frequencies, which was registered by STEREO A and B.

Type II bursts observed in the frequency bands 44÷64 MHz and 3÷16 MHz were initiated by the flank shock associated with CME.

References

- Aschwanden, M.J. Physics of the Solar Corona. An Introduction. - Chichester, UK: Springer-Verlag Berlin, 2004. - P: 892.
- Boischo A. Caractères d'un type d'émission hertzienne associé à certaines éruptions chromosphériques // Academie des Sciences Paris Comptes Rendus. -1957.-244.-P:1326-1329.
- Brazhenko, A.I., Bulatsen, V.G., Vashchishin, R.V., Frantsuzenko, A.V., Konovalenko, A.A., Falkovich, I.S., Abranin, E.P., Ulyanov, O.M., Zakharenko, V.V., Lecacheux, A., Rucker, H. New decameter radiopolarimeter URAN-2 // Kinematika i Fizika Nebesnykh Tel. – 2005. – 5. – P: 43-46.
- Gopalswamy, N. Coronal Mass Ejections and Solar Radio Emissions // Proceedings PRE VII. Austria, 2011. – P: 325-342.
- Gopalswamy, N., Akiyama, S., Mäkelä, P., Yashiro, S., Cairns, I.H. On the Directivity of Low-Frequency Type IV Radio Bursts // eprint arXiv:1605.02223, 2016.
- Hillaris, A.; Bouratzis, C.; Nindos, A. Interplanetary Type IV Bursts // Solar Physics. – 2016. – 291(7). – P: 2049-2069.
- Melnik, V.N. , H. O. Rucker, A. A. Konovalenko, V.V. Dorovskyy, E.P. Abranin, A.I. Brazhenko, B.Thide, A. A. Stanislavskyy. Solar Type IV Bursts at Frequencies 10-30 MHz // Solar Physics Research Trends. - Nova Publishers, 2008. – P: 287-325.
- Stuart, R.T. Moving Type IV bursts // Solar Radio Physics. - Cambridge: Cambridge University Press, 1985. - P: 361-384.

Solar radio burst emission from proton-producing flares and coronal mass ejections

*R. Miteva*¹, *S.W. Samwel*², *V. Krupar*^{3,4,5}

¹ Space Research and Technology Institute, Bulgarian Academy of Sciences, Bulgaria

² National Research Institute of Astronomy and Geophysics (NRIAG), Egypt

³ Universities Space Research Association, USA

⁴ NASA Goddard Space Flight Center (NASA/GSFC), USA

⁵ Institute of Atmospheric Physics (CAS), Czech Republic

E-mail: rmiteva@space.bas.bg

Abstract.

We present the occurrence trends of radio burst types in relations to the origin of solar energetic proton events – flares and coronal mass ejections (CMEs) – during the ongoing solar cycle 24 (2009÷2016). Namely, we analyze the occurrence of type II, type III and type IV radio bursts in specific frequency ranges, either as a support for the flare-origin when the emission originates from the low corona or for the CME-origin, when the radio bursts originate in the high corona.

Introduction

Electrons, protons and heavy ions are energized during acceleration processes in the solar corona and interplanetary (IP) space as evidenced by their remotely observed electromagnetic (EM) emission and in situ detection [*Desai and Giacalone, 2016*]. The radiation due to magnetic reconnection process at solar flares can covers virtually the entire EM range, from gamma to radio wavelengths and is used to deduce the energy range of the accelerated particles as well as the physical mechanisms that take place in the solar atmosphere. In addition, shock acceleration process is expected to take place ahead of coronal mass ejections (CMEs) and is widely used as evidence for particle acceleration in the corona and IP space. [*Klein and Dalla, 2017*] recently reviewed the different acceleration mechanisms of SEP events.

The keV to MeV solar energetic particles (SEPs) cannot enter the terrestrial magnetosphere and are detected only in situ by satellites. Only particles at GeV energies can be detected by ground-based (neutron and muon) detectors via their secondary particles produced during interactions with terrestrial atmosphere. The solar origin is evidenced by the fact that these particles follow in time the eruptions observed at the Sun and the particle profiles show velocity dispersion characteristics.

Radio emission provides a straightforward diagnostic tool to detect and interpret the various radio signatures observed from the low solar atmosphere to Earth see reviews by [*Nindos et al. 2008* and *Pick and Vilmer, 2008*]. Emission tracks in dynamic radio spectral plots are used as evidence for particle escape from the solar corona, their travel through the IP space, and arrival at Earth.

Historically, the different radio emission signatures were organized into five distinct burst types according to a scheme proposed by [*Wild et al. 1963*]. However types II, III and IV are expected to be the relevant ones for space weather [*Warmuth and Mann 2005*]. Nowadays, it is accepted that type II radio bursts are the signatures of MHD shock wave traveling at speeds of the order of 1000 km/s in the corona and faster than the ambient solar wind in the IP space. Type III bursts are generated by electron beams with typical speed around 0.3 of the speed of light, more often observed to propagate outwards to lower frequencies than inwards, towards the surface [*Aschwanden 2004, Pick and Vilmer, 2008*]. Type IV bursts show much more complexity in appearance (as moving/stationary emission patches) and cover much larger frequency and time ranges compared to the other two types. They are regarded as the

emission from electrons in closed magnetic structures, either in the low atmosphere or/and during CME lift-off.

Numerous earlier studies investigate the link between the solar radio emission signatures and SEP events. These works can be roughly divided into studying the occurrence of radio emission types, their timing and/or spectral behavior in relation to in situ observed particles. The present report contributes to the former kind of analysis.

The occurrence of different radio signatures mostly during solar cycle (SC) 23 has been investigated in numerous studies see a comparative study by [Miteva *et al.* 2013] and references therein). Different authors report different percentages of occurrence of types II, III and IV in relation to energetic protons, with types II and/or III being the most frequently observed. The specific choice of the radio wavelength (low, middle, high corona and IP space), energy range (>10 MeV to >100 MeV) and intensity level of the energetic protons (weak vs. major/large events), as well as using relatively small event sample (partial SC coverage), contributes to the possible reasons for the reported differences.

Data

The present analysis is regarded as an extension of an earlier work [Miteva *et al.* 2013], namely we consider the time period after 2009. We started by complementing proton identifications from several on-line event catalogs during the ongoing SC24 (2009÷2016). In total 128 proton events were found. The solar origin identification is according to the set of guidelines proposed by [Miteva *et al.* 2017a,b].

We continue the analysis with the search for radio emission signatures during the time from onset-to-max of the flare (using the GOES soft X-ray emission: <ftp://ftp.ngdc.noaa.gov/STP/space-weather/solar-data/solar-features/solar-flares/x-rays/goes/>) and about one hour prior the CME first occurrence (in LASCO/C2 coronagraph field of view: https://cdaw.gsfc.nasa.gov/CME_list/).

The radio bursts were visually identified by inspecting radio dynamic spectra (quick-look plots) as provided by observatories and databases based on ground-based or satellite data (Table 1). When no radio plot was found, we complemented the identifications with the reported radio bursts by different sources (Table 2).

Results

We collect the number of occurrences of a given burst type and calculate their ratio to the entire event sample. In order to investigate the spectral behavior, we separated the radio frequency into five representative ranges, namely: decimetric (dm: 3÷1 GHz); decimetric to metric (dm–m: 1÷0.3 GHz); metric (m: 300÷100 MHz); metric to Dekametric (m–Dm: 100÷30 MHz); and Dekametric to kilometric range (Dm–km: 30÷0.01 MHz).

In this report we describe radio bursts of types II, III and IV within specific frequency coverage in order to test the flare vs. CME contribution to the escaping particles. In order to limit the influence by multiple accelerators (mixed cases), we require the radio burst to originate either from the very low corona (for flare dominated acceleration) or in the very high corona (CME-dominated acceleration). In the metric range, a mixed contribution from flares and CME is plausible, thus no firm conclusions can be made. We also impose the condition for escape of the radio emission (namely to be observed at low radio frequencies at distances near Earth), although the continuation of a given radio burst may not be entirely due to the expected accelerator and contributions from the alternative accelerator are possible. All results are given in a percentage, namely as a ratio to the entire event sample (128 events).

Table 1 Web-links to the solar radio observatories providing dynamic radio spectra.

| | |
|-------------------------|---|
| Ondrejov | http://www.asu.cas.cz/~radio/info.htm |
| Phoenix | http://soleil.i4ds.ch/solarradio/data/1998-2009_quickviews/ |
| e-Callisto | http://soleil.i4ds.ch/solarradio/callistoQuicklooks/ |
| HiRAS | http://sunbase.nict.go.jp/solar/denpa/index.html |
| Culgoora/Learmonth | http://www.sws.bom.gov.au/World_Data_Centre/1/9 |
| Radio monitoring | http://secchirh.obspm.fr/select.php |
| ARTEMIS | http://artemis-iv.phys.uoa.gr/Artemis4_list.html |
| IZMIRAN | http://www.izmiran.ru/stp/lars/s_archiv.htm |
| Green Bank/Bruny Island | http://www.astro.umd.edu/~white/gb/index.shtml |
| Wind and STEREO | https://solar-radio.gsfc.nasa.gov/wind/data_products.html |

Table 2 Web-links to the solar radio observatories providing radio burst reports.

| | |
|-------------------------|--|
| NOAA | ftp.ngdc.noaa.gov/STP/space-weather/solar-data/solar-features/solar-radio/radio-bursts ftp.ngdc.noaa.gov/STP/swpc_products/daily_reports/solar_event_reports/ |
| Phoenix/e-Callisto | http://soleil.i4ds.ch/solarradio/ |
| HiRAS | http://sunbase.nict.go.jp/solar/denpa/spe_summary/ |
| Culgoora/Learmonth | http://www.sws.bom.gov.au/World_Data_Centre/1/9 |
| Artemis | http://artemis-iv.phys.uoa.gr/DataBaseForWeb/data_set.htm |
| IZMIRAN | http://www.izmiran.ru/stp/lars/MoreSp.html |
| Green Bank/Bruny Island | http://www.astro.umd.edu/~white/gb/index.shtml |
| Wind/WAVES | https://solar-radio.gsfc.nasa.gov/wind/data_products.html |

a) Flare-accelerated particle contribution to SEP events

We test the flare-contribution to the escaping flux by imposing certain constrains on the occurrence of given burst types and the frequency ranges where they are observed. Although we cannot completely exclude energetic particles produced due to the alternative accelerator (CME), we can set a condition allowing us to argue in favor of a flare-accelerated flux escaping into the IP space. We also suppose that the particles escaping the Sun originate from the population produced in the deep solar corona, due to the observed continuity of the radio signatures.

The straightforward choice is to select the case where only type III radio bursts are present in the radio spectrum, without the occurrence of any other burst types (neither type IIs nor type IVs). We add all cases whenever type III bursts are observed continuously from low to high corona, starting from the frequency range 3 GHz to 0.01 MHz and continuing with the range 1 GHz to 0.01 MHz and so on. We found in total 12 events (~9%) that satisfy the condition, however, among them:

- none cover the entire range;
- only 1 covers the range 1 GHz÷0.01 MHz;
- 3 are in the range 300÷0.01MHz;
- 3 are in the range 100÷0.01 MHz and
- 5 are observed only in the IP band (30÷0.01 MHz).

Since the number of type III at lowest frequencies is higher than at highest frequencies, we cannot exclude additional type III generation due to acceleration driven by CME for the latter 5 cases, even without the formation of type IIs there.

An alternative selection criterion is to relax the above condition by allowing the appearance of type IV bursts in the 3 GHz÷300 MHz range and requiring neither type II nor IV to be present in the range 300÷0.01 MHz. However, we could only add 2 more type III events to the 30÷0.01 MHz range.

Thus we find that, with large amount of certainty, only 7/128 radio bursts (~5%) can be due to flares, whereas the other maximum 7 type III events have a probable flare contribution, but CME influence is not excluded.

For comparative purpose, we relax the above criterion, by allowing type II and IV bursts to be present in the radio spectra, however the type III signatures must start from 1 GHz and extend up to 0.01 MHz, respectively. In this case we find 35 type III events (~27%) that are accompanied also by other radio emissions. From this sample 8 type III bursts (~6%) start at the highest frequency investigated here (from 3 GHz). Thus, we can argue in favor of a probable flare-contribution in slightly more than one quarter of all SEP events.

b) CME-accelerated particle contribution to SEP events

The occurrence of type II burst is usually considered as evidence for shock acceleration. In order to exclude the contribution from coronal (i.e., flare-driven) shocks or other flare-related emission, we select type II bursts observed in the range 100÷0.01 MHz allowing for type III and IV to be present also at the same time and range, whereas no low coronal emission of any kind is allowed. In total 15 events (~12%) fulfill this condition. From this sample, we found:

- 4 events (~3%) when type II burst is present in the entire range (100÷0.01 MHz);
- 10 events (~8%) when the type II is present only in the range 30÷0.01 MHz (and always accompanied by type III there);
- 1 event (~1%) when type II burst is present only in the range 100÷30 MHz (however type III is present in the 30÷0.01 MHz range).

Conclusions

During the period 2009÷2016 we investigate the flare and CME contribution to the observed in situ SEP events in terms of solar radio burst signatures. We summarize our preliminary results as follows:

1. Flare-related acceleration is expected in ~27% and ~6% of all SEP cases, depending on the requirement for type III emission starting at 1 and 3 GHz, respectively. With high degree of certainty, only 5% of the all observed SEP events can be considered as flare-dominated.
2. CME-dominated acceleration is found in ~12% of the all SEP events. In ~8% of them type IIs are observed only in the IP range (without radio emission at metric and higher frequencies) and thus the CME is regarded as the primary driver.
3. In the majority of SEP cases, however, the flare and CME contributions cannot be clearly separated by means of occurrence of radio emission signatures as a function of frequency. Other means of data analysis (e.g., temporal and/or spectral studies) need to be explored.

Acknowledgment

This study is partially supported under the Project on Collaborative research between Bulgaria and Russia “On the origin of solar energetic particles: solar flares vs. coronal mass ejections”, funded by the National Science Fund of Bulgaria with Contract № ДНТС/Русия 01/6 (from 23 June 2017). V.K. acknowledges the support of the Czech Science Foundation grant 17-06818Y.

References

- Aschwanden, M. J. (2004) *Physics of the Solar Corona. An Introduction*, Chapter 13, Published by Praxis Publishing Ltd., Chichester, UK, and Springer-Verlag Berlin ISBN 3-540-22321-5
- Desai, M., Giakalone, J. (2016) Large gradual solar energetic particle events, *Living Reviews in Sol. Phys.*, Vol. 13, no. 3
- Klein, K.-L., Dalla, S. (2017) Acceleration and propagation of Solar Energetic Particles, accepted, DOI: 10.1007/s11214-017-0382-4
- Pick, M., Vilmer, N. (2008) Sixty-five years of solar radioastronomy: flares, coronal mass ejections and Sun Earth connection, *Astronomy and Astrophys. Rev.*, Vol. 16, 1-153
- Miteva, R.; Klein, K.-L.; Samwel, S. W.; Nindos, A.; Kouloumvakos, A.; Reid, H. (2013) Radio Signatures of Solar Energetic Particles During the 23rd Solar Cycle, *CEAB*, Vol. 37, no. 2, 541-553
- Miteva R., Samwel S.W., Costa-Duarte M.V. (2017a) Solar energetic particle catalogs: Assumptions, uncertainties and validity of reports, *JASTP*, 9pp., in press
- Miteva R., Samwel S.W., Costa-Duarte M.V. (2017b) The Wind/EPACT proton event catalog (1996–2016), submitted.
- Nindos, A.; Aurass, H.; Klein, K.-L.; Trottet, G. (2008) Radio Emission of Flares and Coronal Mass Ejections. Invited Review, *Solar Physics*, Vol. 253, no. 1-2, 3-41
- Warmuth A., Mann, G. (2005) The Application of Radio Diagnostics to the Study of the Solar Drivers of Space Weather, *Lecture Notes in Physics*, Vol. 656, 49
- Wild, J. P.; Smerd, S. F.; Weiss, A. A. (1963) Solar Bursts, *Annual Review of Astronomy and Astrophysics*, Vol. 1, 291

Eight types of the solar wind and their origins

I.S. Veselovsky^{1,2}, *K.B. Kaportseva*³, *A.T. Lukashenko*¹

¹ SINP MSU, Moscow, Russia

² IKI RAN, Moscow, Russia

³ Faculty of Physics, MSU, Moscow, Russia

E-mail: a_lu@mail.ru

Abstract.

In July 2016 high cadence data from the new DSCOVR satellite, launched at the Lagrange point in February 2015, became available. On the basis of these data a binary (large-small) three-parameter classification of solar wind types, according to the main hydrodynamic parameters (speed, density and temperature), is presented, and examples of the determination of different types of solar wind in real time are given. We get eight types of solar wind: fast-hot-dense, fast-hot-rarefied, fast-cold-dense, fast-cold-rarefied, slow-hot-dense, slow-hot-rarefied, slow-cold-dense, slow-cold-rarefied, comparing to some average values for given time intervals. These types occur at different frequencies and represent consequences of different solar activity sorts. The most interesting situations correspond to extreme values because of magnetospheric effects. This report considers possible solar “sources” of listed types.

Introduction

a) History

It has long been known that the solar wind isn't permanent, but consists of separate plasma streams with different hydrodynamic and magnetic characteristics. The difference between types of streams is conditional, not absolute, so there is still no generally accepted nomenclature, which turns out to be different for different authors.

One of the first publications, where the classification of the solar wind was presented, was the Hundhausen's monograph [*Hundhausen A.J.*, 1972]. It provides a classification based on the comparison of the characteristic time scale of the phenomenon with three physical time scales: time interval t_1 needed for the solar wind to pass through the height scale of density in the corona, 2) the sound wave propagation time t_2 , and, and 3) time of a plasma passage of the length of the proton cyclotron radius t_3 .

In Richardson's with co-authors works (see [*Richardson I.G.*, 2012] and references therein) the solar wind observed near the Earth was divided into three types of streams: 1) corotating high-speed streams, 2) slower, interstream solar wind, and 3) transient flows originating with coronal mass ejections (CMEs) at the Sun.

In the works of Yermolaev and co-authors the classification of solar wind flows into several quasistationary and disturbed types is carried out and their geoefficiency is investigated (see, for example, [*Yermolaev Yu.I.*, 2010]).

b) Binary three-parameter classification

We now introduce a binary classification based on the three main hydrodynamic parameters: proton velocity, proton temperature and proton density. We will assume that wind belongs to one or another type if the parameters deviate from the averaged values by more than a certain threshold. With a smaller value of the threshold zones of each type of the solar wind expand. With more rigid value they narrow down and vanish. We can use different approaches. It depends on what is interesting for us. In this paper we took a threshold of 10%. So if the velocity is greater than 110% of averaged value, we consider that the wind is fast, if it is smaller than 90% of averaged value, we consider that the wind is slow, etc.

This formal approach allows us to determine eight solar wind types: fast-hot-dense (the abbreviation is FHD), fast-hot-rarefied (FHR), fast-cold-dense (FCD), fast-cold-rarefied

(FCR), slow-hot-dense (SHD), slow-hot-rarefied (SHR), slow-cold-dense (SCD) and slow-cold-rarefied (SCR). There is also some situations, if we get threshold greater then zero, when a solar wind stream doesn't belong to any of introduced types.

The attribution of the solar wind to a particular type also depends on the period for which the reference average values of the parameters are calculated as well as the nature of the data smoothing or its absence.

Data

At the DSCOVR spacecraft the fluxgate magnetometer measures the local magnetic field and the Faraday Cup measures solar wind bulk properties (wind speed, temperature and density). We used original DSCOVR data with a 3-second averaging (so called f3s data) without any additional smoothing. These data are presented with a periodicity of three counts per minute (4320 counts per day). The gaps in the data were approximated by a linear function.

The period from August 2016 to June 2017 was taken—eleven full months covered by DSCOVR data or 334 days. For this period averaged velocity, temperature and density are calculated: $\langle V \rangle = 469$ km/s, $\langle T \rangle = 2.42 \cdot 10^5$ K and $\langle n \rangle = 7.22$ cm⁻³. They are used as the reference values.

The following designation have been used: warm colors (orange, yellow, purple, pink) designate hot wind types, cold colors (blue and green)—cold types. Dense solar wind types are designated by dark colors and rarefied—by light colors. For fast wind types we tried to use more intense colors.

Results

a) Statistics

The most frequent for eleven months was SCD (15.1%), FHR (15.1%) и SCR (15.0%) wind types (Table 1). The FCD-type was the rarest (0.238%), and also SHR-type was rare (0.617%). One also can recall that slow wind dominate over fast wind in 2006–2007. It is because of lower solar activity at that time as compared with previous more powerful solar activity cycles [Veselovsky I.S. et al., 2010].

The statistical characteristics of the distribution of hydrodynamic quantities in four types, which are attributed to the same class, for example, the speed of “fast” (or “slow”) winds, differ substantially (Fig. 1). Thus, average speeds are higher for “hot” or “rarefied” winds than for “cold” or “dense” correspondingly (Table 2).

Table 1. Occurrence frequency of solar wind types in percent

| Solar wind type | Aug | Sep | Oct | Nov | Dec | Jan | Feb | Mar | Apr | May | Jun | Full period |
|-----------------|-------|-------|-------|-------|------|-------|------|------|------|-------|------|-------------|
| FHD | 0.83 | 7.2 | 2.2 | 0.67 | 1.4 | 5.2 | 6.9 | 8.2 | 15 | 5.2 | 0.29 | 4.81 |
| FHR | 25 | 16 | 26 | 7.3 | 8.3 | 5.5 | 16 | 34 | 6.3 | 14 | 8.1 | 15.1 |
| FCD | 0.001 | 0.003 | 0.006 | 0.10 | 0.53 | 0.70 | 0.41 | 0.26 | 0.52 | 0.002 | 0.08 | 0.238 |
| FCR | 1.8 | 0.36 | 7.6 | 11 | 20 | 22 | 3.1 | 2.3 | 0.63 | 0.86 | 1.0 | 6.55 |
| SHD | 5.1 | 8.8 | 17 | 0.002 | 0.91 | 0.005 | 0 | 0.97 | 0.22 | 0.25 | 1.6 | 3.17 |
| SHR | 2.8 | 0.10 | 0.17 | 0.01 | 0.60 | 0 | 0.05 | 0.01 | 0.17 | 2.4 | 0.35 | 0.617 |
| SCD | 15 | 16 | 6.6 | 19 | 15 | 13 | 17 | 10 | 12 | 25 | 18 | 15.1 |
| SCR | 0.50 | 0.08 | 0.05 | 29 | 25 | 13 | 9.2 | 20 | 18 | 25 | 26 | 15.0 |

Let us consider, as an illustration, the velocity parameter in more detail. The maximum speed for the entire period was 1160 km/s, the minimum speed was 262 km/s. The distribution of the velocity of the solar wind as a whole for the indicated period is of a multimode nature (Fig. 1), with specific contributions from different types.

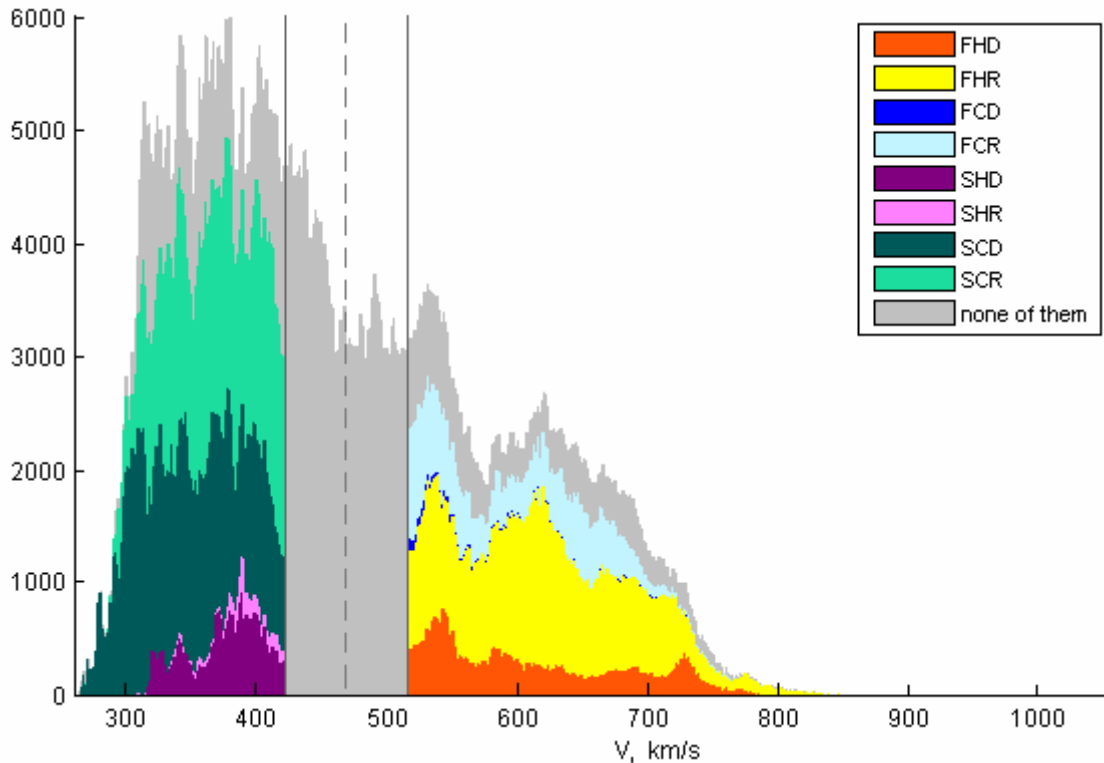


Fig. 1 The cumulative diagram of the contributions of solar wind types to the velocity distribution. The vertical axis represents the number of counts, where the size of the interval is taken equal to 1 km/s. The vertical dashed line shows the average speed for the period from August 2016 to June 2017 (469 km/s), solid lines denote threshold values ($\pm 10\%$). From the top to bottom: cold-rarefied, cold-dense, hot-rarefied, hot-dense wind types. Grey color designate wind, that can't be assigned to any of the eight types.

The situation was different for different months (Fig. 2). Some long trends observed. For the first three months, from August to October, hot and dense wind types dominate. At the end of October the solar wind had become colder and more rarefied, so the FCR and SCR types dominated in further three months. In the February and later the wind became somewhat hotter again. In June the wind was predominantly slow and cold.

Table 2. Average velocities for fast (left columns) and slow (right columns) solar wind types

| № | Type | Velocity, km/s | № | Type | Velocity, km/s |
|---|------|----------------|---|------|----------------|
| 1 | FHD | 614 \pm 73 | 5 | SHD | 376 \pm 28 |
| 2 | FHR | 623 \pm 69 | 6 | SHR | 389 \pm 21 |
| 3 | FCD | 561 \pm 49 | 7 | SCD | 348 \pm 38 |
| 4 | FCR | 598 \pm 58 | 8 | SCR | 366 \pm 33 |

Diagonal yellow strips (FHR), clearly seen in Fig. 2, are manifestations of corotating solar wind streams originating probably from coronal holes. The repetition period is equal approximately to the synodic rotation of the Earth around the Sun. The repetition pattern is not stable: it disappeared in December-January. The possible causes can be related to the non-steady state processes on the Sun as well as to position of the observation points. These points situated in the ecliptic plane and rotate around the Sun. The equatorial plane of the solar rotation inclined against the ecliptic plane. This leads to the seasonal effect. The Sun is north-south asymmetric at that time. All this together could bring to observed variation. The hypothesis can be checked in further studies.

The “red spot” (FHD) in Fig 2. rotates even more slowly around the Sun. It is indicative of differential flows on the Sun surface and interiors. More investigation is required.

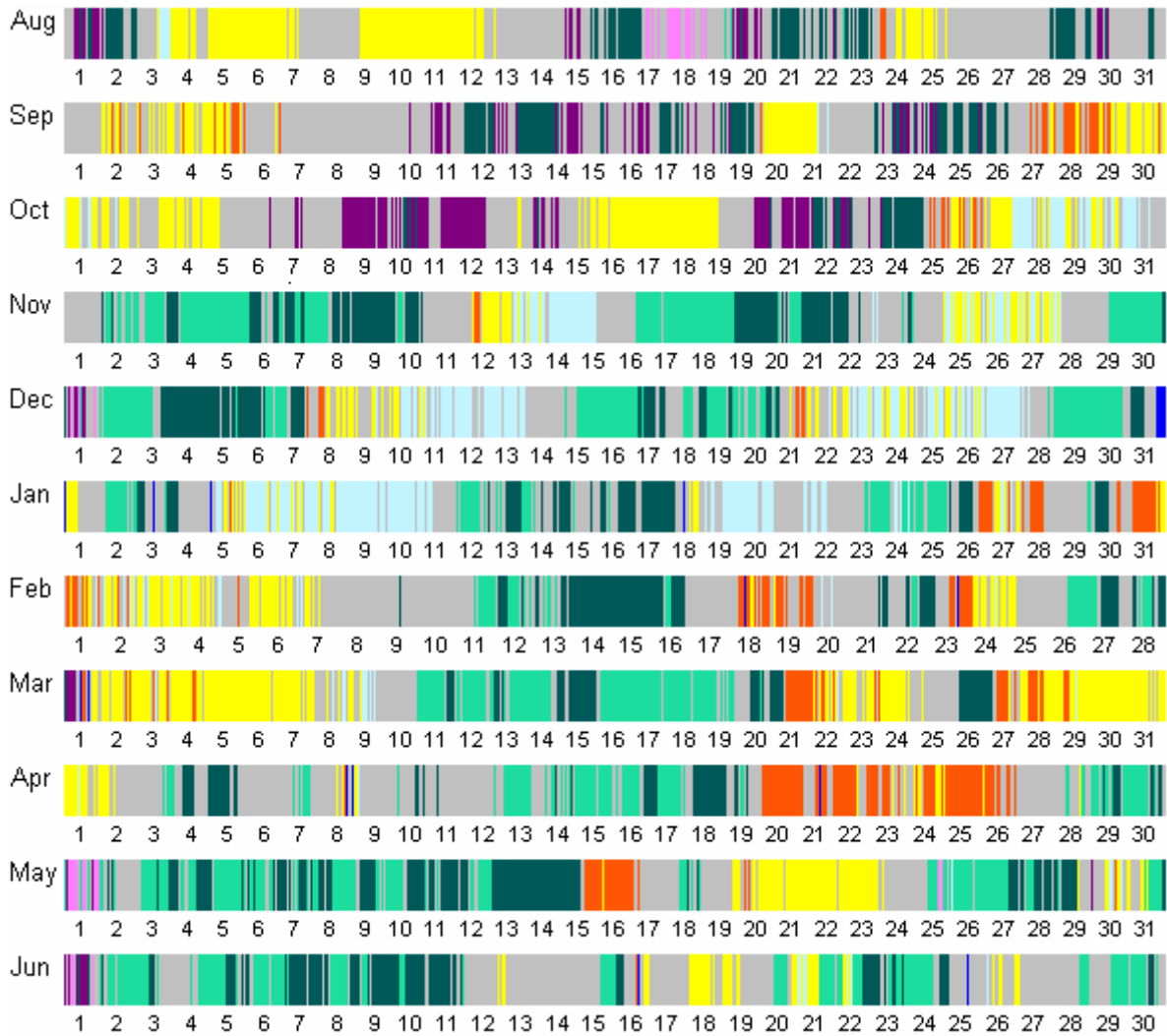


Fig. 2 Alternation of solar wind types. The same color indication as at Fig. 1 is used.

b) Types characterization

FHD: This type is most often found in maximums of the solar activity and is most noticeable in the shock waves after powerful eruptive solar flares [Gosling J.T., 1997]. However, it is also formed in the region of interaction of corotating fast flows at a sufficiently large distance from the Sun, including beyond the Earth’s orbit.

FHR: This is a very common type. Long time flows from coronal holes. On the Earth’s orbit it is most often encountered when the Sun is reversed to the solar cycle decline and is responsible for recurrent geomagnetic disturbances [Mursula K. et al., 2002].

FCD: This rare and short-lived type arises from the release of a cold prominence (protuberance) [Yao S. et al., 2010]. It can contain an anomalously large amount of helium, leading to strong compression of the magnetosphere and unusual geomagnetic storms [Dmitriev A.V. et al., 2014].

FCR: Cold magnetic clouds in a fast wind. Empty “bubbles” (plasmoids [Mullan D.J., 1990]). Remnants of expanded and cooled eruptions. Recall that within the coronal holes are often visible small evolving ephemeral active regions.

SHD: Like Type 1, this type also sometimes occurs in non-stationary flows after eruptive flares and coronal mass ejections [Gosling J.T., 1997].

SHR: This type occurs in the expanding remnants of hot eruptive clouds of plasma, picked up by the general flow.

SCD: Conventional representatives of this type are flows from coronal streamers and pseudostreamers. Heliospheric plasma layers near magnetic sectors also may belong to this type [Sanchez-Diaz E. *et al.*, 2016]. And so uncompressed density enhancements.

SCR: Areas of rarefaction in the tail part of high-speed flows from coronal holes ([Usmanov A.V. *et al.*, 2005] for example). Expanded, cooled and delayed emissions.

c) Duration

How frequent the changes from one solar wind type to another are? Mean durations of continuous periods of solar wind types are minutes. Up to about fifteen minutes for slow and cold types in some months. These intervals are comparable to the frequency of measurements, so this question requires further careful consideration. But if we smooth the experimental data, the statistics for the wind type frequencies have a little change. Exceptions are rare and short-time types, as the FCD and SHR.

Conclusions

1. The introduced classification is evident and plausible. It visually reflects deviations from some average and typical state of the heliospheric plasma at the Earth orbit in both directions for each of the main parameters, which are the three lower moments of the proton distribution function.
2. The DSCOVR spacecraft allows us to investigate small-scale changes in hydrodynamic parameters. This permits to consider and investigate the fine structure of the solar wind: short-scale parameter changes, thin fibers, filaments, and many features that disappear upon averaging.
3. To broaden these results, it is highly desirable in future to consider the degree of plasma magnetization role. The plasma “beta” ratio β is very important indicative factor. High $\beta > 1$ and low $\beta < 1$ regimes represent strikingly different formation conditions of plasma inhomogeneity. It is clear that the number of different solar wind types will twice more in this case.

Acknowledgment

This study was supported by the Program No. 7 of the Presidium of the RAS in 2017.

References

- Dmitriev A.V., Suvorova A.V., Chao J.-K., Wang C.B., Rastaetter L., Panasyuk M.I., Lazutin L.L., Kovtyukh A.S., Veselovsky I.S., Myagkova I.N. (2014) Anomalous dynamics of the extremely compressed magnetosphere during 21 January 2005 magnetic storm. *J. Geophys. Res.*, 119, no. 2, 877–896.
- Gosling J.T. (1997) Coronal mass ejections: An overview. In: Crooker N., Joselyn J.A., Feynman J. (eds.) *Coronal mass ejections*. Geophys. Monograph 99, p. 9–16.
- Hundhausen A.J. (1972). *Coronal expansion and solar wind*. Springer-Verlag, 238 pp.
- Mullan D.J. (1990). Sources of the solar wind: What are the smallest-scale structures? *Astron. Astrophys.*, 232, no. 2, 520–535.
- Mursula K., Hiltula T., Zieger B. (2002) Streamer belt north-south asymmetry and its long-term evolution. In: A. Wilson (ed.) *Solar variability: from core to outer frontiers*. The 10th European Solar Physics Meeting. 9–14 September 2002, Prague, Czech Republic. ESA SP-506, Vol. 1. Noordwijk: ESA Publications Division, p. 29–32.
- Richardson I.G., Cane H.V. (2012). Near-earth solar wind flows and related geomagnetic activity during more than four solar cycles (1963–2011). *J. Space Weather Space Clim.*, 2, A02.
- Sanchez-Diaz E., Rouillard A.P., Lavraud B., Segura K., Tao C., Pinto R., Sheeley N.R.Jr., Plotnikov I. (2016). The very slow solar wind: Properties, origin and variability. *Geophys. Res.*, 121, no. 4, 2830–2841.
- Usmanov A.V., Goldstein M.L., Ogilvie K.W., Farrell W.M., Lawrence G.R. (2005). Low-density anomalies and sub-Alfvénic solar wind. *J. Geophys. Res.*, 110, A01106.
- Veselovsky I.S., Dmitriev A.V., Suvorova A.V. (2010) Algebra and statistics of the solar wind. *Cosmic Res.*, 48, no. 2, 113–128.
- Yermolaev Yu.I., Yermolaev M.Yu. (2010). Solar and interplanetary sources of geomagnetic storms: Space weather aspects. *Izvestiya, Atmospheric and Oceanic Physics*, 46, no. 7, 799–819.

An upgrade of the UTR-2 radio telescope to a multifrequency radio heliograph

A.A. Stanislavsky^{1,2}, *A.A. Konovalenko* *I*, *A.A. Koval*¹, *Ya.S. Volvach*¹

¹ Institute of Radio Astronomy of the NASU, Ukraine;

² V.N. Karazin Kharkiv National University, Ukraine

E-mail: astex@ukr.ua

Abstract.

We present the broadband heliograph based on the UTR-2 radio telescope for obtaining the solar corona images in the frequency range 9-33 MHz with the frequency resolution 4 kHz, the time resolution up to 1 ms, and under the dynamic range about 90 dB. The instrument provides new possibilities to measure the non-thermal radiation in an unprecedented way for a better understanding of the radio emission processes in solar corona. We describe various aspects of the instrument including its antenna system, receiver front end, digital hardware and the data acquisition. This is the lowest-frequency heliograph operating in the world. It allows us to detect radio emission from solar radio sources in the upper solar corona near frequencies of ionosphere cut-off. The performance of the instrument is illustrated with source maps of solar radio bursts at low frequencies during the observational campaigns of 2013.

Introduction

Solar activity is investigated by different means. One of them, very popular, is radio observations. Coronal mass ejections (CMEs), shock waves, electron beams, flares and many others lead to solar radio bursts. Their study permits us to understand solar activity phenomena remotely, since the study of the phenomena in situ is impossible. Solar corona is a unique place. On the one hand, the corona is an origin of solar bursts, but their radio emission propagates through the plasma of corona that has an index of refraction, scattering and so on. All the effects should be taken into account, but this is not a simple task. The corona changes due to many complex processes (flares, electron beams, shock waves and so on). Of course, the bursts observed by ground-based instruments are gleams of such processes. If temporal and frequency properties of solar bursts were examined fairly well, then their source imaging studies remain still limited, especially at low frequencies. This is because the number of radio telescopes suitable to getting a radio image of the Sun at low frequencies is very small. Many years ago the low-frequency facilities were operated at Culgoora [Labrum N.R., 1985] in Australia (40-320 MHz) and at Clark Lake [Erickson W.C., et al., 1974] in the USA (20-110 MHz). Unfortunately, they were taken out of service. Now there is a revival of low-frequency radio astronomy. In this regard, it should be noted the large-scale wide band project LOFAR as well as antenna arrays LWA [Taylor G.B., et al., 2012] and MWA [Tingay S.J., et al., 2013] and the Gaurubidanur radio heliograph (30÷110 MHz) at a few discrete frequencies [Ramesh R., et al., 1998]. The radio heliograph based on the UTR-2 antenna array is also an appropriate instrument for above-mentioned goals. Its advantage lies in the fact that it is the lowest-frequency heliograph operating in the world. The aim of this work is to present the characteristics of this tool as well as its applications in recent solar researches.

Heliograph design

The main performance of the UTR-2 heliograph is determined by the antenna characteristics of UTR-2 [Konovalenko A., et al., 2016]. The broadband T-shaped radio telescope UTR-2 includes three antenna arrays: “North”, “South” and “West”. Each array has four sections. The larger arm “North-South” has 1800 meters along meridian and consists of 1440 wideband dipoles (6 rows by 240 dipoles). The arm “West” spreads over 900 meters along parallel and includes 600 dipoles (100 rows by 6 dipoles). All the dipoles in the arrays

are oriented in the east-west direction and receive only linear polarization. It should be noticed that the use of wide-band dipoles makes it possible to carry out radio observations from 9 MHz to 33 MHz. At the zenith the telescope beam has the angular dimension about $25' \times 25'$ at 25 MHz, and the effective area of the UTR-2 antenna system is about 140000 m^2 . The heliograph image is obtained from signals received with help of the fast scanning of a sky area around the Sun by the pencil-shaped beam of the UTR-2 antenna pattern. In this case the beam takes five consecutive positions along V and eight positions along U coordinate in UV -plane. The complete field of view is a rectangular matrix consisting of 40 elements (pixels). The matrix image contains 5 rows and 8 columns spaced along declination and hour angle, respectively. Basically (but not necessarily) the heliograph uses a serial regime, where the output signals from five beams are recorded one after the other, and the five beams of the antenna array pattern move on sky (see more details in [Stanislavsky A., et al., 2011]). The angular size of the heliograph image at 25 MHz is about $3.3^\circ \times 2.5^\circ$ along hour angle and declination at the zenith direction, respectively. The radio telescope UTR-2 provides the Sun tracking in sky so that the center in the field of view coincides with the solar disk center, while the movement of the pencil-shaped beam in the heliograph frame is performed due to a special fast phase shifter. For shaping pencil beams, the signal from the “West” antenna output is multiplied by signals from outputs of the “North-South” antenna five beams with help of the two-channel receiving-recording device – digital signal processor (DSP) working in the correlation regime [Ryabov V.B., et al., 2010]. Consequently, the system forming beams of the UTR-2 produces five pencil-shaped beams. In the serial regime the output signals from five beams are recorded one after the other by one DSP. The extra phase shift module is only connected with outputs of West array sections. Therefore, the heliograph mode does not interfere with taking signals from North-South sections for studying dynamic spectra of received solar bursts. The system of marker signals is integrated with the noise generator. They allow us to easily get heliogram images from the serial DSP records.

Using the heliograph, we can observe both dynamic spectra of solar bursts and their heliograms. The heliograph images are obtained from signals received due to the fast scanning of a given sky area (including the Sun) by the pencil-shaped beam of the UTR-2 antenna pattern. The heliograms allow us to recognize the source positions of solar burst sources at any fixed frequency and to estimate the source sizes along U and V .

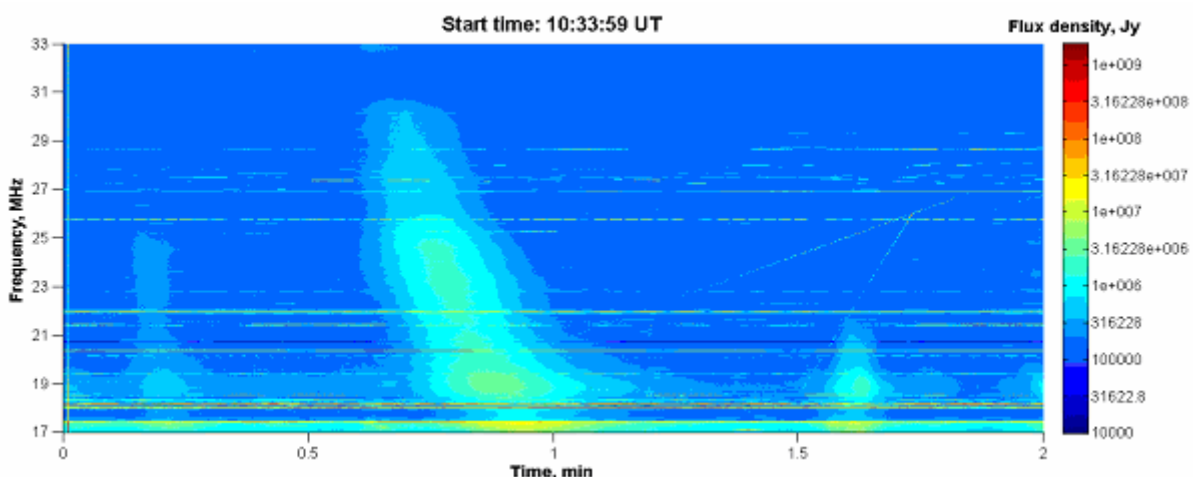


Fig.1. Illustrative dynamic spectrum of a type III burst obtained from the UTR-2 observations on 9 April of 2013. The horizontal bright lines on the dynamic spectrum were caused by intensive interferences due to broadcast radio stations.

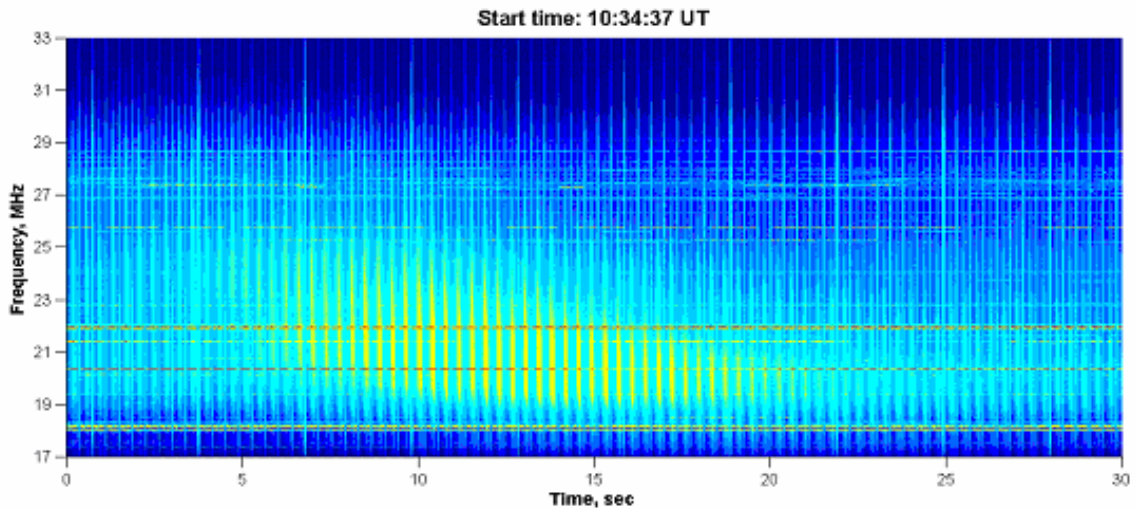


Fig.2. Heliogram records of the type III burst shown in Fig. 1. Bright vertical lines are marker signals.

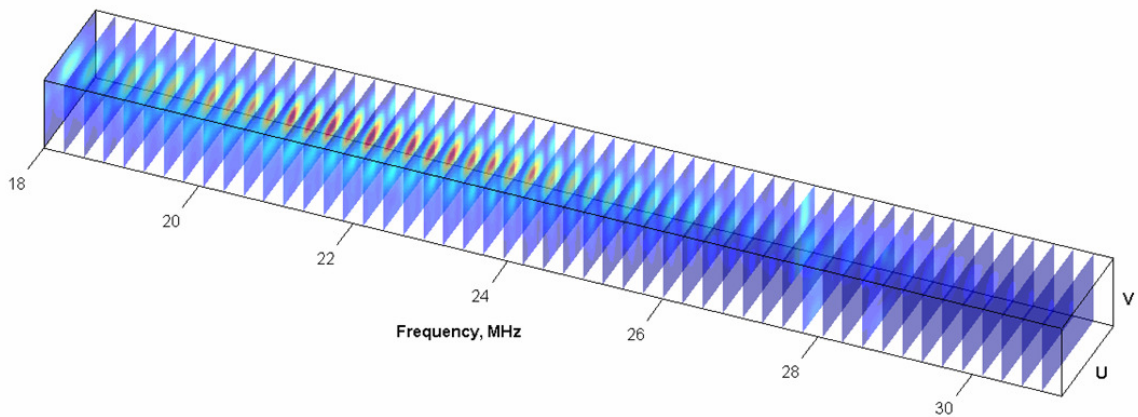


Fig.3. Heliogram of the type III burst.

Data

On 2013 April 9-11 we observed many type III radio and IIIb-III bursts by using both spectral (Fig. 1) and heliographic (Fig. 2) regimes at 16.5-33 MHz. Solar radio signals of each beam are recorded in the form of dynamic spectra with both high temporal (~ 2.482 ms) and top spectral (~ 4 kHz) resolutions. The rate of output heliograph was one image per 3 seconds (Fig. 3). This permitted us to study two-dimensional spatial structures of burst sources in dependence of frequency and time.

The solar III type bursts are the most numerous events filling the low-frequency band (<100 MHz). In decameter wavelengths the type III bursts have typically drift rates about $-(2-4)$ MHz/s. Such radio emission is associated with beams of fast electrons moving outward into interplanetary space along open magnetic field lines (see more details, for example, in Reid and Ratcliffe, 2014). Durations of these bursts can be up to 20 s, while the most are found in the range within 4-10 s in the frequency band 10-30 MHz. The energetic characteristics of decameter type III bursts is that their brightness temperatures can achieve to 10^8-10^{10} K and more. Until recently, the study of type III bursts is restricted by the conventional analysis of frequency-time characteristics from dynamic spectra. The solar burst sources have not been imaged extensively because of the instrumental limitations of previous radio telescopes. On 2013 February 28, over 30 type III radio bursts several hours after the launch of two CMEs were observed by LOFAR tied-array beams imaging and spectroscopy at 30-90 MHz. The study has discovered that the type III bursts occurred at altitudes in excess

of values predicted by 1D radial electron density models, and the non-radial high altitude type III bursts were associated with the expanding flank of a coronal mass ejection (CME). In this connection it should be noticed that our heliograph observations can provide the research by spatially-resolved data for the solar bursts (generated in upper corona) at 9-33 MHz.

During our radio observations on 2013 April 9-11, many sunspots were found on solar disk. Among them were both unipolar and complex sunspot groups. Moreover, most of them were active in the form of solar flares of C and M classes. This explains a poor character (with rare exceptions) of CMEs observed in that time (see more details in https://cdaw.gsfc.nasa.gov/CME_list/UNIVERSAL/2013_04/univ2013_04.html).

Results

Using the UTR-2 heliograph, we observed the evolution of angular structure of burst sources in about 2-3 radii from the center of the Sun. At these heights the angular dimensions of type III burst sources reach about one solar radius and even more. Basically, the heliogram analysis was performed for the type III and IIIb-III bursts. By data processing the serial records were converted into a set of two-dimensional images. Consequently, the three dimensional angular structure evolution of the type III solar burst sources (*UV*-plane frames at selected frequencies in dependence of time) was obtained (see, as an example, Fig. 3). The peak-in-time evolution of such bursts from frame to frame permits us to detect source-motion directions for these bursts. Unfortunately, from the heliograph data we were unable to clearly notice the non-radial high altitude type III bursts associated with CMEs. Probably, this is connected with the fact that the CMEs were too weak. Nevertheless, this remark does not mean that the effects cannot be detected by our instrument in other observations. For these purposes, there must be suitable conditions. Recently, the heliographic observations of stationary type IV radio emission, done on 2014 September 6, at 16.5-33 MHz have been presented [Koval, *et al.*, 2014]. Their analysis earnestly shows that the dynamical motion of radio sources, responsible for this event, manifests the loop response to the CME disturbance.

Conclusions

The angular dimensions of sources of solar radio bursts are still not explored intensively at low frequencies. The two-dimensional heliograph, based on the UTR-2, already gives new information about the space structure of solar burst sources within 9-33 MHz. In the future it would be interesting to provide joint solar observations by our instrument with the LOFAR tied-array beams imaging. They together could perfectly complement each other, operating in different (but close) low-frequency bands.

Acknowledgment

We would like to thank the GOES, STEREO and SOHO teams for developing and operating the instruments and we are grateful for their open data policy. This research was partially supported by Research Grant 0117U002395 from the National Academy of Sciences of Ukraine.

References

- Erickson W.C., J.R. Fisher (1974). A new wideband, fully steerable, decametric array at Clark Lake. *Radio Science*, 9, 387-401.
- Konovalenko A., L. Sodin, V. Zakharenko, et al. (2016). The modern radio astronomy network in Ukraine: UTR-2, URAN and GURT. *Experim. Astron.*, 41, 1-38.
- Koval A.A., A.A. Stanislavsky, Y. Chen, Sh. Feng, A.A. Konovalenko, Ya.S. Volvach (2016). A decameter stationary type IV burst in imaging observations on the 6th of September 2014. *Astrophys. J.*, 826, A125.
- Labrum N.R. (1985). The measurement of solar brightness distribution. In McLean D.J. and Labrum N.R. (eds.), “Solar radiophysics: Studies of emission from the sun at metre wavelengths”, New York, Cambridge University Press, 155-173.
- Morosan D.E. , et al. (2014). LOFAR tied-array imaging of Type III solar radio bursts. *Astron. & Astrophys.*, 568, id.A67.
- Ramesh R., K.R. Subramanian, M.S. Sundararajan, Ch.V. Sastry (1998). The Gauribidanur radioheliograph. *Solar Phys* ., 181, 439-453.
- Reid H.A.S., H. Ratcliffe (2014). A review of solar type III radio bursts. *Res. Astr. Astrophys.*, 14, 773-804.
- Ryabov V.B., D.M. Vavriv, P. Zarka, B.P. Ryabov, R. Kozhin, V.V. Vinogradov, L. Denis (2010). A low-noise, high dynamic range digital receiver for radio astronomy applications: an efficient solution for observing radio-bursts from Jupiter, the Sun, pulsars and other astrophysical plasmas below 30 MHz. *Astron. Astrophys.*, 510, id.A16.
- Stanislavsky A.A., A.A. Koval, A.A. Konovalenko, E.P. Abranin (2011) Heliograph of the UTR-2 radio telescope. <https://arxiv.org/abs/1112.1044>.
- Taylor G.B., et al. (2012). First light for the first Station of the Long Wavelength Array. *J. Astron. Instrum.*, 1, id.1250004-284.
- Tingay S.J., et al. (2013). The Murchison Widefield Array: the Square Kilometre Array precursor at low radio frequencies. *Publ. Astron. Soc. Austral.*, 30, id.e007.

On a role of quadruple component of magnetic field in defining solar activity in grand cycles

Popova E.^{1,2}, *Zharkova V.*³, *Shepherd S.*⁴, *Zharkov S.*⁵

¹ Lomonosov Moscow State University, Russia

² Schmidt Institute of the Earth Physics RAS, Moscow, Russia

³ Northumbria University, UK

⁴ Bradford University, UK

⁵ Hull University, UK

E-mail: valentina.zharkova@northumbria.ac.uk

Abstract.

The aim of this work is revise our prediction of solar activity using a solar background magnetic field as a proxy by the inclusion of eigen vectors of solar magnetic waves produced by quadruple magnetic sources [Popova *et al.*, 2017], in addition to the principal eigen modes generated by two-layer dipole sources [Zharkova *et al.*, 2015]. By considering the interference of two dipole and one quadruple waves we produce the revised summary curve for the last 400 years accounting for the additional minima of solar activity occurred at the beginning of 19th (Dalton minimum) and 20th centuries. Using the dynamo model with meridional circulation and selecting the directions of circulation for quadruple waves, we estimate the parameters of quadruple waves best fitting the observations in the past grand cycle. The comparison shows that the quadruple wave has to be generated in the inner layer of the solar convective zone, in order to provide the additional minima observed in 19 and 20 centuries naturally accounting for Gleissberg centennial cycle. The summary dynamo waves simulated for the dipole and quadruple sources with longer periods of centennial cycle reveal closer correspondence to the solar activity oscillations derived from the average sunspot numbers in the current grand cycle.

Introduction

Modeling and forecasting of solar magnetic activity is a rather difficult task, requiring an understanding of the physical processes occurring in the bowels of the Sun.

Solar magnetic activity is manifested with the appearance of sunspots on the solar surface of the Sun with relatively complicated structure having the main period of about 22 years. The monthly sunspot numbers averaged from observations by many observatories show quasi-regular maxima and minima of solar activity appearing with changing leading magnetic polarity in each hemisphere approximately every 11 years or with the same polarity about every 22 years [Hathaway *et al.*, 2002]. The longest direct observation of solar activity is the 400-year sunspot-number series showed that solar activity can have the almost spotless Maunder and Dalton minima, and the period of very high activity in the most recent 5 cycles [Solanki *et al.*, 2004; Solanki and Krivova, 2011].

The cycles of solar activity are associated with generation and evolution of the solar magnetic field which described by a dynamo mechanism, the simplest version of which has been proposed in [Parker, 1955]. Process of dynamo is based on combining the effects of magnetic field shear and stretching caused by the differential rotation (ω -effect) and twisting of magnetic flux loops over the solar interior depths allowing them to appear on the surface at particular latitudes (α -effect). Such representation provides the solution of dynamo equations in a form of oscillating waves of: a) the poloidal (background) magnetic field traveling from pole to pole in the whole Sun and b) the toroidal (sunspot) magnetic fields (dynamo-waves) appearing from the middle latitudes to the equator.

Large-scale meridional plasma flows (meridional circulation) is expected to include at least two opposing contributions: one is a flow, which transports solar plasma, say, from the

equator to the pole near the surface, and the other is a deeper counter-flow, which returns the plasma to the equatorial region that makes the mass distribution stationary. This process associates the dynamo generators with different radial layers and consequently, the radial variable needs to be included into the dynamo-governing equations for two radial layers where dynamo waves are generated [Parker, 1993; Popova et al., 2013].

The dipole waves are found in the two temporal principal components (PCs) derived from the magnetic observations [Zharkova et al., 2012]. In each cycle there were also two secondary latitudinal components with slightly smaller than dipole amplitudes related to quadruple magnetic sources whose appearances vary from cycle to cycle. The quadruple components derived in latitudinal variations of magnetic fields in cycles 21÷23 [Popova et al., 2013] are shown to contribute to the pairs of latitudinal magnetic waves observed for each cycles revealing their decreasing amplitude and increasing phase difference between latitudinal waves of the pair for a given cycle.

Zharkova et al. [2015] carried the extrapolation of the PCs backward for 800 years, which revealed two grand cycles of duration 370÷400 years superimposed on 22 year-cycles with the features showing a remarkable resemblance to sunspot activity reported in the past including the Maunder and Wolf minimum. The summary curve calculated for the next millennium predicted also further three grand cycles in the next millennium with the closest grand minimum occurring in the forthcoming cycles 25÷27. However, this curve did not predict accurately the occurrence of Dalton minimum and minimum which was observed around 1900 in the current grand cycle (1655-2020).

Popova et al., [2017], considering the interference of two dipole and one quadruple waves, has shown that in dynamo model we can obtain simultaneous presence of global minima similar to the Maunder minimum and the Gleissberg cycle against the background of 22-year oscillations of the magnetic field. So in [Popova et al., 2017] two missing minima in the current grand cycle (1655-2020) was obtained.

Modeling of Gleissberg cycle

We will show how three independent waves can be generated in the solar convective zone (SCZ). For this purpose we will consider dynamo model in layered medium. We assume that one wave is generated only in each layer.

Parker dynamo equations with meridional circulation are derived by averaging the magnetic field over the radius within the thin envelope, where the dynamo mechanism operates, and by neglecting the terms describing the effects of curvature near the pole. In this case, the dynamo equations have the form [Popova et al., 2017]:

| | |
|--|-----|
| $\frac{\partial A_i}{\partial t} = R_{\alpha i} \alpha_i B_i + \frac{\partial^2 A_i}{\partial \theta^2} - V_i \frac{\partial A_i}{\partial \theta}$ | (1) |
| $\frac{\partial B_i}{\partial t} = R_{\omega i} \sin \theta \frac{\partial A_i}{\partial \theta} + \frac{\partial^2 B_i}{\partial \theta^2} - \frac{\partial(V_i B_i)}{\partial \theta}$ | (2) |

Here, i is a number of the layer, B is the toroidal magnetic field, A is the vector potential of the poloidal magnetic field, proportional to the toroidal component and θ is the latitude measured from the pole. The factor $\sin \theta$ describes the decrease in the length of a line of latitude near the pole. The second equation neglects the small contribution of the α -effect, i.e. we use so-called $\alpha\omega$ -approximation. Curvature effects are absent in the diffusion terms. It is assumed that the radial gradient of the angular velocity does not vary with θ .

In the Eq. (1-2) the parameters R_α and R_ω describe intensity of the α -effect and the differential rotation, respectively. We used a simple scheme for the stabilization of the magnetic field growth, namely, the algebraic quenching of the helicity. This scheme assumes

that $\alpha = \alpha_0(\theta) / (1 + \zeta^2 B^2) \approx \alpha_0(\theta)(1 - \zeta^2 B^2)$, where $\alpha_0(\theta) = \cos\theta$ is the helicity in the unmagnetized medium and $B_0 = \zeta^{-1}$ is the magnetic field for which the α -effect is considerably suppressed.

For two layers consider the latitude distribution of the magnetic field for dipole magnetic sources in the form [Zharkova et al, 2015]:

$$\begin{aligned} B(\theta, t) &= b_1 \sin(2\theta) + b_2 \sin(4\theta) \\ A(\theta, t) &= a_1 \sin(\theta) + a_2 \sin(3\theta) \end{aligned}$$

with the dipole symmetry conditions $A(0)=B(0)=A(\pi)=B(\pi)=0$.

By substituting the chosen set of components of magnetic field into the dynamo equations and collecting the coefficients of the sines with similar arguments, one can obtain a dynamical system of six equations containing the two dipole and one quadruple modes.

Suppose that in the third layer a wave is generated from the quadruple source, then we have to consider the latitude distribution of the magnetic field in such form [Popova, 2013]:

$$\begin{aligned} B(\theta, t) &= b_3 \cos(2\theta) + b_4 \cos(4\theta) + b_5 \cos(6\theta) \\ A(\theta, t) &= a_3 \cos(\theta) + a_4 \cos(3\theta) + a_5 \cos(5\theta) \end{aligned}$$

A dynamical system for quadruple source can be obtained in the similar way as for dipole sources, but expanding the terms to include the quadruple source contributions.

In [Popova et al., 2008] it was shown that periods of dynamo waves are regulated by the amplitude of a meridional flow. If in each layer meridional flows have different amplitudes and three waves interfere with each other, then we can obtain double beating effect of these waves. Such double beating effect can lead to simultaneous presence of global minima similar to the Maunder minimum and the Gleisberg cycle against the background of 22-year oscillations of the magnetic field.

Following the technique presented by [Zharkova et al., 2015] (their formula (1) in section on beating effects) we can estimate periods of waves for obtaining double beating effect. Any two interfering waves with the close cyclic frequencies ω_1 and ω_2 can produce a beating effect with their upper frequency, ω_u being the average of these two, $\omega_u = 1/2(\omega_1 + \omega_2)$ and the lower frequency, ω_l , being their difference, $\omega_l = 1/2(\omega_1 - \omega_2)$. In result, the resulting wave has high frequency oscillations with the average frequency ω_u and low-frequency oscillations of its amplitude with the averaged frequency ω_l , that constitutes the beating effect and occurrence of global minima with the period T_l , in addition to the regular ones with the period T_u .

By substituting the relation for cyclic frequency $\omega = 2\pi f = 2\pi/T$, where f is a frequency and T is a period of wave, one can derive the formulae for the periods caused by the interaction of two waves, or the beating effects, $T_u = 2(T_1 T_2)/(T_2 + T_1)$ and $T_l = 2(T_1 T_2)/(T_2 - T_1)$. Here T_1 and T_2 are the periods of two interacting waves.

For the beating effect of three waves: two dipole waves with periods T_1 and T_2 and one quadruple wave with period T_3 one can have the following expressions for the resulting periods of interfering waves: $T_{22} = 2(T_1 T_2)/(T_2 + T_1)$, $T_{GM} = (T_1 T_2)/(T_2 - T_1)$, $T_{sec} = (T_1 T_3)/(T_3 - T_1)$, where T_{22} is the period of the 22-year cycle, period T_{sec} corresponds to the Gleisberg cycle, and T_{GM} corresponds to period of a grand cycle.

In order to match the observations and to achieve known periods of solar activity, e.g. $T_{22} \approx 22$ years, $T_{GM} \approx 400$ years, $T_{sec} \approx 100$ years, one would need to have two dipolar waves with $T_1 \approx 21.41$, $T_2 \approx 22.62$, and one quadrupolar wave with $T_3 \approx 27.24$. For $T_{sec} \approx 80$ and same T_{22} and T_{GM} we obtained $T_3 \approx 29.24$, for $T_{sec} \approx 90$ years $T_3 \approx 28.1$.

Using our dynamo model with meridional circulation we can estimate the approximate location of the wave sources in depth of SCZ. In our dynamo model the wave period is regulated by the amplitude of the meridional flow. Knowing the periods of the obtained waves, we can estimate the value of meridional flows that lead to the existence of waves with the such periods. The helioseismological data [Zhao *et al.*, 2013] gives us that the meridional flow more intense closer to the surface, so we can suggest that wave generated in media with more intense meridional flow is closer to the surface.

In case of absence of meridional circulation, or $v=0$, for magnetic field with dipolar symmetry the harmonic oscillations are reproduced at $-220 < D < -100$, and for the magnetic field with the quadruple symmetry at $-410 < D < -110$. The period of magnetic field oscillations is smaller than the one observed in Sun. In order for our model to achieve the observed period of a solar cycle of activity, the meridional flows should be included with the magnitudes equal to several model units. In this case, the range of dynamo-numbers for reproducing harmonic oscillations is not much different from the case of the absence of meridional flow, while the periods of oscillation are now close to the observed ones.

Let us assume that the dynamo-numbers in all layers are the same and equal to -170 and calculate dipolar and quadruple magnetic field oscillations. We obtain the period of these oscillations $T_1=21.41$ is achieved with $v \approx -2.6$ model units, $T_2=22.62$ with $v \approx -2.7$, and $T_3=27.24$ with $v \approx -2.56$ (for $T_3 \approx 29.24$, $v \approx -2.58$; for $T_3 \approx 28.1$, $v \approx 2.563$). Meridional circulation is directed against the direction of the wave motion. The quadruple source, according to our research, has to be located deeper than the dipole one.

In our model because of quadruple source is deeper dipole the generated wave decays rather quickly with a distance during its emergence to the surface, quadruple field can have a smaller amplitude as compared to the dipole field in the layer where the interaction of waves occurs. This reasoning confirms the finding of PCA [Zharkova *et al.*, 2012] reporting the secondary latitudinal magnetic field components caused by quadruple sources [Popova *et al.*, 2013] to have the amplitudes ranging from 0.2 to 0.7 of the dipole one.

Extending these model simulations of the joint dipole and quadruple waves to the simulations of the summary curve for the 2000 years, similar to that presented by Fig.6 in [Zharkova *et al.*, 2015] we can obtain the summary curves (Fig.1) with a quadruple wave with the amplitude a factor 0.3 of the dipole wave amplitude is presented in the top tree plots and the original summary curve derived for dipole waves from observations [Zharkova *et al.*, 2015] in the bottom plot. Fig.1a is obtained for 80 year Gleissberg cycle, Fig.1.b for 90 year Gleissberg cycle, and Fig.1.c for 100 year Gleissberg cycle. It can be seen that the inclusion of a quadruple wave with smaller than the dipole wave amplitude affects the overall appearance of solar activity and allows us to detect some additional minima showing the occurrence of numerous secular minima in the past 800 years accounting for Gleissberg cycle (see Fig.1, top plot).

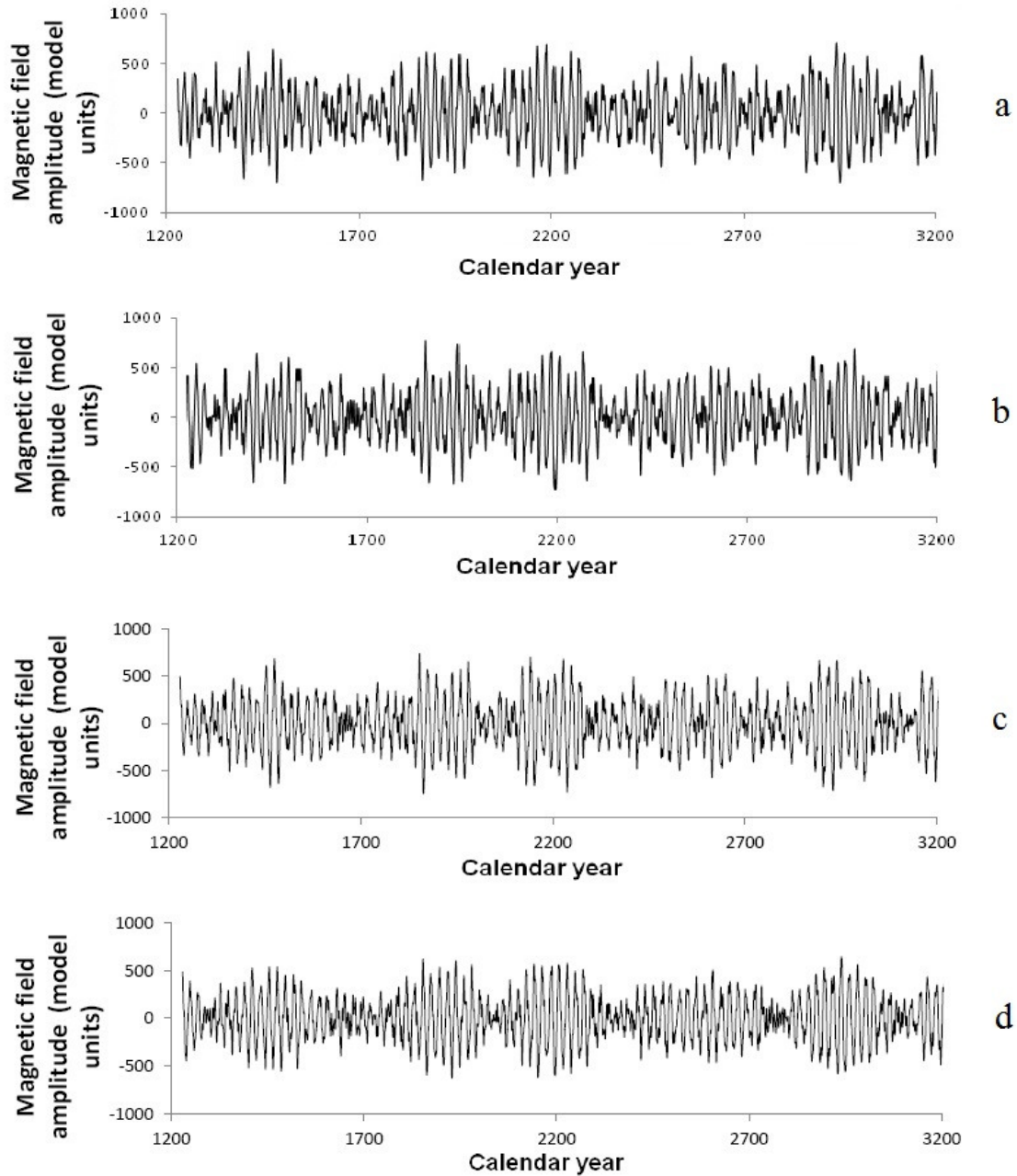


Fig. 1 Variations on a millennium timescale of the joint summary curve derived for dipolar and quadrupolar magnetic fields a) for 80 year Gleissberg cycle, b) for 90 year Gleissberg cycle, c) for 100 year Gleissberg cycle; d) the original summary curve derived for dipole waves from observations [Zharkova et al., 2015].

Conclusions

1. Quadruple wave and two dipole waves with the periods of about 22 years leading to a grand cycle of about 400 years produce the double beating effect, which, in turn, leads to the additional minima of magnetic field occurring about every 100 years, called Gleissberg cycle.
2. SCZ is the most likely location where this quadruple wave has to be generated, in order to match to the observed timing and amplitude of the additional minima of Gleissberg's cycle in the grand cycles defined by a superposition of the dynamo waves generated in the inner and outer layers.

Acknowledgment

The authors acknowledge with thanks that this work was initiated during the visit by EP to Northumbria University funded by the Royal Society. This research was also partially funded by the grant ref. 16-17-10097 of Russian Science Foundation (PI- H. Popova).

References

- Akasofu S-I, P.D. Perreault, F. Yasuhara, C.-I. Meng (1973). Auroral substorms and the interplanetary magnetic field. *J Geophys Res*, 78, 7490–7508.
- Despirak, I.V., A.A. Lyubchich, Kh.K. Birnat, A.G. Yakhnin (2008), Poleward expansion of the westward electrojet depending on the solar wind and IMF parameters. *Geomagn. Aeron.*, 48, no. 3, 284-292.
- Hathaway, D. H., Wilson, R. M., Reichmann, E. J. (2002). Group Sunspot Numbers: Sunspot Cycle Characteristics. *Sol. Phys.* 211, 357-370.
- Parker, E. N. (1955). Hydromagnetic Dynamo Models. *Astrophys. J.* 122, 293-314.
- Parker, E. N. (1993). A solar dynamo surface wave at the interface between convection and nonuniform rotation. *Astrophys. J.* 408, 707-719.
- Popova, E. P. (2013). A dynamical system for the parker dynamo in the case of quadrupole symmetry of the magnetic field. *Astronomy Reports*, 57, 310-315.
- Popova E.P., Reshetnyak M.Yu, Sokoloff D.D. (2008). Meridional circulation and dynamo-wave propagation. *Astronomy Reports*, 52, 157-163.
- Popova E.P., Zharkova V., Shepherd S., Zharkov S. (2017). On a role of quadruple component of magnetic field in defining solar activity in grand cycles, *Journal of Atmospheric and Solar-Terrestrial Physics*, 2017, *J.Atmos.Solar Ter.Phys.* <https://doi.org/10.1016/j.jastp.2017.05.006>
- Popova, E., Zharkova, V., Zharkov, S. (2013). Probing latitudinal variations of the solar magnetic field in cycles 21-23 by Parker's Two-Layer Dynamo Model with meridional circulation. *Annales Geophysicae*, 31, 2023-2038.
- Solanki, S. K., Krivova, N. A. (2011). Analyzing Solar Cycles. *Science*, 334, 916-917.
- Solanki, S. K., Usoskin, I. G., Kromer, B., Schussler, M., Beer, J. (2004). Unusual activity of the Sun during recent decades compared to the previous 11,000 years. *Nature*, 431, 1084-1087.
- Zhao J., Bogart R.S, Kosovichev A.G., Duvall Jr. T.L., and Hartlep, T., 2013, *Astrophys. J.L.*, 774, L29
- Zharkova, V. V., Shepherd, S. J., Popova, E., Zharkov, S. I. (2015). Heartbeat of the Sun from Principal Component Analysis and prediction of solar activity on a millenium timescale. *Nature Scientific Reports*, 5, 15689.
- Zharkova, V. V., Shepherd, S. J., Zharkov, S. I. (2012). Principal component analysis of background and sunspot magnetic field variations during solar cycles 21-23. *Mon. Notices of RAS*, 424, 2943-2953.

Spatial properties of the complex decameter type II burst observed on 31 May 2013

*V.V. Dorovskyy*¹, *V.N. Melnik*¹, *A.A. Konovalenko*¹, *A.I. Brazhenko*², *H.O. Rucker*³

¹ Institute of Radio Astronomy of NANU, Kharkov, Ukraine,

² Poltava Gravimetric Observatory of NANU, Poltava, Ukraine,

³ Commission for Astronomy of AAS, Graz, Austria.

E-mail: vlad.dorovskyy@gmail.com

Abstract

We present the results of observations of complex powerful type II burst associated with narrow Earth-directed CME, which was ejected at around 11 UT on 31 May 2013. The observations were performed by radio telescope UTR-2, which operated as local interferometer, providing the possibility of detection of the spatial parameters of the radio emission source. There are also polarization data from URAN-2 radio telescope.

The CME was detected by two space-born coronagraphs SOHO/LASCO/C2 and STEREO/COR1-BEHIND, and was absolutely invisible for STEREO-AHEAD spacecraft.

The associated type II burst consisted of two successive parts of quite different appearance on the dynamic spectrum. The first burst was narrow in frequency, had cloudy structure and was completely unpolarized while the second one represented rich herring-bone structure and exposed high degree of circular polarization. Both parts of the whole event reveal band splitting and well distinguished harmonic structure.

The sources of the type II bursts elements were found to be of about 15 arcmin in size in average, with the smallest ones reaching as low as 10 arcmin.

Introduction

Solar type II bursts are the manifestations of the CME movement through the solar corona and originate from the shock formed ahead of CME. In its turn CME is one of the most effective drivers of the space weather changes. Though type II bursts are observed in wide frequency range the bursts detected at low frequencies are believed to be connected with the potentially most geoeffective CMEs [*Gopalswamy, N., et al., 2005*].

The geoeffectiveness of CME is mostly defined by its mass, velocity and direction. The velocity of CME can be detected in three ways: by coronagraph observations in visible light, by the frequency drift rate of type II bursts and by the speed of the type II source displacement. The first method gives correct results for CMEs which propagate close to the sky plane and is not applicable for Earth-directed CMEs (when observing from Earth). This problem can be solved by multi-spacecraft observations such as STEREO mission. In addition this technique also allows to define the direction of CME movement. However the accuracy of this method depends on mutual positions of STEREO satellites with respect to Earth and these positions are changing with time. The second method is indirect and model dependent one. In addition it gives the radial component of the velocity vector and is inaccurate for CMEs which move at the substantial angle to the density gradient. The third method deals with real spatial displacement of the source of type II burst with time regardless the chosen coronal model.

It is known also that type II bursts reveal a wide variety of morphological features, such as fundamental and harmonic emission, band splitting, cloudy structure, herring-bone (HB) structure etc. The interpretations of all these features are based on their spectral properties assuming some models of plasma distributions in the corona and the shock. For instance the band splitting is attributed to the emission from ahead and behind the shock (upstream and downstream emission [*Vršnak, B., et al., 2004*]), HB sub-bursts are manifestation of the

electron acceleration towards and outwards the Sun. Spatial measurements with high time and frequency resolution may confirm or call these assumptions into question.

Thus study of the spatial properties of the sources of type II bursts may improve the quality and reliability of the space weather diagnostics and will lead to better understanding of underlying physics as well.

Observations

Since 2011 observations of solar radio emission at the UTR-2 radio telescope are carried out in the interferometric mode which gives an opportunity for estimation of the sizes and locations of solar radio bursts sources. The UTR-2 radio telescope having effective collecting area of up to 150000 m² consists of 12 separate sections which can be configured in different ways. For solar observations the sections were grouped in three separated in space antennas: North, West and South by 4 sections in each thus forming a local interferometer with two orthogonal bases each 674 m long.

As a backend two spectropolarimeters DSPZ [Ryabov, V.B., *et.al.*, 2010] are used. These digital analyzers calculate complex correlation function in instantaneous frequency band 10-32 MHz for each of two bases. Then the absolute value of the correlation function carries information about the size of the source via visibility function while the phase of the correlation function is determined by the source angular displacement.

On 31 May 2013 complex powerful type II burst was observed by UTR-2, URAN-2 and NDA radio telescopes. The overall view of the burst is shown in Figure 1. The whole event started at 11:12 UT with the group of type III bursts. In this particular case these type III bursts are the precursor of following type II bursts and coincide in time with solar flare of class C1.1 above the active region NOAA11761 (S18E23). The type II burst itself consists of two parts separated in time. First part lasted from 11:22:30 till 11:25:30 UT and the second one – from 11:28 till 11:39 UT. Both parts of the burst exhibit band splitting. The lanes were separated in frequency by 4.5 MHz and 6 MHz respectively. The dynamic spectrum obtained by the NDA shows also the harmonic structure of the bursts (see Figure 2). The burst appeared to be bounded both above 65 MHz and below 10 MHz. No sign of type II burst at lower frequencies was found by SWAVES receivers onboard STEREO spacecraft.

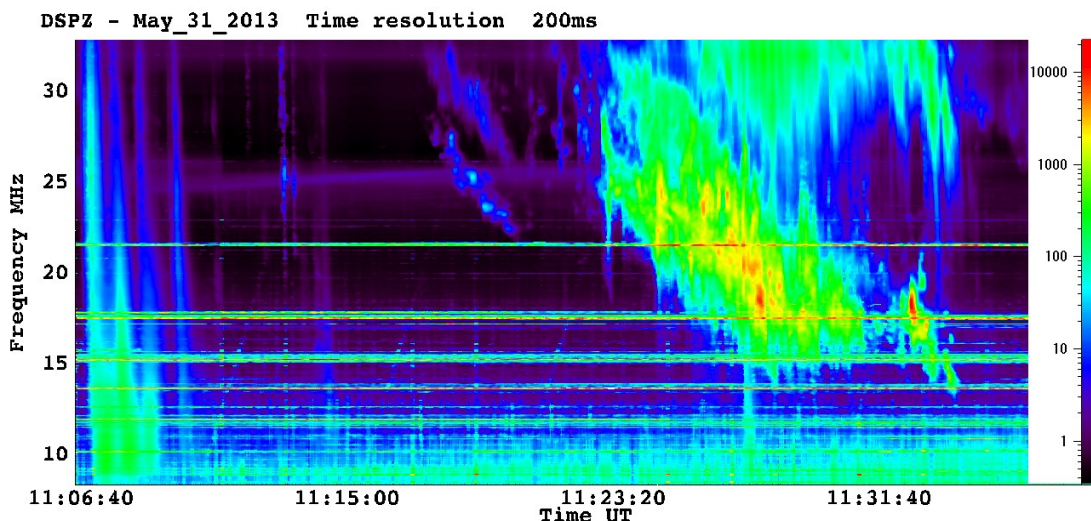


Fig. 1 Type II burst recorded on 31 May 2013 by UTR-2 radio telescope.

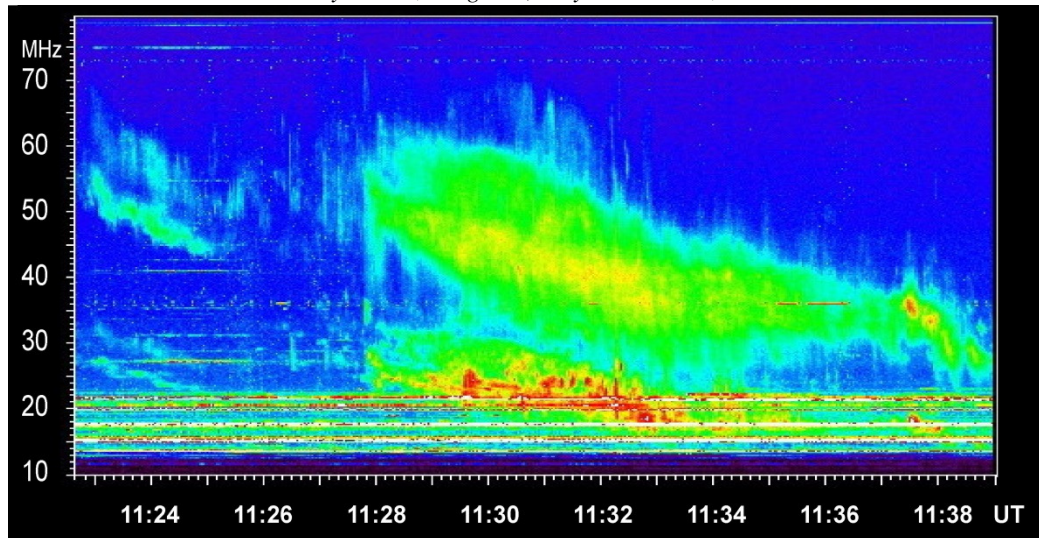


Fig. 2 Type II burst recorded on 31 May 2013 by NDA radio telescope.

This type II burst was apparently initiated by the CME recorded by coronagraphs SOHO/LASCO-C2 at 12:12 UT and by STEREO-B/COR1 at 11:20. At the same time this CME was not visible for STEREO-A spacecraft.

Analysis and discussion

a) Determination of the direction and the speed of the CME propagation using optical data

The views of CME from different locations and mutual positions of the satellites are shown in Figure 3. The CME of interest is marked with white arrows. The speeds of the CME measured from SOHO and STEREO-B spacecraft are $281 \text{ km}\cdot\text{s}^{-1}$ and $341 \text{ km}\cdot\text{s}^{-1}$ respectively. Taking into account the fact that this CME isn't visible for STEREO-A satellite we may conclude that this CME propagated at angle $\sim 30^\circ$ Eastward to the line of sight with the velocity of about $340 \text{ km}\cdot\text{s}^{-1}$. In this case the CME moves practically in the sky plane for STEREO-B vehicle and is 30° projection for the SOHO spacecraft. For such a trajectory STEREO-A couldn't observe the CME because it was completely behind the Sun.

b) Determination of the CME speed via frequency drift rate of the type II bursts.

It is well known that in frames of plasma emission mechanism the frequency drift rate of any burst depends on the density profile and the source velocity

For current analysis we apply the Newkirk corona model. For the fundamental component of the discussed burst the drift rate is not constant for the burst lifetime. In the beginning the drift rate was about $-40 \text{ km}\cdot\text{s}^{-1}$, that corresponded to the radial velocity of about $800 \text{ km}\cdot\text{s}^{-1}$. The tail of the type II bursts has practically no drift. The radial velocity of the first part of the bursts is more than twice higher than that of the CME speed according to coronagraph data. The possible reason of such a discrepancy is discussed below.

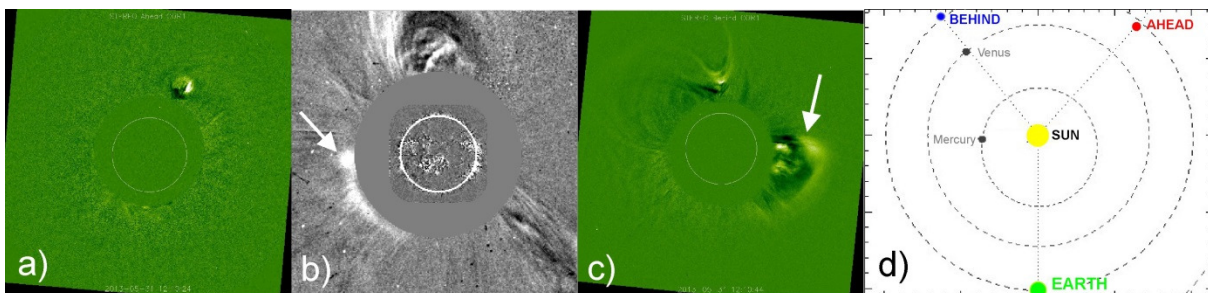


Fig. 3 View of the CME at 12:12 UT from STEREO-A (a), SOHO (b) and STEREO-B (c) apparatus and the positions of the STEREO spacecraft on 31 May 2013 (d).

c) Using spatial properties of the type II burst for retrieving CME parameters

The possibility of estimation of the radio sources sizes and positions was shown in [Shepelev, V.A., 2015].

The size of radio source is determined through the visibility function [Thompson, A.R., et.al., 1986]

$$\gamma = \exp \left[- \left(\frac{\pi \theta L}{2\lambda \sqrt{m_2}} \right)^2 \right] \quad (1)$$

where θ is the half-maximum angular size of a source, L is the base length of the interferometer and λ - is the wavelength of the radio emission. Note that equation (2) is only valid for sources with Gaussian brightness distribution. In the case when the interferometer is composed of the element of the same array (providing identical antenna parameters) the visibility function can be calculated as

$$\gamma = \frac{P_c}{\sqrt{P_1 \cdot P_2}} \quad (2)$$

where P_c is the absolute value of the correlation function, and P_1 and P_2 are the power received by two antennas of the interferometer. Using equations (1) and (2) it is possible to get the source size along the direction of baseline.

In its turn the phase of a correlation function allows to define angular deflection of a source from the interferometer axis.

The spatial properties of the first part of the type II burst with band splitting are shown in Figure 4.

We have analyzed spatial properties of two lanes of one type II burst taken at one moment of time. The source of higher frequency lane is drawn in red while lower frequency lane is marked with blue color. Their sizes are almost equal ($14'$ and $16'$ respectively) and this gives us the effective brightness temperatures of these sources of $2 \cdot 10^{12} \text{K}$ and $4 \cdot 10^{11} \text{K}$. It is also evident that higher frequency lane is situated closer to the Sun than lower frequency lanes. This speaks in favor of upstream and downstream model of band splitting of type IIs. In the same way we have analyzed how the source moves in space with time. Apparently the source moves outwards the Sun (Figure 5). The velocity obtained from this displacement is around $900 \text{ km} \cdot \text{s}^{-1}$.

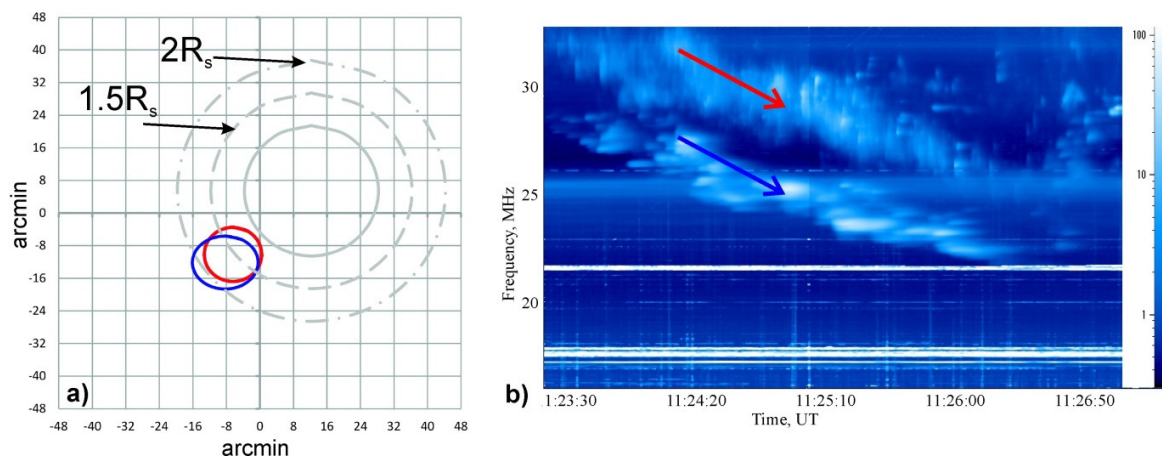


Fig. 4 Positions and sizes of the sources of type II burst with band splitting (a) and corresponding dynamic spectrum (b).

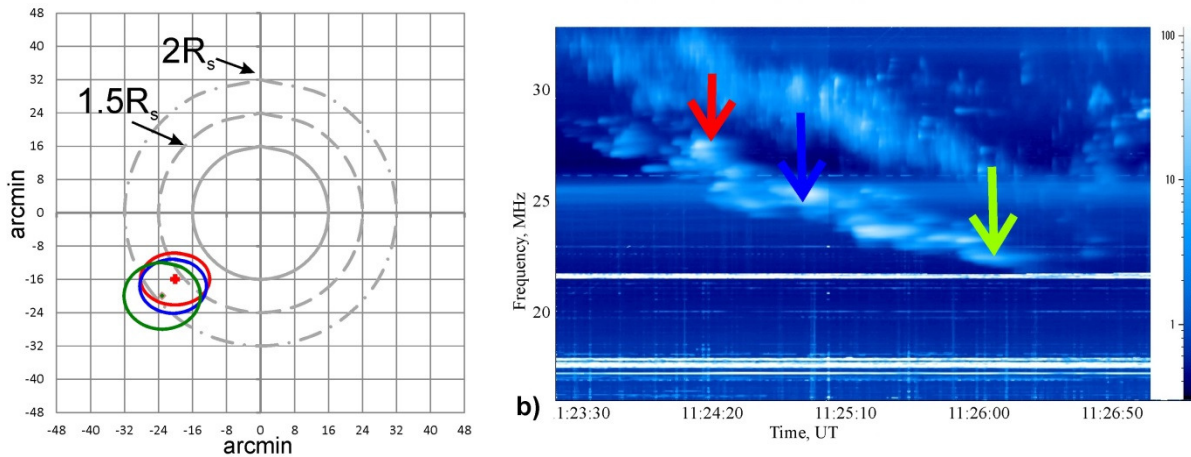


Fig. 5 Displacement of the type II burst source with time (a) and its spectrum (b)

This velocity is very close to that obtained from the frequency drift rate and much higher than velocity provided by coronagraphs. To our opinion this discrepancy may possibly be connected with migration of the radio source across the shock surface. Indeed the obtained source size is much less than the size of CME itself and thus the source may change its position at the shock with time causing apparent increase of its velocity.

The formation of the HB structure is generally attributed to the electron beams acceleration at the shock in two opposite directions. Figures 6 and 7 evidently illustrate the inward and outward movement of the HB sub-bursts with opposite frequency drift signs. The velocities of these movements are about $0.3c$, and are close to the type III electrons velocity.

d) Polarization properties of the type II burst.

Data from URAN-2 radio telescope allow to measure the polarization of radio emission. For this particular burst the fundamental HB sub-bursts reveal high degree of circular polarization reaching as high as 70%. The fundamental counterparts are weakly polarized. This is in good agreement with theoretical view. On the contrary both the fundamental and the harmonic components of the first part of the type II burst (without HB structure) are completely unpolarized. This may indicate that the sources of different parts of type II burst are located at different sites with different conditions.

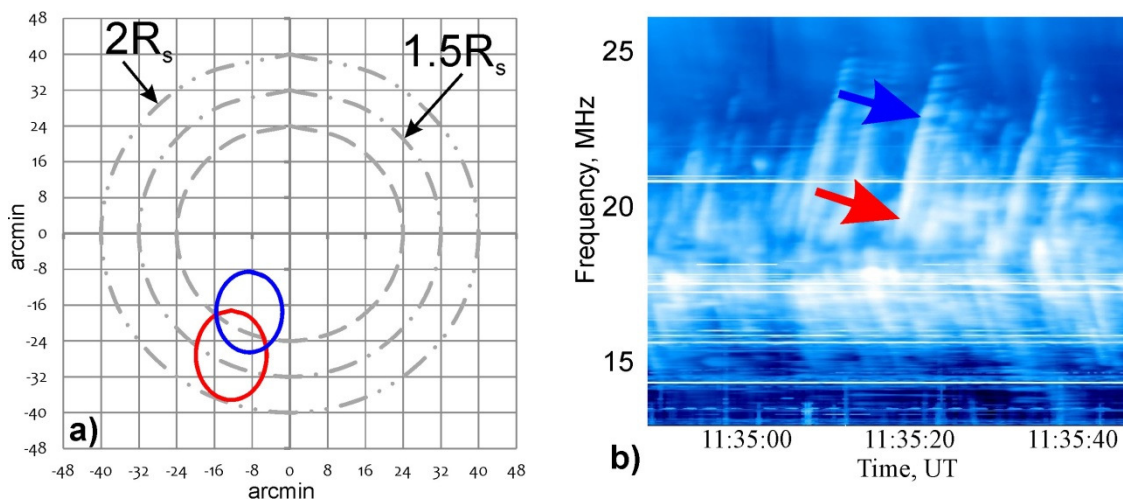


Fig. 6 Displacement of the reverse HB sub-bursts source with time (a) and its spectrum (b).

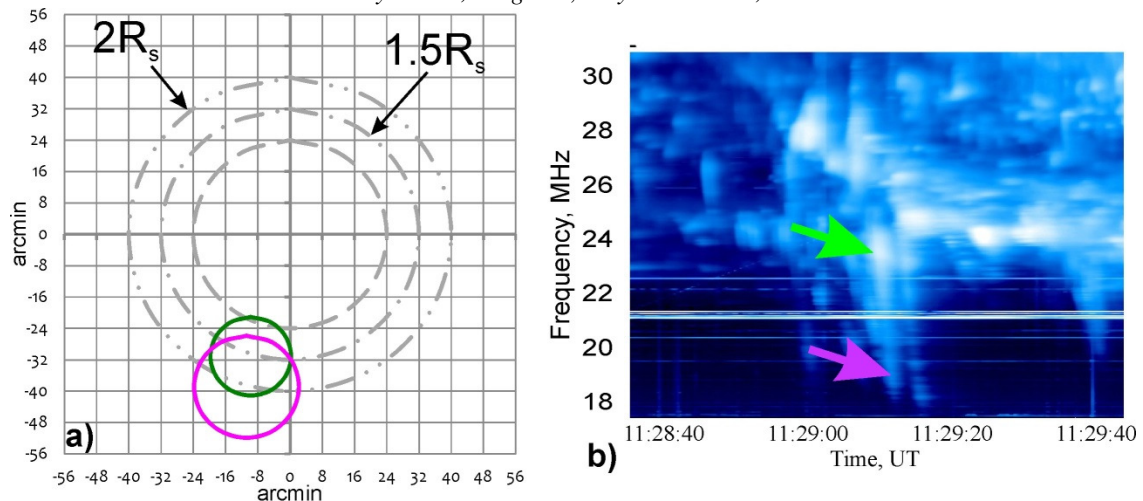


Fig. 7 Displacement of the reverse HB sub-bursts source with time and its spectrum (b)

Conclusions

1. The possibility of detecting of spatial properties of solar radio bursts is shown.
2. The speeds of the type II sources were obtained both by the frequency drift rate (model dependent value) and by the source spatial displacement (model independent value).
3. For this separate type II burst the speeds obtained from optic observations are at least three times smaller than defined both from frequency drift rate and the spatial displacement.
4. The sizes of the type II burst appeared to be much smaller than the sizes of the shock with which they are associated. They are also smaller than normal type III bursts sources.
5. Band splitting is likely the result of emission from ahead and behind the shock front.
6. HB structure is probably the result of electrons acceleration towards and outwards the Sun.
7. Different fragments of the type II burst of the same frequency may originate from different parts of the shock surface.

Acknowledgment

The work was partially performed under the support of the European FP-7 project SOLSPANET (F9P7-People-2010-IRSES-269299).

References

- Gopalswamy, N., E. Aguilar-Rodriguez, S. Yashiro, S. Nunes, M.L. Kaiser, R. A. Howard (2005). Type II radio bursts and energetic solar eruptions. *J Geophys Res: Space Physics*, 110, no A12, CiteID A12S07.
- Ryabov, V. B., D.M. Vavriv, P. Zarka, B.P. Ryabov, R. Kozhin, V.V. Vinogradov, L. Denis. (2010) A low-noise, high-dynamic-range, digital receiver for radio astronomy applications: an efficient solution for observing radio-bursts from Jupiter, the Sun, pulsars, and other astrophysical plasmas below 30 MHz. *Astronomy and Astrophysics*, 510, id.A16.
- Shepelev, V. A., (2015). Determination of angular parameters of the sources of solar radio emission at decameter wavelengths. (in Russian), *Radiophysics & Radioastronomy*, 20,20-29.
- Thompson, A.R., J.M. Moran, and G.W. Swenson, (1986). *Interferometry and Synthesis in Radio Astronomy*, Wiley-Interscience, New York, USA.
- Vršnak, B., J. Magdalenic, P.Zlobec. (2004). Band-splitting of coronal and interplanetary type II bursts. *Astronomy and Astrophysics*, v.413, p.753-763.

The collection and compile data on SPE for the period 20th ÷ 23rd cycles of solar activity

Ishkov, V. ¹, Zabarinskaya, L. ², Sergeeva N. ²

¹ Pushkov Institute of Terrestrial Magnetism, Ionosphere and Radio Wave Propagation RAS
(IZMIRAN), Moscow, Troitsk, Russia,

² Geophysical Center RAS, Russia, Moscow, Russia
E-mail: ishkov@izmiran.ru

Abstract

The ongoing research into problems of the solar sources and their effects on the near-Earth space made it necessary to organize such content as a database and Catalogues for all the observation period of any geo-efficient phenomenon and, where possible, include all characteristics of the events themselves and the sources of these events in the Sun. It is especially important that the information is homogeneous and organized based on the series of similar Catalogues covering long time intervals (6 separate editions from 1970 to 2008).

A large volume of information contained in these Catalogues has demanded to implement improved and modern methods of its presentation. For easy reference, the navigation tools were created in the Catalogues allowing the user to move rapidly between different parts of the Catalogues, and perform quick search and access to the necessary events and its descriptions in them. A result of that initiative is presented in the Catalogue of Solar Proton Events (SPE) in the 23rd cycle of solar activity (1996÷2008) and in the sequence of Catalogues provided 5 separate editions for the period 1970 to 1996 (from the 20th to 22nd cycles of solar activity).

Introduction

In the age of space exploration the promotion of scientific research on the solar active phenomena made it necessary to classify solar flare data, detect the sources and study the effects occurring in the Sun on the near-Earth space. The uniform representation for solar proton events (SPE) is particularly important.

It would be more efficient, in this case, to deal with the series of the similar Catalogues involving lengthy intervals. The sequence of Catalogues provided 6 separate editions [1, 2, 3, 4, 5, 6] covers the time span 1970÷2008 (the 20th÷23rd cycles of solar activity) and will be later supplemented by the 24th cycle and future cycles of solar activity. The data on solar proton events with generation of protons for which the maximum flux of protons with energy of $E_p > 10$ MeV (million electron volts) exceeded $J_p \geq 1 \text{ cm}^{-2} \cdot \text{s}^{-1} \cdot \text{sr}^{-1}$ (pfu) were collected and systematized in these Catalogues.

Experience has shown that the choice of that threshold values for energy and number of the registered particles provides a reliable identification of the sources of proton increases in the Sun with reasonably certain time for the beginning of particle arrivals to a observation point and allows to determine well enough an initial flare event at which a generation of solar protons in the active area of the Sun, especially for events with a difficult profile, begins.

Threshold values with high energies and proton fluxes sharply decrease the statistical base of the events; the decrease of the energy and thresholds of proton fluxes creates difficulties related to identifying the proton sources due to the particles accelerated through the interplanetary medium.

In all published Catalogues the identical base of data presentation proposed in the first Catalogue of the International Team [7] is accepted. The volume of SPE data constantly increases from publication to publication. This is due to the fact that the scientists and researchers obtain more complete and various data on solar cosmic rays, the number of spacecrafts increases and the research equipment is constantly improved.

The Catalogues of Solar Proton Events (Fig. 1), as described in the present article, were prepared by the researchers from the scientific institutions of the USSR (mainly from Russia) which focus on studying the solar-terrestrial relations. That has allowed comprehensively to comprise the whole problem and each event in particular.

The fact that the editions of Catalogues are characterized by small quantities and difficult accessibility for researchers, in WDC for STP, Moscow they were published in electronic format (PDF files) using the modern equipment (the specialized book scanner) and software (ScanSoft PaperPort). At present, all these Catalogues are in open access and can be found on the web site of the WDC: http://www.wdcb.ru/stp/online_data.ru.html#ref113

The Catalogues contain the measurements of the particle flux values recorded by spacecrafts, balloons and by ground-based neutron monitors. Besides, the Catalogues contain the measurements of the particle flux values for ionospheric absorption of cosmic radiation in the Earth's polar caps. The processes occurring in the Sun were determined on the basis of radiation in optic, X-ray and radiofrequency ranges of the electromagnetic spectrum accompanying the solar flares events.

The information provided in all published Catalogues is available from open sources, the foremost of which were original data of outer space monitoring, as well as the periodicals named "Solar Geophysical Data" and "Solar Data" [1970÷1986].

Catalogue of solar proton events (SPE) in the 23rd cycle of solar activity

The last Catalogue [6] contains data on SPE for the time interval 1996÷2008. There were 142 such events in the solar cycle 23. In addition to the data on the solar proton fluxes observed by several spacecraft the Catalogue gives information on the particle sources and concomitant X-ray, optic, and radio emission over the entire range available for observation. The integral energy spectrum in the maximum of the intensity-time profile (so called time of maximum spectrum) is included for each SPE.

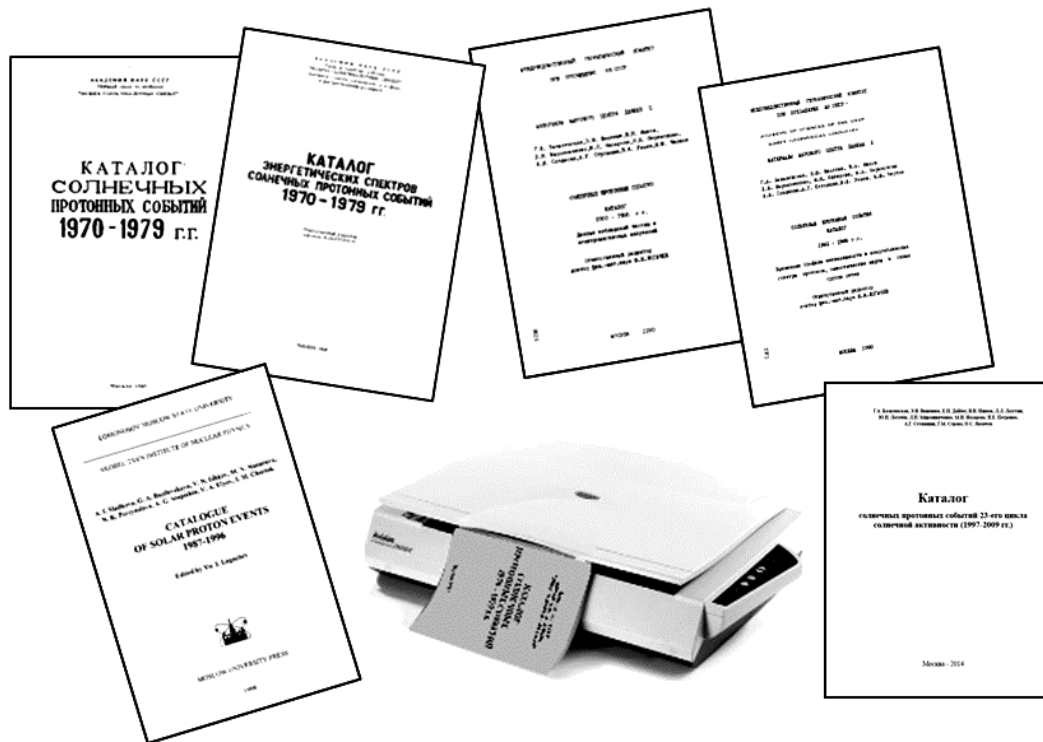


Fig.1. The sequence of Catalogues provided 6 separate editions covering the period from 1970 to 2008 (from the 19th to 23rd cycles of solar activity) are available on the website of WDC for STP.

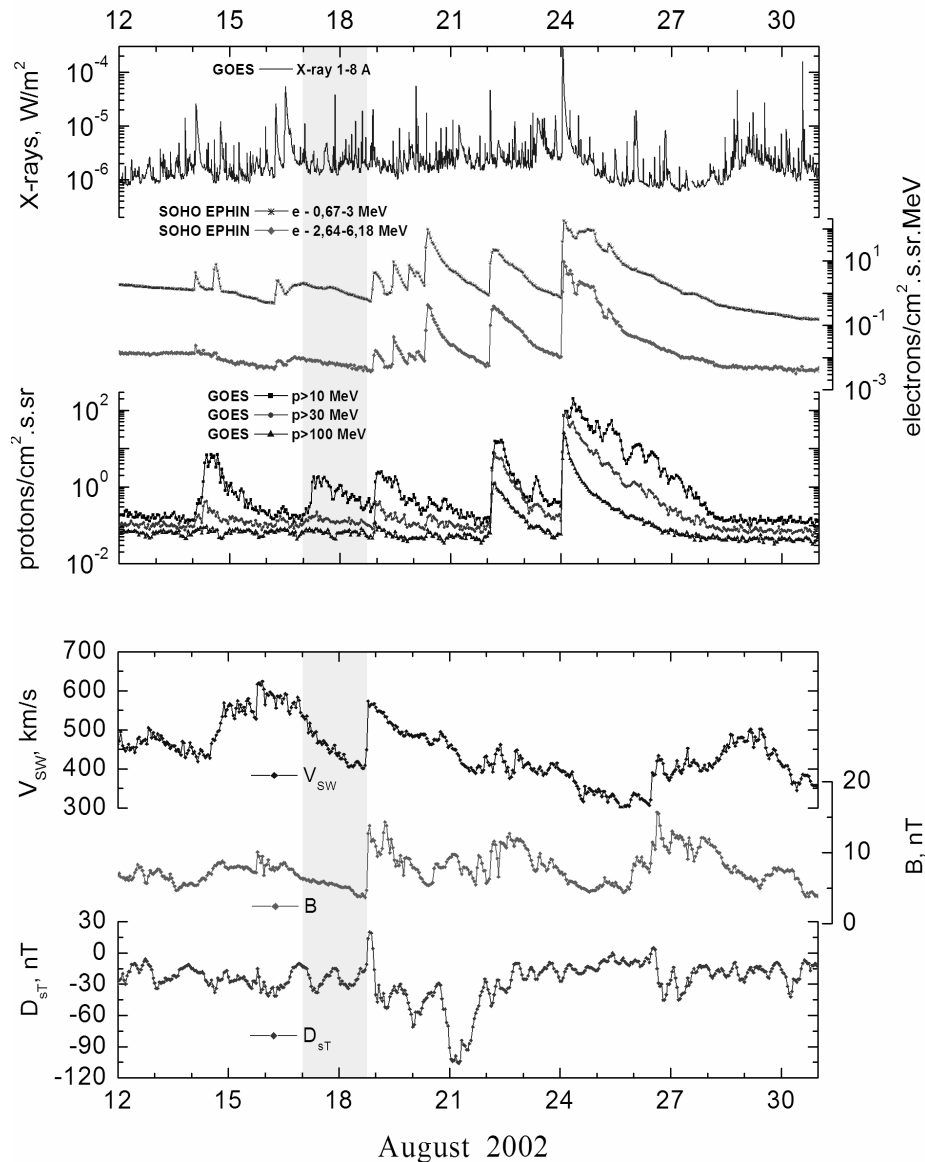


Fig.2. The overview plots showing the situation in the Sun and near-Earth space for the time interval covering the event described (X-rays, electron and protons fluxes, solar wind speed, strength of interplanetary magnetic field, and the Dst- index). during the time interval around this event. The time interval related to given event is slightly shadowed.

Each event in the mentioned Catalogue, in contrast with previous issues, is now illustrated by the plots of temporal behavior of X-ray, electron and protons fluxes, solar wind speed, strength of interplanetary magnetic field, and the Dst- index during the time interval around this event (Fig. 2). It allows to estimate the situation in the heliosphere for all time of SPE investigation.

After the overview figures, the time profiles of the proton fluxes are presented in larger scale as measured by several instruments in various energy ranges (Fig.3). The upper panels give the integral fluxes recorded by spacecraft ACE and GOES and the lower panel gives the differential fluxes recorded onboard SOHO. These spacecrafts situated inside the magnetosphere on the geostationary orbit (GOES) and at the libration point L1 (ACE and SOHO) give the most full information about particles before, during and after the start of the event.

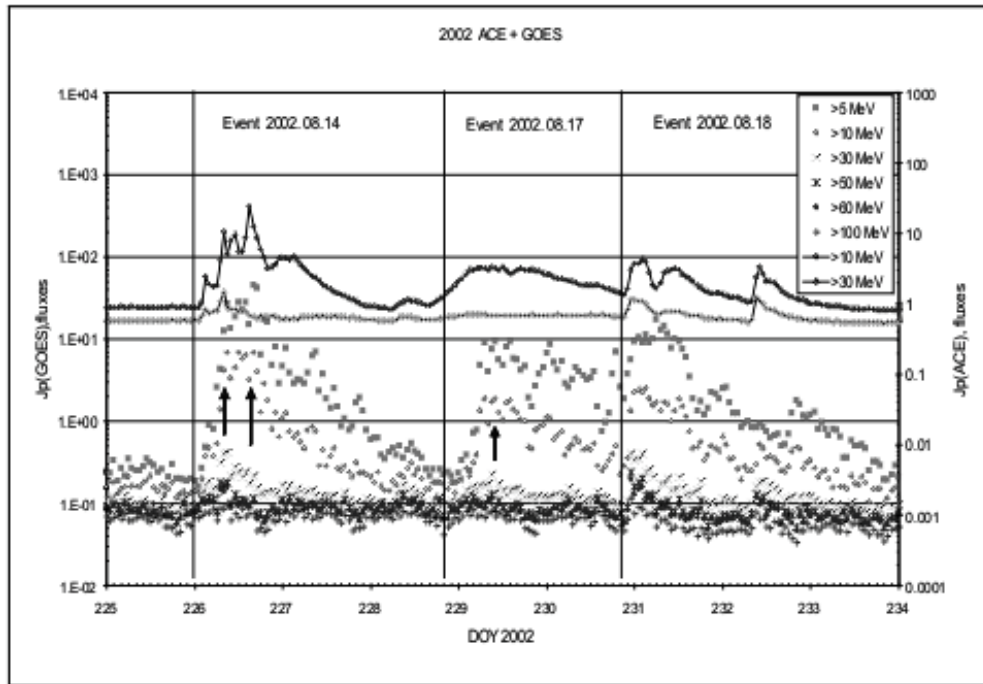


Fig.3. The time profiles of the proton fluxes measured by spacecrafts ACE and GOES (at the top), and SOHO (at the bottom).

After the time profiles of the proton fluxes for given event the plots of the integral energy spectra of protons at the time(s) of maximal intensity of the event are depicted (Fig. 4). The integral energy spectra were drawn according to the maximal proton fluxes of all energies contributed to the event. The proton fluxes registered in limited intervals of energy were converted to integral values. In the case of several intensity maxima in a given event the spectra were constructed for each maximum separately.

There follows the particle flux tables for a given event. The tables contain the particle flux values at various energies in the maximum of the intensity-time profile (or in each maximum if you have more than one) as recorded by different spacecraft. The unit of measurement for the event duration is a day. Note that this parameter shows strong variations depending on the instrument and the different proton energies. The duration is measured with accuracy not worse than ± 1 day.

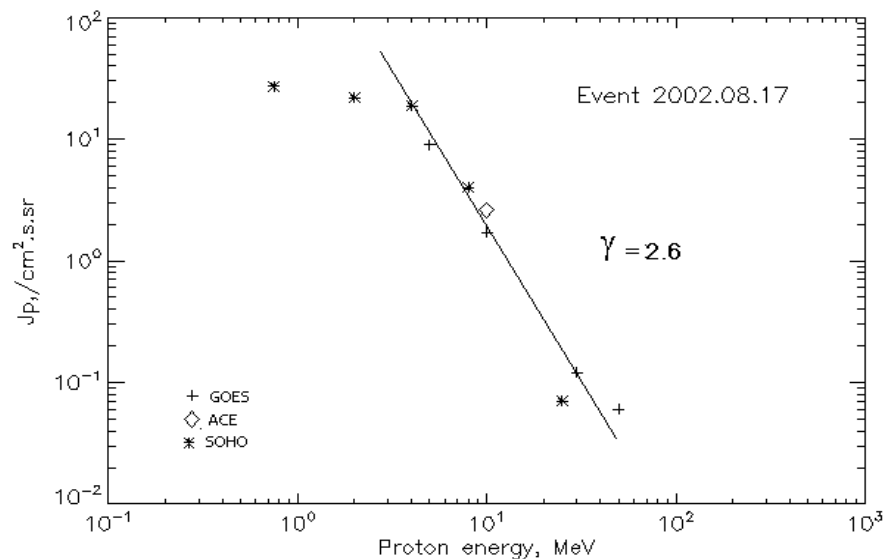


Fig.4. The integral energy spectra for protons at the time(s) of maximal intensity of the event which occurred on 17 August 2002.

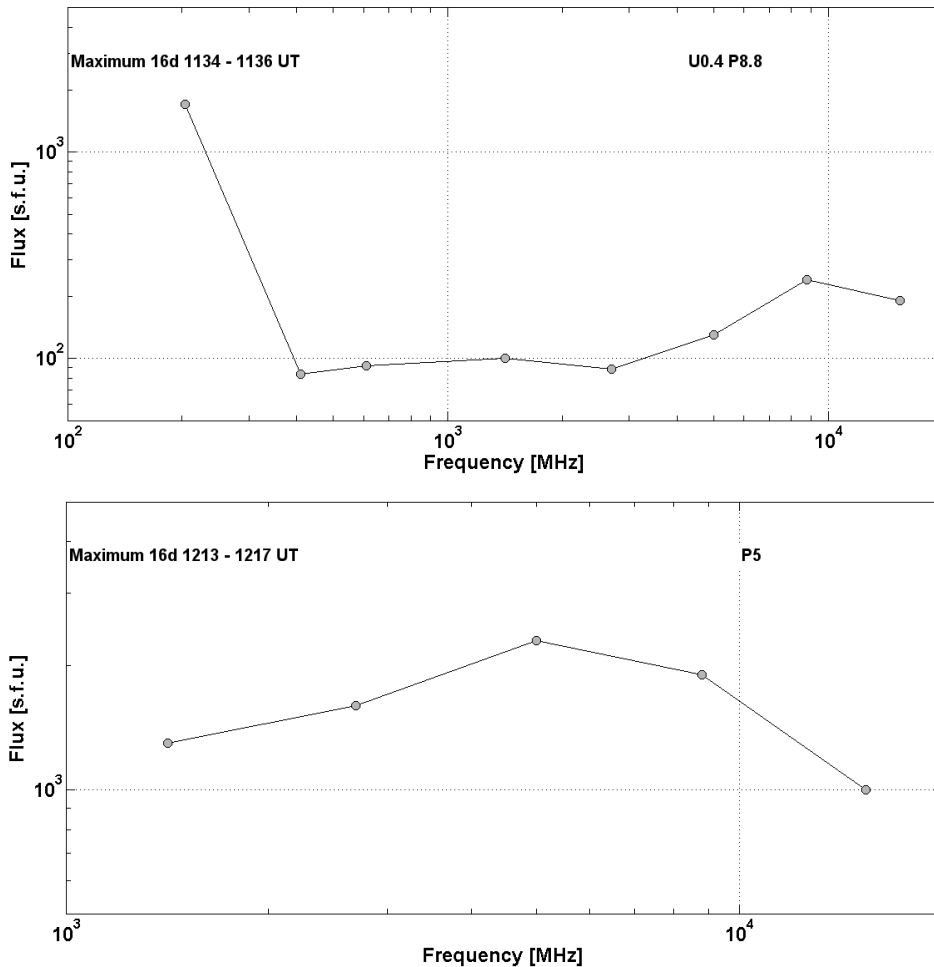


Fig. 5. The plots of radio spectrum in the decimeter and centimeter range of wavelengths are presented. These spectra allow to estimate and potentially identify patterns that are typical of flare events.

The following is the information on the observed solar flare phenomena, the sources of the given proton events, indicating their confidence level. The parameters and characteristics for the flare event are set out in table format with numerical values. The tables in the Catalogue described in this paper were organized into blocks with all observed ranges of electromagnetic radiation (optics, soft and hard X-rays, gamma and radio radiation), the neutrons of solar origin, dynamical phenomena within H α line and continuous spectrum (WL– in white light), including the main features of coronal mass ejection (CME) in the solar flare event.

After the tables the plots of radio spectrum in the decimeter and centimeter range of wavelengths are included (Fig. 5). This radio frequency spectrum provide the opportunity to evaluate and potentially identify regularities unique to flare events which are the sources of SPE.

Presentation of Catalogue in the 23rd cycle

A large volume of information in the Catalogue of solar proton events (SPE) in the 23rd cycle has demanded to implement improved and more modern methods of its presentation. Adobe Acrobat Professional DC (Pro) is an ideal platform for creating rich interactive document which has made it easier to use, navigate and understand. In simple navigation schemes, you can successfully move the viewer through an entire document using only two buttons □ one set to Go To Next Page and one set to Go To Previous Page. For more targeted

navigation, you can create buttons that go to specific pages, events and their description by using the Go To Page action and entering a specific page or event number (Fig.6).

For easy reference the navigation tools were used in the Catalogues allowing the user to move rapidly from the page "Contents" to the selected parts of the Catalogue and back.

The sequence of Catalogues provided 6 separate editions covering the period from 1970 to 2008 (from the 20th to 23rd cycles of solar activity) are available on the website of WDC for SEP. Digital Object Identifiers (DOI) were assigned to all of these Catalogues of solar proton events (SPE). From that point, the Catalogues have the persistent identifiers and CrossRef metadata records which provide an opportunity for citation of data sets in scientific publications available through an online platform (Fig. 7). This was done within the ESDB (Earth Science DataBase) project carried out by the Geophysical Center, RAS. This project aims to create modern system for registration, publication and citation of geophysical data with the digital object identifiers (DOI) to be used for the identification of intellectual property in the virtual environment.

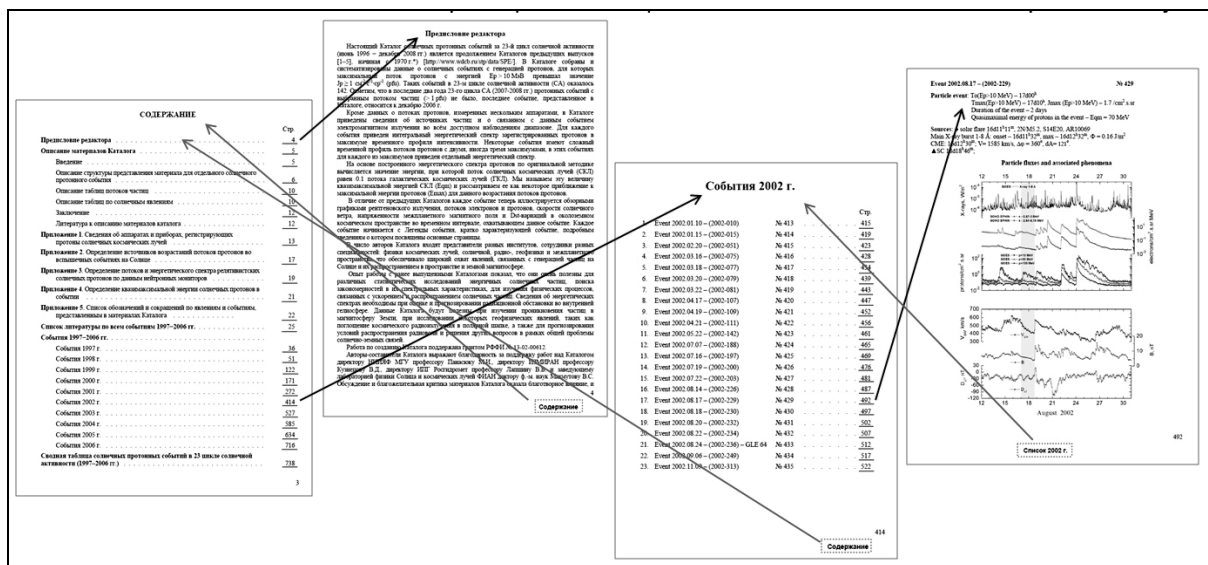


Fig.6. The scheme of links using the transitions between the different parts of the Catalogue and quick search of the appropriate events and their parameters in the Catalogue.

This project is designed to enhance the visibility and accessibility of geophysical data to scientific research, to facilitate the process of the retrieval, identification and publication of these data, and also to promote a culture of data citation similar to other research sources of information (magazines, articles, books, etc.).

Conclusion

All publications of the mentioned Catalogues followed the format of the well-known catalogue [7] and taken together, they comprise a set of homogenous data in ascending order according to the solar cosmic rays. They were created for collecting, organizing and providing information about all registered SPE and can be used as the reference book on solar flare events (SPE), sources of SPE, and active areas in which the conditions for proton flares were formed. The Catalogue of solar proton events (SPE) in the 23rd cycle is addressed to the wide range of professionals in the field of solar-terrestrial physics, who examine the solar active phenomena or radiological space flights safety, and the researchers interested in solar impact on the atmosphere and the biosphere of the Earth.



Earth Science DataBase
GEOPHYSICAL CENTER RAS

Please enter the doi that you want to resolve:

Каталог солнечных протонных событий 23-го цикла солнечной активности (1996–2008 гг.)

Ю. И. Логачёв¹, Г. А. Базилевская², Э. В. Ващенко³, Е. И. Дайбог¹, В. Н. Ишков^{4,5}, Л. Л. Лазутин¹, Л. И. Мирошниченко^{4,1}, М. Н. Назарова⁷, И. Е. Петренко⁷, А. Г. Ступишин⁶, Г. М. Сурова¹, О. С. Яковчук¹

Редактор: Ю. И. Логачёв¹

Аннотация
Настоящий Каталог является продолжением Каталогов предыдущих пяти выпусков, содержащих данные о солнечных протонных событиях (СПС) начиная с 1970 г. В Каталоге собраны и систематизированы данные о СПС с генерацией протонов, для которых максимальный поток протонов с энергией $E_p > 10$ МэВ превышал значение $J_p \geq 1$ см⁻²·с⁻¹·ср⁻¹ (pfu). Таких событий в 23-м цикле солнечной активности оказалось 142.

Кроме данных о потоках протонов, измеренных несколькими космическими аппаратами, в Каталоге приведены сведения об источниках частиц и о связанном с данным событием электромагнитном излучении во всём доступном наблюдением диапазоне. Для каждого события приведен интегральный энергетический спектр зарегистрированных протонов в максимуме временного профиля интенсивности.

В отличие от предыдущих Каталогов каждое событие теперь иллюстрируется обзорными графиками рентгеновского излучения, потоков электронов и протонов, скорости солнечного ветра, напряженности межпланетного магнитного поля и Dst-вариаций в околоземном космическом пространстве во временном интервале, охватывающем данное событие.

Данные хранятся в Мировом центре данных по солнечно-земной физике, Москва (<http://www.wdcb.ru/stp/index.en.html>). Данные находятся в свободном доступе.

doi: [10.2205/ESDB-SAD-P-001-RU](https://doi.org/10.2205/ESDB-SAD-P-001-RU)

Цитирование: Логачёв Ю. И., Г. А. Базилевская, Э. В. Ващенко, Е. И. Дайбог, В. Н. Ишков, Л. Л. Лазутин, Л. И. Мирошниченко, М. Н. Назарова, И. Е. Петренко, А. Г. Ступишин, Г. М. Сурова, О. С. Яковчук. Каталог солнечных протонных событий 23-го цикла солнечной активности (1996–2008 гг.). *ESDBrepository*, ГЦ РАН, Москва, doi: 10.2205/ESDB-SAD-P-

URL for downloading:
http://www.wdcb.ru/stp/data/SPE/Catalog_SPE_23_cycle_SA.ru.pdf,
http://www.wdcb.ru/stp/data/SPE/Catalog_SPE_23_cycle_SA.pdf (Англоязычная версия)

Fig.7. The response page of the Catalogue located in the main repository of ESDB <http://esdb.wdcb.ru/>. This page provides detailed descriptions of data, DOI name, URL address of the database.

The experience with the previously published Catalogues has shown that they are very useful for various statistical research on vigorous solar particles and identification of patterns in their spectral characteristics. In addition, they are useful in studying the physical processes related to acceleration and propagation of solar particles. The information about energy spectra is necessary for assessment and prediction of a radiation levels in an internal heliosphere. The Data available in the Catalogue of solar proton events (SPE) in the 23rd cycle are useful for studying the particle penetration into the terrestrial magnetosphere and some geophysical phenomena, such as absorption of a cosmic radiation in a polar cap. The Catalogue data would aid in forecasting the conditions of radio wave propagation and other questions concerning a general problem of solar-terrestrial interactions.

References

- [1] S.T. Akiniyan, G.A. Bazilevskaya, V.N. Ishkov et al. Catalogue of solar proton events 1970 – 1979 // Edited by Yu.I. Logachev. Moscow, IZMIRAN, 1982. 184 p. http://www.wdcb.ru/stp/data/SPE/SPE_1970-1979.pdf.
- [2] G.A. Bazilevskaya, E.V. Vashenyuk, V.N. Ishkov et al. Catalogue of energy spectra of solar proton events 1970÷1979 // Edited by Yu. I. Logachev. Moscow, IZMIRAN, 1986. 236 p. [http://www.wdcb.ru/stp/data/SPE/SPE_1970-1979_\(SPECTRA\).pdf](http://www.wdcb.ru/stp/data/SPE/SPE_1970-1979_(SPECTRA).pdf).
- [3] G.A. Bazilevskaya, E.V. Vashenyuk, V.N. Ishkov et al. Solar Proton Events. Catalogue 1980 – 1986. Data on particles and electromagnetic emission // Edited by Yu.I. Logachev. Materials of the World Data Center B, Soviet Geophysical Committee of the Academy of Sciences of the USSR, Moscow, 1989. 160 p. [http://www.wdcb.ru/stp/data/SPE/SPE_1980-1986_\(SPECTRA\).pdf](http://www.wdcb.ru/stp/data/SPE/SPE_1980-1986_(SPECTRA).pdf).
- [4] G.A. Bazilevskaya, E.V. Vashenyuk, V.N. Ishkov et al. Solar Proton Events. Catalogue 1980 – 1986. Plots of the time profiles and energetic spectra of protons, synoptic charts and schemes of sunspot groups // Edited by Yu.I. Logachev. Materials of the World Data Center B, Soviet Geophysical Committee of the Academy of Sciences of the USSR, Moscow, 1990. 204 p. http://www.wdcb.ru/stp/data/SPE/SPE_1980-1986.pdf.
- [5] A.I. Sladkova, G.A. Bazilevskaya, V.N. Ishkov et al. Catalogue of solar proton events 1987 – 1997. // Edited by Yu.I. Logachev. Moscow University Press, Moscow, 1998. 246 p. http://www.wdcb.ru/stp/data/SPE/SPE_1987-1996.pdf.
- [6] Yu.I. Logachev, G.A. Bazilevskaya, V.N. Ishkov et al. Catalogue of Solar Proton Events in the 23rd Cycle of Solar Activity (1996÷2008). 2016, doi: 10.2205/ESDB-SAD-P-001-RU. http://www.wdcb.ru/stp/data/SPE/Catalog_SPE_23_cycle_SA.ru.pdf, http://www.wdcb.ru/stp/data/SPE/Catalog_SPE_23_cycle_SA.pdf (in English) [ftp://ftp.ngdc.noaa.gov/STP/space-weather/interplanetary-data/solar-proton-events/documentation/solar-proton-events_1996-2008_logachev-et-al\(2016\).pdf](ftp://ftp.ngdc.noaa.gov/STP/space-weather/interplanetary-data/solar-proton-events/documentation/solar-proton-events_1996-2008_logachev-et-al(2016).pdf)
- [7] H.W. Dodson, E.R. Hedeman, R.W. Kreplin, et al. Catalog of solar particle events 1955 ÷ 1969. Ed. Z. Švestka and P. Simon. Dordrecht, Holland, Boston-USA: Reidel Publ. Com, 430 p. 1975.

Influence of solar and geomagnetic activity on the ionosphere over Bulgaria

Bojilova R.¹, Mukhtarov P.¹

¹ National Institute of Geophysics, Geodesy and Geography - BAS, Bulgaria
E-mail: bojilova@geophys.bas.bg

Abstract

An analysis was made of the seasonal dependence of the response of the maximum electron density of the ionosphere to the geomagnetic activity and the short-periodic variations of the ionizing solar radiation. The research was based on data from Ionsospheric Station - Sofia from 1995 to 2014. Crosscorrelations and delay times between the relative values of the critical frequencies of the ionospheric F region with the planetary geomagnetic activity index Kp and the solar radio emission wave with a wavelength of 10.7 cm for each calendar month of the year are investigated. The results can be used to create empirical models of ionospheric characteristics, depending of variations of solar and geomagnetic activity.

Introduction

In the present paper an attempt was made to determine the summarized characteristics of the response of the maximum electron density of the ionosphere under the influence of geomagnetic anomalies and short periodic variations of the solar ionizing radiation. The main focus is on determining the seasonal dependencies of these responses. A cross-checking analysis was used to determine not only the degree of interconnection of solar and ionospheric processes, but also the delay time of the ionosphere response.

The seasonal dependence of the geomagnetic response of the medium latitude ionosphere is due to the seasonal change in the dynamic mode of the atmosphere. Under the influence of the solar plasma flows into the polar oval, the neutral air temperature increases and the atomic oxygen / nitrogen (O / N₂) ratio changes, which directly affects the rate of recombination. Heated air is transferred from the meridional component of the wind from high to medium latitudes and leads to negative ionospheric anomalies (a decrease in electron density), which is the most typical manifestation of ionospheric anomalies of geomagnetic origin in summer and equinox months [Prölss, 1995].

Variations of the solar ionizing radiation cause positive anomalies in the ionosphere. The changes in electron density within the 11-year solar cycle is not the subject of the present study. Variations in solar activity with a time scale of less than one month are considered. Both with high and low solar activity, such variations are observed in connection with the rotation of the Sun around its axis with a period of about 27-days.

Data

The values for the planetary index of geomagnetic activity Kp are obtained from NOAA - <https://www.ngdc.noaa.gov>. The data from the vertical sounding of the ionosphere with radio waves (foF2) are from Ionsospheric Station "Plana" at NIGGG-BAS.

The values of the solar F10.7 radio emission flux are obtained from NASA-<https://omniweb.gsfc.nasa.gov/>.

The used ionospheric, solar and geomagnetic data are processed according to the goals of the present study. From the measured values of the critical frequencies of the ionospheric F-region (foF2) (which are related to the maximum electron concentration with the dependence $Nm[cm^{-2}] = 1,24 \cdot 10^4 foF2^2 [MHz]$) - Relative deviations from the stationary diurnal course are calculated [Kutiev, I., P. Muhratov, 2001].

$$\Phi(t) = \frac{foF2(t) - foF2_m(UT)}{foF2_m(UT)}$$

Stationary 24-hour values are obtained by averaging the critical frequency values over a 31-day period centered on the current day for the same universal time that is in the current hour t . In this way, the diurnal, seasonal and solar dependence of foF2 is filtered out.

Values of F10.7 are processed in a similar manner:

$$F107_{rel} = \frac{F107 - F107_m}{F107_m}$$

The mean values of F10.7 (F10.7m) were obtained by averaging a 31-day running segment centered on the current day. The planetary geomagnetic activity indices are filtered by removing the running average for 31 days.

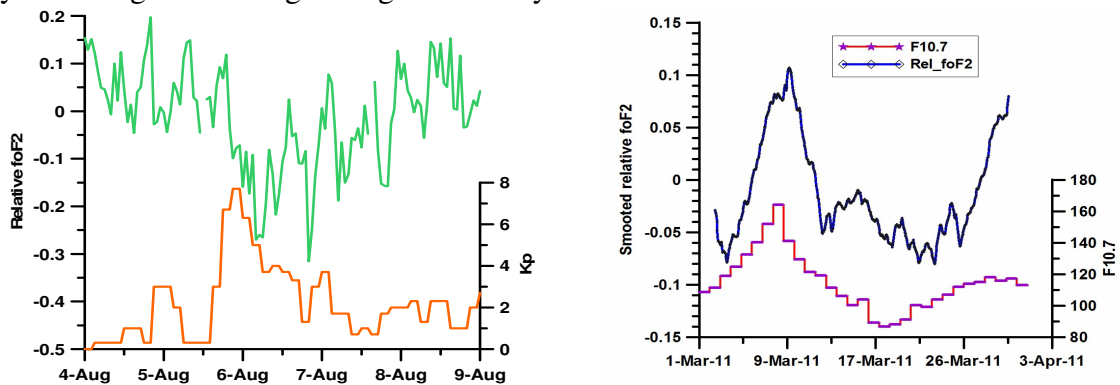


Fig. 1. Geomagnetic storm in August 2011 and solar variation in March 2011.

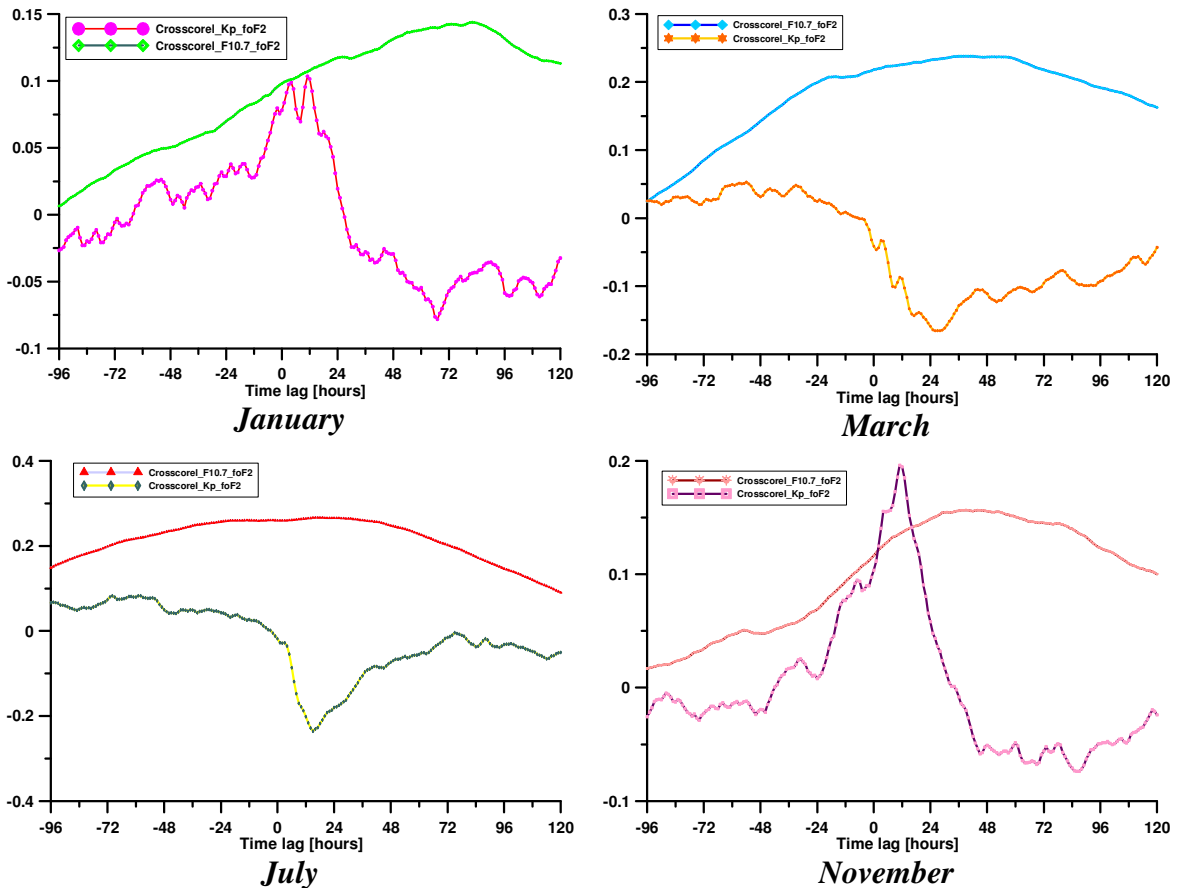


Fig. 2. Normalized crosscorrelation functions between relative foF2 and solar and geomagnetic indices.

Two examples illustrating the purpose of the present study are shown on Fig. 1. The left panel shows the course of the Kp index during a geomagnetic storm in August 2011 and the relative critical frequency. The negative ionosphere response as well as the delay and the geomagnetic anomaly are clearly visible. The right panel shows the solar activity fluctuation in March 2011 and the relative critical frequency (smoothed by three-day running averages). The face is a positive response of the ionosphere, also with some delay.

Crosscorrelation analysis

Calculations of normalized crosscorrelation functions between solar and geomagnetic indexes and relative critical frequencies are based on the values for each calendar month of the years from 1995 to 2014.

Fig. 2 shows the results for typical winter, spring, summer and autumn months. The crosscorrelation functions with the geomagnetic index Kp for the months of January and November indicate the presence of two types of response - positive with little delay and negative with significant delay.

From the presence of a positive and negative response of the ionosphere it can be concluded that two physical mechanisms of ionospheric response appear in the winter months [Andonov *et al.*, 2011; Mukhtarov *et al.*, 2013]. In the summer, the Kp correlations show only a negative response, with significantly less delay. Correlations with the solar activity are positive, showing a longer delay in the winter months.

Fig. 3 shows the seasonal course of the maximum (per module) values of the correlation functions and their corresponding time delays. The negative response of the geomagnetic disturbances is strong during the summer months (high negative correlations) with a little delay in time and decreases in the winter months with the delay increasing. The ionospheric response to variations in solar activity increases during the summer months compared to winter. However, the delay does not show a pronounced seasonal course.

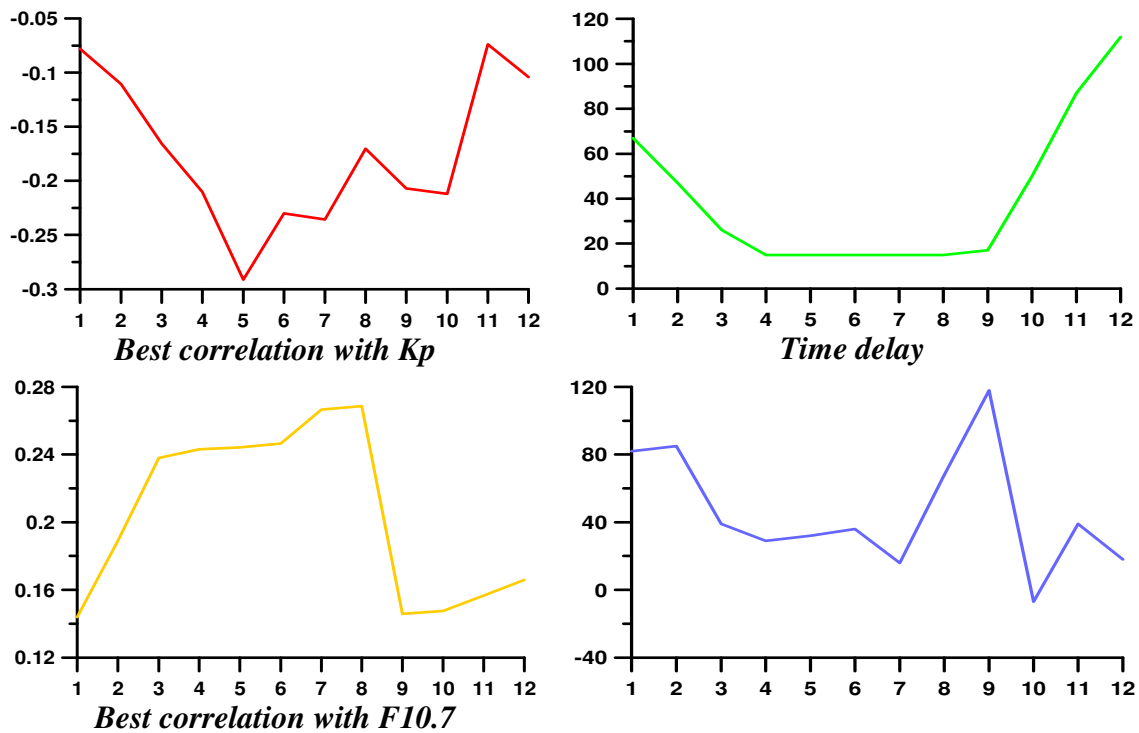


Fig.3 Maximal crosscorrelation between relative foF2 and solar and geomagnetic indices and corresponding time delay.

Conclusion

The correlation analysis of the response characteristics of the maximum ionospheric density of the variations in solar and geomagnetic activity shows the presence of a pronounced seasonal dependence due to the different mechanisms of formation of the ionospheric F-region in different seasons. While the direct ionization processes dominates during the summer season in low solar zenith angles, the process of transferring charged particles during the winter plays a significant role. Moreover, the mechanisms of transporting heated neutral air from polar to medium latitudes during geomagnetic anomalies is strongly dependent on the total meridional circulation of the atmosphere. In the winter season, the transmission is hampered by the predominant reverse direction of the meridian wind, which can explain the reduction of the negative response and the increase of the delay. The reason for the positive response during the winter season with a negligible delay should be sought in the processes above the maximum of the electron density [Mukhtarov, P. and Pancheva, D., 2012]. The results obtained may prove useful in the development of empirical ionospheric models

References

- Andonov, B., P. Mukhtarov and D. Pancheva. "Empirical model of the TEC response to the geomagnetic activity over the North American region." *Advances in Space Research* 48.6 (2011): 1041-1048.
- Kutiev, Ivan, and Plamen Muhratov. "Modeling of midlatitude F region response to geomagnetic activity." *Journal of geophysical research* 106.A8 (2001): 15501-15510.
- Mukhtarov, P., B. Andonov and D. Pancheva. "Global empirical model of TEC response to geomagnetic activity." *Journal of Geophysical Research: Space Physics* 118.10 (2013): 6666-6685.
- Mukhtarov, Plamen and Dora Pancheva. "Thermosphere-ionosphere coupling in response to recurrent geomagnetic activity." *Journal of Atmospheric and Solar-Terrestrial Physics* 90 (2012): 132-145.
- Prölss, G. W. (1995), Ionospheric F region storms, in *Handbook for Atmospheric Electrodynamics*, vol. 2, edited by H. Volland, pp. 195–248, CRC Press, Boca Raton.

Features of upper Ionosphere Modification by Interactive Tropical Cyclons from Cosmos-1809 Satellite and Interkosmos Bulgaria-1300 Data

*B. Boychev*¹, *G. Belyaev*², *V. Kostin*², *O. Ovcharenko*², *E. Trushkina*²

¹ Space Research and Technology Institute – Bulgarian Academy of Sciences

² Institute of Terrestrial Magnetism Ionosphere and Radio Wave Propagation RAS

Abstract

The data analysis of the on-board instruments set of the Kosmos-1809 and IKB-1300 satellites is presented for the following events:

1. Sequences of 5 hurricanes in the Atlantic Ocean in September 1981.
2. Sequences of 3 super-typhoons in the Western Pacific in November 1990.
3. Continuous sequence of tropical cyclones (TC) after the Pinatubo and Hudson volcanoes eruptions 1991.

It is shown that the effects of two interacting TC impact on the ionosphere differ from those of single TC. Self-organization of a single TC leads sequentially to the formation above it in the stratosphere of an anticyclone, and above - to a vertical flooded jet, which cause different effects in the ionosphere. If the developing of the first TC causing the second TC arises at a distance of ~ 20 degrees, the Ne structure and other plasma parameters of the upper ionosphere change. The strongest volcanic eruptions in the twentieth century (1991) threw a significant amount of aerosols into the stratosphere. Stratospheric changes for interacting TC and perturbations after volcanic eruptions apparently cause a redistribution of infrasound along the TC track which can lead to the formation of a new TC.

Introduction

Tropical cyclones are the most powerful processes in the atmosphere, redistributing the energy stored in the oceans. The National Hurricane Center (NHC) is the division of the United States' National Weather Service responsible for tracking and predicting weather systems within the tropics between the Prime Meridian and the 140th meridian west poleward to the 30th parallel north in the northeast Pacific Ocean and the 31st parallel north in the northern Atlantic Ocean. Information on other oceans is available on the website of tropical cyclone warning centers for the northwest Pacific in Hawaii (the Joint Typhoon Warning Center). Information on meteorological parameters at altitudes up to the lower stratosphere and calculations of the trajectories of the motion of the TC is presented. However, there are many unclear questions about the physics of TC development. Earlier, the authors of the reports [Belyaev G., 2015; Kostin, V.M., 2015; Isaev, N.V., 2010] attempted to explain the features of the upper ionosphere plasma, which were observed from satellites over the TC. It was suggested that a flooded stream of neutral atoms is formed above the stratospheric anticyclone over the TC. The heating of the stratosphere and the formation of a jet can occur because of the self-organization of nonlinear acoustic waves propagating upward [Aburjania, 2013]. Intensive lightning discharges in the TC can be a source of acoustic waves. Neutral atoms of the jet flying above ~ 230 km move along ballistic trajectories and reach heights of more than 1000 km where they can be ionized. Selected electromagnetic effects with their participation were observed by e/m satellite complexes [Belyaev G., 2015; Kostin, V.M., 2015]. The flooded jet is supported by surface oscillations that propagate upward along the jet. Feedback is created by the generation of infrasonic vibrations that propagate down the stream. Infrasound reaches surface of the ocean and extends along the surface, enhances ocean-atmosphere heat exchange. This leads to an intensification of the TC.

However, in many cases there are interacting TC [Dong, K., 1983]. Back in the 1970s the important role of the stratospheric state for the self-organization of atmospheric processes was

statistically demonstrated [Sadler, J.C., 1976]. In the present work, the satellites Cosmos-1809 and IKB-1300 data during the development of interacting TC are presented. Particular attention is paid to the development of the TC and its impact on the ionosphere after the eruption of the volcanoes PINATUBO and HUDSON in 1991.

These eruptions were the strongest in the 20th century. The eruption in August to October 1991 was a large plinian eruption with a VEI of 5, that ejected 4.3 km³ bulk volume (2.7 cubic km of dense rock equivalent material). Parts of the glacier melted and ran down the mountain as mud flows (see glacier run). In addition to the ash, a large amount of sulfur dioxide gas and aerosols were ejected in the eruption. These contributed to those already in the atmosphere from the even larger Mount Pinatubo eruption earlier in the year and helped cause a worldwide cooling effect over the following years. Ozone was also depleted, with the Antarctic ozone hole growing to its largest levels ever recorded in 1992 and 1993. Effects both from volcanic explosions [Cheng, K., 1992] and changes in the propagation of radio waves in the low-frequency range have been observed in the ionosphere [Labytzke, K., 1994].

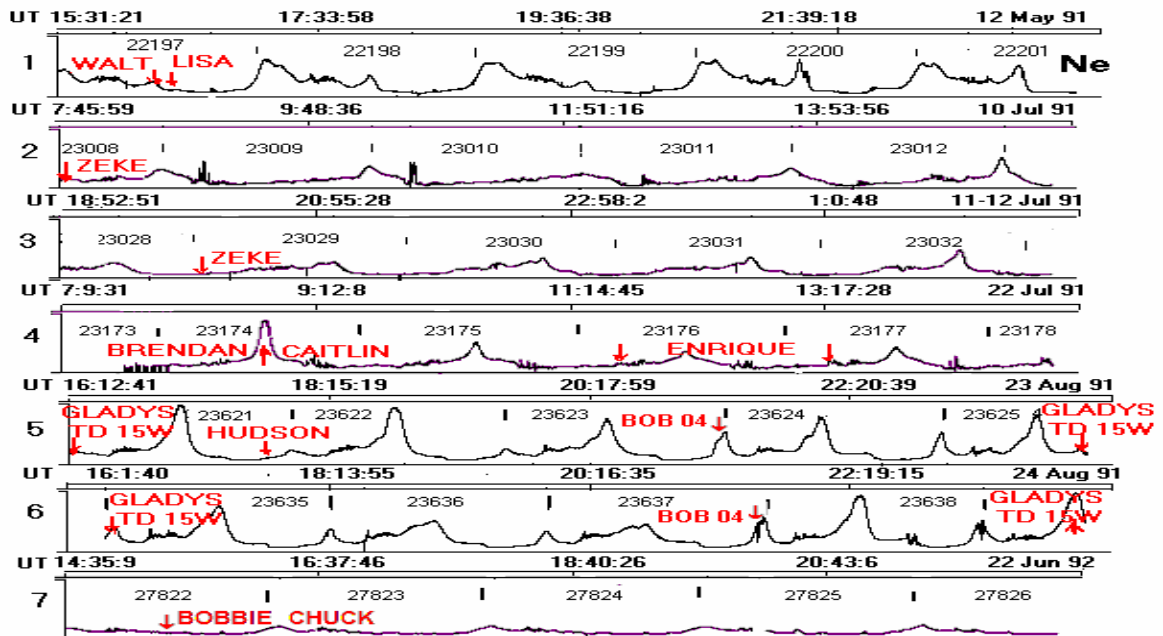


Fig.1. Ne (t.v.) changing along the trajectory of the satellite Cosmos-1809 before and after the Pinatubo volcano eruption. The numbers of revolutions are indicated and the moments of the latitude of the nearest TC passing are marked.

Influence of PINATUBO and HUDSON volcanic eruptions on the dynamics of the TC and ionosphere according to the Cosmos-1809 satellite data

Analysis of the results of the electron density Ne measurements in the upper ionosphere by the Cosmos-1809 satellite during the global monitoring of plasma parameters in 1990-1993 showed that after the strongest eruptions of Pinatubo and Hudson volcanoes in the summer of 1991 the average value of Ne decreased. The change in the plasma density along the trajectory of the satellite is shown in Figure 1. This fact agrees well with the global cooling of the Earth's atmosphere by 0.5 degrees for 4 years.

However, in some cases, when the satellite passed over the zone of TC impact, anomalous parameters of the ionosphere were noted. Figure 1 shows the individual fragments of Ne monitoring during periods of interacting TC development. The numbers of revolutions that are longitudinally shifted by 26.1 degrees, shifted in time by 104 minutes, shifted according to local time by 4 minutes are indicated. The moments of passing the latitude of the nearest TC are marked. The TC parameters are taken from the JTWC annual report [Rudolph, D.K., 1991].

Walt was the first super typhoon in the western North Pacific this year. On May 12, he was in the stage of alone typhoon of the 5th category (a wind of 140 kt). The revolution 22197 passed at LT = 1 over Walt (panel 1 Fig.1). But the anomalous Ne increase is noted at the revolution 22200, when the morning terminator passed through Walt and ionization of the neutral atoms injected by the typhoon into the ionosphere occurred. A similar situation was considered in detail in [Belyaev G., 2015].

Walt developed as part of an equatorial convective process known as a "westerly burst" [Lander, M.A., 1990] at the same time a twin, Tropical Cyclone Lisa, developed in the Southern Hemisphere by 5-7 May. Figure 2 shows the change in Ne, E140 Hz and 4600 Hz in the morning sector at the orbits closest to the two TC interaction zone the intensity of which was below 30kt. There is a slight increase in Ne at the revolutions west of 22106, passing along the meridian of the TC, which corresponds to an additional vertical removal of hydrogen atoms from the lower ionosphere above the center of Walt. The confirmation of this fact is an increase in the frequency of the lower hybrid oscillations and the output of the spectral maximum of the noise from the E4600 Hz channel, which is presented on the revolution 22109. The second minimum in the E4600 Hz channel at latitude of 25 degrees is associated with the entry of neutral excited hydrogen atoms moving along inclined trajectories to the area of influence of the Chinese 3SA transmitter. An electron flux with energies of 3-5eV is generated over the VLF transmitters in the ionosphere, which ionizes the excited hydrogen atoms. This effect was noted in [Kostin, V.M., 2015]. The same features in the E4600 Hz channel are noted at the 22106-22108 revolutions. The ionization of the flux of excited helium atoms above the center of the Lisa TC enhances the cyclotron oscillations at the helium frequency, which is noted in the E140 Hz channel.

The continuous sequence of TC from July to December 1991 arose in the western part of the Pacific Ocean after the eruption of the Pinatubo and Hudson volcanoes. The first in this chain was ZEKE (Fig.3). Parameters of the ionosphere plasma along the ZEKE meridian during the birth of TC AMY (LT = 4) are shown. There is a slight Ne increase at the zenith and heating of electrons in the vicinity of the geomagnetic equator. Strong anomalies of electrostatic oscillations are observed over the Australian NWC ULW transmitter (21.8 S, 114.2 E), which operated at a frequency of 19.8 kHz. The anomalous Ne values on July 22 at the 23174 revolution (panel 4 in Fig.1), were caused by the effect of the interacting BRENDAN and CAITLIN Tcs at the ionosphere.

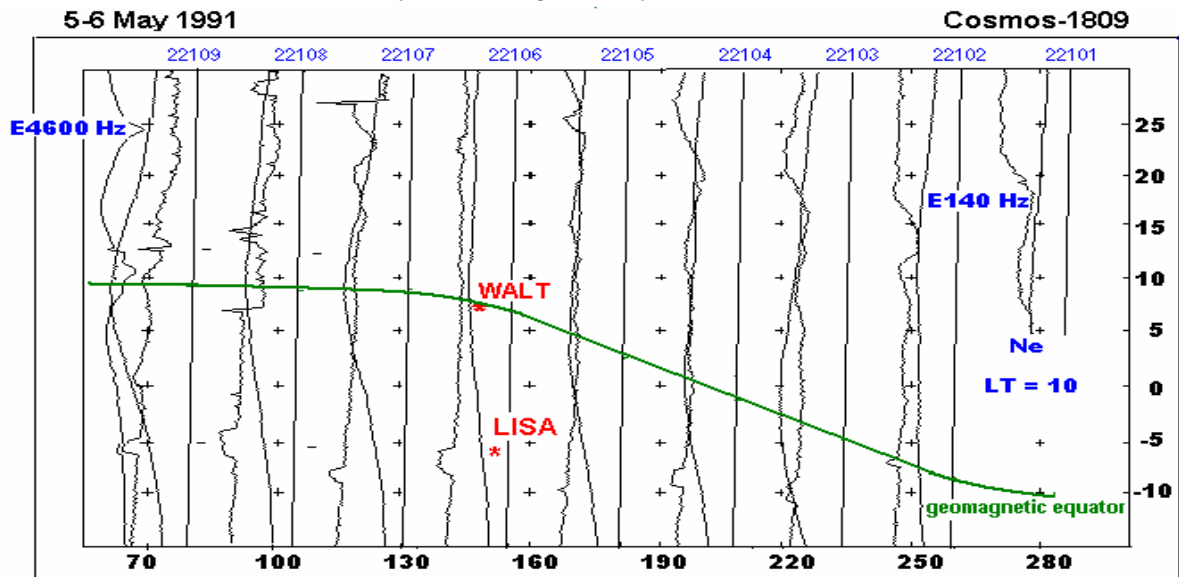


Fig.2. Parameters of the upper ionosphere plasma on the revolutions closest to the development zone of the pair TC-WALT and LISA at the phase of the tropical storm.

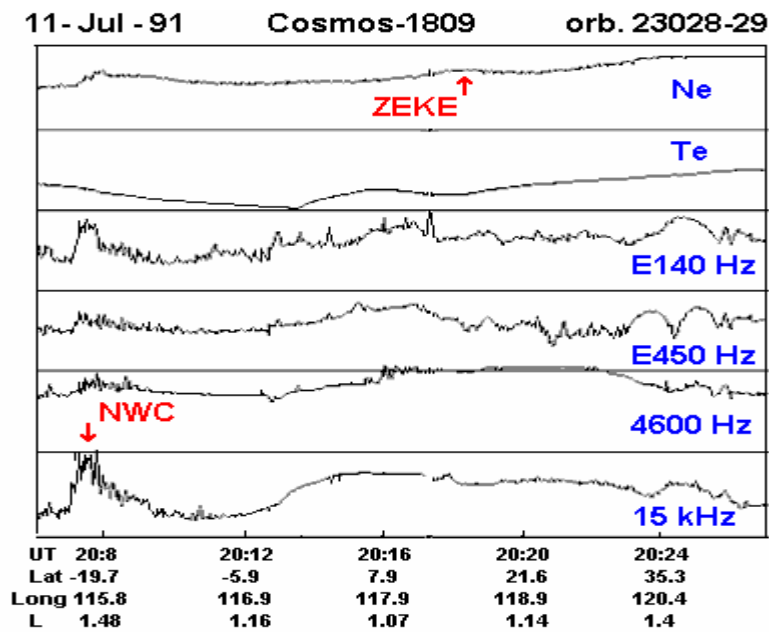


Fig.3. Upper ionosphere plasma parameters above the typhoon ZEKE and the volcano Pinatubo.

In August 1991 the acoustic impact of explosive eruptions of the Hudson volcano led to a significant Ne increase in the daytime ionosphere (panels 5 and 6 in Fig.1). It should be noted an interesting event when the typhoon GLADYS (tropical depression BOB 04) and Chinese VLF transmitter acted on the ionosphere at one L-shell (Fig.4). A stable cavity was formed at this L-shell in the E4600 Hz channel, which is connected with the increased injection of hydrogen atoms in this region.

By 15 June 1992, the monsoon trough became established in its normal climatological location across the South China Sea, The central Philippine Islands and extended into the Caroline Islands. By 21 June, Bobbie’s formation (TD) in the central Caroline Islands coincided with that Chuck over the central Philippine Islands. The binary pair remained within 1390km of each and appeared to undergo relative cyclonic rotation about a common

midpoint for three days. The characteristic changes of Ne are presented in panel 7 of Fig.1. The chain of typhoons in this region was formed until December.

In June and July the hurricanes of the Atlantic Ocean were not formed. The events of 1992 require further detailed consideration.

Ionosphere during the development of PAGE and OWEN super typhoons in the Asia-Pacific trough

Very strong ionosphere effects were observed during the amplification of up to 5 categories of interacting TC. The inclusion on November 21, 1990 of the Cosmos-1809 satellite equipment coincided with the beginning of the enhancement of the PAGE, OWEN and SINA TC. The "stopping" of the tropical storm Page (1990) (the trajectory in two days passed a loop with a width of ~ 2 degrees) caused an intensification of the tropical depression Owen and SINA. First warning due to improved upper- and lower-level organization increased deep convection, increasing wind speeds in the synoptic data. Tropical Storm Owen starting its explosive intensification phase.

In Fig.5 it is shown the change of Ne on November 21, observed at 10 consecutive revolutions at the LT = 19.5 sector. It is noted that the successive passage of the evening terminator through the TC caused Ne decreasing at 19817 -19819 revolutions. An additional narrow maximum of Ne over PAGE, OWEN and SINA unlike strong single TC [Belyaev G., 2015; Kostin, V.M., 2015; Isaev, N.V., 2010] was not observed. This indicates that above the interacting TC there is no formation of a vertical jet of neutral atoms above 200 km.

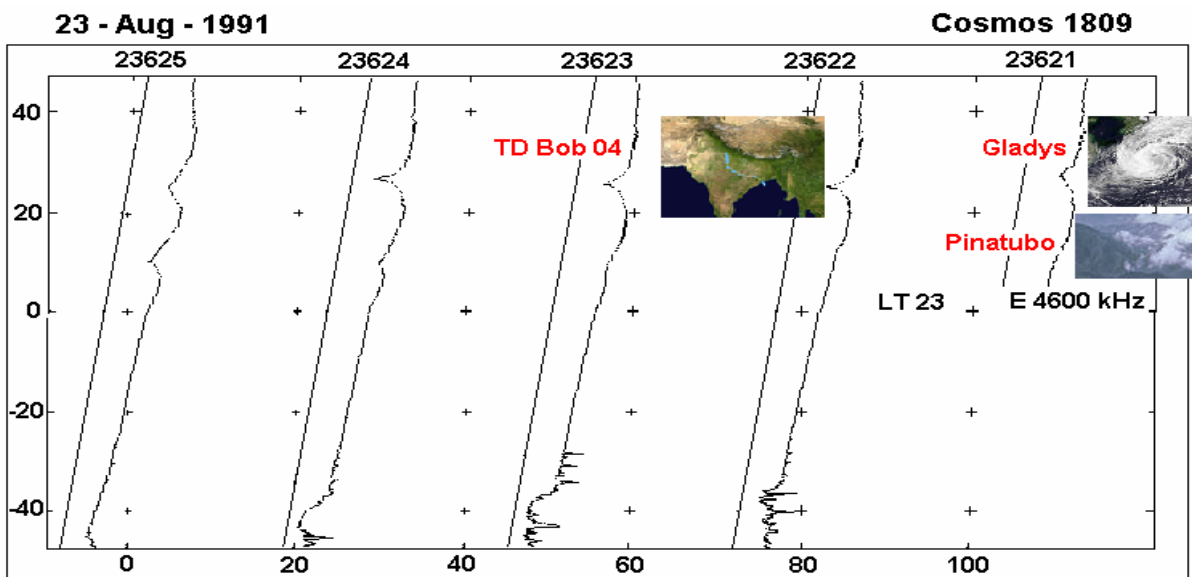


Fig.4. The intensity of the upper ionosphere plasma oscillations in the channel 4600 Hz (near the lower hybrid resonance) on revolutions west of the typhoon GLADYS and the volcano Pinatubo 2 weeks after the eruption of the Hudson volcano.

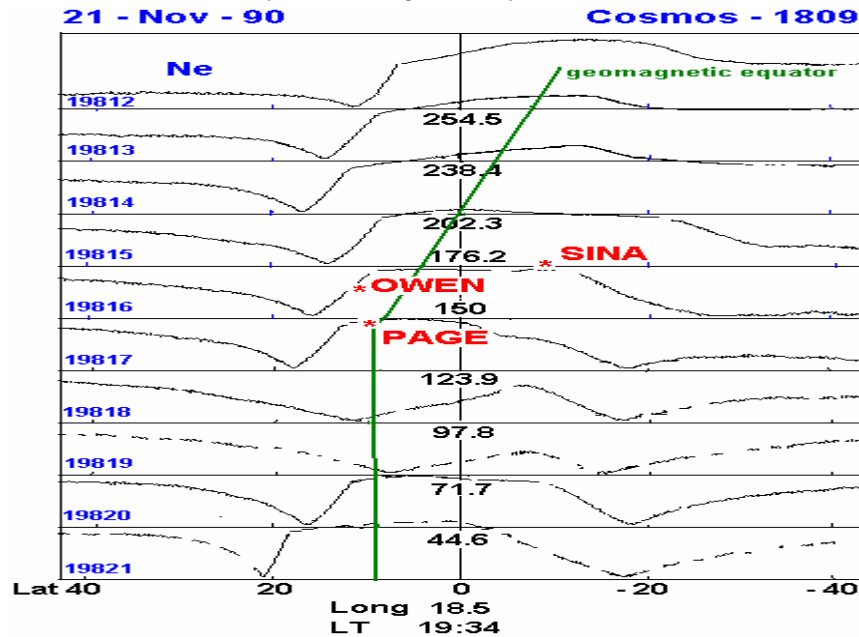


Fig.5. The Ne changing in the ionosphere evening sector on the day of PAGE, OWEN and SINA TC intensive interaction.

In the future, there was a synchronous development of the TC during the week to typhoons of the fifth category which was observed on 28 November. In the ionosphere evening sector, there was Ne decrease by three orders of magnitude on $L \sim 3$, and a wide maximum of the plasma pressure was formed along the geomagnetic equator. In the morning sector, the PIV transmission zones are identified according to the device for measuring ELF-VLF plasma oscillations. Relaxation of ionosphere disturbances was observed on December 3.

The interaction scheme for Page, Owen and Sina is presented in Fig.6. This Landsat7 image of clouds off the Chilean coast near the Juan Fernandez Islands shows a unique pattern called a von Karman vortex street. It is assumed that the same mechanism underlies the emergence of tropical disturbances (TD) Page, Owen and Sina. TD will be strengthened if the mechanism increasing the heat exchange ocean-atmosphere works. It is shown in Fig.6 that TS

Page with developed vertical movement above the tropopause is blown by a stratospheric wind which follows from the synoptic chart. In this case the Karman vortices must also be formed. When the vortices in the stratosphere coincide vertically with vortices in the troposphere, a redistribution of the vibrational energy of the wind takes place. The amplified infrasonic oscillations in the TD following the first TS, reach the ocean surface and enhance heat exchange. There is an intensification of TD. In this case the TD Owen was strengthened to a typhoon of category 5 first. Then there was TD Sina increase to fifth category TC. When they retired from the TS Page, it also increased to a typhoon of category 5. Thus the interacting TC differs from a single TC over which the vertical movement in the stratosphere is transformed into a flooded jet.

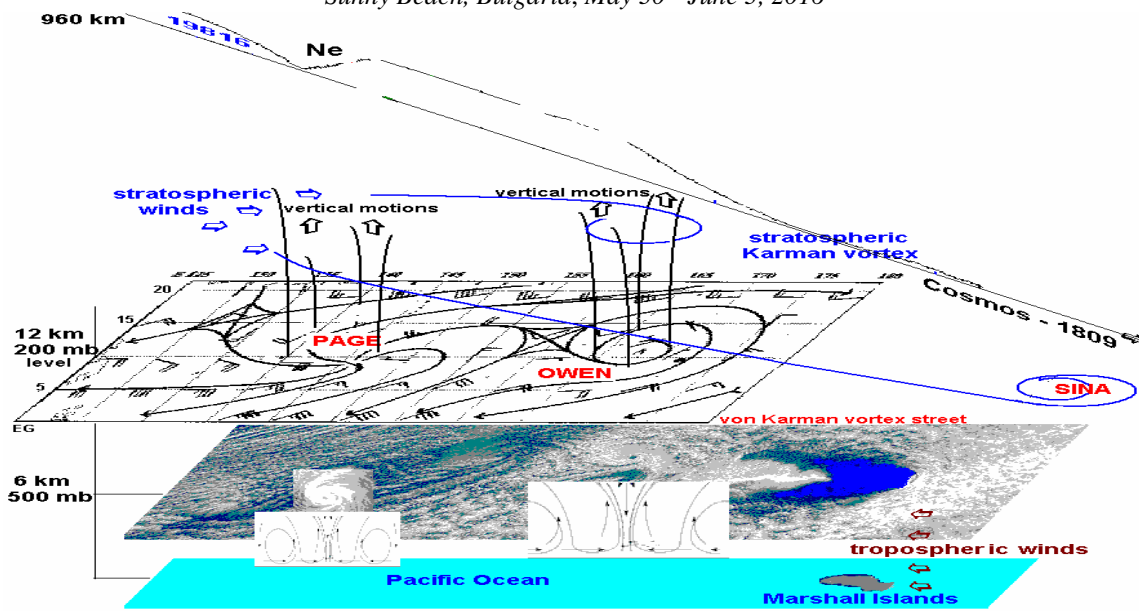


Fig.6. Scheme of TC PAGE, OWEN and SINA interaction.

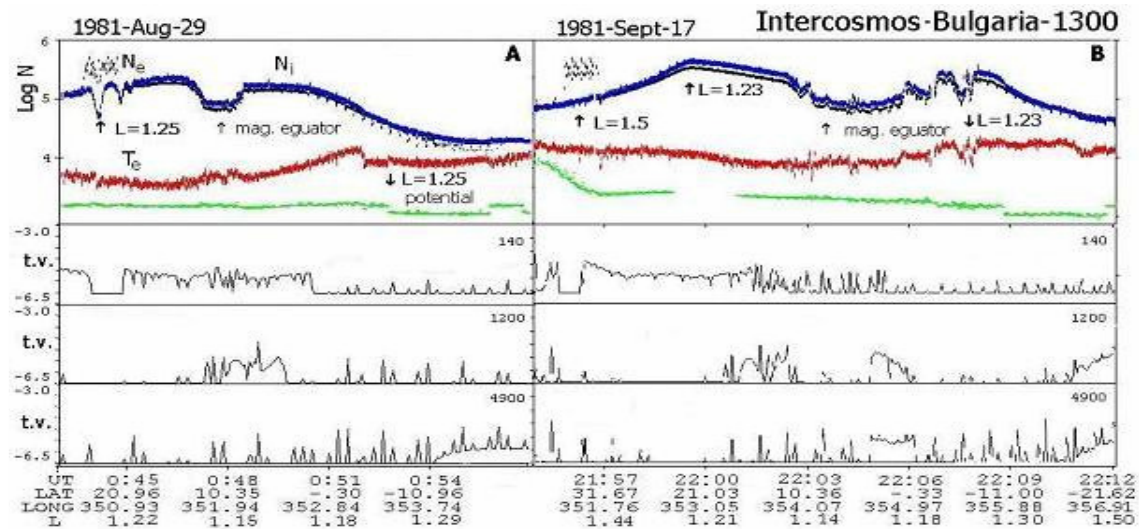


Fig.7. Upper ionosphere plasma parameters during the hurricane chain generation in the Atlantic Ocean (A) and in the period of its completion by the interaction of hurricanes HARVEY and IRENE.

Ionosphere during the development of a chain of hurricanes from African tropical waves according to the satellite IKB-1300 data

The study of the ionosphere features over the Brazilian anomaly was one of the first tasks of the IKB-1300 satellite. Most of the working inclusions occurred over the Atlantic Ocean. In the 1981 season, only in September there was a continuous sequence of hurricanes in the Atlantic Ocean [Lawrence, M.B., 1982]. Most hurricanes are formed from a tropical wave starting from the African continent.

It is shown in Fig.7A one of the precursors of the amplification of TD EMILY - a characteristic cavern in Ne which was previously shown by the authors in [Kostin, V.M., 2015]. If a second TC develops at a distance of ~ 20 degrees, the Ne structure and other plasma parameters of the upper ionosphere change. So the weakening of hurricane Harvey (1981) led to the intensification of hurricane Irene, with the center of the stratospheric anticyclone locating between them. A number of local depressions of Ne with scales along the trajectory of the satellite to several hundred kilometers were observed in the ionosphere.

Summary

1. Effects in the upper ionosphere during the interaction of two TC were observed at their mutual removal up to 2500 km.
2. There are noted: Wide areas of increased Ne above the zone of TC development and geomagnetic equator. The local zones of the increased level of electrical oscillations near the cyclotron frequencies of hydrogen and helium are attached to magnetic L-shells, based on the E-layer above the TC. There is also a sharp increase in the frequency of the lower hybrid oscillations and the output of intense oscillations from the registration band in the E4600 Hz channel.
3. Narrow vertical jet of neutral particles at an altitude of about 960 km (Cosmos-1809 orbit) does not separated above the interacting TC centres.
4. Interacting TC as well as single TC modifies the zones of influence on the ionosphere of the VLF transmitters which are at a distance of thousands of kilometers apart.

References

- Aburjania, G.D., Kharshiladze, O.A. and Chargazia, K.Z. Self-organization of IGW structure in an inhomogeneous ionosphere: 2. Nonlinear vortex structure // *Geomagn. Aeron.* V. 53. No. 6. P. 750. 2013.
- Belyaev G., Boychev B., Kostin V., Trushkina E., and Ovcharenko O. Modification of the ionosphere near the terminator due to the passage of a strong tropical cyclone through the large Island // *SunGeo.* V. 10. No.1. P. 31. 2015.
- Cheng, K., Huang, Y.N., and Chen, S.W. Ionospheric disturbances observed during the period of Mount Pinatubo Eruption in June 1991 // *J. Geophys. Res.* V. 97. P. 11695. 1992.
- Dong, K. and Neumann, C.J. On the relative motion of binary tropical cyclones // *Monthly Weather Review.* Vol. 111. P. 945. 1983.
- Isaev, N.V., Kostin, V.M., Belyaev, G.G., Ovcharenko, O.Ya. and Trushkina, E.P. Disturbances of the Topside Ionosphere Caused by Typhoons // *Geomagn. Aeron.* Vol. 50. No. 2. P. 243. 2010.
- Kostin, V.M., Belyaev, G.G., Boychev, B., Trushkina E.P. and Ovcharenko O.Ya. Ionospheric precursors of the intensification of isolated tropical cyclones to the IKB-1300 and Cosmos-1809 satellite data // *Geomagn. Aeron.* V. 55. No. 2. P. 246. 2015.
- Labytzke, K. Stratospheric temperature changes after the Pinatubo eruption // *J. Atm. Terr. Phys.* V. 56. No. 9. P. 1227. 1994.
- Lander, M.A. Evolution of the cloud pattern during the formation of tropical cyclone twins symmetrical with respect to the equator // *Monthly Weather Review.* Vol. 118. P. 1194. 1990.
- Lawrence, M.B. and Pelissier, J.M. Atlantic Hurricane Season of 1981 // *Monthly Weather Review.* Vol. 110. P. 852. 1982.
- Rudolph, D.K. and Guard. C.P. 1991 Annual Tropical Cyclone Report // Joint Typhoon Warning Center Guam.
- Sadler, J.C. Tropical Cyclone Initiation by the Upper-Tropospheric Trough // Naval Environmental Prediction Research facility Technical Paper. No. 2-76, 103 pp. 1979.

On-line catalogs of solar energetic protons at SRTI-BAS

R. Miteva and D. Danov

Space Research and Technology Institute, Bulgarian Academy of Sciences, Sofia, Bulgaria
E-mail: rmiteva@space.bas.bg

Abstract.

We outline the status of the on-line catalogs of solar energetic particles supported by the Space Climate group at the Space Research and Technology, Bulgarian Academy of Sciences (SRTI-BAS). In addition to the already compiled proton catalog from Wind/EPACT instrument, in the current report we present preliminary results on the high energy SOHO/ERNE proton enhancement identifications as well as comparative analysis with two other proton lists. The future plans for the on-line catalogs are briefly summarized.

Introduction

The importance of solar energetic particles (SEPs: electrons, protons and heavy ions from keV up to GeV energies) in space weather research, in addition to flares and coronal mass ejections (CMEs), has already been recognized [Schwenn 2006; Pulkkinen 2007]. The risk for SEP produced radiation doses outside the terrestrial magnetosphere is regarded as a severe problem to be solved in order to secure the safety of humans during future space travel flights (<https://oig.nasa.gov/audits/reports/FY16/IG-16-003.pdf>).

Mitigating the negative effects of space weather drivers is the reason for the observational and theoretical efforts spent in understanding them. The forecasting SEP and flare events is the subject of numerous recently completed and ongoing EU-projects. Many of the forecasting schemes rely on long series of events in order to test and train the forecasting methods (e.g. by machine-learning techniques). This is one of the possible applications for the comprehensive SEP event lists prepared from data provided by different space-borne instruments, in addition to academic-oriented research.

Due to various reasons (e.g., service interruption, event detection threshold, magnetic field line connection, etc.) a single spacecraft is unable to provide a complete list of all SEP events observable at Earth. In a recent study, Miteva *et al.* [2017b] summarized a number of probable instrumental, positional and selection effects that may influence the completeness of a SEP catalog. The different instruments provide observations in several energy channels, particle species, and locations (geostationary orbit, around L1, along the Earth orbit).

In the present report we summarize the current status of the SEP cataloguing performed at the Space Climate group in the Space Research and Technology, Bulgarian Academy of Sciences (SRTI-BAS). The preparation of several catalogs is in progress and using proton data from Wind/EPACT [von Roseninge *et al.* 1995] and SOHO/ERNE [Torsti *et al.* 1995] instruments is now confirmed. The first version of the proton catalog based on Wind/EPACT data was announced by [Miteva *et al.* 2016], where the main guidelines for the proton identification were presented, as well as the on-line platform of the catalog. This preliminary version of the Wind/EPACT proton event catalog was used in a study by [Miteva *et al.* 2017a] to explore the solar cycle trends. The finalized version of the proton catalog is now completed and used for comparative and statistical studies [Miteva *et al.* 2017b,c]. At present, we continue with the analysis of proton enhancements above ~20 MeV from the SOHO/ERNE instrument. All particle catalogs (with information on their proton event characteristics – time and peak intensity, overview plots and solar origin – flares and CMEs) will be stored at the dedicated web-site: <http://newserver.stil.bas.bg/SEPcatalog>.

Catalogs of Solar Energetic Particles

© SRTI-BAS 2017 Last modified 05/18/2017 17:17:48

[Wind/EPACT proton event catalog](#)

[SOHO/ERNE proton event catalog](#)

[Other particle catalogs](#)

Supported by
Space Climate Group
Space Research and Technology Institute
Bulgarian Academy of Sciences

Contact: R. Miteva
Web-support: D. Danov

Fig. 1 Overview of the main page of the dedicated website (status: May 2017) hosting the catalogs: <http://www.stil.bas.bg/SEPcatalog/> (<http://newserver.stil.bas.bg/SEPcatalog/>).

On-line catalogs

The dedicated web-site for the particle catalogs has been recently updated. The overall structure is enhanced to include two new sections designed for other SEP catalogs, as shown in Fig. 1.

a) Wind/EPACT proton event catalog

The Wind/EPACT proton event catalog lists the in situ proton enhancements in two energy channels, as ~25 and ~50 MeV. The on-line structure of the catalog has been described in an earlier contribution [Miteva *et al.* 2016] with event sample ranging from over 350 low energy protons to over 300 high energy protons. The first version of the proton catalog (1996÷2015) with the purpose to do a research study was used in Miteva *et al.* [2017a] for investigating the solar cycle trends of the energetic protons, using ~360 low energy and ~340 high energy protons. In a subsequent data analysis completed recently, the complex proton event profiles were re-examined and all conspicuous proton enhancements were identified as individual events. Thus the number of events in the final event list is increased. These modifications of the proton catalog were used in two follow-up studies covering the period 1996÷2016. The first study focuses only over solar cycle (SC) 23 [Miteva *et al.* 2017b] using 280 low and 262 high energy Wind/EPACT protons and presents a comparative analysis between several proton catalogs. The second study presents in a consistent way the Wind/EPACT proton event catalog [Miteva *et al.* 2017c] in the period 1996–2016, namely the event identification, comparison with other event lists as well as statistical analysis, based on the finalized event list of 429 low energy and 397 high energy protons. The full details can be found in the dedicated publications. The release of the catalog (open access) is scheduled before the end of 2017. Information on proton event identifications after 2016 is planned to be provided on yearly basis, namely early in the subsequent year, since the proton data is not delivered in real time.

SOHO/ERNE proton event catalog

© SRTI-BAS 2017 Last modified 05/19/2017 16:03:33

Solar cycle 23: 1996-2008

[Back to list of Catalogs](#)

Solar cycle 24: 2009-present

This catalog lists the proton enhancements from the **H**igh **E**nergy **D**etector (**HED**) aboard [SOHO/ERNE](#) instrument identified during solar cycle 23 (1996-2008) and the ongoing solar cycle 24 (since 2009). The catalog provides the following information: peak time (in UT) and peak intensity for the solar proton events in the different HED energy channels (in the range 17÷131 MeV). Further information is given as a comment.

Explanatory notes:

Peak time: identified at the maximum of the particle profile (local enhancements are not considered).
 J_p : peak proton intensity after subtraction of the pre-event level.

The reported here onset/peak times and J_p are based on non-smoothed data.

Abbreviations:

N/A: onset not found and/or it was fully masked by previous ongoing event
nd: next day
pd: previous day
p: peak is poorly defined
SXR: soft X-ray
u: uncertain

Contact: [R. Miteva](#)

Links: [Space Climate Group Homepage](#)
[Space Research and Technology Institute Homepage](#)

Fig. 2 Preliminary structure of the on-line version of the SOHO/ERNE proton event catalog.

b) SOHO/ERNE proton event catalog

The new upgrade of the on-line catalog includes analysis of proton enhancements from the SOHO/ERNE instrument (Fig. 2), accessed from the main web-page (Fig. 1).

We explore the proton data recorded by the SOHO/ERNE high energy detector (HED) above 17 MeV. A recent work by *Paassilta et al.* [2017] describes the instrument and presents a proton catalog over the energy range 55–80 MeV. We completed a preliminary analysis on the highest energy channel, 101–131 MeV (mean value of 116 MeV), using 5-min data smoothing and proton onset time determination when the proton flux reaches three standard deviations above a pre-event background level. The event number in the period 1996–2015 is 68 events. For illustrative purpose we present here the results as a comparison between the occurrences of protons at similar and higher energies. Namely, in Fig. 3 we present the scatter plots between the ~116 MeV SOHO/ERNE protons and protons detected by the GOES >100 MeV as reported by [*Papaioannou et al.* 2016], left plot, and SOHO/EPHIN >500 MeV as given by [*Kühl et al.* 2017], right plot. The \log_{10} – \log_{10} Pearson correlation coefficients and the bootstrapping uncertainty (based on 1000 calculations) are also given on each plot. A better correlation of 0.76 ± 0.06 is obtained for the SOHO/ERNE and GOES data despite the fact that the satellites are different and at different location. Lower correlation is obtained with the higher energy protons from SOHO/EPHIN is 0.56 ± 0.11 . For comparison, the calculated cross-correlation correlation between GOES and SOHO/EPHIN protons is very high, 0.92 ± 0.04 .

The analysis of the SOHO/ERNE proton events in the remaining eight high energy channels is in progress and all results will be reported in a dedicated publication. The new proton catalog will be finally released as on-line table (Fig. 2).

c) Other particle catalogs

Additional particle data (proton and/or electron) are under consideration. The finally selected data and the details on the particle enhancements will be given at the web-site.

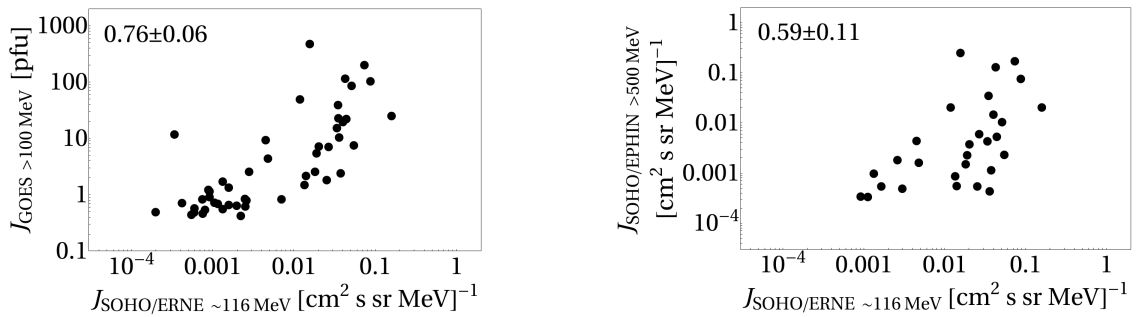


Fig. 3 Scatter plots between the peak proton intensity from SOHO/ERNE ~116 MeV with GOES >100 MeV (left) or with SOHO/EPHIN >500 MeV protons (right), respectively. The $\log_{10} \pm \log_{10}$ Pearson correlation coefficient and its uncertainty are given on each plot.

Conclusions

1. The proton catalog from Wind/EPACT instrument is now completed: proton onset and peak time, peak proton intensity, onset-to-peak proton fluence in the two available energy channels and the associated solar origin are identified. Overview plots are provided. The catalog release is scheduled following the publication of a dedicated paper.
2. The data analysis on the proton enhancements from SOHO/ERNE in nine energy channels (17–131 MeV) is in progress under the Bulgarian–Russian project for collaborative research: “On the origin of solar energetic particles: solar flares vs. coronal mass ejections”.

Acknowledgment

This study is partially supported by the National Science Fund of Bulgaria with Contract № ДНТС/Русия 01/6 (from 23 June 2017).

References

- Kühl, P., Dresing N., Heber B., Klassen A. (2017) Energetic particle events with protons above 500 MeV between 1995 and 2015 measured with SOHO/EPHIN, Sol. Phys, Vol. 292: 10, 13pp.
- Paassilta M., Raukunen O., Vainio R., Valtonen E., Papaioannou A., Siipola R., Riihonen E., Dierckxsens M., Crosby N., Malandraki O., Heber B., Klein K.-L., (2017), Catalogue of 55–80 MeV solar proton events extending through solar cycles 23 and 24, JSWSC, Vol. 7, A14, 19pp.
- Papaioannou, A.; Sandberg, I.; Anastasiadis, A.; Kouloumvakos, A.; Georgoulis, M. K.; Tziotziou, K.; Tsiropoula, G.; Jiggins, P.; Hilgers, A. (2016) Solar flares, coronal mass ejections and solar energetic particle event characteristics, JSWSC, Vol. 6, A42, 29 pp.
- Pulkkinen T. (2007) Space Weather: Terrestrial Perspective, Living Rev. Solar Phys., 4, (2007), 1, <http://www.livingreviews.org/lrsp-2007-1>
- Miteva R., Samwel S.W., Costa-Duarte M.V., Danov D. (2016) Proceeding of Eighth Workshop “Solar Influences on the Magnetosphere, Ionosphere and Atmosphere”, Sunny Beach, Bulgaria, 27–30, edited by K. Georgieva, B. Kirov and D. Danov. ISSN: 2367-7570
- Miteva R., Samwel S.W., Costa-Duarte M.V., Malandraki, O.M. (2017a) Solar cycle dependence of Wind/EPACT protons, solar flares and coronal mass ejections, Sun and Geosphere, Vol. 12, no. 1, 11–19
- Miteva R., Samwel S.W., Costa-Duarte M.V. (2017b) Solar energetic particle catalogs: Assumptions, uncertainties and validity of reports, JASTP, 9pp., in press
- Miteva R., Samwel S.W., Costa-Duarte M.V. (2017c) The Wind/EPACT proton event catalog (1996–2016), 42 pp., submitted.
- von Rosenvinge, T. T.; Barbier, L. M.; Karsch, J.; Liberman, R.; Madden, M. P.; Nolan, T.; Reames, D. V.; Ryan, L.; Singh, S.; Trexel, H.; Winkert, G.; Mason, G. M.; Hamilton, D. C.; Walpole, P. (1995) The Energetic Particles: Acceleration, Composition, and Transport (EPACT) investigation on the WIND spacecraft, Space Sci. Rev., Vol. 71, no. 1-4, pp. 155-206
- Schwenn, R. (2006) Space Weather: The Solar Perspective, Living Rev. Solar Phys., 3, (2006), 2, <http://www.livingreviews.org/lrsp-2006-2>
- Torsti, J.; Valtonen, E.; Lumme, M.; Peltonen, P.; Eronen, T.; Louhola, M.; Riihonen, E.; Schultz, G.; Teittinen, M.; Ahola, K.; Holmlund, C.; Kelhä, V.; Leppälä, K.; Ruuska, P.; Strömmer, E. (1995) Energetic Particle Experiment ERNE, Sol. Phys., Vol. 162, no. 1-2, pp. 505-531

A Look on the Solar Diameter Data Analysis over the Centuries.

J.P. Rozelot¹, A.G. Kosovichev², A. Kilcik³

¹ Université de la Côte d’Azur, Grasse, France

² New Jersey Institute of Technology, USA

³ Akdeniz University, Antalya, Turkey

E-mail: jp.rozelot@orange.fr

Abstract.

The measurement of the Sun’s diameter has been first tackled by the Greek astronomers from a geometric point of view. Their estimation of $\approx 1800''$, although incorrect, was not truly called into question for several centuries. The first pioneer works for measuring the Sun’s diameter with an astrometric precision were made around the year 1660 by Gabriel Mouton, then by Picard and La Hire. A canonical value of the solar radius of $959''.63$ was adopted by Auwers in 1891. In spite of considerable efforts during the second half of the XXth century, involving dedicated space instruments, no consensus was reached on this issue. However, with the advent of high sensitivity instruments on board satellites, such as the Michelson Doppler Imager (MDI) on Solar and Heliospheric Observatory (SoHO) and the Helioseismic and Magnetic Imager (HMI) aboard NASA’s Solar Dynamics Observatory (SDO), it was possible to extract with an unprecedented accuracy the surface gravity oscillation f modes, over nearly two solar cycles, from 1996 to 2017. Their analysis in the range of angular degree $\ell = 140 \div 300$ shows that the so-called “seismic radius” exhibits a temporal variability in anti-phase with the solar activity; This new look on such modern measurements of the Sun’s global changes from 1996 to 2017 gives a new way for peering into the solar interior.

Introduction.

The first determinations of the diameter of the Sun have been made by the Greek astronomers through brilliant geometric procedures. Aristarchus of Samos (circa 310-230 BC), was able to set up the solar diameter D_{\odot} as the 720th part of the zodiacal circle, or 1800 seconds of arc ($''$) (i.e. $360^{\circ}/720$). A few years later, Archimedes (circa 287-212 BC) wrote in the *Sand-reckoner* that the apparent diameter of the Sun appeared to lie between the 164th and the 200th part of the right angle, and so, the solar diameter D_{\odot} could be estimated between $1620''$ and $1976''$ (or $27^{\circ}00''$ and $32^{\circ}56''$ [Lejeune, 1947; Shapiro, 1975]. Their results, albeit somewhat erroneous, were not truly called into question during several centuries. The first pioneer works for measuring the Sun’s diameter were made around the year 1660 by Gabriel Mouton, immediately followed by Jean-Félix Picard and Philippe de La Hire. But, in spite of considerable efforts since the 17th century, which can be considered as the turning point of the astrometric estimate of the solar diameter, and the development of new instrumentation and techniques, both on the ground and in space, the scientific community is still working on an accepted worldwide definition and value of the solar diameter. Yet, a critical analysis of the measurements and errors deduced from observations of the Venus transits in 1874 and 1882, and through a network of heliometers which were observing the Sun during the years 1873-1886 in Germany at Breslau, Gotha-Strassburg, Göttingen, Berlin and Hamburg [Auwers, 1891] concluded that the diameter of the Sun could be set up at $(1919.26 \pm 0.10)''$. Combined with the Astronomical Unit value commonly used at that time, i.e. $149\,597\,900\,000$ m, it turns out that the solar diameter was $R_{\odot} = 695\,996.9$ km. This $959''.63$ value for the solar radius was referenced as a canonical one up to 2015. In 2002, the General Assembly of the International Astronomical Union in Pekin (CN) reconsidered the value of the Astronomical Unit (AU), which was adopted as $149\,597\,870\,700$ m, and consequently the solar radius became $695\,996.7$ km, which is not significantly different. As a matter of historical curiosity, the Allen Astrophysical quantities, in the 1955 edition gives

$R_{\square} = (6.960 \pm 0.001) \times 10^{10}$ cm, the limb shape is circular to precision $\pm 0''.01$, and the semi-diameter plus “irradiation” = $961''.2$ (for observing the limb). The same Allen Astrophysical quantities, in the third edition (1973) states $R_{\square} = 6.9599(7) \times 10^{10}$ cm, still gives the semi diameter plus “irradiation”, and substitutes the circular shape by oblateness with the equator-pole semi-difference = $0''.05$. Lastly, the Allen Astrophysical quantities published in 2010 gives $R_{\square} = (6.95508 \pm 0.00026) \times 10^{10}$ cm, the oblateness of $0''.0086$, and the “irradiation” correction disappears. This R_{\square} estimate was based on the determination made by [Brown and Christensen-Dalsgaard, 1998] who combined photoelectric measurements with models of the solar limb-darkening function. They further found that the annual averages of the radius are identical within the measurement error of ± 0.037 Mm.

However, in 2015 the International Astronomical Union General Assembly in Honolulu (USA) recommended that the solar radius R_{\square} must be set at $6.957 \cdot 10^8$ m. As the AU was already determined, it turns out now that the angle subtended by the solar radius at the center of the Earth is $959''.22$ and cannot be changed for the time being. This account for a difference of $0''.41$ or 297 km in comparison with the Auwers value.

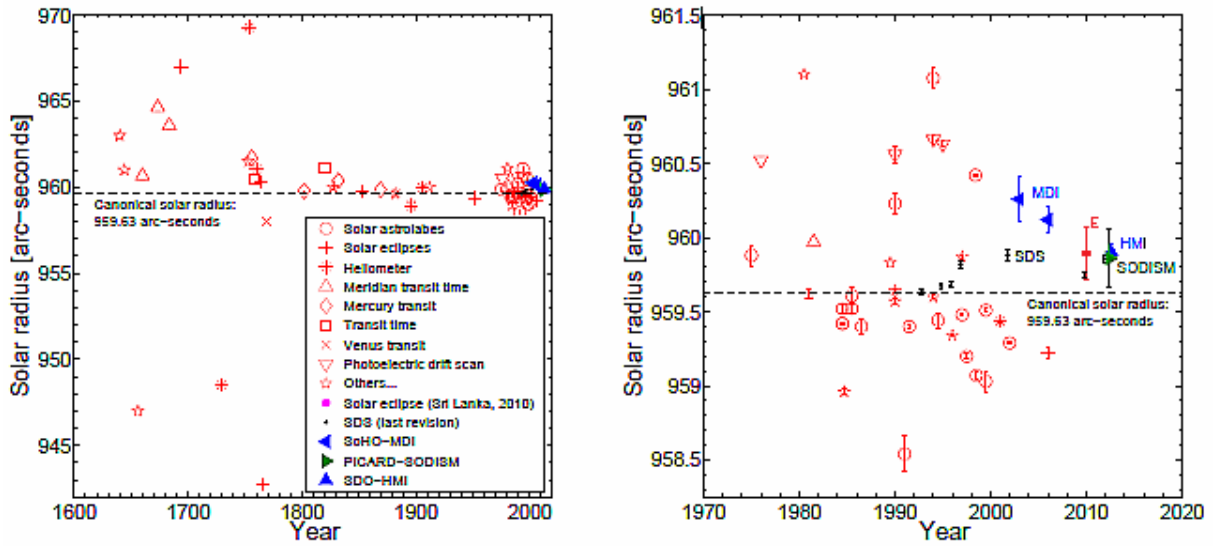


Figure 1. (Left) Solar radius measurements (red symbols) made since the seventeenth century according to the survey of historical measurements made by [Rozelot and Damiani, 2012]. Blue symbols: space measurements. The mean value of all these measurements is about the canonical value of $959''.63$. (Right). Focus on the solar radius measurements made since 1970. Symbol E shows the solar eclipse determination in Sri Lanka (ground measurement) by [Adassuriya et al., 2011], i.e. $(959.89 \pm 0.18)''$. Black circles: SDS balloon flight measurements [Sofia et al. 2013]. Blue symbols: space measurements from SoHO-MDI and SDO-HMI satellites. Green symbol: PICARD-SODISM measurement obtained during the transit of Venus (outside the atmosphere); according to [Meftah et al., 2014].

Figure 1 shows in the left panel the solar radius measurements made since the seventeenth century according to the survey of historical measurements compiled by [Rozelot and Damiani, 2012]. Space measurements made by the Michelson Doppler Imager (MDI) on Solar and Heliospheric Observatory (SoHO) [Scherrer et al., 1995], the Helioseismic and Magnetic Imager (HMI) aboard NASA's Solar Dynamics Observatory (SDO) [Scherrer et al., 2012], and the SODISM aboard CNES PICARD [Meftah et al., 2014], satellites have been added (in blue). The mean value of all these measurements is close to the canonical value of $959''.63$. The right panel shows the solar radius measurements made since 1970 and leads to the same conclusion. Note that data can be found in [Wittmann, 1977], from 1836 to 1975, or [Djafer et al., 2008, Table 1] or [Kuhn et al., 2004]; the survey can be completed by the data listed in [Rozelot et al., 2016]. Figure 1 exhibits a great dispersion, spanning several tenths of

arc-second, meaning that even with gradually increasing accuracy, by different means or techniques, including space measurements, the results obtained so far do not allow to determine without ambiguity an estimation in absolute value of the solar diameter, as well as its variation or its constancy as a function of solar activity.

Determination of the solar diameter through eclipses has been done also since long ago as they present some decisive advantages, the main one being due to the occultation that takes place in space, and so is free from atmospheric effects [Lamy *et al.*, 2015]. The first possibility to determine the solar radius was made on the basis of the annular eclipse observed by Clavius in 1567. This eclipse with the standard solar radius should have been total, while the solar photosphere exceeded the lunar limb to show the observed ring. Under this exceptional circumstance, the diameter of the Sun was exactly the diameter of the Moon [Stephenson *et al.*, 1997], and thus can be computed. A survey of solar radius measurements made during eclipses has been made in ([Damiani *et al.*, 2012], Fig. 2.) and can be complemented with the work of [Lamy *et al.*, 2015] who found a mean radius of (959.99 ± 0.06) ” or $(696\,258 \pm 44)$ km during the eclipses of 2010, 2012, 2013, and 2015.

Helioseismology can provide an interesting alternative. With accurate measurement of f-mode frequencies by the GONG (Global Oscillations Network Group) [Harvey *et al.*, 1996] and by the SoHO/MDI [Scherrer *et al.*, 1992] and SDO/HMI space instrument [Scherrer *et al.*, 2012], it has been shown that global helioseismology provides important information about the physics of localized structures beneath the surface of the Sun, and it has been suggested also to use the f modes to estimate the solar radius, which is thus called the “seismic radius”. The procedure has been described by [Schou *et al.* 1997] and explained in details in [Dziembowski *et al.*, 2001] and in [Di Mauro, 2003]. Results lead to a seismic radius less than the photospheric one, reduced by approximately 300 km, and it is this value which was adopted by the IAU GA in Honolulu (USA) in 2015, as seen above.

This discrepancy was solved by [Habereitter *et al.*, 2008] from radiative transfer calculations with the help of a code named COSI (a combination of a model atmosphere code in spherical symmetry and the spectrum synthesis program SYNSPEC, adapted to the solar atmosphere). The authors determined a distance of 0.333 ± 0.008 Mm between the height where $\tau_{5000} = 1$ at disk center and the position of the 500 nm inflection point of the intensity profile at the limb. This correction may explain the differences between the f-mode frequencies derived from model calculations and observations.

If there is no consensus today, this could be due to several reasons: (i) there is no unique method of estimation of the Sun’s radius, as just said above (some observers define the radius as the distance to the point of inflexion in the limb profile, whilst the theoretical solar models assume the solar surface to be located at a point where the optical depth is of order unity), (ii) instrumental effects (point-spread function, spatial resolution, optical distortion, temperature variations) not properly taken into account, (iii) atmospheric turbulence on the observed Sun’s full disk pictures or on the Sun’s limb, which are not corrected, (iv) different instruments observing at different phases of the Solar Cycle and, (v) observations not made at the same wavelengths. As regards to this last issue, certain instruments observed in the continuum at different wavelengths, while others observed in the center of a Fraunhofer line, as was done for example at the Mount Wilson observatory (USA). In addition, there are instruments that used a narrow band pass, such as MDI on board SoHO (0.0094 nm) and Mount Wilson (0.014 nm), whereas others used a wide spectral domain on the order of hundreds of nanometers, as it was done by the CCD astrolabes.

How large are the temporal variations of the solar diameter?

The temporal dependence of the solar diameter is a long standing question. The turning point was made in 1874 when it was argued that the changes were proportional to the inverse

of the solar activity (the so-called Secchi-Rosa [1874] law). Observational determinations lead up to now to conflicted results.

On **mid-term variations**, i.e. along two or three solar cycles, at least four groups of observers have claimed that the solar radius varies in phase with surface activity, seven groups of observers have reported radius changes in antiphase with surface activity, while four groups of observers have reported no significant change at all [Stothers, 2006, and references herein]. From space [Kuhn *et al.*, 2004] have reported that during Solar Cycle 23, between the solar minimum and solar maximum, the radius of the Sun did not change by more than ± 7 mas (14 mas peak to peak, i.e. ≈ 10 km).

On **long term variations** (secular trends) [Eddy, 1978], analyzing daily meridian transit timings of the Sun made at the Royal Greenwich Observatory (UK) evidenced a secular decrease of the solar diameter of about 2.25 arcsec/century. A few years later, an analysis of observations of 23 transits of Mercury in front of the Sun between 1736 and 1973 by [Shapiro, 1980] have shown no indication of any significant change in the diameter of the Sun yielding a decrease of the angular diameter, as viewed from the Earth, of under 0.3 arc second per century, incompatible with the value obtained by Eddy. [Gilliland, 1981] analyzing five different data sets, concluded that a secular decrease of $\approx 0''.1$ per century over the last 265 years is likely. Other works from [Wittmann, 1980, Stephenson *et al.*, 1997, Parkinson, 1988], and [Toulmonde, 1997] did not support the assumption of a secular decrease. [Vaquero *et al.*, 2015] reported that the solar semi-diameter observed at the Cadiz (SP) Naval observatory from 1773 to 2006, do not present any significant trend in the past 250 years, or if any should be inside the $1''.77$ measurements uncertainty. An analysis of the Kodaikanal (IN) daily digitized white light solar pictures, from 1923 to 2011, shows an apparent decrease of the solar radius of less than 5.8 mas per year [Hiremath *et al.*, 2017].

On **theoretical grounds**, [Callebaut *et al.*, 2002] were certainly the first to point out that changes in solar gravitational energy, in the solar upper layers, necessarily involve variations in the size of the envelope. The mechanism is simple. Bearing in mind the definition of the energy $E_g = -\int (Gm/r) dm$, (where r is the radial coordinate and G the gravitation constant) and assuming hydrostatic equilibrium, a thin shell of radius dr containing a mass dm in equilibrium under gravitational and pressure gradient forces will be expanded or contracted if any perturbation of these forces occurs. In [Fazel *et al.*, 2008], the authors improved the method and show that any variations of the size of the solar envelope must be within a few km of amplitude over a Solar Cycle, a value in perfect agreement with those deduced from inversion of the f-modes in helioseismology.

The study **of the solar oscillation f modes** provided by the two space missions SoHO (Solar and Heliospheric Observatory) and SDO [Solar Dynamics Observatory] from 1996 to 2017 has been made by [Kosovichev and Rozelot, 2017] in the scope to analyze the coefficients of rotational frequency splitting -that measure the latitudinal differential rotation-, together with the asphericity coefficients -that gives the profile of the limb shape over the heliographic latitudes- [Reiter *et al.*, 2015]. As above mentioned, the f mode frequencies permit also to extract the seismic radius and its variations with the solar cycle. The analysis is focused on the low-frequency medium-degree f-modes observed in the range of $\nu = 140-300$, where the kinetic energy is concentrated within a layer of approximately 15 Mm deep. The properties of these modes are affected by the surface magnetism and temperature/sound-speed changes, but also reflect large-scale variations in the near-surface shear layer [NSSL]. This layer (called ‘leptocline’ [Godier and Rozelot, 2001]) presumably plays an important role in the solar dynamo [Pipin and Kosovichev, 2011].

The f-mode frequency variations, $\langle \Delta\nu/\nu \rangle$, averaged for the whole common subset of modes in the whole observed angular degree range, $\nu = 137-299$ have been calculated for 72-day periods. The quantity $-2/3 \langle \Delta\nu/\nu \rangle$ representing a proxy of the relative seismic radius

variations, $\langle \Delta R_{\text{seis}}/R_{\text{seis}} \rangle$ is displayed in Figure 2a. It exhibits a modulation with amplitude of about 2.3×10^{-5} in Solar Cycle 23 and about 1.2×10^{-5} in Cycle 24. It is clear that the seismic solar radius varies in phase opposition with the solar cycle (Figure 2b) with a very small time lag which has been found at (0.044 ± 0.019) yr (correlation coefficient 0.94). When the averaging includes the f-modes of $\nu = 140\text{-}200$, the seismic radius modulations are as twice as small, but the phase relation remains. As earlier pointed out by Lefebvre and Kosovichev [2005] and Lefebvre et al. [2007], the seismic radius variations are not constant and non-homologous in this subsurface layer: their examination requires a careful helioseismic inversion procedure, and will give us a real insight into changes of the solar stratification.

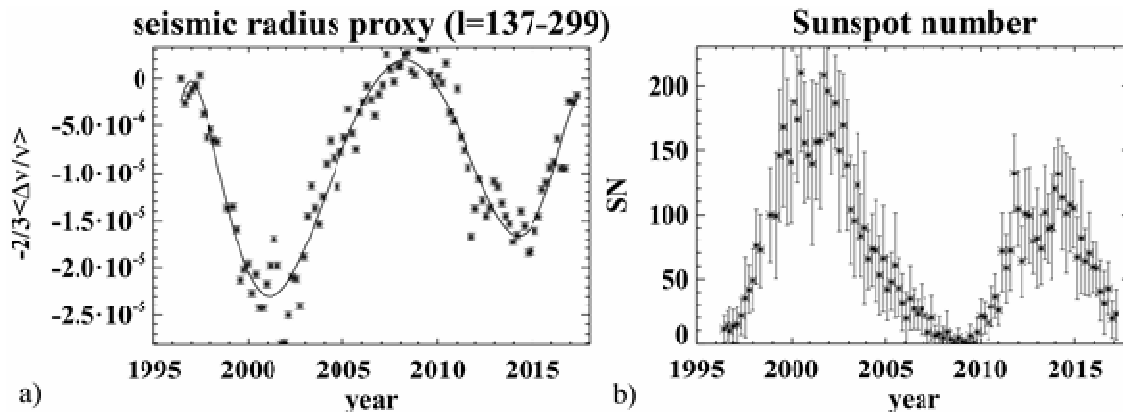


Figure 2. a) Variation of the seismic radius proxy, $\langle \Delta R_{\text{seis}}/R_{\text{seis}} \rangle = -2/3 \langle \Delta v/v \rangle$ relative to the first measurement in 1996, as deduced from the analysis of the f mode frequencies extracted from the MDI and HMI data from 1996 to 2017. The solid curve shows a polynomial fit. b) The sunspot number, SN, averaged for the 72-day periods corresponding to the intervals of the helioseismic analysis. (After [Kosovichev and Rozelot, 2017]).

Conclusion.

Due to the progress achieved these last years in high angular resolution and in the precise determination of ephemerides, it would be believed that the size of the Sun (and its deviation from a perfect sphere) could be known at a very high precision, or, at least, as well known as stellar radii obtained nowadays by interferometry. In spite of sophisticated techniques, the direct measure of the size of the Sun and its possible temporal variations, both on short term and secular variations remain vitiated by significant errors of measurements, both at the ground level (mainly due to atmospheric turbulence) and in space (limb shape displacement). A statistical analysis allows in principle to differentiate between different scenarios, but such a study has not been achieved so far in the absence of relevant data over a sufficient time span.

Helioseismology data obtained for nearly two solar cycles of observations from space provide a powerful tool for determining the variability of the seismic solar radius. The results show that the solar subsurface layer is shrinking or expanding not at the same level during the successive solar cycles. This may help to peer inside the solar interior and permit to investigate other important properties of the subsurface dynamics of the Sun, which previously were not accessible. However, the helioseismology data on their own do not provide variations of the photospheric radius. Further understanding of the solar radius variations will require detailed theoretical modeling of the structure and dynamics of the leptocline.

Acknowledgment.

The authors thank Katya Georgieva for her kind invitation to the Sunny Beach Summer School in Bulgaria. One of us (JPR) thanks also the International Space Science Institute (ISSI) in Bern (CH) where he is repeatedly invited as a visitor scientist.

References.

- Adassuriya, J., Gunasekera, S., and Samarasinha, N., Determination of the Solar Radius based on the Annular Solar Eclipse of 15 January 2010, *Sun and Geosphere* 6, 17–22 (Nov. 2011).
- Auwers, A., “Der Sonnendurchmesser und der Venusdurchmesser nach den Beobachtungen an den Heliometern der deutschen Venus-Expeditionen”, *Astronomische Nachrichten*, 128, Issue 20, 361 (1891).
- Brown, T. M., and Christensen-Dalsgaard, J., Accurate Determination of the Solar Photospheric Radius, *Astrophysical Journal*. 500, L195-L198 (1998).
- Callebaut D.K., Makarov, V. I., Tlatov, A. G., Gravitational energy, solar radius and solar cycle, In Proceedings of the Second Solar Cycle and Space Weather Euroconference, 24-29 September 2001, Vico Equense, Italy. H. Sawaya-Lacoste ed., ESA SP-477, Noordwijk, ISBN 92-9092-749-6, 209-212 (2002).
- Di Mauro, M.P., Helioseismology: A Fantastic Tool to Probe the Interior of the Sun, In “The Sun's Surface and Subsurface: Investigating Shape”, *Lecture Notes in Physics*, J.-P. Rozelot (ed.), Springer, Vol. 599, 31-67 (2003).
- Djafer, D., Thuillier, G., Sofia, S.A, Comparison among Solar Diameter Measurements Carried Out from the Ground and outside Earth's Atmosphere, *Astrophysical Journal*, 676, Issue 1, 651-657 (2008).
- Dziembowski, W.A., Goode, P.R., Schou, Does the Sun Shrink with Increasing Magnetic Activity? *Astrophysical Journal*, 553, Issue 2, 897-904 (2001).
- Fazel, Z., Rozelot, J. P., Pireaux, S., Lefebvre, S., Ajabshirizadeh, A., Gravitational energy and luminosity variations, *New Astronomy* 13, 65–72 (2008).
- Gilliland, R.L., Solar radius variations over the past 265 years, *Astrophysical Journal*, 248, Sept. 15, 1144-1155 (1981).
- Godier, S., Rozelot, J.P., A new outlook on the ‘Differential Theory’ of the solar Quadrupole Moment and Oblateness, *Solar Physics*, 199, 217-229 (2001).
- Haberreiter, M., Schmutz, W., Kosovichev, A. G., Solving the Discrepancy between the Seismic and Photospheric Solar Radius, *Astrophysical Journal Letters*, 675, Issue 1, L53 (2008).
- Harvey, J. W., Hill, F., Hubbard, R. P. et al., The Global Oscillation Network Group (GONG) Project, *Science*, 272, Issue 5266, 1284-1286 (1996).
- Hiremath, K.M., Rozelot, J.P., Gramapurohit, D., Gurumath S.R., Ramasubramanian, V., Nearly century scale variation of the Sun’s radius, *Astrophysics Journal*, to be published (2017).
- Kosovichev, A.K., Rozelot, J.P., Solar Cycle Variations of Rotation and Asphericity in the Near-Surface Shear Layer, *Journal of Atmospheric and Terrestrial Physics*, to be published (2017).
- Kuhn, J.R., Bush, R.I., Emilio, M., Scherrer, P., On the Constancy of the Solar Diameter, *Astrophysical Journal*, 613, Issue 2, 1241-1252 (2004).
- Lamy, P., Prado, J.Y., Floyd, O., Rocher, P., Faury, G., Koutchmy, S., A Novel Technique for Measuring the Solar Radius from Eclipse Light Curves - Results for 2010, 2012, 2013, and 2015, *Solar Physics*, 290, 2617-2648 (2015).
- Lefebvre, S., Kosovichev, A.K., Changes in the Subsurface Stratification of the Sun with the 11-Year Activity Cycle, *Astrophysical Journal*, 633, L149–L152 (2005).
- Lefebvre, S., Kosovichev, A.K., Rozelot, J.P., Helioseismic Test of Nonhomologous Solar Radius Changes with the 11 Year Activity Cycle, *Astrophysical Journal*, 658, L135-L138 (2007).
- Lejeune, A., La dioptre d’Archimède, *Annales Société Scientifique de Bruxelles, Série 1, Vol. LXI, 27, 27-47* (1947).
- Meftah, M., Irbah, A., Hauchecorne, A., Solar astrophysical fundamental parameters, *Proceedings of the SPIE, Volume 9143, id. 91431R 10 pp.* (2014).
- Pipin, V.V., Kosovichev, A.K., *Astrophysical Journal*, 738, 104, 8 pp. (2011).
- Reiter, J., Rhodes Jr. J., Kosovichev, A.G., Schou, J., Scherrer, P.H., Larson, T.P., A method for the estimation of p-mode parameters from averaged solar oscillation power spectra, *Astrophysical Journal*, 803, 42pp (2015).
- Rozelot, J. P. and Damiani, C., Rights and wrongs of the temporal solar radius variability, *European Physical Journal H* 37, 709–743 (2012).
- Rozelot, J.P., Kosovichev, A.G., Kilcik, A., A brief history of the solar diameter measurements: a critical quality assessment of the existing data, *arXiv:1609.02710* (2016).
- Shapiro, A.E., Archimedes’s measurement of the Sun’s apparent diameter *Journal of Historical Astronomy* 75-80 (1975).
- Scherrer, P. H., Schou, J., Bush, R. I., Kosovichev, A. G. et al., The Helioseismic and Magnetic Imager (HMI) Investigation for the Solar Dynamics Observatory (SDO), *Solar Physics*, 275, 207–227 (2012).
- Scherrer, P.H., Bogart, R. S., Bush, R. I., Hoeksema, J. T., Kosovichev, A. G., Schou, J. et al., The Solar Oscillations Investigation - Michelson Doppler Imager, *Solar Physics*, 162, 129-188 (1995).
- Schou, J., Kosovichev, A.G., Goode, P.R., Dziembowski, W.A, Determination of the Sun's Seismic Radius from the SOHO Michelson Doppler Imager, *Astrophysical Journal Letters*, 489, L197 (1997).

Proceedings of
Ninth Workshop “Solar Influences on the Magnetosphere, Ionosphere and Atmosphere”
Sunny Beach, Bulgaria, May 30 - June 3, 2016

- Secchi, A., Rosa, P., Observations des diamètres solaires, Comptes Rendus Acad. Sc. Vol. LXXIII and LXXIV, (1874).
- Stephenson, F.R., Jones, J.E., Morrison, L.V., The solar eclipse observed by Clavius in A.D. 1567, *Astron. Astrophys.* 322, 347–351 (1997).
- Stothers, R.B., A virial theorem investigation of magnetic variations in the Sun, *Astrophysical Journal*, 653, L73–L75, (2006).
- Toulmonde, M., The diameter of the Sun over the past three centuries, *Astronomy and Astrophysics*, 325, 1174–1178 (1997).
- Vaquero, J. M., Gallego, M. C., Ruiz-Lorenzo, J. J., López-Moratalla, T., et al., Monitoring the Solar Radius from the Royal Observatory of the Spanish Navy since 1773, *Solar Physics*, 291, 1599-1612 (2015).
- Wittmann, A., The diameter of the Sun, *Astronomy and Astrophysics*, 61, no. 2, 225-227 (1977).
- Wittmann, A., Tobias Mayer's observations of the sun - Evidence against a secular decrease of the solar diameter, *Solar Physics*, 66, 223-231 (1980).

Unified model of the AGN

Kr.D.Yankova

Space Research and Technology Institute – Bulgarian Academy of Sciences

E-mail: f7@space.bas.bg

Abstract.

In this paper will considering the appropriate model for a unified description of active and sleeper cores and micro-quasars for completeness. To this aim will investigate the expansion of advective hypothesis in GR. Will analyzed the behavior on the emerging connections on the disk to the other components of quasars. We discuss development of the advective mechanism outside the disk.

1. Introduction

At low (planetary atmospheres or rings) and high (ADAF) rapidly changing temperatures, advection occurs in incomplete regimes, as the individual uncoordinated variation of one or another component of the velocity. As a consequence deforms the geometry of the middle flux of the disc. Various authors have described this cases the sub-and super-Eddington flows. Models suggest a flow deformation, such as: rotation of the velocity vector for radial advection, see, Beloborodov (1998), Bisnovaty-Kogan (1998, 1999) Bisnovaty-Kogan& Lovelace (2002), Chen et al. (1997), Narayan et al. (1997), Narayan & Yi (1995); or orbital advection for low- magnetic discs, where orbital speed vector is added to the Keplerian velocity see Fabian et al. (2012). At these types of advection action of $\partial v_i / \partial t$ - component is ignored.

At smoothly reaching to ultra-high temperatures, however, as shown in (Yankova (2013), Yankova, 2015), there are no conditions for the deformation of flow. Advection unfolds gradually its full capacity as a mechanism and establishes in mode of self-induction at virial temperatures.

2. Mechanism and self-induction

We constructed geometrically thin, optically thick, one-temperature Keplerian disc in a normal magnetic field, around a black hole.

Model is based on the fundamental equations of the magneto-hydrodynamics of fluids: the continuity equation (Eq. 1.1), equation of motion (Eq. 1.2), equation of the magnetic induction (Eq. 1.3), equation of heat balance (Eq. 1.4) and equation of state (1.5).

$$\frac{\partial \rho}{\partial t} + \nabla \cdot (\rho v) = 0 \quad \nabla \cdot v = 0 \quad \nabla \cdot B = 0 \quad (1.1)$$

$$\frac{\partial v}{\partial t} + v \cdot \nabla v = -\frac{1}{\rho} \nabla p - \nabla \Phi + \left(\frac{B}{4\pi\rho} \cdot \nabla \right) B + \vartheta \nabla^2 v \quad (1.2)$$

$$\frac{\partial B}{\partial t} = \nabla \times (v \times B) + \eta \nabla^2 B \quad \eta = \frac{c^2}{4\pi\sigma} \quad (1.3)$$

$$\rho T \frac{\partial S}{\partial t} - \frac{\dot{M}}{2\pi r} T \frac{\partial S}{\partial r} = Q^+ - Q^- + Q_{mag} \quad (1.4)$$

$$p = p_r + p_g + p_m \quad (1.5)$$

Here $v = (v_r, r\Omega, v_z)$ is velocity of flux; ρ - mass density; $B = (B_r, B_\phi, B_z)$ - magnetic field; p - pressure; $\Phi = -\frac{GM}{r-r_g}$ - pseudo-Newtonian gravitational potential; r_g – Schwarzschild radius

of the central object; ϑ - kinematical viscosity; η - magnetic viscosity; σ - magnetic turbulent conductivity; T - temperature; S - entropy; \dot{M} - accretion rate; Q_{adv} - advective term; Q^+ - viscosity dissipation; Q_{mag} - magnetic dissipation; Q^- - radiative cooling; p_r – radiative pressure; p_g – gas pressure; p_m – magnetic pressure.

In our research, in contrast to the other models, we provide the advection in the form of the complete advective term (1.6), which is naturally produced in the equations describing the flow dynamics:

$$\frac{\partial(\rho v_i)}{\partial t} + \frac{\partial}{\partial x_j} (\rho v_i v_j) = \rho \left(\frac{\partial v_i}{\partial t} + v_j \frac{\partial v_i}{\partial x_j} \right) = \rho \frac{Dv_i}{Dt} \quad (1.6)$$

In the presented new interpretation of physics at the left side of the equation for the motion: full complete advective term to act as complete differential: This means that arises a shifting of the average flux with velocity v_i in any direction, while flow maintaining its nature and character movement.

When the advection is non-dominant mechanism (without jumps-stress in temperature), there is not a condition to flow deformations:

- does not indicate the individual modification of one or other of the velocity components.
- It is not ignored the action of the first component $\partial v_i / \partial t$.

2.1. Contribution of the magnetic field

Magnetic field in the case of the black hole is a result of the primary distribution of the residual charge at collapse and the action of gravity-magnetic dynamo thereafter. This feature allows, if the dynamo is activated close enough to collapse; BH may to hold a substantial part of the MF of ancestor. So on Kerr black hole, remains weak but sufficient vital MF within ergosphere. It develops in the disc and is closely related to the evolution of the advection to mode self-induction.

2.1.1 Magnetic field in the disk:

Determine the direction of the middle flow displacement in the disc uniquely. For field normal to the plane of the disc the term $B_r B_\phi$ the right side of the equation of motion leads to a radial advection Campbell et al. (1998) – the solution as a whole transfers into smaller radii, retaining his Keplerian character.

It provides additional dissipative mechanism, which directly affects the development of the gradient of entropy in the disc and increases the effectiveness of radial accretion to 1.5 times.

Prevents transition the regime to the dominant mode, as transmitting energy to electrons. So acts as a buffer and prevents two-temperature separation of the environment or sudden temperature changes therein. Instead that redirected surpluses to nonlinear structures.

2.2. Sign of the entropy

Negative gradient of entropy $\partial_t S$ determined the basic criterion for development and the self-induction on the advection.

In the hot magnetic disks along with both type dissipations and nonlinear interactions in the spectrum transitions the MR-modes which emit additional photons Hirose (2009), works compacting the plasma. It is due of the most important contribution of the field - by partially freezing the current leads the plasma, she follows it and is compacting. This means that together with the natural processes of absorption and scattering in the disk, works refraction of formed radiation in layers of the rings Yankova (2014). Optically dense fluidal lightguides, holds radiation in the flow. Thus energy is saved to disk in the form of heat and radiation, and manages the radial gradient of entropy. Negative entropy creates conditions for energy absorption of the instabilities and leads them to new state by irreversible transition - turning them into (vortex-) structures; Stimulates feedback and naturally intensifies the effects of heating from nonlinear interactions. This inverse cascade provides necessary thermal excitation to maintain advection in self-induction mode. (See the effectiveness by MF above).

Although we ignore the self-gravity of the advective ring, it directly affects the MF and the current in it, along with the background potentials at the central object. So although we do

not take this interaction into account in the nonrelativistic case, it is reflected in the behavior of the EMF and the following him plasma and therefore on the advective mechanism.

2.3. Spirals

Results of researches of magnetized accretion disk and particular solution on the model have shown that there are three types of spirals:

Tidal spiral that is logarithmic and the one number for high-temperature $T > 10^6 \text{K}$ accretion disks occurs in the outer regions where the influence of the magnetic field is weak (Iankova (2007), Iankova, 2009).

MHD spirals occur in the inner regions, where localized precession spiral in hydrodynamic models (Matsuda et al.2000). Magneto-rotation instabilities hinder precession spiral to appear, but at the expense of this the activity MR-instabilities act as a catalyst for other of the numbers of spiral waves Kaburaki (1999) and thus determined the corresponding number of MHD-helices in the disc.

Advective spiral - advective pseudo rings Iankova (2007, 2009), Yankova (2012, 2013, 2014, 2015) are sections the advective spiral. Elliptic instability in the disk fragments the advective spiral into parts. For advective ring-shaped fragments, there are no forbidden regions of the disk. Advective spirals are Keplerian, because they are obey the specific properties of the gravitational field of the black hole. Their behavior gives rise to the question of fundamental nature of deformationless advection as a mechanism for which the other types of advection represent specific boundaries.

3. Advective mechanism in the general relativity

Model which was built in the Galilean transformations Iankova (2007, 2009); Yankova (2012-2015) with pseudo-Newtonian correction Abramowicz et al. (1988) ; Igumenshchev & Abramovich (2000) opens opportunities for natural upgrade Yankova (2016), and it should be noted that the restriction $v^2 / c^2 \sim 4 \cdot 10^{-2} \ll 1$ for Newtonian approximation for most of the real objects is not applicable. The model is especially effective in its zone of applicability, but it is useful and because of that its results provide a fundamental reason for the transition to General Relativity GR.

3.1. Central object - Kerr black hole

To start with the central object: The metric of the uncharged or charged Kerr black hole is presented with the decisions of Kerr and Kerr-Newman and, in the absence of a cosmological term, has the general appearance:

$$ds^2 = g_{tt} dt^2 + 2g_{t\varphi} dt d\varphi + g_{\varphi\varphi} d\varphi^2 + g_{rr} dr^2 + g_{\theta\theta} d\theta^2 \quad (2.1)$$

with relevant coefficients. A stationary metric means that the angular momentum of a concrete orbit J does not variation over time in the manifold. Here the θ is a conical angle, because in the Kerr metrics the spherical symmetry is broken and replaced by the axis-symmetry (The Galactic Black Hole 2003).

3.2. Model accretion flow

Should be noted that until now we have neglected the flow self-gravity, operating only with the field of the compact object, under the conditions of GR it is not applicable approximation. Cylindrical symmetry of the disk in combination with the difference relaxation periods on the flow for the horizontal and vertical spatial components provides a metric of the type:

$$ds^2 = g_{tt} dt^2 + 2g_{t\varphi} dt d\varphi + g_{\varphi\varphi} d\varphi^2 + g_{rr} dr^2 + dz^2 \quad (2.2)$$

The interesting thing in the case of disk accretion is that advection manages to force more photons to move in orbits for massive particles because they cannot leave the mainstream due to high flow density

Then the stress tensor ${}_{\mu\nu} = \begin{pmatrix} T_{00} & T_{0i} \\ T_{i0} & T_{ij} \end{pmatrix} = \begin{pmatrix} ed & md \\ efd & mfd \end{pmatrix}$ for massive and non-massive

particles is common (it looks the same way and is a simple superposition the stress tensors), this also applies to sum self-gravity flow $\rho_{eq} = \rho_{mater} + \rho_{rad}$

3.3. Advective ring and advective screw

Advective rings and the advective screw are segments of the advective spiral whose self-gravities determine their metrics reduced due to their spatial limitations.

3.3.1 Advective ring

$$ds^2 = g_{tt} dt^2 + 2g_{t\phi} dt d\phi + g_{\phi\phi} d\phi^2 + dr^2 + dz^2 \quad (3.1)$$

In classical dynamics, the advective ring in the disk (1.6) is the main carrier of the hidden activity. Its good description in GR is important and is especially valuable if, after appropriate analytical treatment, it resembles the classic case:

$$\frac{\partial(\rho v_i)}{\partial t} + \frac{\partial}{\partial x_j} (\rho v_i v_j) = \rho \left(\frac{\partial v_i}{\partial t} + v_j \frac{\partial v_i}{\partial x_j} \right) = \rho \frac{Dv_i}{Dt} \quad (3.2)$$

(*) naturally arises question a mechanism of the deformationless advection is there causal connection with the metric of space-time, regardless of the thermal excitation? Question is rhetorical. With its quality of a complete differential, the advection should exactly to follow the metric of the manifold (see self-induction advection above). (eq.:3.1 & 3.3 and Giuseppe Frè (2013)).

3.3.2 Advective screw

Advective screw is a continuation of the advective spiral after the last stable disc orbit from the inner edge to and into the compact object:

$$ds^2 = g_{tt} dt^2 + 2g_{t\phi} dt d\phi + g_{\phi\phi} d\phi^2 + dr^2 + dz^2 \quad (3.3)$$

This form is a direct consequence of the above conclusion (*) and the full appearance of the advective screw should be expressed in a relativistic system analogous to (3.2-3.4)

Until the horizon of the black hole only advective terms in the motion equation (1.6) are unlocked, but around and under event horizon in over-virial $T > 10^{9 \rightarrow 14}$ K temperatures are unlocked and thermodynamic-advective terms $\rho T \frac{\partial S}{\partial t} - \frac{\dot{M}}{2\pi r} T \frac{\partial S}{\partial r} \cong \dot{M} T \frac{DS}{Dt}$. Where

$\dot{M} \cong 4\pi r h \bar{\rho}_{eq} v_j$ - rate of accretion; r- the reached orbit, h- half-thickness of the disc, ρ_{eq} - equatorial density and v_j the middle course velocity. Then in GR the analog lookalikes as:

| | |
|--|-------|
| $\Gamma \left(\dot{M} \frac{D}{Dt} S \right)$ | (3.4) |
|--|-------|

represents TD-advective complete differential. In view of the fact that advection occurs and develops exactly in the disk component of the quasar we have the right to consider the TD-complete differential precisely in this common type.

4. Conclusions

In the post-Newtonian development with the transition to GR and the dropping out of classical restrictions is most important to be checked whether the advantages of the concept are preserved:

- Equations to remain nonlinear; and
- Moreover in new conditions, components the derivatives of velocity are equal in rights in regard to self-consistent changes in speed.

In This article is specified the main direction of our future research. The aim is a summary of the developed analytical model for the structuring of disk components of AGNs in GR. Will be seeking answers to the following problems:

1. To identify in what way the development of non-deformable/ deformationless advection in general relativity, validation it as a fundamental mechanism;
2. To determine and displayed the nature of causal connection which provides a non-thermal control on the advection mechanism;
3. To obtain estimates of the degree of unification of the model and
4. Other issues that could arise in the course of the research.

To modulate these problems and quality interpret results will seek optimal set theoretical and experimental tools, including observation at a sufficiently large number of sources, suitable numerical methods and methods of polarimetry.

References

- Abramowicz M. A., Czerny, B., Lasota, J. P., Szuszkiewicz, E., 1988 Slim accretion disks, *ApJ*, 332 646-658.
- Beloborodov, A. M.: 1999, *Accretion Disk Models*, arXiv: astro-ph/9901108.
- Bisnovatyi-Kogan, G.S.: 1998, *Accretion Disc Theory: From the Standard Model Until Advection*, arXiv: astro-ph/9810112.
- Bisnovatyi-Kogan, G.S.: 1999, *Accretion Discs Around Black Holes: Development of Theory*, arxiv astro-ph/9911212.
- Bisnovatyi-Kogan, G.S., Lovelace, R.V.E.: 2002, *Advective Accretion Disks and Related Problems Including Magnetic Fields*, arXiv:astro-ph/0207625v1.
- Campbell C. G., Papaloizou J. C. B., Agapitiu V.: 1998, *Magnetic field bending in accretion discs with dynamos*, *MNRAS* 300, 315-320.
- Chen, X., Abramowicz, M. A., Lasota, J.P.: 1997, *Advection-dominated Accretion: Global Transonic Solutions*, *ApJ* 476, 61-69.
- Fabian, A.C., Wilkins, D.R., Miller, J.M., Reis, R.C., Reynolds, C.S., Cackett, E.M., Nowak, M.A., Pooley, G.G., Pottschmidt, K., Sanders, J.S., Ross, R.R., Wilms, J.: 2012, *On the determination of the spin of the black hole in Cyg X-1 from X-ray reflection spectra*, <http://www.astro.umd.edu/symbol%7126%7d%25chris/publications/papers/fabian12a.pdf>
- Giuseppe Frè P, 2013, *Gravity, a Geometrical Course I*
- Hirose S., Krolik J. H., Blaes O., 2009, *Radiation-Dominated Disks Are Thermally Stable*, *AJ*, 69116.
- Iankova Kr.D., 2007, *Accretion disk with advection and magnetic field*, BG-Ursi School and Workshop on *Waves and Turbulence Phenomena in Space Plasmas*, 1–9 July, 2006, Kiten, Bulgaria, BSSPP Proceedings, Series No. 1, pp 143-146, 2007, <http://sp.phys.uni-sofia.bg/Kiten06/Pres/Iankova.pdf> .
- Iankova Kr.D., 2009, *Stability and evolution of magnetic accretion disk*, *Publ. Astron. Soc. "Rudjer Bošković"*, No. 9, pp 327-333, Belgrade (2009). http://aquila.skyarchive.org/6_SBAC/pdfs/31.pdf;
- Igumenshchev, I.V., Abramovich, M.A.: 2000, *Two-dimensional Models of Hydrodynamical Accretion Flows into Black Holes*, *ApJ* 130, 463-484.
- Kaburaki Os., 1999, *Analytic Model for Advection-Dominated Accretion Flows in a Global Magnetic Field*, arXiv: astro-ph/9910252.
- Narayan, R., Kato, S., Homn, F.: 1997, *Global Structure and Dynamics of Advection-dominated Accretion Flows around Black Holes*, *AJ* 476, p. 49.
- Narayan, R., & Yi: 1995, *Advection-Dominated Accretion around Black Holes*, *ApJ* 452, 71.
- Matsuda T, Makita M, Fujiwara H, Nagae T, Haraguchi K, Hayashi E, H.M.J. Boffin: 2000, *Numerical simulation of accretion discs in close binary systems and discovery of spiral shocks*, *Astrophysics and Space Science* 274: 259–273, 2000.
- THE GALACTIC BLACK HOLE (2003) *Lectures on General Relativity and Astrophysics*, Institute of Physics, Publishing Bristol and Philadelphia
- Yankova Krasimira, 2012, *Structure of accretion disk in the presence of magnetic field*, *Publications of the Astronomical Society "Rudjer Boskovic"*, vol. 11, pp. 375-383. <http://adsabs.harvard.edu/abs/2012PASRB..11..375Y>
- Yankova Kr.D.: 2013, *Generation and development of the disk corona*, *Proceedings of the VIII Serbian-Bulgarian Astronomical Conference (VIII SBAC)*, *Publ. Astron. Soc. "Rudjer Bošković"* vol. 12, 375-381. http://wfpdb.org/ftp/8_SBAC_D1/pdfs/34.pdf
- Yankova Kr., 2014, *Theoretical analysis on the development in relationships of the system disk – corona*, *Proceedings SES 2014*, ISSN 1313-3888 , 35-40, 2015.
- Yankova Kr.: 2015, *MHD of accretion-disk flows*, *BlgAJ*, Vol. 22, p. 83. <http://adsabs.harvard.edu/abs/2015BlgAJ..22...83Y>
- Yankova Kr., 2016, *SSTRI-BAN, Proceedings Seventh Workshop “Solar Influences on the Magnetosphere, Ionosphere and Atmosphere”*, ISSN 2367-7570, <http://ws-sozopol.stil.bas.bg/2016Sunny/Proceedings2016.pdf>

The Energy Barrier and Collision Number of $O^+ + H_2(v=0, j=0)$ Reaction in the Earth Ionosphere

Yaşar M., Canyılmaz M.

Department of Physics, Firat University, 23169 Elaziğ, Turkey
E-mail: mehmetyasar@firat.edu.tr

Abstract

In this work, we discussed the effect of $O^+ + H_2 \rightarrow OH^+ + H$ reactive reaction on the Earth ionosphere. It used that reaction rate constant and total cross sections which is calculated as a function of altitude. Also all the parameters related with the ionosphere are calculated for the 38.400N, 39.120E coordinates and year, day and time are taken as 2009, equinox, local time (12:00) respectively. It was shown that the reaction rate constant and cross section values are decreasing with ionospheric height. The total collision number between O^+ and H_2 takes the maximum values at the lower ionosphere and decreases with increasing height in upper ionosphere. The energy barrier is much closed to each other for all months and increased with the altitude.

Keywords: *Collisions, gas kinetic theory, Ionosphere, reaction processes.*

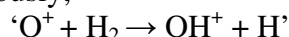
1. Introduction

The Earth's ionosphere is located at the height of 60-1000 km containing free electrons and ions (Brasseur and Solomon, 2005). Changes in the ionospheric system are crucial importance on communications, navigation and the exploration of the near earth space. Thus the study of the ionospheric phenomena has become an important field of present day's research [Itikawa, 2007; Mangla and Yadav, 2011].

The ionosphere has a very complex structure due to its physical and chemical composition. The description of the photochemical processes and the ionosphere chemical kinetics in the theoretical model, with the account of chemical composition of the neutral particles and ions considered, includes the processes of photoionization, photodissociation, dissociative recombination, radiative recombination, collision mechanism, etc. [Richards, 2011; Whitten and Poppof, 1964].

The role of O^+ and H_2 particles on the Earth's ionosphere chemistry is very important according to density changes in the upper and lower ionospheric height so many researchers have done studies on these particles. In these studies, theoretical models have been used to investigate the effects of artificially injected H_2 gas on plasma densities in the ionospheric F region and the overlying protonosphere. It has been found that the release of modest amount H_2 gas can produce significant perturbations in the ionosphere and protonosphere [Bernhardt et al., 1975]. Also the effect on ionosphere of O^+ and H_2 was separately investigated by them and no attempt was made the effects on the earth ionosphere by combining kinetic theory-based models with the cross sections in the 0.02-0.1 eV collision energy range and state to state rate constants values for the $O^+ + H_2 \rightarrow OH^+ + H$ reaction that have been obtained using a quantum wave packet method.

In this study, total reaction rate constants and cross sections obtained for the reaction [Gómez-Carrasco et al., 2014] previously;



and used to investigate the effects in the ionosphere.

2. Methodology

The theoretical analysis of ionosphere chemistry modification must be carried out due to a large number of factors, such as the great increases in the energy regime of the earth ionosphere system, the change in density and temperature during the collision and the abrupt disconnections. Also several statistical quantities such as collision frequency, potential energy

barrier and total number of reactive collisions must be taken in to account and so shall find quantitative relationships between statistical quantities characterizing molecular collisions (such as mean free path, etc.) and basic physical properties of the gas (such as concentration, temperature, height, etc.). These terms are closely related to each other and to other fundamental molecular quantities.

2.1. Total Collision Number

A chemical reaction is explained as a simple collision with the following relative velocity dependent cross section:

$$\sigma(g) = \sigma_0 H(g - g_0) \quad (1)$$

where $H(g)$ is the Heaviside step function and the velocity threshold, g_0 , is the velocity of relative motion which is sufficient to overcome the potential energy barrier:

$$g_0 = (2U_2/m)^{1/2} = (8kT/\pi m)^{1/2} \quad (2)$$

Z_{12} which is the number of reactive collisions per unit volume can be calculated. This can be done by substituting the cross section of the chemical reaction [Gombosi, 1994]:

This equation is valid for both the forward and the reverse reaction. The main difference between this two reactions is that the forward reaction involves the collision of different (unlike) molecules, therefore $K_{12}=1$, while the reverse reaction involves the collision of two like molecules, therefore $K_{12}=1/2$.

The threshold velocity can be expressed in terms of the barrier potential energy, U_0 :

$$Z_{12} = K_{12} \sigma_0 n_1 n_2 (v_1^2 \pm v_1'^2)^{1/2} e^{-(U_0/kT)} (1 + U_0/kT) \quad (3)$$

3. Results

The reaction dynamics of the ‘ $O^+ + H_2 \rightarrow OH^+ + H$ ’ reactive reaction have been investigated in this study. All parameters are calculated for the $38.40^{\circ}N, 39.12^{\circ}E$ coordinates and year, day and time are taken as 2009, equinox, local time (12:00) respectively, together with the ionospheric temperature and density data are obtained from IRI (International Reference Ionosphere) website [Blitza, 2012, 2014; IRI Web Program].

O^+ is active particle, while H_2 molecule is stationary in this reaction. Also, we need to match the reaction formation temperature with ionospheric temperature. We have calculated total collision number of two particles ($Z_{O^+H_2}$) and barrier potential energy (U_0) by using the equation (2) and (3).

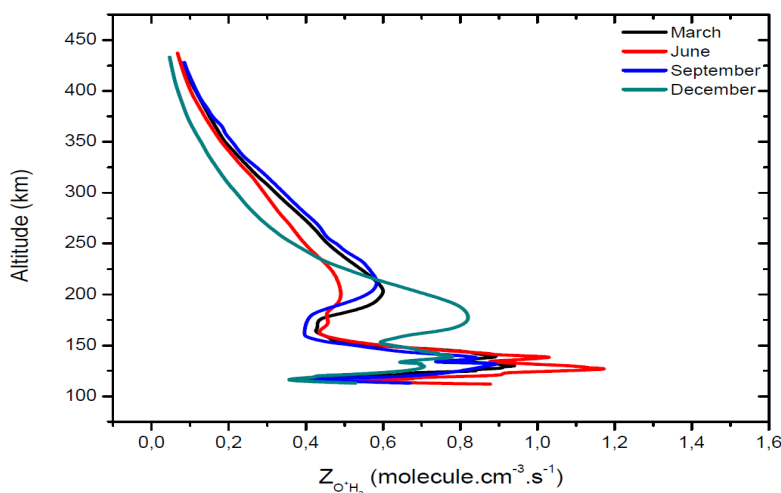


Figure 1. Variation of the total collision number of the reaction in the ionosphere.

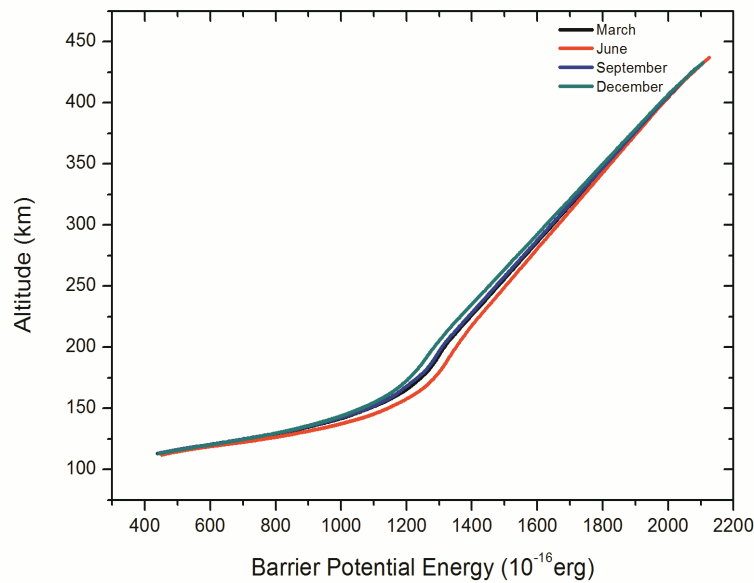


Figure 2. Variation of barrier energy and the ionospheric height.

4. Conclusion

In this study we have analyzed $O^+ + H_2 \rightarrow OH^+ + H$ reactive reaction under ionospheric conditions. $Z_{O^+H_2}$ has the maximum values at the lower height (about 100-150 km) and decrease with increasing height in upper ionosphere. Because H_2 density is too much at the lower ionosphere and decreasing dramatically with the ionospheric height, the total collision number at the subionosphere has the greatest value and also O^+ ion density is very small at these altitudes. As the altitude rises, the barrier energy also increases and there is no big difference between the months.

Acknowledgment

The authors wish to thank Niyazi Bulut for his contributions.

References

- Itikawa, Y., (2007). Molecular Processes in Plasmas Collision of Charged Particles with Molecules. Springer.
- Mangla, B., Yadav, M., (2011). Chemistry of Upper Ionosphere- A Study. Int. J. Adv. Eng. Sci. 1, 1.
- Richards, P. G., (2011). Reexamination of Ionospheric Photochemistry. J. Geophys. Res. 116, A08307.
- Whitten, R.C., Poppof, I.G., (1964). Ion Kinetics in the Lower Ionosphere. J. Atmos. Sci. 21, 2.
- Bernhardt, P. A., Park, C. G., Banks, P.M., (1975). Depletion of the F2 Region Ionosphere and the Protonosphere by the Release of Molecular Hydrogen. Geophys. Res. Lett. 2, 8, 341-344.
- Gómez-Carrasco, S., Godard, B., Lique, F., Bulut, N., Klos, J., Roncero, O., Aguado, A., Aoiz, F., Castillo, J., Goicoechea, J., Etxaluze, M., Cernicharo, J., (2014). OH^+ In Astrophysical Media: State-to-State Formation Rates, Einstein Coefficients and Inelastic Collision Rates with He. Astrophys. J. 794, 33, 16.
- Bilitza, D., Brown, Steven A., Wang, Matthew Y., Souza, Jonas R., Roddy, Patrick A., (2012). Measurements and IRI Model Predictions during the Recent Solar Minimum. J. Atmos. Sol. Terr. Phys. 86, 99-106.
- Bilitza, D., Altadill, D., Zhang, Y., Mertens, C., Truhlik, V., Richards, P., McKinnell, L.- A., Reinisch, B., (2014). The International Reference Ionosphere 2012 - a model of international collaboration. J. Space Weather Space Clim. 4, A07, 1-12. (URL<http://omniweb.gsfc.nasa.gov/vitmo/iri2012_vitmo.html>)

Occurrence of TEC fluctuations and GPS positioning errors at different longitudes during auroral disturbance

I.I. Shagimuratov¹, S.A. Chernouss², M.V. Filatov², I.V. Despirak²,
N.Yu. Tepenitsyna¹, I.I. Efishov¹

¹ WD IZMIRAN, Kaliningrad, Russia;

² Polar Geophysical Institute, Apatity, Russia.

E-mail: shagimuratov@mail.ru

Abstract

In this report the occurrence analysis of the GPS TEC fluctuations associated with auroral disturbances during the January 7, 2015 storm and impact the disturbance on GPS precise positioning is presented. We used observation of GPS stations located at the European, American and Asian sectors. The magnetograms of the IMAGE network were used as an indicator of the auroral activity. As measure of the TEC fluctuation activity was used the rate of TEC (ROT) and intensity fluctuations evaluated by index ROTI. The intensity fluctuations essentially differed on longitude. We have also analyzed an impact of the geomagnetic disturbances on the Precise Point Positioning (PPP) errors. The positioning errors were determined using the GIPSY-OASIS software (APS-NASA). The storm-time the 3D position error (P3D) reached the values more than 10m, while during quiet time they did not exceed 10-20 cm. We found a correlation of the positioning errors with ROTI.

Introduction

Total electron fluctuations at high latitudes are caused presence of different scale irregularities in the ionosphere. The TEC fluctuations are occurred as phase fluctuations of GPS/ GLONASS signals. There are numerous papers are concerned this problem [Aarons J., 1997; Spogli L., et al., 2009; Prikryl P., et al., 2013; Cherniak I., 2015]. The GPS measurements are importance as for investigation of physical processes in the high latitude ionosphere as well as for study of influence of auroral activity on GPS/GLONASS navigation. Strong TEC fluctuations can complicate phase ambiguity resolution and to increase the number of undetected and uncorrected cycle slips and loss of signal lock in GPS navigation and positioning errors. [Chernouss S. A., et al., 2011]

The increase intensity of TEC fluctuations in auroral ionosphere are followed by auroral activity [Shagimuratov I.I., et al., 2015]. The relation between intensity TEC fluctuations and GPS positioning errors is presented by Jacobsen K.S., et al., 2014, 2016 over Europe. In this paper the occurrence of TEC fluctuations and positioning errors at American, Asian and European sectors during geomagnetic storm on January 07, 2015 is discussed.

Data and method

The TEC measurements for individual satellite passes served as raw data. As a measure of fluctuations activity the rate of TEC (ROT, in the unit of TECU/min, 1 TECU=10¹⁶ (electron/m²) at 1 min interval was used. As a measure intensity fluctuations index ROTI was used [Pi et al., 1997]. $ROTI = \sqrt{\langle ROT^2 \rangle - \langle ROT \rangle^2}$

Index ROTI was calculated with 10 min. interval. The Precise Point Positioning (PPP) were determined using the GIPSY-OASIS software (APS-NASA). The storm was rather moderate. Maximal value of the index D_{ST} reached near -100 nT, K_p reached about 6. Maximal auroral activity was observed on 09-12 UT when driven phase of the storm was developed. Previous analysis of the storm pointed that maximal intensity of TEC fluctuations is occurred during substorm activity [Shagimuratov I.I., et al., 2015]. As indicator of substorm activity was used magnetometers data of the Scandinavian chain.

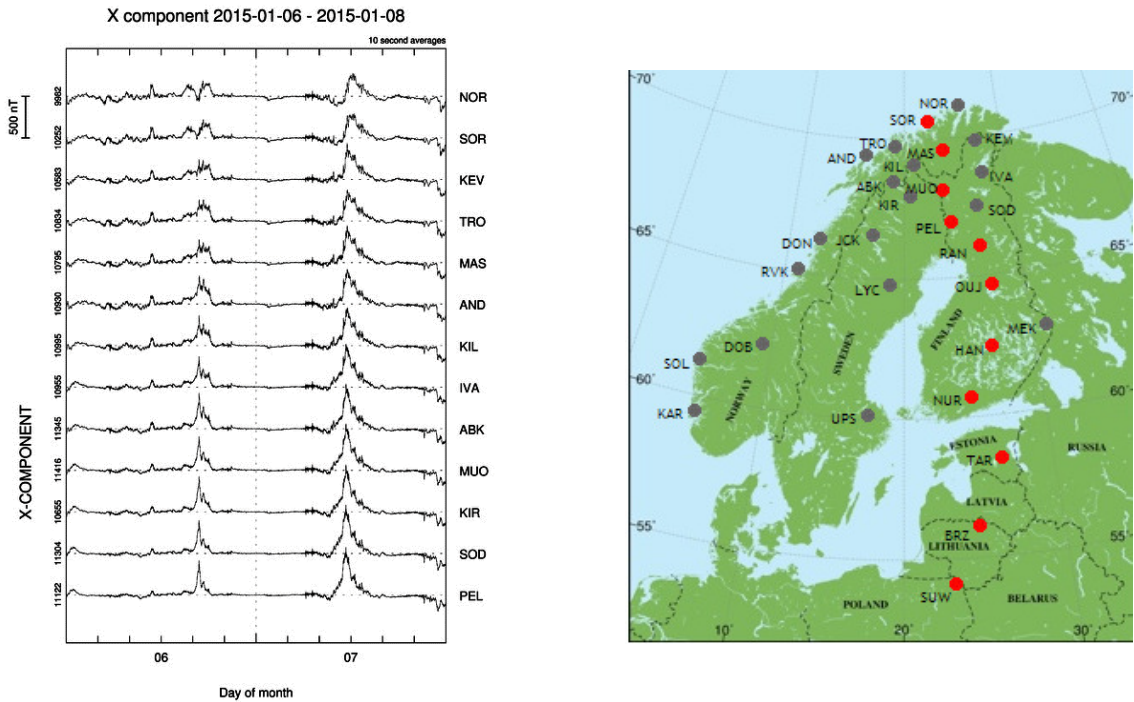


Fig.1 IMAGE magnetometers data on 6-7 January 2015 and the map of IMAGE stations

Results

We analyzed the temporal occurrence of the TEC fluctuations by using standard 30 sec. GPS phase measurements. Fluctuation activity was evaluated by rate of TEC (ROT) at 1 min. interval. On their base we formed a picture which demonstrates behavior of ROT over station for all satellite passes on 24-hour interval. The intensity of TEC fluctuations was evaluated by index of ROTI which was calculated with 10 min. interval. The latitudinal – temporal behavior of ROTI was presented in Geographic Latitude – UT coordinates. For analysis of the longitudinal development TEC fluctuations we used GPS stations located in auroral zone where strong fluctuations were observed. In Fig.2 occurrence of TEC fluctuations for American (SG27 station), European (TROM), Asian (TIXI) sectors are presented. The occurrence of fluctuations on different longitudes is very similar. A rather good consistency is in the time evolution of the substorm activity (Fig.1) and TEC fluctuations (Fig.2). Maximal effect both of them takes place on 09-13 UT. The fluctuations are observed on indifferent azimuths of satellite passes at the same time. Intensity of fluctuations is less in Europe relative America and Asia. It is associated with LT dependence of occurrence TEC fluctuations in the auroral ionosphere. The fluctuations are usually registered in the auroral oval region and close to the local midnight. The auroral activity in Europe was occurred at day time, in America and Asia it was at night hours. Ordinary, at day time, the TEC fluctuations on auroral and subauroral stations are weak. Intensive fluctuations are occurred around 12 UT at all longitudes as it can see on circular diagrams (Fig.2) We see also the so-called UT effect.

For analysis of impact of TEC fluctuations to the Precise Point Positioning (PPP) errors we used the Automatic Precise Positioning Service ([www. apps gdgps.net](http://www.apps.gdgps.net)). Using this service, we calculated the 3D positioning error (P3D) defined as the offset of the detrended coordinate from its median value (x_0, y_0, z_0) and calculated for each epoch i as [Jacobsen K.S., et al., 2014]:

$$P_{3D}(i) = \sqrt{(x(i) - x_0)^2 + (y(i) - y_0)^2 + (z(i) - z_0)^2}$$

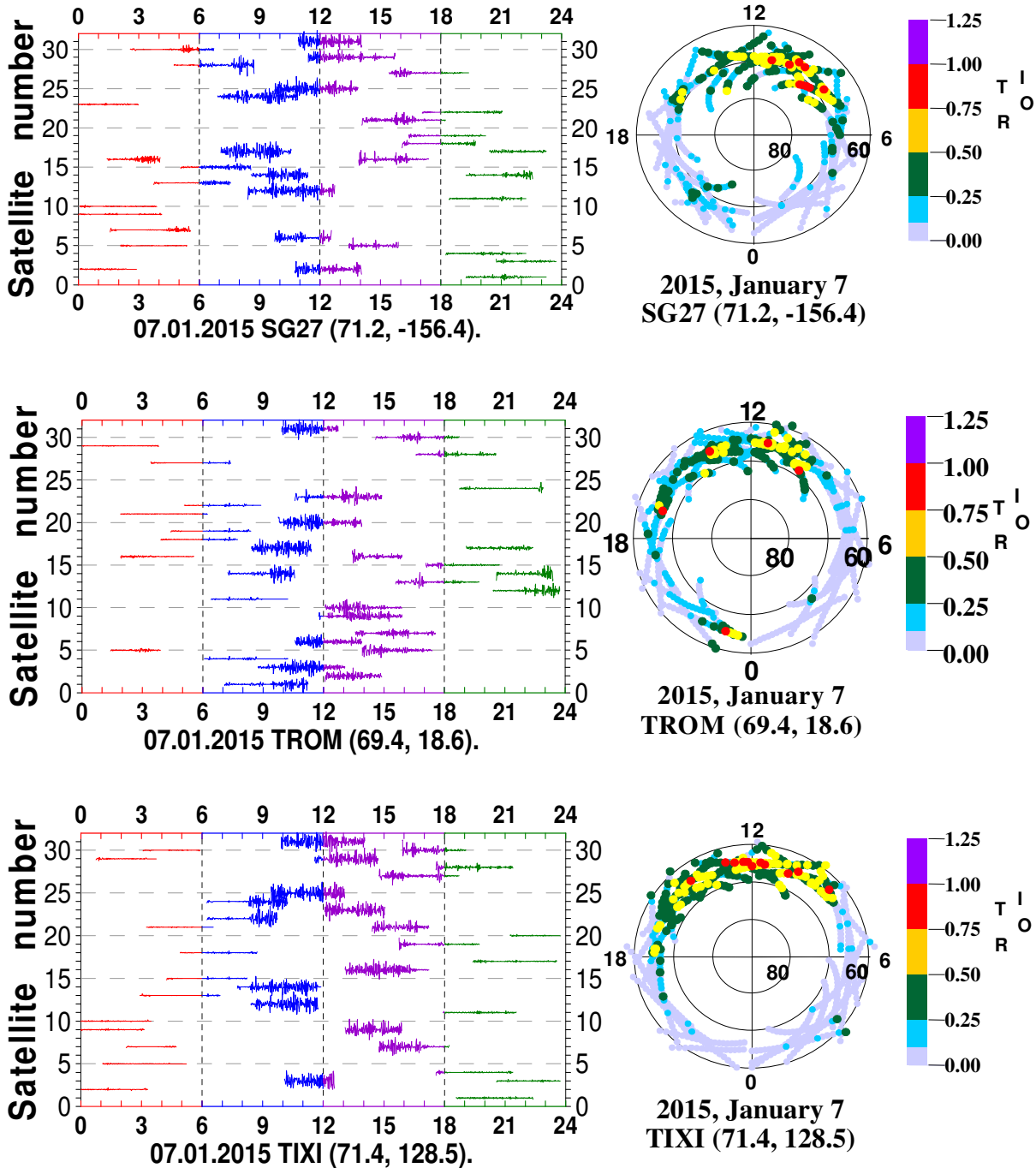


Fig.2. Temporal occurrence of TEC fluctuation activity (left panels) and intensity (right panels) at different longitudes during storm day on January, 2015.

We calculated the 3D positioning errors with 5 min interval ($i=5$). In Fig.3 the 3D positioning errors (ΔP) and ROTI for SG27, TROM and TIXI stations are presented. It can be seen that at American and Asia during storm positioning errors can reach more than 10 m. At the same time for Europe the error was less than 1 m. The errors depend very nonlinearly on ROTI. Such effect was obtained also by *Jacobsen K.S., et al., 2014*.

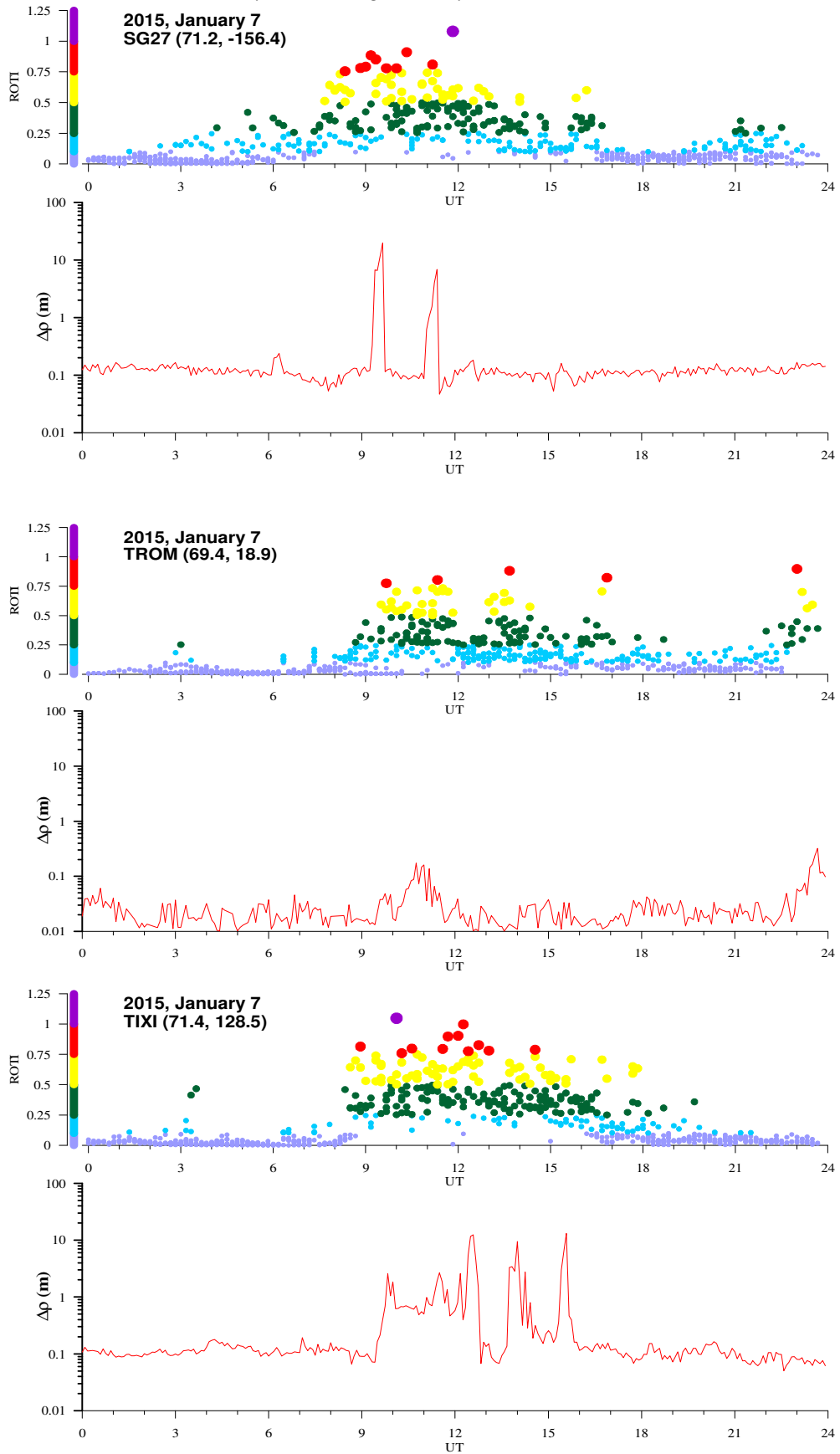


Fig.3. Diurnal variations of ROTI and 3D positioning errors during storm day at GPS stations located at different longitudes.

Summary

We have analyzed an occurrence of the GPS TEC fluctuations associated with auroral disturbances during January 7, 2015 storm and impact the disturbance on GPS precise positioning. Maximal auroral activity was observed at 09-12 UT. For Europe it was occurred during day time, for Alaska and Asia it was during night time. It is known that in auroral zone maximal intensity of fluctuations usually is observed in the local night. Index ROTI was used as measured intensity of TEC fluctuations. Maximal value of ROTI was registered over Alaska and Asia sectors. It was found that fluctuation activity was observed over all longitude sectors at the same UT time (UT effect).

Over Europe the auroral activity was occurred during day time, so TEC fluctuations at this sector were rather weak in comparison with American and Asian sectors TEC ones.

We calculated 3D positioning errors (ΔP) with 5 min interval using the GIPSY-OASIS software. We found the high correlation of the GPS positioning errors with ROTI. The positioning error increases exponentially with increasing of ROTI values. During maximal auroral activity, on 09-12 UT, the positioning errors reached more than 10 m over the auroral ionosphere in Alaska and Asia regions. At the same time the positioning errors were less than 0.5 m in Europe.

Acknowledgments

We thank the Institutes who maintain the IMAGE Magnetometer Array. The paper was supported by grants of RFBR: 16-05-01077, 17-45-510341; and partly supported by Program No 7 of the Presidium of the Russian Academy of Sciences (RAS).

References

- Aarons J. (1997). GPS system phase fluctuations at auroral latitudes. *J. Geophys. Res.*, 102 (A8), 17219-17231.
- Chernouss S.A., N.V. Kalitenkov (2011). The dependence of GPS positioning deviation on auroral activity. *Remote Sensing*, 32, no. 1, 3005-3017.
- Cherniak I., I. Zakharenkova, R.J. Redmon (2015). Dynamics of the high-latitude ionospheric irregularities during the 17 March 2015 St. Patrick's Day storm: ground-based GPS measurements. *Space Weather*, 13 (9), 585-597.
- Jacobsen K.S., Y.L. Andalsvik. (2016). Overview of the 2015 St. Patrick's day storm and its cosequences for RTK and PPP positioning in Norway. *J. Space Weather Space Clim.*, 6(A9), doi: 10.1051/swsc/2016004.
- Jacobsen K.S., M. Dahnn (2014). Statistics of ionospheric disturbances and their correlation with GNSS positioning errors at high latitudes. *J. Space Weather Space Clim.* 4(A27), doi: 10.1051/swsc/2014024.
- Pi X., A.J. Manucci, U.J. Lindqwister, C.M. Ho (1997). Monitoring of global ionospheric irregularities using the worldwide GPS network. *Geophys. Res. Lett.*, 24, 2283-2286.
- Prikryl P., R. Ghoddousi-Fard, B.S. Kunduri, E. Thomas, A. Coster, T. Jayachandran, E. Spanswick, D.W. Danskin (2013). GPS phase scintillation and proxy index at high latitudes during a moderate geomagnetic storm. *Ann. Geophys.*, 31 (5), 805-816.
- Shagimuratov I, S.A. Chernouss, Iu. Cherniak., I. Efshov, M. Filatov, N. Tepenitsyna (2015). Phase fluctuations of GPS signals and irregularities in the high latitude ionosphere during geomagnetic storm. *Sun and Geosphere*, 11 (2) 101-108.
- Spogli L., L. Alfonsi, G. De Franceschi, V. Romano, M.H.O. Aquino, A. Dodson (2009). Climatology of GPS ionospheric scintillations over high and mid-latitude European regions. *Ann. Geophys.*, 27 (9), 3429-3437.

Recently Revealed New Type of Daytime VLF Emissions Observed under Quiet Space Weather Conditions

*J. Manninen*¹, *T. Turunen*¹, *N.G. Kleimenova*², *M. Rycroft*³, *L.I. Gromova*³

¹ Sodankyla Geophysical Observatory, Sodankyla, Finland

² Schmidt Institute of the Physics of the Earth RAS, Moscow, Russia

³ CAESAR Consultancy, Cambridge, UK

⁴ IZMIRAN RAS, Troitsk, Moscow

E-mail: jyrki.manninen@gmail.com

Abstract.

The natural electromagnetic waves at audio frequencies termed Very Low Frequency (VLF) emissions are typically generated in the magnetosphere via the electron-cyclotron resonance mechanism. These whistler-mode waves are guided to the ionosphere by the geomagnetic field line with the upper cut-off frequency at half of the equatorial electron gyrofrequency ($f_{ce}/2$) at a given L-shell. Based on the VLF signals observed in Northern Finland at Kannuslehto (KAN, L ~ 5.5, $f_{ce}/2$ ~ 2.5 kHz), recently we revealed a new and previously unknown daytime type of VLF-emissions at frequencies well above 4-5 kHz. These emissions have neither been seen before because they were hidden by strong impulsive sferics originating in lightning. The peculiar VLF signals, discovered after filtering out the sferics, were studied. It is shown here that these emissions, which have a complicated spectral structure, occur during the winter around local noon under quiet solar and geomagnetic conditions (VSW < 400-500 km/s, BIMF < 5÷7 nT, Np < 5÷8 cm⁻³, AE < 150÷200 nT). We suppose that these waves are generated deep inside the magnetosphere at much lower L-values than KAN. However, the details of the generation and propagation mechanisms of these newly discovered VLF emissions remain unclear.

Introduction

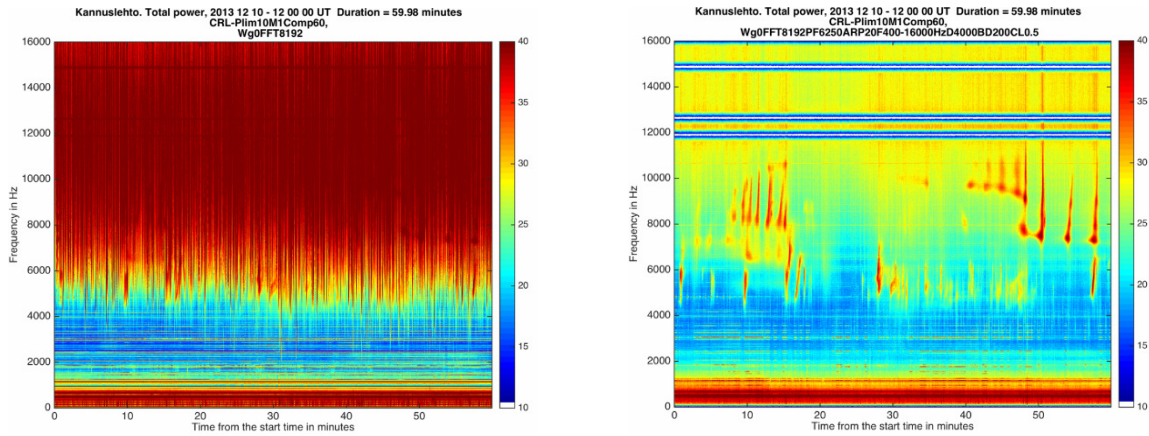
The natural electromagnetic waves at audio frequencies are called Very Low Frequency (VLF) emissions [Helliwell R.A., 1965]. The most typical natural VLF emissions are widely known as chorus, hiss and different kinds of quasi-periodic emissions. They are generated in the magnetosphere via the electron-cyclotron resonance mechanism [Trakhtengerts V.Y. and M.J. Rycroft, 2008]. These whistler-mode waves are guided to the ionosphere by the geomagnetic field lines with the upper cut-off frequency at a half of the equatorial electron gyrofrequency ($f_{ce}/2$) at a given L-shell [Carpenter D.L., 1968]. Despite significant successes of many ground-based and satellite observations, the full nature and behaviour of different VLF waves is not yet fully understood.

Many naturally occurring VLF waves at higher frequencies (above 4-6 kHz) could not be studied due to strong atmospherics (sferics) originating in lightning discharges and hiding all other waves. To study these waves, we have to apply special digital programs, which filter out the strong impulsive sferics.

It is well known that many magnetospheric waves are generated under solar wind and geomagnetic disturbances. However, here we present new and totally unexpected natural high-frequency electromagnetic VLF waves occurring during quiet space weather conditions.

Observations

Our study is based on the VLF signal observations made at Kannuslehto (KAN, L ~ 5.5, geographic coordinates 67.74°N, 26.27°E) in Northern Finland. The VLF emissions were recorded digitally in the frequency band of 0.2–39 kHz by two orthogonal magnetic loop antennas oriented in the North-South and East-West directions. The threshold of the receiver sensitivity is about 0.1 fT, (i.e. ~ 10⁻¹⁴ nT² Hz⁻¹). Due to the high sensitivity of the equipment

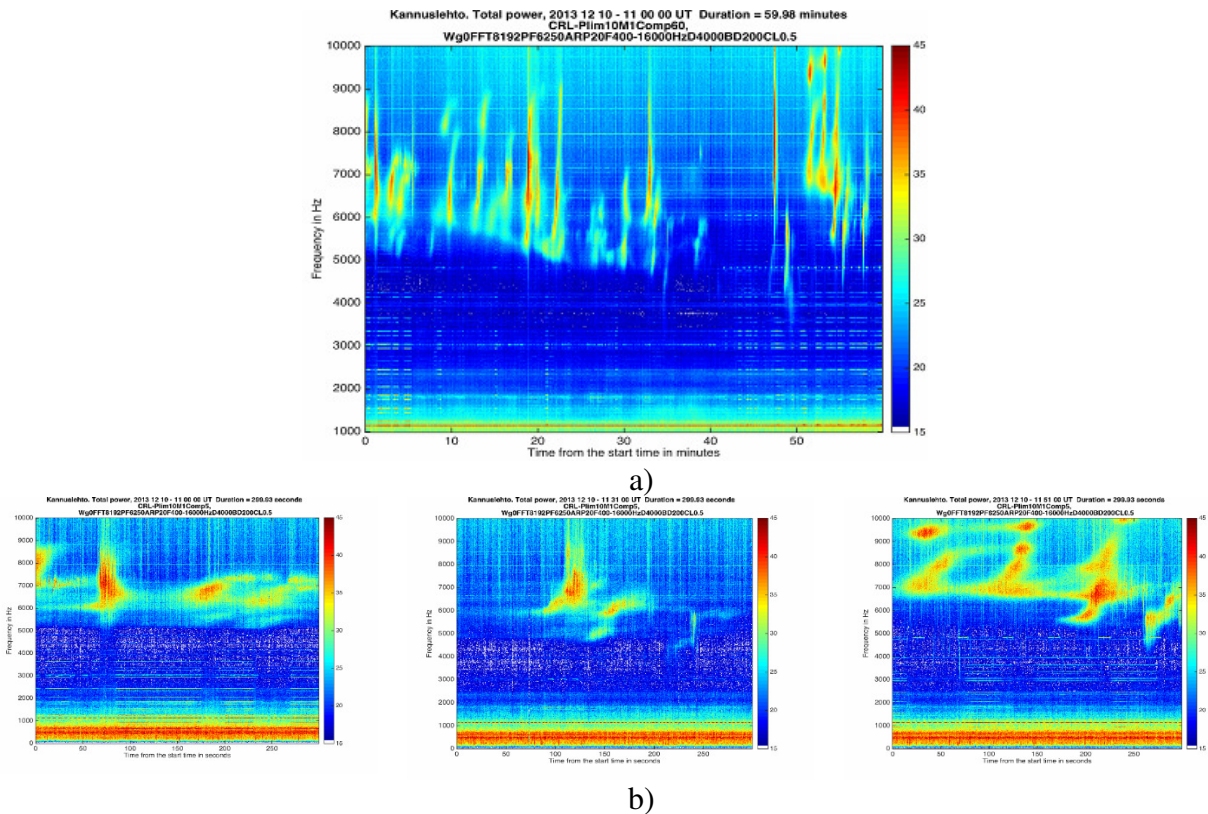


a) b)

Fig. 1. a) – An example of the initial raw spectrogram, b) – the same data after filtering out the sferics. Three high-frequency blue horizontal lines – removed radio transmitter traces.

a very strong level of sferics at frequencies higher than about 3-4 kHz is recorded. To study the waves hidden by sferics we have to apply a specially designed digital program to filter out strong impulsive sferics. An example of a raw unfiltered VLF one-hour spectrogram and the same data after filtering-out the sferics is plotted in Fig.1.

It is seen that a new and very unusual spectral structure of signals appears after filtering. These recently revealed VLF emissions have never been seen before because the signals were hidden by strong impulsive sferics. Figure 2 presents a more detailed dynamic spectra of the discussed waves.



a) b)

Fig.2. a) - The one-hour spectrogram of the newly revealed type of VLF emissions at 11-12 UT on December 10, 2013, and b) - 5-min spectrograms starting at 11.00, 11.31 and 11.51 UT.

Very complex unusual spectral features of the signals are seen. In the one-hour spectrograms, the signals look like sticks or wands, but their fine spectral structure is very peculiar and varies with time. Sometimes the signal shapes resemble flying birds as shown in Fig. 2 (b). When the recordings of these waves are played through a loudspeaker they sound like bird song; we call these events “bird-emissions”. Our first results of these investigations are published in *Manninen J. et al.* [2016, 2017].

These new emissions are usually observed for several hours and contain short burst-like structures at frequencies higher than 4 kHz, even up to 15 kHz. As a rule the signal frequency increases with time, but sometimes a wide frequency band could generate simultaneously as it shown in Fig. 3 representing the different fine spectral structures of the discussed VLF “bird-emissions”. The signal frequency change could indicate a change of the magnetospheric source location of these emissions.

The “bird-emissions” are typically right-hand polarized signals, suggesting that KAN was located in the vicinity of the wave exit area from the ionosphere.

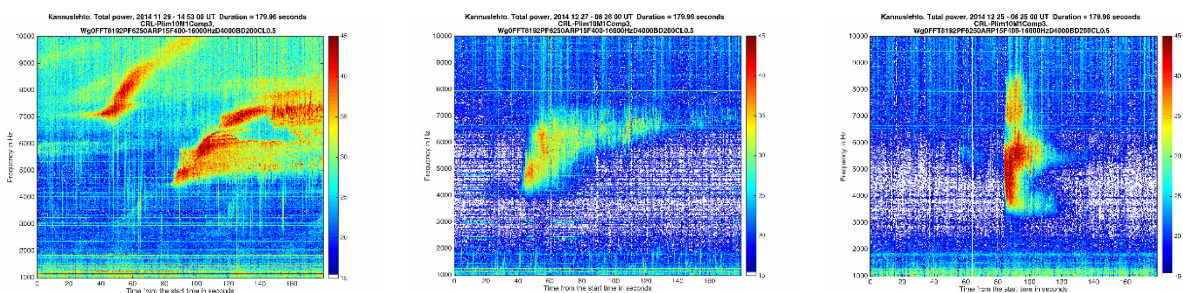


Fig.3. Examples of 3-min VLF spectrograms demonstrating different dynamic spectra of the newly revealed type of VLF emissions.

In five Finnish winter-time VLF campaigns (2006-2016) at different phases of the solar cycle, the discussed VLF emissions were observed only in the day time, with the maximum near local magnetic noon at 09-15 MLT. This is shown in Fig. 4 representing the “bird-emissions” occurrence distribution in the winter campaign 2014-2015 when these emissions were recorded in 52 out of 59 days of observation.

A similar result was also obtained during the winter campaign 2015–2016, when the “bird-emissions” were recorded in 75 out of 91 days of observation. So, these emissions are typical winter daytime VLF phenomena.

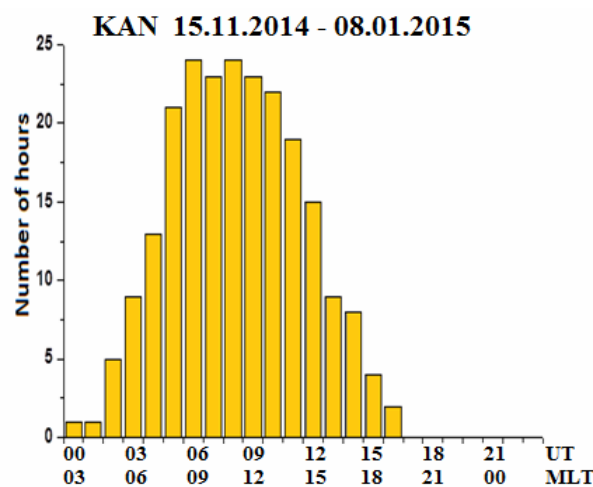


Fig. 4. The diurnal variations of the occurrence of “bird-emissions” in 2014-2015, the total duration of events was ~230 h. (adapted from *Manninen J. et al.* [2017]).

As a rule, the long lasting “bird-emissions” are observed under quiet space weather conditions. Typically, in this time, the solar wind speed and density are low ($V_{SW} < 400\text{-}500$ km/s, $N_p < 5\text{-}8$ cm⁻³) as well as the geomagnetic activity ($AE < 150\text{-}200$ nT). However, the “bird-emissions” occur a few days after periods of moderate geomagnetic disturbances.

The typical example of the space weather state during the discussed VLF emissions observed in KAN on 29 November 2014 at 11-17 UT ($K_p = 0\text{-}1$), four days after strong magnetic disturbances with $K_p = 5$, is presented in Fig. 5. The Van Allen Probe satellite data (not presented here) show that, during this event, KAN was mapped inside of the plasmasphere, but in the vicinity of the plasmapause.

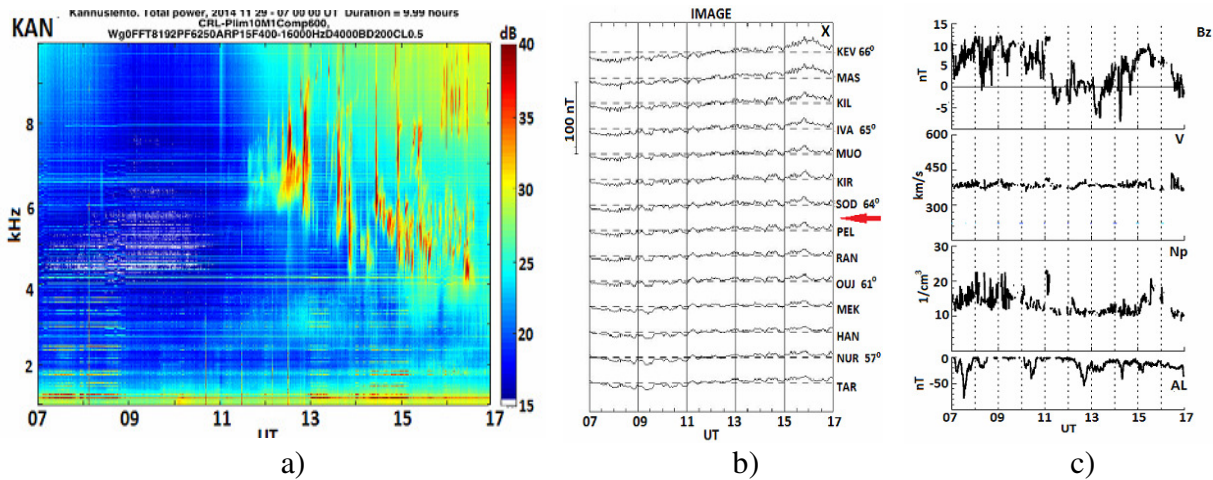


Fig. 5. a) - The spectrogram of “bird-emissions” 29 November 2014, b) - magnetograms from Scandinavian IMAGE chain, and c) - parameters of the IMF and solar wind.

The studied VLF emissions have been observed both in the presence and absence of typical lower frequency VLF emissions like chorus, hiss, and quasi-periodic events. An example of the simultaneous occurrence of the “bird-emissions” observed on 1 January 2015 at frequencies above ~4 kHz and the much stronger hiss-like emissions at the frequency less 4 kHz, is given in Fig. 6.

It is seen that the “bird-emissions” frequency increased with time, supporting the shift of the wave source location to the lower L-shells. However, the hiss-like signals’ frequency did not change in the same way. We could conclude that they were from different origins.

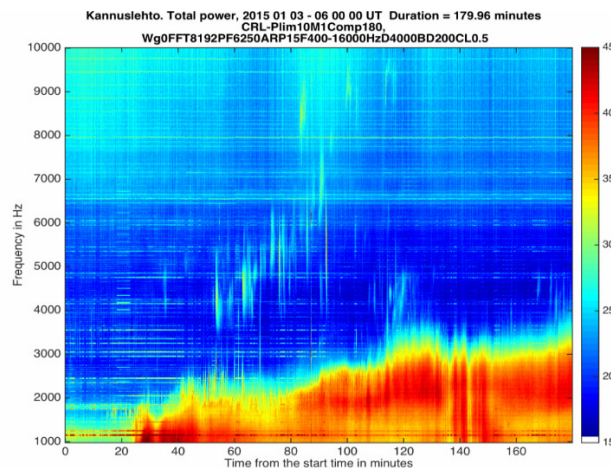


Fig. 6. The example of the 3-hours spectrogram with simultaneous occurrence of the “bird-emissions” and the hiss-like emissions.

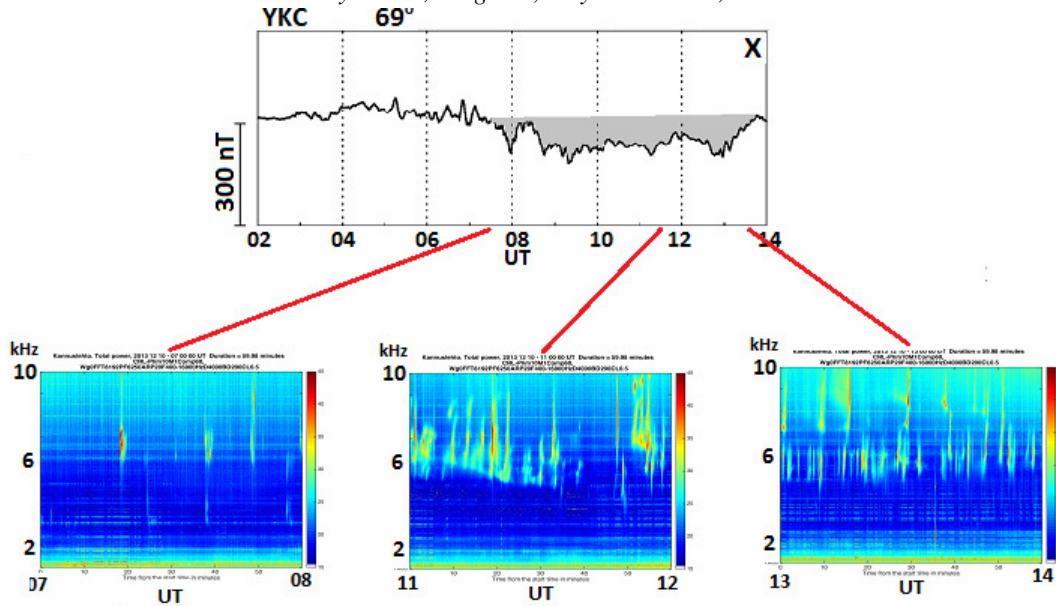


Fig. 7. The example (December 13, 2013) of night high-latitude magnetic substorm observed at YKC station (MLT = UT-8 hours) during the “bird emissions” recorded at KAN (MLT = UT+3 hours).

We note that the “bird-emissions” are typically observed during the daytime, when the dayside geomagnetic activity under non-disturbed space weather is usually small (there were no magnetic disturbances at the Scandinavian IMAGE meridian). However, in the night sector, at high-latitudes of the auroral zone, minor magnetic substorms are frequently recorded (Fig. 7), which provide an injection of energetic charged particles into the magnetosphere.

Discussion

The VLF whistler-mode waves are generated by a cyclotron instability of radiation belt energetic particles in the inner magnetosphere [Trakhtengerts V.Y. and M.J. Rycroft, 2008]. The frequency of excited waves is controlled by the equatorial electron gyrofrequency f_{ce} , which is proportional to the local magnetic field strength. Thus, the emission frequency shift, presented in Fig. 3, indicates the special dynamics of the magnetosphere location of the wave generation source.

The waves, generating near the magnetic equator, are guided to the ionosphere by magnetic field aligned enhancements of electron density [Carpenter D.L., 1968]. The ducted VLF emissions reaching the ionosphere have an upper cut-off frequency at half the equatorial electron gyrofrequency f_{ce} , that is the maximum frequency which can propagate in a duct [Carpenter D.L., 1968].

The f_{ce} value at magnetic field line corresponding to the KAN location ($L \sim 5.5$) is ~ 5 kHz. Thus, the wave propagated roughly along the KAN magnetic field line, can reach the ground only at $f \leq 2.5$ kHz. Such waves are seen as strong hiss-like emissions in the bottom part of the spectrograms in Fig. 6. Thus, the “bird-emissions”, observed in KAN at frequencies above 4–6 kHz, should be generated at lower L-shells where the equatorial electron gyrofrequency f_{ce} is higher than 5.5 kHz.

However, it is not clear how these waves propagate in the magnetosphere and how they can occur above the ionosphere at $L \sim 5.5$ with small wave normal angles to the local geomagnetic field direction (which is a condition for the wave penetrating through the daytime ionosphere to be recorded on the ground [Bespalov P. A., V. G. Mizonova, 2004]).

Summary

Based on the VLF observations in Northern Finland at Kannuslehto (KAN, $L \sim 5.5$, where $f_{ce} \sim 5.5$ kHz), we revealed new and totally unexpected natural VLF electromagnetic emissions at frequencies higher than 4 kHz, i.e. well above $f_{ce}/2$ at $L \sim 5.5$.

These emissions are observed as right-hand polarized waves lasting for several hours in the daytime and containing short ($\sim 1-3$ min) burst-like structures.

The low solar wind and geomagnetic activity ($V_{SW} < 400-500$ km/s, $N_p < 5-8$ cm⁻³, $AE < 150-200$ nT) are the favourable conditions for the VLF wave generation and propagation. These emissions appear after moderate geomagnetic disturbances or in the late recovery phase of geomagnetic storms.

We suppose that these emissions are generated deep in the magnetosphere via an electron-cyclotron instability at much lower L -values than KAN ($L \sim 5.5$). A small substorm developing in the night sector could be a source of the electrons injected into the magnetosphere from the magnetotail and trapped into the Earth’s radiation belts.

However, the details of the mechanism of the generation and propagation of these newly discovered VLF emissions remain unknown.

Acknowledgements

The research was supported by the Academy of Finland (grant no. 287988 for N.K. and L.G.), and the University of Oulu (grant for M.R.). We are grateful to the technical staff of SGO for their valuable assistance in organising the field campaigns. The work of N.K. was partly supported by the Program No 9 and No 15 of the Presidium of the Russian Academy of Sciences (RAS).

References

- Bespalov, P. A. and V. G. Mizonova (2004). Reflection coefficient of whistler mode waves normally incident on the ionosphere. *Geomagn. Aeron.*, 44, no. 1, 49–53.
- Carpenter, D.L. (1968). Ducted whistler-mode propagation in the magnetosphere: A half-gyrofrequency upper intensity cut-off and some associated wave growth phenomena, *J. Geophys. Res.*, 73, 2919–2928.
- Helliwell, R.A. (1965). Whistler and related ionospheric phenomena. –Stanford: Stanford Univ. Press.
- Manninen, J., T. Turunen, N. Kleimenova, M. Rycroft, L. Gromova, and I. Sirviö (2016). Unusually high frequency natural VLF radio emissions observed during daytime in Northern Finland. *Environ. Res. Lett.*, 11, 124006, doi:10.1088/1748-9326/11/12/124006
- Manninen, J., T. Turunen, N. G. Kleimenova, L. I. Gromova, and A. E. Kozlovsky (2017). A new type of daytime high-frequency VLF emissions at auroral latitudes (“Bird emissions”). *Geomagn. Aeron.*, 57, no. 1, 32–39.
- Trakhtengerts, V.Y., and M.J. Rycroft (2008). Whistler and Alfvén Mode Cyclotron Masers in Space. – Cambridge, U.K.: Cambridge Univ. Press.

The Large-Scale Ionosphere TEC Disturbances before Two Power Chilean Earthquakes

L.M. Ishkova, Yu.Ya Ruzhin, I.N. Bershadskaya

Pushkov Institute of Terrestrial Magnetism, Ionosphere and
Radio Wave Propagation of Russian Academy of Sciences
Moscow, Troitsk, Russia
E-mail: ishkova@izmiran.ru

Abstract

The analysis results of the large-scale space-time variations of total electron content of the South American ionosphere before two powerful Chilean earthquakes on February 27, 2010 (M=8.8) and on April 1, 2014 (M=8.2), according to GPS network station data, are presented.

It was studied the development in quite geomagnetic conditions of anomalous daily TEC disturbances (δ TEC) in extended ionosphere regions. It was concluded that the reaction of the South American ionosphere to seismic processes in the Andes seismic zone was similar at these periods. The correspondence of δ TEC variations to space-time picture of seismic activity in the Andes seismic zone was noted.

Introduction

The ionospheric phenomena associated with seismic activity have been discussed for over 30 years. These include the studies of electromagnetic phenomena that were observed before and after powerful earthquakes, and work to detect ionospheric precursors of earthquakes [Warwick *et al.*, 1982; Oraevsky *et al.*, 1994, Ruzhin, Depueva, 1996; Hayakawa *M.*, 1999].

New opportunities in studying the space-time characteristics of the ionosphere modification before earthquakes are provided by the use of the Global Positioning System (GPS) [Ruzhin *et al.*, 2000a, b; 2002; Liu *et al.*, 2004; Zakharenkova *et al.*, 2006; Ruzhin *et al.*, 2016]. The analysis of GPS observations showed that variations of the ionosphere total electron content (TEC) are very sensitive to changes in the F2-layer electron concentration and can be effectively used to detect ionospheric earthquake precursors. The correlation coefficient between TEC and foF2 reaches a value of 0.9. Since the electron concentration at the F2-layer maximum is one of the ionospheric parameters most sensitive to seismic activity, we can use TEC data to estimate spatial scales and temporal dynamics of seismoionospheric effects practically in any seismic active region of the world.

In 2000, precursors in the TEC parameter of the ionosphere were detected [Ruzhin *et al.*, 2000a, b; 2002b] for 2 earthquakes: the first with magnitude $M = 7.8$ occurred on August 17, 1999 near Izmit (Turkey) and the second with magnitude 7.5 on November 12, 1999 at a small distance (less than 100 Km) from the epicenter of the first earthquake.

The Figure 1 shows the variations of TEC for 5 days for each of them. One can clearly see the repeatability: in each case, a positive anomaly of the PES lasting almost 20 hours appears for 2 days and the subsequent negative, almost a day before the earthquake.

Thus, for the first time the identity for the same place of anomalies of TEC precursors (both in time and in the amplitude of the variations: 4-5 TECU) was shown for the first two earthquakes (the magnitude of each ST is more than 7.0, the same fault, the same season) and found a repetition of their morphology, which is a sign of the locality of their manifestation. These events, according to the data of the European GPS network, then were studied in detail by [Zakharenkova *et al.*, 2006].

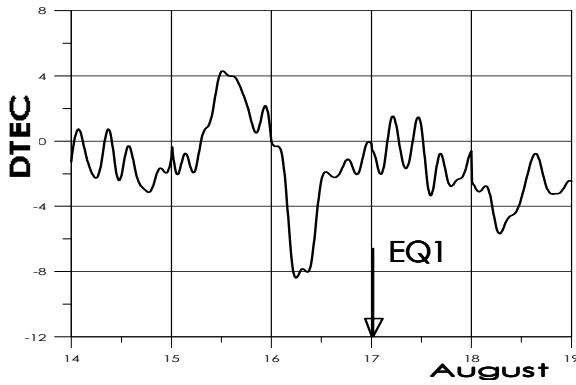


Fig. 1.a. Turkey, 17.08.1999, $M=7.8$. The Izmit earthquake occurred at 00:01:39 UT (3:01 a.m. local time), and was centred at 40.702 N., 29.987 E., which places the epicentre about 11 kilometres South-East of the Izmit.

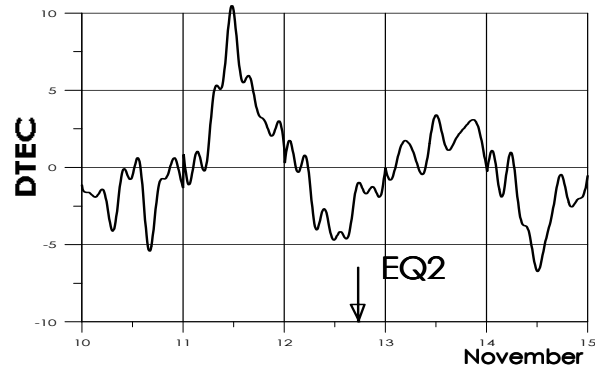


Fig. 1.b. Turkey, 12.11.1999, $M=7.5$. The second earthquake (EQ2) with magnitude of 7.5 occurred at November 12, 1999 (16:57:19 UT) on the short distance (less of 100km) from EQ1 epicentre and was centred at 40.8N, 31.2E.

Initial data

The character of daily TEC variations was analyzed in the periods February 17-27, 2010 and March 25-April 3, 2014 in relation to the corresponding ten-day medians (δTEC values, %; local time interval $\Delta t = 2$ hours) in the longitude sector $-30^\circ \div -105^\circ$ ($\Delta\lambda = 15^\circ$) and in the latitude range $20^\circ \div -60^\circ$ ($\Delta\phi = 5^\circ$).

The second half of February 2010 was characterized by a number of earthquakes of moderate intensity in the Andes seismic zone, including in the Chilean earthquake epicenter area. Particularly intensive foreshock activity was noted in the preparation area of the earthquake with $M = 6.3$, which occurred on February 27 (15:45UT, $\phi=24.87^\circ$ S, $\lambda=65.60^\circ$ W) in 1300 km to the north of the Chilean earthquake epicenter several hours after its main impact.

In the third decade of March 2014, on the eve of the powerful Chilean earthquake, there was an intense foreshock activity, including with magnitudes $M \geq 5.0$, practically at the epicenter of the main impact. In addition, there have been seismic events along the Andes seismic zone.

Table 1 provides the information on the parameters of the Chilean earthquakes, as well as the information on some events in the Andes seismic zone on February 2010 and on March-April 2014 to illustrate the results presented below in Figures 2-7.

Table 1. The Andes seismic activity on February, 2010 and on March-April, 2014.

| Дата | Время, UT | $\phi, ^\circ$ | $\lambda, ^\circ$ | h, км | Магнитуда |
|-------------------|--------------|----------------|-------------------|-----------|------------|
| 23.02.2010 | 15:16 | 15.9 | -91.2 | 10 | 5.6 |
| 25.02.2010 | 03:15 | 11.1 | -86.1 | 24 | 5.7 |
| 27.02.2010 | 06:34 | -36.1 | -72.9 | 22 | 8.8 |
| 27.02.2010 | 15:45 | -24.8 | -65.6 | 10 | 6.3 |
| 27.02.2010 | 19:54 | 10.8 | -43.4 | 10 | 5.8 |
| 28.02.2010 | 10:26 | -1.1 | -80.3 | 35 | 5.2 |
| 27.03.2014 | 23:50 | -29.1 | -68.7 | 10 | 5.7 |
| 28.03.2014 | 14:36 | 11.6 | -86.5 | 46 | 5.6 |
| 01.04.2014 | 23:46 | -19.6 | -70.7 | 25 | 8.2 |
| 02.04.2014 | 16:13 | 7.9 | -82.3 | 25 | 6.0 |

Analysis results

Analysis of spatial distribution of the maximum daily δTEC values (max δTEC , %) in a given latitude-longitude grid for each day of the periods considered made it possible to conclude that the reaction of the South American ionosphere to preparation processes of the Chilean earthquakes at these periods was similar.

The correspondence of δTEC variations to the space-time picture of seismic activity in the Andes seismic zone was noted.

The characteristic features of anomalous TEC perturbations before the Chilean events were the development of strong positive disturbances relative to the median level (from 30 to 50-60% and higher) at distances up to several thousand kilometers a few days before the main shocks and in change of positive phase by negative phase for 3-4 days before the main shocks. It is not contradict with the radii of the earthquake preparation zones (with magnitudes 8.8 and 8.2) in accordance with the Dobrovolsky formula [*Dobrovolsky et al.*, 1979; *Ruzhin, Depueva*, 1996] could reach 6600 and 3600 km, respectively.

The space-time scales of TEC anomalous ionosphere disturbances at both periods were different on different days, at different latitudes and longitudes. In general, the maximum characteristics of positive disturbances (δTEC values, their duration in daily course and spatial scales) are higher than similar characteristics of negative TEC disturbances. The maximum durations of positive disturbances, up to 5-8 hours at night and morning hours, were noted at latitudes from -20° to -30° on March 27, 2014. The duration of TEC negative disturbances was within 1-3 hours.

The strongest positive ionosphere TEC disturbances in the periods considered were on March 27, 2014. Table 2 gives information about positive TEC disturbances (δTEC values and their duration, in hours, in the daily course) on March 27, 2014 in the latitude range from -10° to -40° . As can be seen from Table 2 and Figure 3, especially large TEC disturbances took place in the latitude range from -20° to -30° .

Figures 2-7 show the spatial distributions of maximum daily δTEC , % values in the South American region on February 22, 2010 and March 03, 2014; February 24, 2010 and March 30, 2014; February 27, 2010 and April 1, 2014. These figures characterize the phases of positive TEC disturbances, the transition to the phases of negative perturbations and disturbances on the days of the main shocks in the periods considered, respectively.

Table 2. Maximum daily δTEC , % on March 27, 2014.

| φ° | March 27, 2014 | | | | | | |
|-----------------|-----------------|--------------|-------------|--------------------|--------------|--------------------|--------------------|
| | λ° | -105° | -90° | -75° | -60° | -45° | -30° |
| -10 | | 25.0 | 15.7 | ≤ 1 h 36.1 | 3 h 54.6 | 2 h 63.1 | 18.8 |
| -15 | | 3 h 45.7 | 4 h 42.3 | 2 h 62.3 | 4 h 70.3 | 2 h 52.2 | 29.2 |
| -20 | | 5 h 60.9 | 6 h 72.2 | 5 h 83.2 | 5 h 106.8 | 3 h 55.1 | ≥ 3 h 53.6 |
| -25 | | 5 h 60.8 | 6 h 84.6 | 7 h 81.0 | 6 h 111.0 | 5 h 59.8 | ≥ 2 h 70.3 |
| -30 | | 4 h 56.1 | 4 h 69.2 | 8h 72.6 | 3 h 67.6 | ≤ 1 h 39.1 | ≥ 2 h 65.3 |
| -35 | | 3 h 53.9 | 4 h 43.6 | 2 h 60.3 | 3 h 60.3 | 1 h 38.9 | 29.5 |
| -40 | | 3 h 48.5 | 3 h 45.6 | 1 h 49.6 | 2 h 78.2 | 3 h 36.2 | 28.0 |

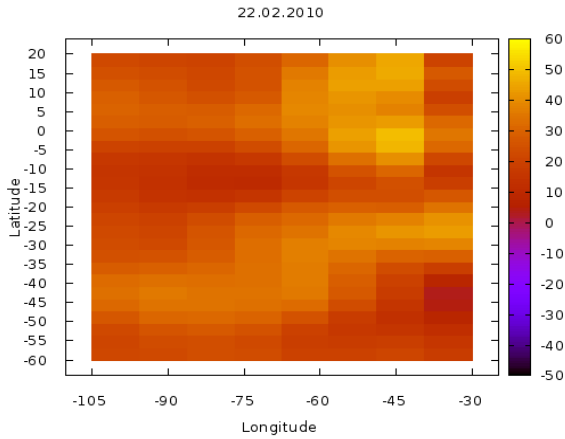


Fig. 2. February 22, 2010. Maximum $\delta\text{TEC}=54.7\%$ (04LT, $\varphi=0^\circ$, $\lambda=-45^\circ$).

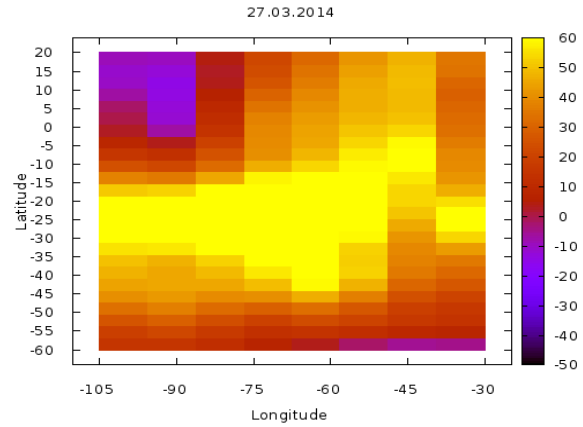


Fig. 3. March 27, 2014. Maximum $\delta\text{TEC}=111.0\%$ (03LT, $\varphi=-25^\circ$, $\lambda=-60^\circ$).

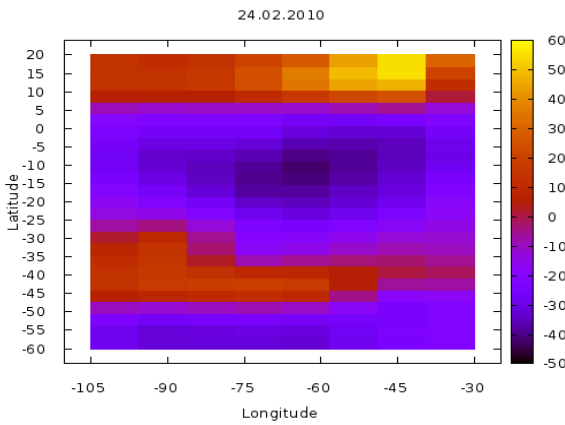


Fig. 4. February 24, 2010. Maximum $\delta\text{TEC}=59.2\%$ (22LT, $\varphi=15^\circ$, $\lambda=-45^\circ$) and $\delta\text{TEC}=-46.2\%$ (03LT, $\varphi=-10^\circ$, $\lambda=-60^\circ$).

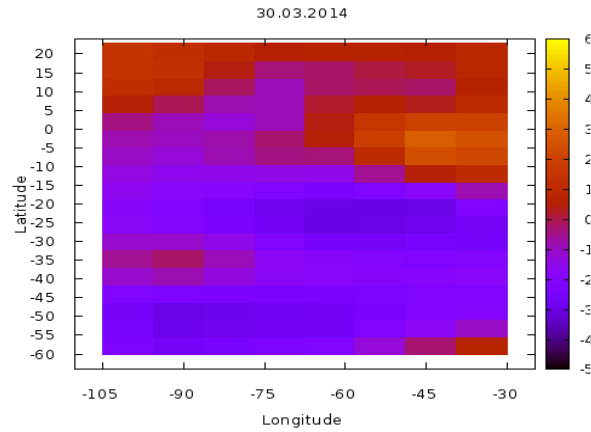


Fig. 5. March 30, 2014. Maximum $\delta\text{TEC}=31.8\%$ (22LT, $\varphi=0^\circ$, $\lambda=-45^\circ$) and $\delta\text{TEC}=-36.2\%$ (02LT, $\varphi=-20^\circ$, $\lambda=-45^\circ$).

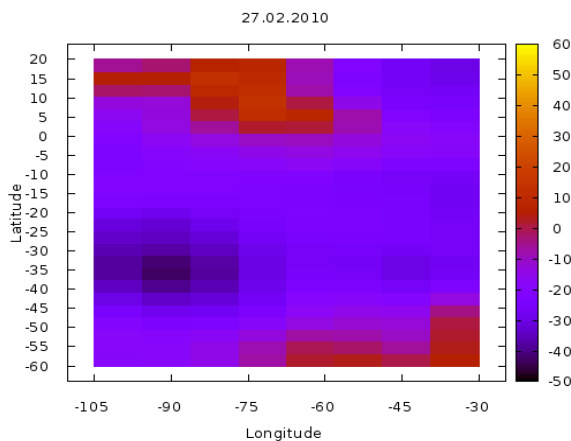


Fig. 6. February 27, 2010. Maximum $\delta\text{TEC}=-46.9\%$ (01LT, $\varphi=-35^\circ$, $\lambda=-90^\circ$).

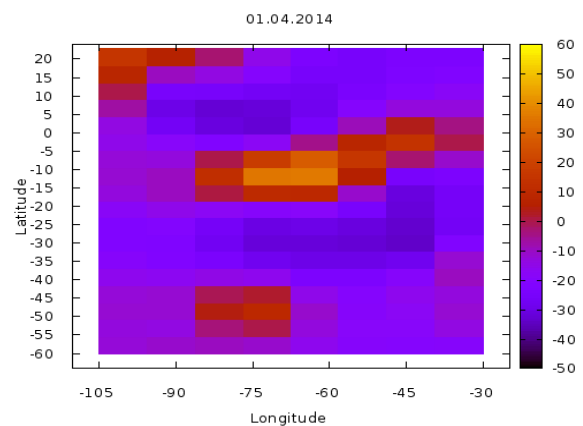


Fig. 7. April 1, 2014. Maximum $\delta\text{TEC}=58.0\%$ (20LT, $\varphi=-10^\circ$, $\lambda=-75^\circ$) and $\delta\text{TEC}=-35.2\%$ (02LT, $\varphi=-30^\circ$, $\lambda=-45^\circ$).

The following results are obtained of estimates of TEC disturbance spatial scales (with $|\delta\text{TEC}| \geq 30\%$).

The maximum extents of ionosphere regions with positive TEC disturbances on February 22, 2010 were 4500 km at latitude -25° and 2700 km along the meridian -60° in the range of latitudes from -20° to -45° . The lengths of ionosphere with negative TEC disturbances on February 27, 2010 were respectively 2800 km at latitude -30° and 2200 km along the meridian -90° .

On March 27, 2014 the extents of ionosphere regions with positive TEC disturbances reached 7800 km at latitude -20° and 6600 km along the meridian -45° in the range of latitudes from 20° to -40° . It is important to note that the maximum daily values of δTEC along the meridian -45° in this region of latitudes were observed at the same local time - 4LT (7UT). The maximum positive diurnal values of δTEC at 7UT occurred also along the meridian -60° (03LT) in the latitude range from 20° to -30° . The length of these disturbances along the meridian -60° was 5500 km.

The lengths of regions with negative TEC disturbances on April 1, 2014 were 3000 km at latitude -25° and 2200 km along the meridian -45° .

High values and long duration of positive TEC disturbances near the epicenter area on the eve of the Chilean earthquake on April 1, 2014 were caused by intensive foreshock activity, including with magnitudes $M \geq 5.0$, practically at the epicenter of the main shock of this earthquake.

Conclusions

1. A conclusion was drawn about a similar pronounced character of the reaction of the South American ionosphere to seismic processes in the Andes seismic zone on the eve of powerful earthquakes on February 27, 2010 and April 1, 2014.
2. The characteristic features of the anomalous TEC disturbances of the ionosphere on the eve of both earthquakes consisted in the development of strong positive disturbances from 30 to 50-60% and higher relative to the median level at distances up to several thousand kilometers a few days before the main shock and in the change of the positive phase of TEC disturbances by the negative phase in 3-4 days before the main shock.
3. The correspondence of character of δTEC variations to the space-time pattern of seismic activity along the Andes seismic zone in the periods considered is noted.
4. The use of GPS data with sufficient space-time resolution made it possible to investigate in detail the space-time dynamics of development of anomalous TEC disturbances in the extended regions of the South American ionosphere.

References

- Dobrovolsky I.R., Zubkov S.I., Myachkin V.I. (1979). Estimation of the size of earthquake preparation zones. *Pageoph.*, 117, 1025-1044.
- Hayakawa M. (Eds.). (1999). *Atmospheric and Ionospheric Electromagnetic Phenomena Associated with Earthquakes*. Terra Scientific Publishing Company, Tokyo, Japan, 996 p.
- Liu J.Y., Chuo Y.J., Shan S.J., Tsai Y.B., Chen Y.I., Pulinets S.A., Yu S.B. (2004). Pre-earthquake ionospheric anomalies registered by continuous GPS TEC measurement. *Annales Geophysicae*, 22, 1585-1593.
- Oraevsky V.N., Ruzhin Yu.Ya., Depueva A.Kh. (1994). Seismo-ionospheric precursors and atmospheric electricity. *Turk. J. of Phys.*, 18, no. 11, 1229-1234.
- Ruzhin Yu.Ya., Depueva A.Kh. (1996). Seismoprecursors in space as plasma and wave anomalies. *J. Atm. Electricity*, 16, no. 3, 271-288.
- Ruzhin Yu.Ya., Oraevsky V.N., Shagimuratov I.I. (2000a). Comparison of Ionosphere TEC above the Turkey during Solar Eclipse action and before two strong Earthquakes at 1999. *Proc. 10th Intern. Symposium on Equatorial Aeronomy, Antalya, Turkey*, P9-8, 4 p.
- Ruzhin Yu.Ya., Oraevsky V.N., Shagimuratov I.I. (2000b). Anomalies of Ionospheric TEC above the Turkey before two strong Earthquakes at 1999. *Proc. 15th Wroclaw EMC Symposium*, 508–512.
- Ruzhin, Yu.Ya., Oraevsky V.N., Shagimuratov I.I. and Sinelnikov V.M. (2002). Ionospheric precursors of earthquakes revealed from GPS data and their connection with “sea-land” boundary. *Proc. 16th Wroclaw EMC Symposium*, 723-726.
- Ruzhin Yu.Ya., Smirnov V.M. Pulsed TEC during 20 minutes before the Chile earthquake. (2016). *Handbook: The 2nd International Workshop of CSES Mission, Beijing, China*, 26-30.
- Zakharenkova I.E., Shagimuratov I.I., Krankowski A. et al. (2006). Ionospheric precursors observed during the Mediterranean region earthquakes. *Proc. 18th International Wroclaw Symposium and Exhibition on Electromagnetic Compatibility*, 85–90.
- Warwick J. W., C. Stoker, and T. R. Meyer. (1982). Radio emission associated with rock fracture: possible application to the great Chilean Earthquake of May 22, 1960. *J. Geoph. Res.*, 87, no. 4, 2851–2859.

Role of the IMF $|B_z|/|B_y|$ in the appearance of the daytime high-latitude magnetic bays

*L.I. Gromova*¹, *S.V. Gromov*¹, *N.G. Kleimenova*², *L.A. Dremukhina*¹

¹ Pushkov Institute of Terrestrial Magnetism, Ionosphere, and Radio wave Propagation RAS,

² Schmidt Institute of the Physics of the Earth RAS, Moscow, Russia

E-mail: gromova@yandex.ru

Abstract

Solar wind-magnetosphere interaction manifests in different geomagnetic disturbances. We study several dayside magnetic bays observed at the IMAGE high-latitude stations in the post-noon sector under different IMF $|B_z|/|B_y|$ and IMF orientation. We found that when IMF $|B_z|/|B_y| < 1$, i.e. the IMF B_y magnitude dominated over the IMF B_z , the positive or negative magnetic bays appeared correspondingly to the IMF B_y sign both for northward and southward IMF B_z . Thus, the IMF B_y sign controlled the direction of the appropriate ionospheric current. We showed that under the positive IMF B_y the dawn convection vortex expanded to the afternoon sector, and the dusk convection vortex expanded to the pre-noon sector under the negative IMF B_y . The high-latitude field-aligned currents (FACs) related to the ionospheric convection should increase in the near-noon sector that leads to an enhancement of the corresponding high-latitude ionospheric currents. Contrary to that, when the IMF B_z was more intensive than the IMF B_y , i.e. $|B_z|/|B_y| > 1$, the appearance of negative or positive dayside bays did not depend on the IMF B_y sign and more often controlled the IMF B_z sign. Such dayside bays could be mapped into the poleward expanding area of the ionospheric convection and upward FACs. We conclude that geomagnetic IMF effects in the dayside polar sector significantly depend on the IMF $|B_z|/|B_y|$ ratio.

Introduction

As it is well known, under a positive B_z component of the Interplanetary Magnetic Field (IMF), there is no new energy input into the magnetosphere, however, in the polar regions dayside bay-like magnetic disturbances could occur associating with the high-latitude ionospheric electric currents [e.g., *Iwasaki*, 1971; *Friis-Christensen and Wilhjem*, 1975; *Feldstein*, 1976, *Feldstein et al.*, 2006]. We call such magnetic disturbances “dayside polar substorms”. Previously we found such magnetic disturbances during several magnetic storms [e.g., *Kleimenova et al.*, 2015; *Gromova et al.* 2017].

The controlling role of the ratio of IMF B_z and B_y components in the dynamics of the high latitude geomagnetic and ionospheric disturbances has been demonstrated previously basing on the satellite and ground-based data, but mainly with a dominant IMF B_y component [e.g. *Friis-Christensen et al.*, 1985; *Zhou et al.*, 2000; *Vennerstrom et al.*, 2002 and some others].

The aim of our study is to show the role of the ratio of IMF B_z and B_y components in the dayside magnetic bay signature under the different IMF orientation. We analysed the ground-based observations from Scandinavian IMAGE magnetometer chain.

Observations

Data

Our study is based on

- 1) the ground-based IMAGE magnetometer data (<http://www.ava.fmi.fi/MIRACLE>),
- 2) IMF data sets of the 1-min resolution OMNI database (<http://omniweb.gsfc.nasa.gov>),
- 3) the AMPERE data based on the magnetic measurements on 66 low-altitude globally distributed Iridium communication satellites (<http://ampere.jhuapl.edu/products/plots>).
- 4) the maps of the ionospheric convection pattern from SuperDARN (<http://vt.superdarn.org>).

Events under $|B_z| < |B_y|$

Figure 1(a,b) presents the IMF B_z and B_y components and difference magnetograms constructed on the base of magnetic data of the high-latitude stations of Scandinavian magnetometer chain IMAGE (MLT = UT +3 h) for events of 4 August 2010 (Fig. 1a) and 22 January 2015 (Fig 1b). The both of the events were observed when the IMF B_y magnitude dominated over the IMF B_z ($|B_z|/|B_y| < 1$) but the IMF orientation was different. It is seen that the positive (yellow) or negative (blue) magnetic bays were observed at the IMAGE high-latitude stations in the post-noon sector. The bay sign was controlled by the IMF B_y sign, both for northward and southward IMF B_z .

Event under $|B_z| > |B_y|$

The event of 23 June 2015 (Fig. 1c) occurred when the IMF B_z was more intensive than the IMF B_y , ($|B_z|/|B_y| > 1$). As it is shown in Fig.1c, the strong long-duration negative magnetic bay was observed in the dayside sector of the polar latitudes and its sign was controlled the IMF B_z sign.

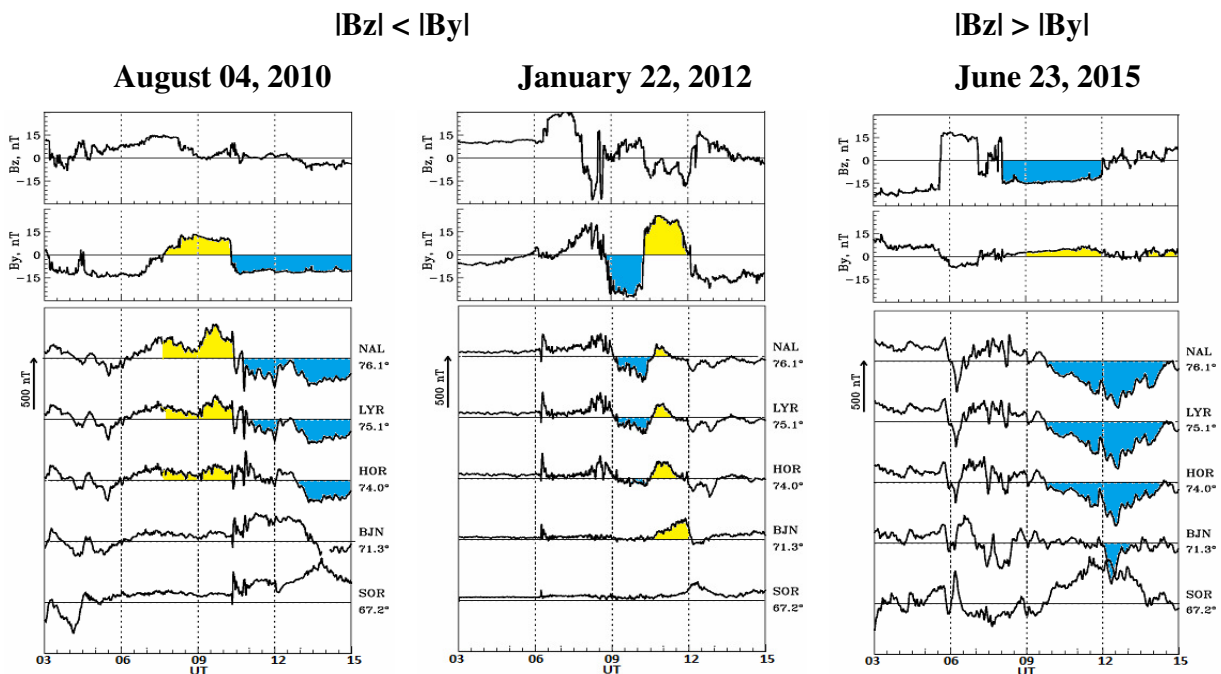


Fig. 1. The IMF B_z and B_y and IMAGE difference magnetograms a) – August 04, 2010, b) – January 22, 2012, c) - June 23, 2015. Examined dayside magnetic bays are marked by yellow/blue depending on IMF B_y or B_z component.

Discussion

Ionospheric and field-aligned currents and convection under $|B_z| / |B_y| < 1$

Figure 2 and 3 present the IMF B_z and B_y and the distribution of the horizontal vectors of the geomagnetic field constructed from difference magnetograms of X and Y from the high-latitude IMAGE stations and AMPERE modeled plots under positive (near 09 UT) and negative (near 11 UT) IMF B_y on 4 August 2010, (Fig. 2) and under negative (near 09 UT) and positive (near 11 UT) IMF B_y on 22 January 2012 (Fig. 3).

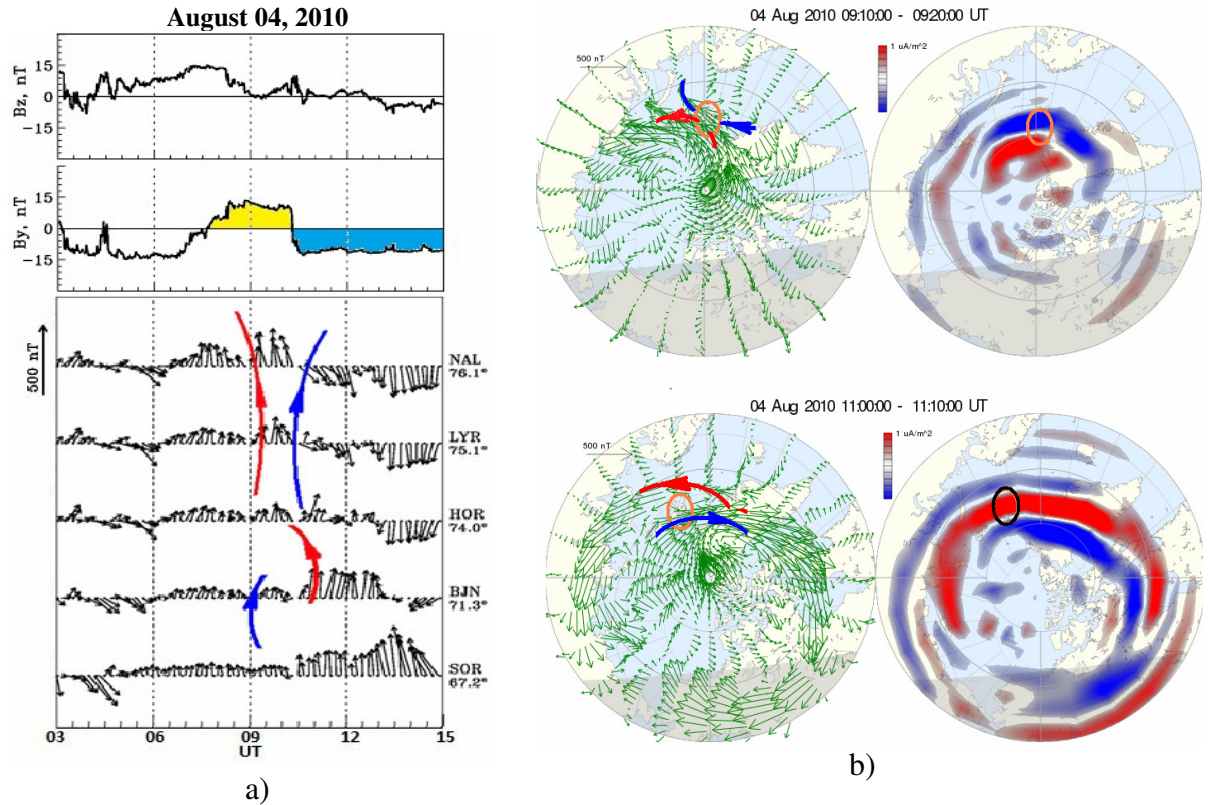


Fig.2. Event of August 4, 2010: a) - The IMF B_z and B_y and the horizontal vectors of the geomagnetic field; b) - The AMPERE data. Upward currents are shown in red and downward currents in blue. Circles show the location of the high latitude IMAGE stations.

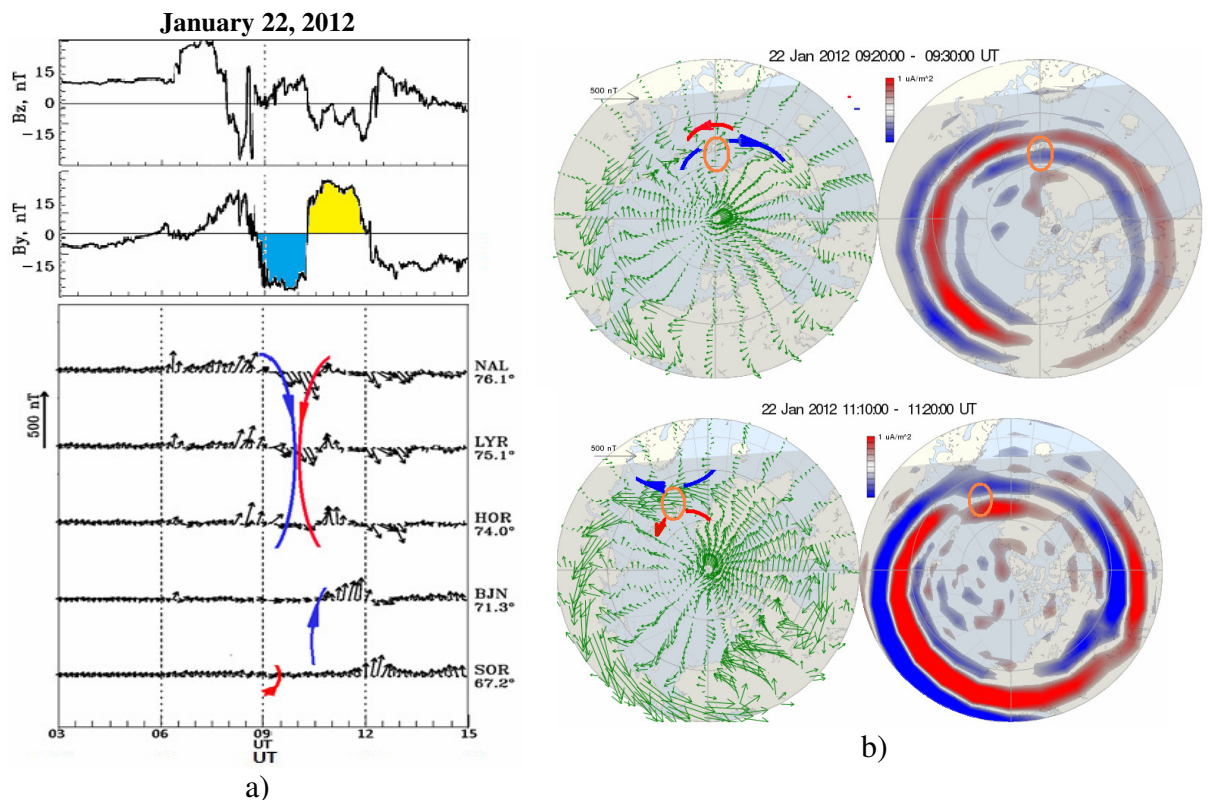


Fig.3. The same as in Fig. 2 but for the event of January 22, 2012

The horizontal vectors of the geomagnetic field (Fig 2a, Fig3a) were constructed from IMAGE magnetometer chain data on the base of so called difference magnetograms that represent the magnetic variations compared to the most magneto-quiet 2009 level [Levitin A.E. et al., 2014]. The AMPERE modeled plots (Fig. 2b, Fig 3b) based on the magnetic measurements on 66 low-altitude globally distributed Iridium communication satellites demonstrate spherical harmonic fit to the reduced magnetic field residual data showing the horizontal plane vector data of magnetic perturbation (left duals) and the radial current density (right duals).

The ground and AMPERE magnetic vectors demonstrate the *clockwise vortex* above the high latitude IMAGE stations and the *counter-clockwise* one above the lower latitude stations at 09 UT and opposite vortices around 11 UT on the 4 August, 2010. On 22 January 2012 the *counter-clockwise* vortex is seen above the high latitude IMAGE stations and the *clockwise* one above the lower latitude stations at 09 UT and opposite vortices around 11 UT. Accordingly to this, increasing of the downward and upward FACs caused the polar electrojets enhancement. The sequence of positive and negative bays occurred under the positive or negative IMF B_y be probably caused by the eastward or westward polar electrojets respectively.

The convection vortices for the both events are shown in Fig.4. It is seen that the dawn convection vortex expanded to the post-noon sector (under IMF $B_y > 0$), and the dusk convection vortex expanded to the pre-noon sector (under IMF $B_y < 0$). The related to the ionospheric convection high-latitude FACs of Region 1 increase in the near-noon sector that leads to an enhancement of the corresponding high-latitude ionospheric currents.

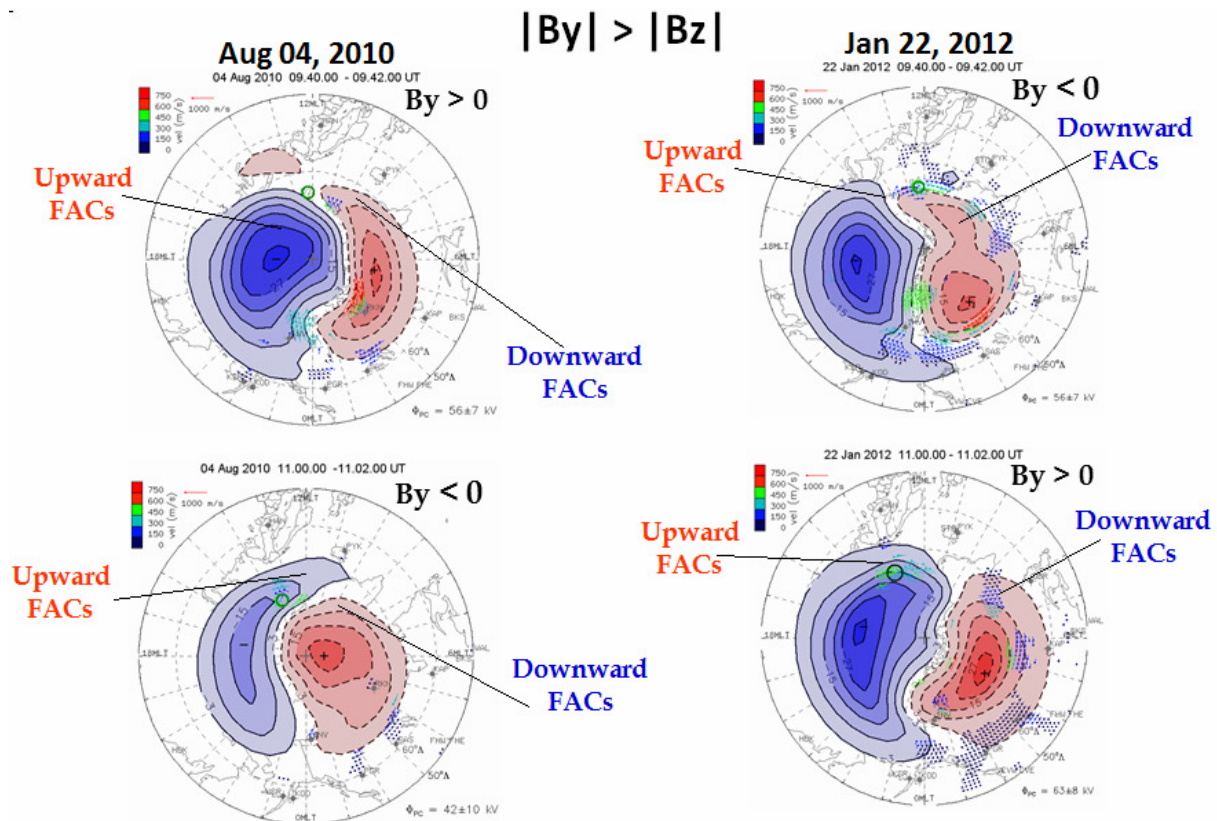


Fig. 4. The convection vortices above IMAGE stations. Circles show the location of the high latitude IMAGE stations.

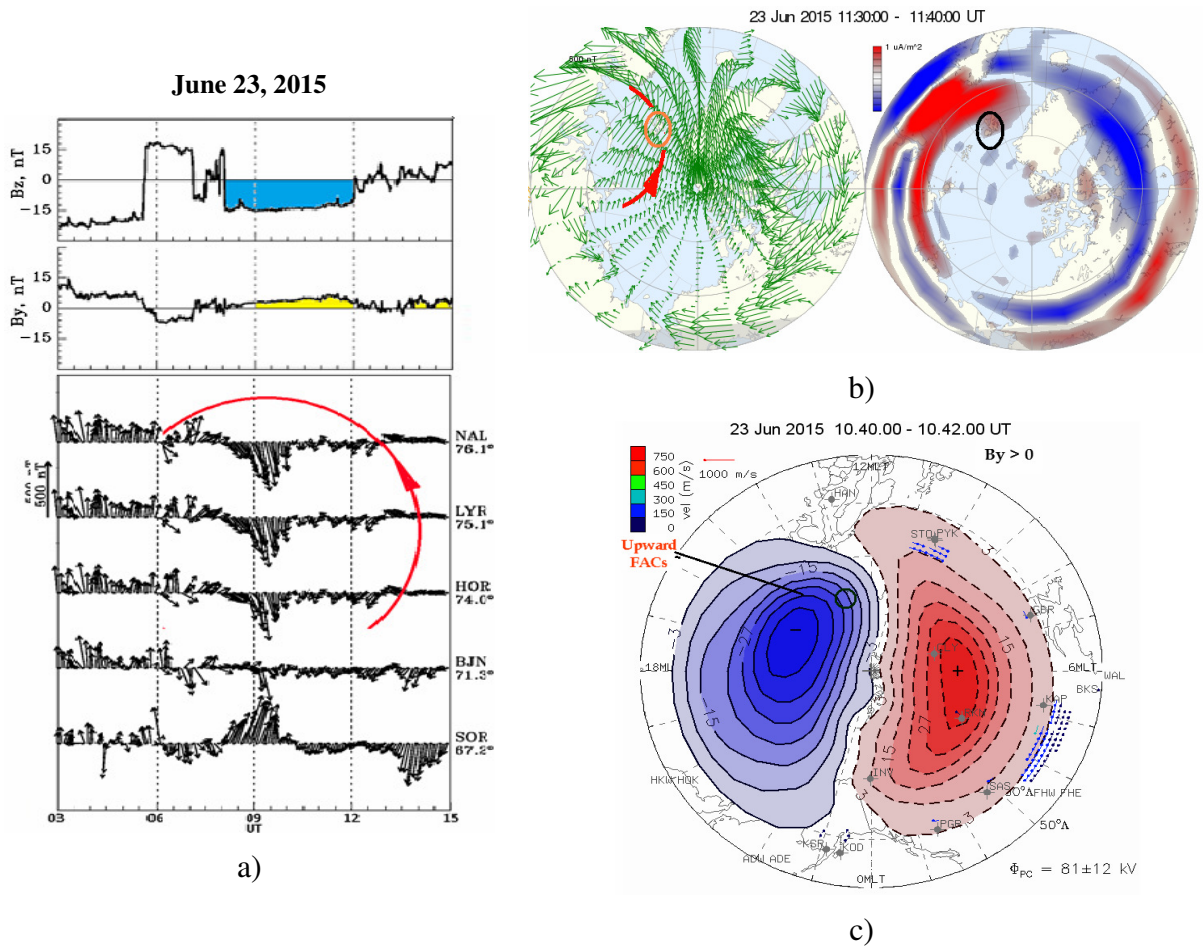


Fig. 5. The same as in Fig. 2 but on June 23, 2015

Thus, when the IMF B_y magnitude dominated over the IMF B_z ($|B_z|/|B_y| < 1$), the positive or negative magnetic bays appeared correspondingly to the IMF B_y sign both for northward and southward IMF B_z . In this way, the IMF B_y sign controlled the direction of the appropriate ionospheric current.

Ionospheric and field-aligned currents and convection under $|B_z|/|B_y| > 1$

Figure 5 presents the IMF B_z and B_y , the distribution of the horizontal vectors of the geomagnetic field (Fig. 5a), AMPERE modeled plots (Fig. 5a) and the convection maps (Fig. 5a) for events of 23 June 2015.

The ground magnetic vectors demonstrate the counter-clockwise magnetic vortex above high latitude IMAGE stations that corresponds to the upward FAC. The AMPERE model demonstrated very intensive upward FACs expanded poleward. It is supposed, that due to negative IMF B_z dominated over the IMF B_y , the intensification of the FACs of Region 1 in the polar latitudes produced the dayside negative magnetic bay.

Almost symmetrical morning and evening the convection vortices formed the westward ionosphere current in the post-noon sector that caused the negative bay intensification.

Thus, when the IMF B_z was more intensive than the IMF B_y , ($|B_z|/|B_y| > 1$), the appearance of negative or positive dayside bays did not depend on the IMF B_y sign and more often controlled the IMF B_z sign.

Summary

- We found that when the sign of dayside polar magnetic bays (i.e. the direction of the polar latitude ionospheric current) is controlled by the IMF Bz or IMF By depending on the ratio of the IMF $|B_z|/|B_y|$.
- We showed that if the IMF ($|B_z|/|B_y| > 1$, the sign of the dayside polar bays are more often controlled by the IMF Bz sign. Such dayside bays could be mapped into the poleward expanding area of the ionospheric convection and upward FACs.
- However, if the IMF ($|B_z|/|B_y| < 1$, the sign of the dayside polar bays are controlled by the IMF By sign.
- We showed that under the positive IMF By the dawn convection vortex expanded to the afternoon sector, and the dusk convection vortex expanded to the pre-noon sector under the negative IMF By. The high-latitude Region 1 FACs related to the ionospheric convection should increase in the near-noon sector that leads to an enhancement of the corresponding high-latitude ionospheric currents.

Acknowledgements

The work of N.K. was partly supported by the Program No 15 of the Presidium of the Russian Academy of Sciences (RAS).

References

- Feldstein, Y.I. (1976), Magnetic field variations in the polar region during magnetically quiet periods and interplanetary magnetic fields, *Space Sci. Rev.*, 18, no. 5/6, 777-861.
- Feldstein, Y.I., V.A Popov., J.A Cumnock., A.. Prigancova, L.G Blomberg, J.U. Kozyra, B.T. Tsurutani, L.I. Gromova, and A.E. Levitin (2006), Auroral electrojets and boundaries of plasma domains in the magnetosphere during magnetically disturbed intervals, *Ann. Geophys.*, 24, 2243-2276.
- Friis-Christensen, E., and , J. Wilhelm (1975), Polar cap currents for different directions of the interplanetary magnetic field in the Y-Z plane. *J. Geophys. Res.*, 80(10), 1248 – 1256.
- Friis-Christensen E., Y. Kamide, A.D. Richmond, and S. Matsushita (1985), Interplanetary magnetic field control of high-latitude electric fields and currents determined from Greenland magnetometer data. *J. Geophys. Res.*, 90(A2), 1325 – 1338.
- Gromova L.I., N.G. Kleimenova, A.E. Levitin, L.A. Dremukhina, E.E. Antonova, S.V. Gromov (2017), High-latitude daytime magnetic bays as effects of strong positive IMF Bz: case study. *Sun and Geosphere.V.12*, no 2, 125-131.
- Iwasaki, N. (1971), Localized abnormal geomagnetic disturbance near the geomagnetic pole and simultaneous ionospheric variation, *Rep. Ionos. Space Res. Japan.*, 25, 163-286
- Kleimenova, N.G., Gromova, L.I., Dremukhina, L.A., Levitin, A.E., Zelinskii, N.R., and Gromov, S.V. (2015), High_latitude geomagnetic effects of the main phase of the geomagnetic storm of November 24, 2001 with the northern direction of IMF, , *Geomagn. Aeron. (Engl. Transl.)*, 55, no 2,174–184.
- Levitin, A.E., Gromova, L.I., Gromov, S.V., and Dremukhina, L.A. (2014), Quantitative estimation of local geomagnetic activity relative to the level of the magnetically quiet period in 2009, *Geomagn. Aeron. (Engl. Transl.)*, 54, no 3, 292–299.
- Vennestrom S., T. Moretto, N. Olsen, E. Friis-Christensen, E. Stampe, and J. Watermann (2002), Field-aligned currents in the dayside cusp and polar cap region during northward IMF, *J. Geophys. Res.*, 107(A8), 1188-1193.
- X.-W. Zhou, C. T. Russell, and G. Le (2000), Local time and interplanetary magnetic field of field-aligned currents at high altitudes, *J. Geophys. Res.*, 105(A2), 2433-2539 – 1338.

Space weather effects in atmospheric electric field variations

N. G. Kleimenova¹, S. Michnowski², A. Odzimek², M. Kubicki²

¹ Schmidt Institute Physics of the Earth RAS, Moscow, Russia

² Institute of Geophysics PAS, Warsaw, Poland

E-mail: kleimen@ifz.ru

Abstract

The vertical atmospheric electric field (E_z) near the Earth surface under “fair” weather could represent the state of the global atmospheric electric circuit, which is controlled mainly by the world thunderstorm and shower clouds activity. However, magnetosphere–ionosphere disturbances could influence this state as well. Here we present our main results of the study of the E_z effects caused by geomagnetic storms and substorms representing an important factor of the space weather. Our results are based of the E_z observations at the high-latitude station Horsund (Spitsbergen) and mid-latitude station Swider (near Warsaw, Poland). For the first time, the effect of the magnetic storm, associated with the coronal mass ejections, was revealed in the mid-latitude atmospheric electricity as the strong daytime E_z negative anomalies in relation with night-side magnetosphere substorms. However, at the polar latitudes, the auroral magnetic substorms lead to the simultaneous E_z deviations which were positive in the local morning and negative in the evening according to the station location relatively to the “positive” or “negative” center of the ionosphere convection vortex. Moreover, it was found the relationship between the occurrence of the daytime E_z variations near the open/closed field line boundary and an enhancement of the region 1 field aligned currents (FAC). Thus, ground-based E_z recordings could be one of the very sensible tools to study solar wind-magnetosphere-ionosphere-atmosphere interactions.

Introduction

Atmospheric electricity is one of the important geophysical topics. More than one hundred years ago it was discovered that the atmospheric electric field exists near the Earth surface even in the absence of local thunderstorm activity. The concept of the global atmospheric electric circuit was formulated by [Wilson C.T.R. 1920]. The global circuit is formed between the surface of the Earth and the ionosphere, both of which are good electrical conductors in comparison with the weakly conducting atmosphere between them.

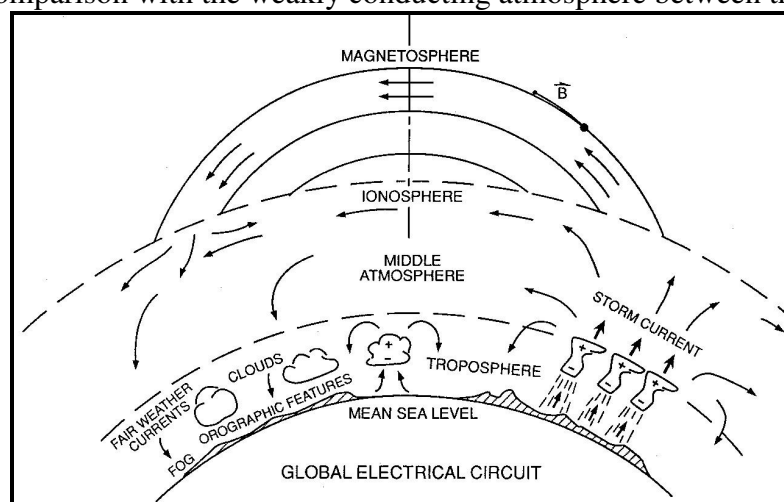


Fig.1. Schematic diagram of the Earth's global atmospheric electric circuit

The vertical atmospheric electric field (E_z) averaging ~ 100 V/m at the ground level represents the state of the global atmospheric electric circuit, which is controlled mainly by the world thunderstorm and other electrified clouds activity. Thunderstorms generate an electrical potential difference between the Earth's surface and the ionosphere, mainly by

means of the conduction current [Williams E.R. and S.J. Heckman, 1993]. Because of this, the ionosphere is positively charged relative to the Earth. The schematic diagram showing the general features of the Earth’s global circuit is presented in Fig. 1. Thunderstorm activity draws current upward from the ground. The ionosphere disperses the current globally, and it leaks back to the surface. In this manner, a variable potential averaging ~250 kV is maintained between the ionosphere and the Earth.

As the global atmospheric electric circuit is closed through the ionosphere, it can be affected by magnetospheric and ionospheric disturbances. It has been suggested and further discussed [e.g., Sao K., 1967; Olson D.E., 1971; Markson 1981; Bandilet O.I. et al. 1986; Apsen A.G. et al., 1988; Michnowski S., 1998; Tinsley, 2000; Frank-Kamenetsky A.V. et al., 2001; Nikiforova N.N. et al., 2003, 2005; Kleimenova N.G. et al., 1995, 1998, 2008, 2010, 2013, 2016, and many others] that solar influences due to the ionospheric electric field disturbances, energetic electron precipitation and cosmic ray flux which may affect the global electric circuit state. Recent overviews of the global atmospheric electric circuit and its coupling with the magnetosphere-ionosphere are presented by [Rycroft M.J. et al. 2000, 2008, Rycroft M.J. and Harrison R.G. 2011, Williams E. and Mareev E. 2014]. Despite being postulated very long ago, the global electric circuit is still poorly quantified.

The very important result has been obtained by the measurements of the atmospheric electric field in the air at the Atlantic, Indian, and Pacific oceans during four global cruises of the wooden non-magnetic vessel named “Carnegie” The daily average E_z variation calculated from measurements on “Carnegie” demonstrates a variation in universal time with a minimum around 03-04 UT and a maximum around 18-20 UT and is known as the Carnegie curve (Fig. 2). The variation is believed to originate from the regular daily variations in the world electrified cloud activity in the main centres in Asia, Africa, and America.

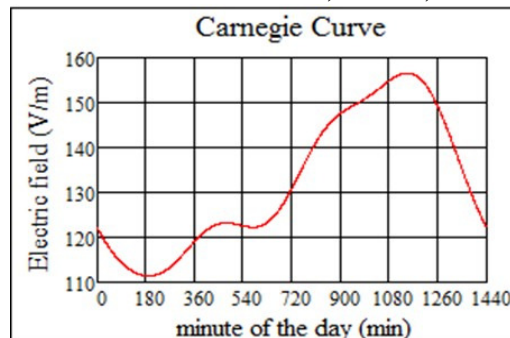


Fig. 2. The universal diurnal E_z variation - Carnegie curve

The aim of this paper is to show the effects in atmospheric electricity (E_z) caused by geomagnetic storms and substorms which represent an important factor of space weather. These effects could be different at the middle and auroral latitudes because the magnetic storm disturbances may even be manifested at middle latitudes and the substorm ones – at the auroral.

Observations and results

Our results are based on the data of the variations in the vertical component of the atmospheric electric field (E_z), observed at two ground-based points: the mid-latitude Polish Geophysical Observatory Swider located near Warsaw (SWI, corrected geomagnetic coordinates: $\Phi'=47.81^\circ$, $\Lambda'=96.81^\circ$) and the Polar Polish Station Hornsund located in Spitsbergen (HOR, corrected geomagnetic coordinates: $\Phi'=74.01^\circ$, $\Lambda'=110.51^\circ$). The recording equipment was described in detail by [Kubicki M. 2001], and the average diurnal variations of E_z at Swider and Hornsund are described in [Kubicki M. et al. 2016]. We call the E_z deviations positive if the E_z magnitude increases and negative ones if the E_z magnitude decreases.

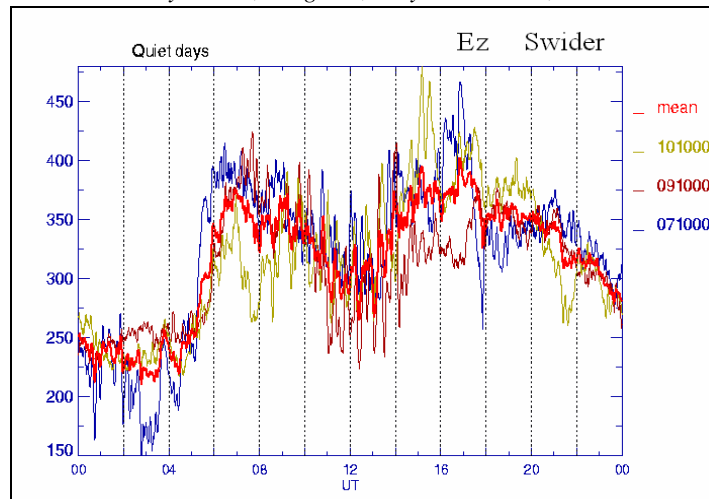


Fig. 3. E_z daily variations at Swider under quiet geomagnetic conditions.

To avoid meteorological influences on the records, we used E_z data, obtained only under so called “fair weather” conditions, which request the absence of a rain, snow, fog, lower clouds, and wind velocity more 6 m/s.

Middle latitudes

The daily average variations in E_z at Swider were calculated by analysing the 30 selected magnetically quiet days of the observations under the fair weather conditions in 1998-2002. The average curve of the E_z daily variations (red) and the initial data of three days in October 2000 are shown in Fig. 3a.

Since the largest magnetosphere and ionosphere disturbances are observed during the magnetic storm main phase, we can assume that some mid-latitude E_z effects could be observed exactly in this time. The analysis of E_z Swider data has been performed during 14 magnetic storms [Kleimenova N.G. et al., 2008, 2013]. To study magnetic storm effects, the E_z data were compared with the similar data in the nearest magnetically quiet time. The E_z effects of two magnetic storms (13-14 October 2000 and 23-24 May 2000) are shown in Fig. 4 where the Dst variations are given in the upper part of the graphics (Fig. 4a).

It is seen that the strongest storm-time E_z deviations (Fig. 4c), i.e. $E_z - E_z(\text{quiet})$, there were observed during the main phase (the lowest Dst values) of the magnetic storms. The distinguished daytime E_z negative anomalies (Fig. 4c) were found in association with night-side magnetic substorm onsets (CMO station, Fig. 4d) under any local magnetic activity (BEL and SOD stations, Fig. 4d).

Similar E_z effects were observed during all considered magnetic storms.

Thus, for the first time the effect of the magnetic storm main phase was established in the mid-latitude atmospheric electricity. We supposed that the considered E_z deviations could be associated with the interplanetary electric field penetration into the magnetosphere. Another plausible reason could be related to the common ionosphere conductivity increasing due to substorm energetic electron precipitation because the high-latitude ionosphere is an important part of the global atmospheric electric circuit.

Polar latitudes

We analysed the morning and evening E_z variations at Hornsund station, which were observed simultaneously with the substorms developing at lower, i.e. auroral, latitudes in Scandinavia [Kleimenova N.G. et al., 2010, 2013]. In that time, this station can be mapped within the auroral oval and in the region of its polar boundary, depending on the level of

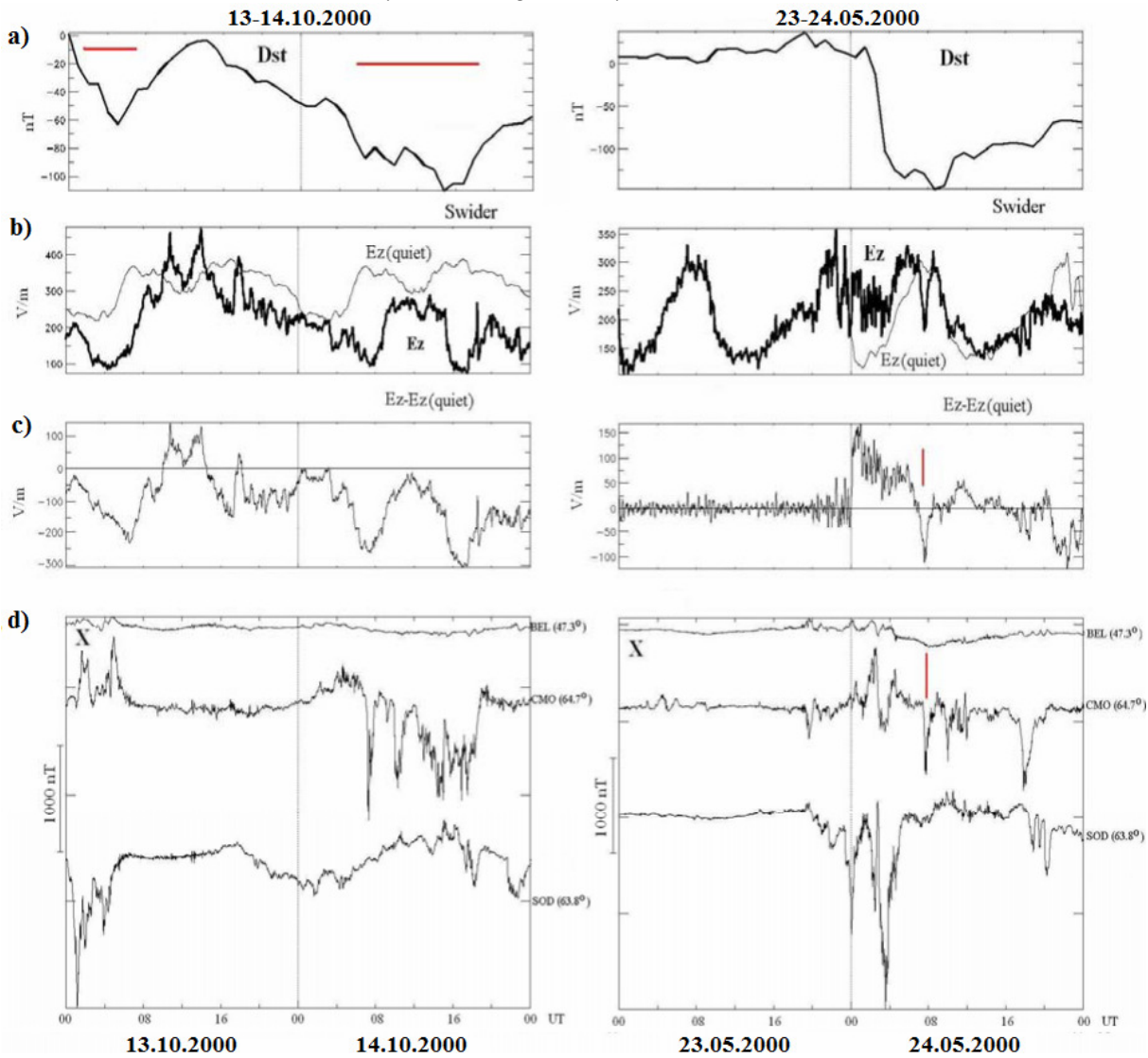


Fig. 4. a) Dst-variations; b) The storm-time E_z (thick curve) and the quiet-time E_z (thin curve); c) The calculated difference between these values; d) The magnetograms from BEL (near Swider), and auroral latitude CMO (night-side), and SOD (day-side) stations, after [Kleimenova N.G. et al. 2008].

geomagnetic activity. About 20 substorms were selected in 2004-2006 for this study. Two examples of the revealed effects of the auroral latitude substorm influence on the simultaneous polar latitude E_z behaviour are shown in Fig. 5a with the correspondent maps of the polar ionosphere plasma convection (Fig. 5b).

It was found that the polar latitude E_z variations, related to substorms, were “positive” in the local morning when the Horsund station was located under the “positive” ionosphere convection vortex associated with region 1 downward field aligned currents (FAC). In the evening, when Horsund station was located under the “negative” ionosphere convection vortex, i.e. in the area of the upward FAC, the E_z deviations were “negative”. Thus, we could speculate that the sign of E_z excursion depends on the station location relatively to the position of the “positive” or “negative” centers of the polar ionosphere plasma convection.

Magnetic storms and substorms, caused by solar wind and interplanetary magnetic field disturbances, could influence to the global electric circuit state via changing of ionosphere conductivity due to particle precipitations or via cosmic rays, or via the direct interplanetary electric field penetration into the magnetosphere, or via the polar cap convection changes.

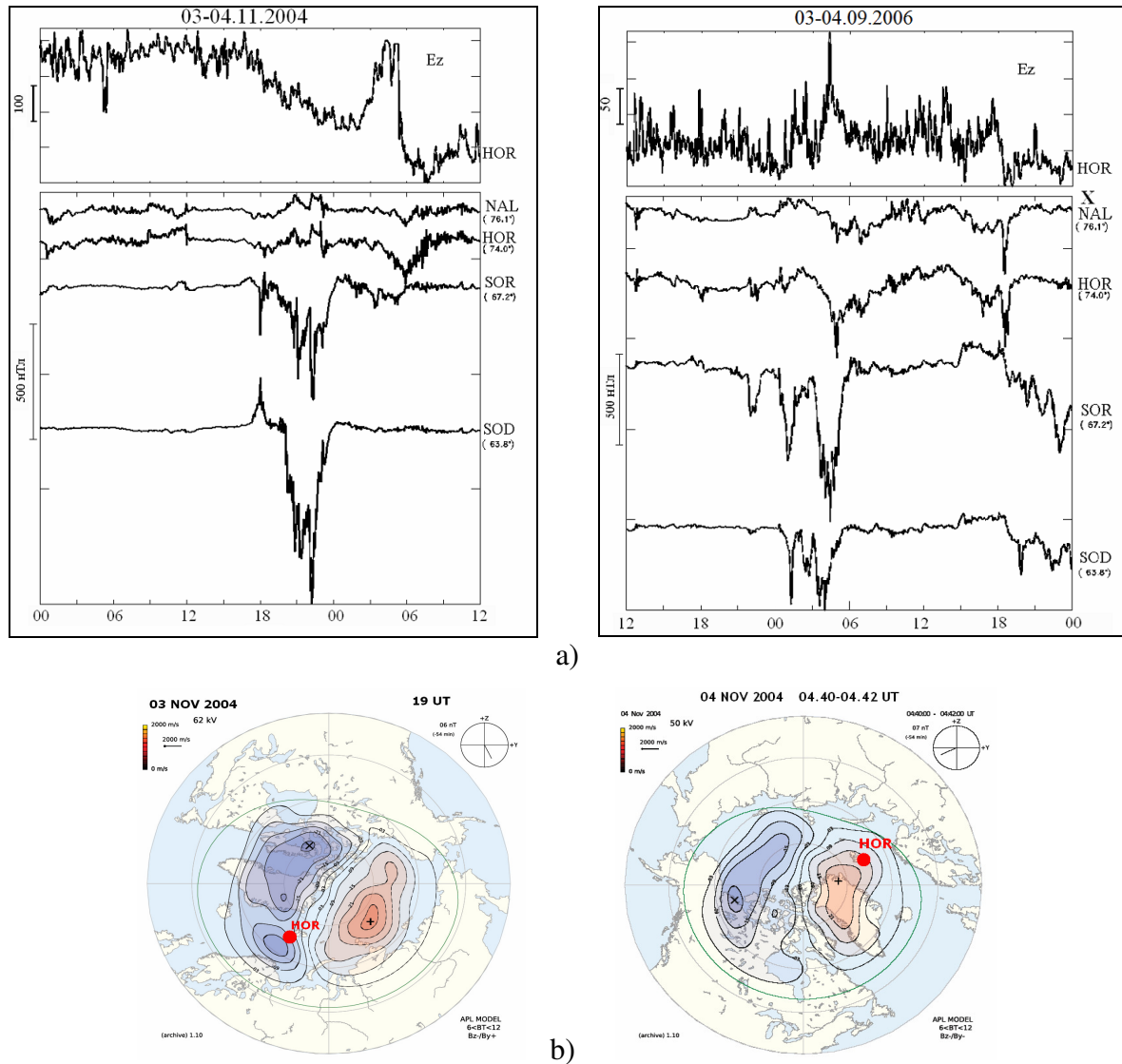


Fig. 5. a) - Two examples of the negative E_z deviation during the night substorms and the positive E_z deviation during the morning substorms (after Kleimenova et al., 2010), b) – the polar ionosphere convection maps in the substorm correspondent time

Thus, the variations in the *atmospheric electricity* both in middle and polar latitudes represent one of the final stage of the *solar wind-magnetosphere-atmosphere coupling*.

Summary

1. The global atmospheric electric circuit state is controlled not only by the world thunderstorm activity but by magnetosphere-ionosphere disturbances (space weather conditions) as well.
2. The effect of the magnetic storm main phase was established in the mid-latitude atmospheric electricity. The strong daytime E_z negative anomalies were found in association with night-side magnetosphere substorm onsets under any local magnetic activity.
3. The substorm related E_z effects were observed at high-latitudes. The polar latitude E_z deviations associated with simultaneous substorms at auroral latitudes were “positive” in the local morning and “negative” in the local evening. We speculate that the sign of E_z excursion depends on the station location relatively to the position of the positive or negative center of the polar ionosphere plasma convection.

Acknowledgements

This work was partly supported by the statutory activities in frame of the IGF PAS grant No 3841/E-41/S/2017 of the Ministry of Science and Higher Education of Poland. The work of N.K. was partly supported by the Program No 9 and No 15 of the Presidium of the Russian Academy of Sciences (RAS).

References

- Apsen A.G., Kh.D. Kanonidi, S.P. Chernysheva, D.N. Chetaev, and V.M. Sheftel' (1988), Magnetospheric effects in atmospheric electricity, 150 pp. M., Nauka (in Russian).
- Bandilet, O.I., Kh.D. Kanonidi, S.P. Chernishova, and V.M. Sheftel' (1986), Effects of magnetospheric substorms in atmospheric electricity. *Geomagn. Aeron.*, 26, no 1, 159–160.
- Frank-Kamenetsky A.V., O.A. Troshichev, G.B. Burns, and V.O. Papitashvili (2001), Variations of the atmospheric electric field in the near-pole region related to the interplanetary magnetic field, *J. Geophys. Res.*, 106, 179-190.
- Kleimenova N.G., S. Michnowski, N.N. Nikiforova, and O.V. Kozyreva (1998), Variations of atmospheric electric field vertical component at the evening sector of polar latitudes (obs.Hornsund), *Geomagn. Aeron.*, 38, no. 6, 149-156.
- Kleimenova N.G., O.V. Kozyreva, S. Michnowski, and M. Kubicki (2008), Effect of magnetic storms in variations in the atmospheric electric field at midlatitudes, *Geomagn. Aeron.* 48, no. 5, 622-630.
- Kleimenova N.G., O.V. Kozyreva, M. Kubicki, and S. Michnowski (2010), Morning polar substorms and variations in the atmospheric electric field, *Geomagn. Aeron.* 50, no. 1, 48-57.
- Kleimenova N., O. Kozyreva, S. Michnowski, and M. Kubicki (2013), Global atmospheric electric circuit response to geomagnetic disturbances, *J. Atmos. Solar-Terr. Phys.*, 99, 117-122.
- Kubicki M. (2001), Results of atmospheric electricity and meteorological observations S. Kalinowski geophysical observatory at Świder, *Publ. Inst. Geophysics Polish Acad. Sci.*, D-56, no. 333, 3-7.
- Kubicki M., Odzimek A. and M. Neska (2016), Relationship of ground-level aerosol concentration and atmospheric electric field at three observation sites in the Arctic, Antarctic and Europe, *Atmos. Res.* 178-179, 329-346.
- Markson R. (1981), Modulation of the Earth's electric field by cosmic radiation, *Nature* 291, 304-308.
- Michnowski S. (1998), Solar wind influences on atmospheric electricity variables in polar regions, *J. Geophys. Res.*, 103, D12, 13939-13948.
- Nikiforova N.N., N.G. Kleimenova, O.V. Kozyreva, M. Kubicki, and S. Michnowski (2003), Influence of auroral-latitude precipitation of energetic electrons on variations in the atmospheric electric field at polar latitudes (Spitsbergen Archipelago), *Geomagn. Aeron.*, 43, no. 4, 29-35.
- Nikiforova N.N., N.G. Kleimenova, O.V. Kozyreva, M. Kubicki, and S. Michnowski (2005), Unusual atmosphere electric field variations during the main phase of the huge magnetic storm of October 30, 2003 at the Polish mid-latitude station Swider, *Geomagn. Aeron.*, 45, no.1, 148-152.
- Olson D. E. (1971). Evidence for auroral effects on atmospheric electricity, *Pure Appl. Geophys.*, 84, 118–138.
- Rycroft M. J., S. Israelsson, and C. Price (2000), The global atmospheric electric circuit, solar activity and climate change, *J. Atmos. Sol.-Terr. Phys.*, 62, 1563–1576.
- Rycroft M. J., R.G. Harrison, K.A. Nicoll, and E.A. Mareev (2008), An overview of Earth's global electric circuit and atmospheric conductivity, *Space Sci. Rev.* 137, 83-105.
- Rycroft M.J., and R.G. Harrison (2011), Electromagnetic atmosphere-plasma coupling: the global atmospheric electric circuit, *Space Sci. Rev.*, 168, 363-384.
- Sao K. (1967), Correlation between solar activity and the atmospheric potential gradient in the Earth's surface in the polar regions, *J. Atmos. Terr. Phys.*, 29, 213-215.
- Tinsley B.A. (2000), Influence of solar wind on the global electric circuit, and inferred effects on cloud microphysics, temperature, and dynamics in the troposphere. *Space Sci. Rev.* 94 (1–2), 231–258.
- Wilson C.T.R. (1920), Investigations on lightning discharges and on the electric field of thunderstorms, *Phil. Trans. Roy Soc. London, A.*, 221, 73-115.
- Williams E.R. (2009), The global electrical circuit: A review, *Atmos. Res.* 91, no. 2-4, 140-152.
- Williams E., and E. Mareev (2014), Recent progress on the global electrical circuit, *Atmos. Res.* 135-136, 208-227.

Transient variations in global electrical circuit caused by different factors and their relation to cloud formation

P.T. Tonev

Space Research and Technology Institute, Bulgarian Academy of Sciences
E-mail: ptonev@bas.bg

Abstract.

Short-term (seconds to hours) transient variations of ionosphere-earth electric current J_z in global electric circuit (GEC) are studied related to their possible role at tropospheric altitudes in formation of clouds by controlling of the rate of nucleation and growth of ice crystals and water droplets, and thus influencing weather and climate. Two possible factors of transient changes in GEC leading to such variations of electric current J_z are considered here: i) Intense cloud-to-ground lightning discharges (CGLD) leading to an effect on the ionospheric potential and thus on current J_z ; and ii) Effects of solar proton events (SPE) on GEC through changes in conductivity in polar strato- and mesosphere. It is shown here that the effect of intense CGLD is negligibly small. On the other hand, during strong SPE, large rapid variations in columnar resistance at high and polar latitudes can arise (due to transient variations in conductivity profile) leading to changes in the electric current J_z at these (as well as at lower) latitudes. Particularly, considerable changes in conductivity profile at high and polar latitudes could occur in stratospheric layers of high aerosol density where conductivity is strongly depleted before the onset of SPE. SPE thus can cause strong transient variations in GEC affecting current J_z at level of cloud tops at high latitudes, as well as on global scale.

Introduction

The role in formation of tropospheric clouds is studied of electric current of density J_z flowing from ionosphere to ground in global electric circuit (GEC) by fair-weather conditions. The current J_z ($1\div 6$ pA/m²) causes accumulation of space charge on droplets and aerosol particles, that affects the rate of scavenging of cloud condensation nuclei and ice forming nuclei (Tinsley, 2010). The magnitude of J_z and its temporal changes (diurnal, as well as shorter transient variations) are determinable for these non-linear processes which play role in formation of clouds and invigoration of storms, thus affecting weather and climate.

The transient variations of J_z are estimated by us as arising from different factors of inner (related to active processes in GEC such as lightning discharges), or outer type (causing changes of GEC parameters, mainly concerning conductivity profiles). Here we consider: 1) Intense cloud-to-ground lightning discharges (CGLD): the response of GEC includes transient changes (from seconds to minutes) of the ionospheric potential V_1 , and thus of current J_z ; 2) Rapid transient variations of atmospheric conductivity σ , mainly at high latitudes and at stratospheric and upper altitudes. It is shown here that while factor 1) is insignificant for transient variations of the current J_z at cloud tops, factor 2), i.e. SPE may have considerable effects on J_z , and thus, possibly, on cloud formation.

Effects of intense CGLD on ionospheric potential V_1 and current J_z

Intense cloud-to-ground lightning discharges (CGLD) with charge moment change $>\sim 1000$ C \times km occur with global rate of the order of or less than 1 s⁻¹, thus having distinguishable effect on the ionospheric potential V_1 on the background of the rest of lightning discharges of global rate 50 s⁻¹. An intense CGLD causes extremely small relative variations $r_J = \Delta J_z / J_z$ of the current J_z at ground: $\sim 0.005 - 0.04\%$ on the minute time scale (Fullekrug, 2004). Under quasi-static conditions when capacitive features of the atmosphere with quasi-exponentially increasing conductivity are taken into account, the modeling shows also increase of the ratio r_J with altitude, as follows from the model example below. We consider a positive CGLD and a region where remote clouds are forming under presence of J_z

with following parameters. The CGLD transports $Q = 100$ C from 10 km height in 1 ms. Boundaries of developing cloud are $z_{c\pm} = 10$ and 4 km. The conductivity in the cloud is reduced 10 times; the transition layer from adjacent air is 100 m. The continuity equation $\nabla \cdot \mathbf{J}_M = 0$ for the Maxwell's current $\mathbf{J}_M = \mathbf{J}_C + \mathbf{J}_D$ is used to determine r_j , where J_C and J_D are the conduction and displacement currents in terms of an equivalent electric circuit. The temporal deviations of the ionospheric potential ΔV_1 and of ionosphere-ground current at cloud top level (6-10 km) ΔJ_{zct} are estimated: $\Delta V_1 = -420$ V; $\Delta J_{zct} = -1.4 \times 10^{-15}$ Am⁻². Thus, we conclude that the effect of intense CGLD on variations of ionosphere-earth current J_z of typical value ~ 2 pA/m² at cloud tops is much below 1%, and is thus negligible.

Effects of SPE on 20.01.2005 (GLE69) on stratospheric electricity at high latitudes

For approximate estimations of the impact of SPE on conductivity profiles in GEC, we analyze data from balloon-borne measurements of electric field \mathbf{E} and current J , and conductivity σ implemented at balloon payload in Antarctic stratosphere between points with geographic coordinates (70.9°S, 10.9°W) and (71.4°S, 21.5°W), and altitudes $z_B = 30.9 \div 33.2$ km during the day of SLE (Kokorowski et al., 2006). Data for the proton flux from GOES 11 (for protons with energies >1, 5, 10, 30, 50, 60 and 100 MeV) is demonstrated in Fig.1. Balloon-born data for σ (Fig.2a), components of \mathbf{E} (Fig.2b), and vertical current J_z (Fig.2c) are shown in Fig.2. The SEP arrival at $t_0 = 06:51$ UT is marked by rapid and huge increase in all energy channels. After the SPE onset a slow decrease takes place except of two isolated rapid increases in low energy channels (>1 and >5 MeV) at $t_{1,2} = 13:48$ UT and 15:58 UT.

Before the onset of SPE σ , E_z and J_z are typical (σ is few $\times 10^{-10}$ S/m; E_z and J_z are downward, and the average J_z is ~ 2 pA/m²). Also, E_z values are highly dispersed. After the SPE onset at time $t = t_0$ the behavior of \mathbf{E} and J_z shows several peculiar changes listed below.

Rapid increase of conductivity σ occurs by at least one order of magnitude at altitude $z_B = 31 \div 33$ km where ionization occurs effectively by protons of energies close to 100 MeV. The electric field is no more turbulent; the vertical field E_z initially drops almost to zero (as reaction to local conductivity increase), but then until time t_1 E_z and J_z increase in general, so that J_z increases 2 \div 3 times than its typical value. At time t_1 E_z almost suddenly becomes close to zero and remains constant until time t_2 at which E_z has its second jump. Paradoxically, close after time t_2 the electric field and current reverse to upward with J_z large again (>5 pA/m²). Although paradoxically, jumps of E_z and J_z at ~ 30 km almost coincide by time with jumps in low energy (several keV) proton flux which is effective for ionization at 85 \div 90 km.

Based on interpretations of these experimental results made below and on model studies we study further the effects of SPE on GEC (in particular, on conductivity profiles) at global scale, and how these effects are reflected on the electric current J_z at cloud tops.

Possible explanation of data

a) SPE and the factor of pre-existing aerosol layers

The assumed relation between SPE and GEC is realized through large variations of conductivity in atmospheric regions at polar and high latitudes which cause rapid changes in column resistance R leading to transients in GEC. The enhanced ionization in atmospheric regions by solar proton flux leads to increase of conductivity σ , and thus to decrease of the column resistance R . The resistance R is a sum of column resistances for atmospheric regions: $R = R_T + R_{SB} + R_{SA} + R_M$ where index T is for the troposphere, SB and SA are for the stratosphere below and above the height z_B of the balloon, and M is for the mesosphere and mesopause. For typically undisturbed conductivity profile $\sigma(z)$ $R_T \gg R_{SB} \gg R_{SA} \gg R_M$ due to quasi-exponential rise of conductivity with altitude, so that R is affected only by changes in

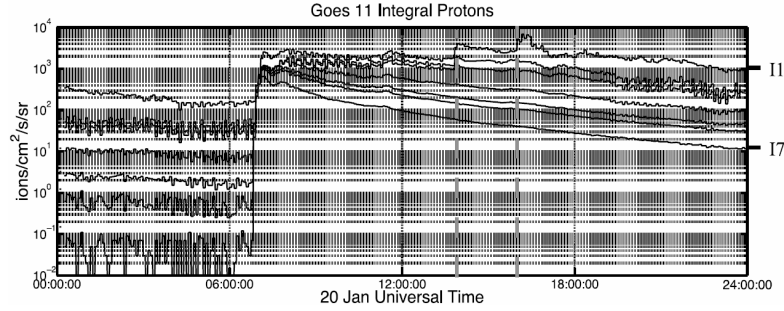


Fig. 1. One-minute-averaged GOES 11 integral proton channels January 20, 2005. Channels 11-17 are plotted for integral amounts greater than 1, 5, 10, 30, 50, 60 and 100 MeV protons.

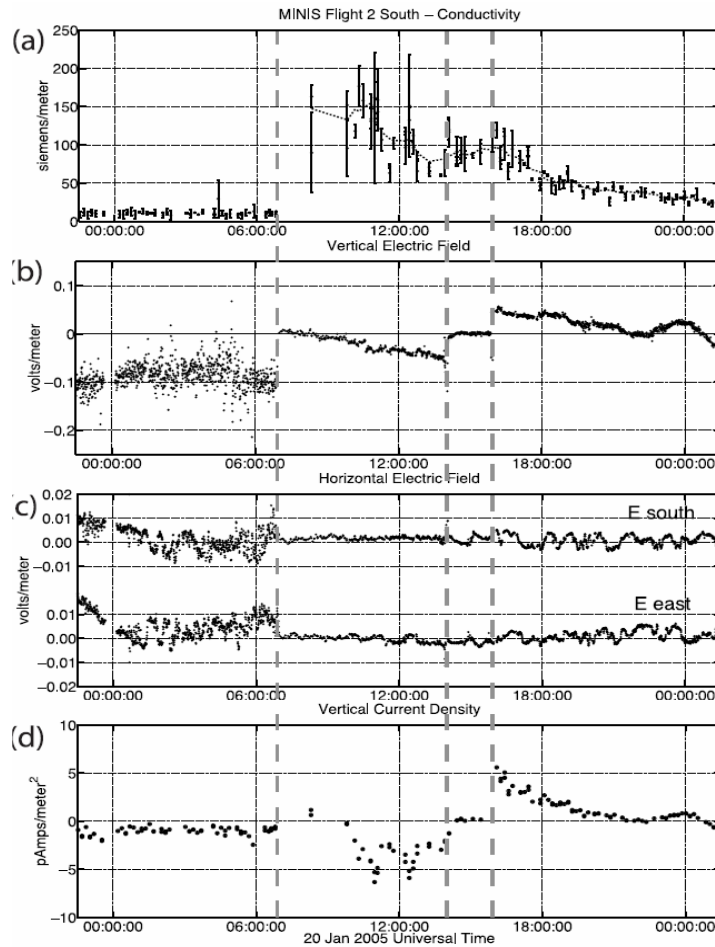


Fig. 2. Data from the balloon payload: (a) Conductivity σ (b) One-minute-averaged vertical electric field E_z . Typical error bars are 10–15 mV/m. (c) Horizontal electric field. The dashed gray lines mark the SEP onset and the sudden jumps in the vertical electric field. (d) Vertical current density (TZ06).

R_T whose variations during SPE cannot exceed few percent (Kokorowski et al., 2012). However, this case is not always valid: the stratospheric column resistance $R_S = R_{SB} + R_{SA}$ can become comparable to the tropospheric resistance if a layer exists in the stratosphere of highly reduced conductivity, as predicted by Tinsley (2005) and Tinsley and Zhou (2006) cited further as TZ06. According to conductivity model by TZ06, a layer could be formed in the polar stratosphere (at 40 km altitude, with 10 km semi-thickness) containing ultra-fine aerosol particles of large density whose origin are the most powerful volcano eruptions. Conductivity in this layer is dramatically reduced due to the rapid attachment of ions to particles with much bigger mass. The conductivity profile for Antarctica obtained by TZ06 is shown in Fig.3.

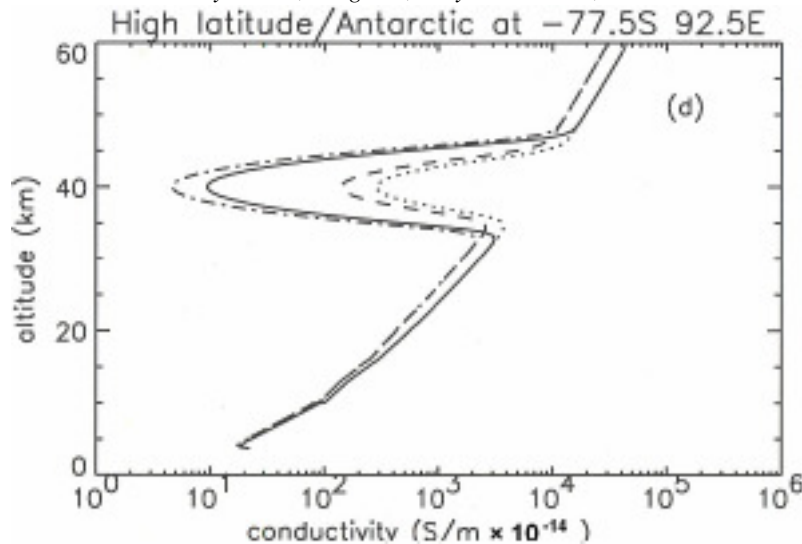


Fig. 3. Profiles of conductivity in Antarctica for December, for high and low volcanic and solar activities (TZ06) The solid and dot-dashed lines are for solar minimum and solar maximum, respectively, for high volcanic activity; the dotted and dashed lines are for solar minimum and solar maximum, at low volcanic activity.

When ionization in the layer is not forced by energetic solar proton flux, the stratospheric resistance R_S is comparable to (or even larger than) R_T . With the onset of SPE the ionization rate in the aerosol layer can become larger than the ion-particle attachment rate, so that conductivity strongly increases and the resistance R_S becomes much less than R_T . In this case the onset of SPE causes decrease of resistance R due to the drop of stratospheric resistance. If the horizontal scale of the aerosol layer at high latitudes is large enough, the transient changes of the column resistance R during SPE, thus realized, would lead to global-scale transient variations in GEC, particularly, in the ionospheric potential V_I and the current J_z .

Besides this hypothetical, other types of layers of reduced conductivity σ have been observed, e.g. noctilucent clouds (NLC) in the summer mesopause (~ 2 km thin layer at ~ 85 km altitude), where σ is as low as 4×10^{-13} S/m (Holzworth and Goldberg, 2004).

b) Account for the role of ionospheric convection and trans-polar potential

The observed large increase of the current J_z and its reversal later on during SPE is hard to explain only by the effect of the considered aerosol layer in the stratosphere. The trans-polar potential difference in the auroral ionosphere can be considered as another factor for explanation of behavior of J_z . Park and Dejnakarindra (1977) showed by modeling that the ionospheric electric fields with horizontal scale > 200 km are mapped almost without attenuation down to lower stratosphere as horizontal electric fields E_{IC} . The related electric currents J_{IC} can be considered as an extension of the electric current system in the ionosphere related to the convection. Then, the total current J in the stratosphere at high latitudes is a sum $J = J_0 + J_{IC}$, where J_0 is generated from inner sources in GEC.

The specific energy spectrum of proton flux during the considered SPE determines enhancement of conductivity above 30 km up to two orders of magnitude or more (Kokorowski et al., 2012, their Fig.9) when there are no pre-existing layers of reduced σ . This conductivity increase leads to expressed growing of currents J_{IC} formed below the ionospheric structures of trans-polar potential which 'extend' the closure region of ionospheric currents. If J_{IC} is not small related to J_0 , then this 'extension' of auroral ionospheric system of currents can explain the behavior of J_z demonstrated in Fig.2. Also, the jumps in J_z at times $t_{1,2}$ can be explained as result of change of relative significance of J_{IC} in the total current J , as well as of R_M in the column resistance $R_{SH} + R_M$ of the region above the balloon altitude $z_B \sim 32$ km.

Effect of SPE onset on column resistance and current J_z in Antarctica

The relative change of the column resistance R for Antarctica by SPE (20.01.2017) is obtained using the model TZ06. The variation of R is used further to determine the initial change in J_z . Before the SPE onset we use the conductivity profile from Fig.3, for solar minimum and low volcanic activity. The following equation is valid for the ion density n in stratospheric layer with presence of aerosol particles (TZ06):

$$dn/dt = q - \alpha n^2 - n \sum_i \beta_i S_i \quad (1)$$

Here q is the ion pair production rate, α is the ion-ion recombination rate, and β_i is an effective coefficient of attachment to aerosol particles differentiated by type i with density S_i . We adopt the profiles of α and $\sum_i \beta_i S_i$ from TZ06. Eq.(1) is solved by steady-state conditions with ionization rate q which takes place before, as well as after the SPE arrival. In the first case the ionization is only by galactic cosmic rays. Values of q are (Usoskin et al., 2011):

| Altitude, km | q (before SPE onset), cm^{-3} | q (after SPE onset), cm^{-3} |
|-----------------|---|--|
| 30 | 20 | 1200 |
| 40 | 4.5 | 1700 |
| 50 | 1.0 | 800 |

The relative increase of conductivity by SPE arrival is approximated as equal to the relative increase of ion density n obtained from Eq.(1). The results for the total column resistances R before and after SPE onset are:

| Column resistance R | Before SPE onset, $\Omega \text{ m}^2$ | After SPE onset, $\Omega \text{ m}^2$ |
|--------------------------|---|--|
| | 4.6×10^{16} | 4.4×10^{16} |

The effect of change of column resistance R on the ionosphere-ground current J_z is studied by neglecting the role of currents J_{IC} from ionospheric origin. This effect depends on the scale of region of the stratospheric aerosol layer. The approximate relative change of J_z is obtained by assumption that the aerosol layer is confined at latitudes $\lambda > \lambda_B$, for different boundary λ_B :

| λ_B | $J_z(\lambda > \lambda_B, t > t_0) / J_z(\lambda > \lambda_B, t < t_0)$, % | $J_z(\lambda < \lambda_B, t > t_0) / J_z(\lambda < \lambda_B, t < t_0)$, % |
|-------------|--|--|
| 80° | 4.6 | -0.22 |
| 70° | 4.7 | -0.84 |
| 60° | 4.9 | -2.12 |

where t_0 is the onset time of the SPE. These preliminary estimations show that the effect of SPE is mainly at high latitudes $\lambda > \lambda_B$ where the ionosphere-ground current J_z increases by almost 5%. At lower latitudes ($\lambda < \lambda_B$) J_z has relatively small decrease.

Conclusions

1. Effect of solar proton events (SPE) on variability of ionosphere-ground electric current J_z is examined in relationship with cloud formation.
2. Such effect is active when a layer of fine aerosols in polar stratosphere pre-exists.
3. Lightning discharges do not affect transient variations of the current J_z .

References

- Fullekrug, M. (2004), The contribution of intense lightning discharges to the global atmospheric electric circuit during April 1998, *Journal of Atmospheric and Solar-Terrestrial Physics* 66 (2004) 1115–1119
- Holzworth, R.H., R.A. Goldberg, Electric field measurements in noctilucent clouds, *J. Geophys. Res.*, 109, D16203, doi:10.1029/2003JD004468, 2004.
- Kokorovski, M., J. G. Sample, et al. (2006), Rapid fluctuations of stratospheric electric field following a solar energetic particle event, *Geophys. Res. Lett.*, 33, L20105, doi:10.1029/2006GL027718.
- Kokorowski, M., A. Seppälä, J. G. Sample, R. H. Holzworth, M. P. McCarthy, E. A. Bering, E. Turunen (2012), Atmosphere-ionosphere conductivity enhancements during a hard solar energetic particle event, *J. Geophys. Res.*, 117, A05319, doi:10.1029/2011JA017363, 2012
- Park C.G. and M. Dejnakarindra (1977), The effects of magnetospheric convection on atmospheric electric fields in the polar cap, In: *Electrical Processes in Atmospheres, Proc. 5th Int. Conf. on Atmospheric Electricity, Garmisch-Partenkirchen, 2-7 September 1974*, ed. by H. Dolzelek and R. Reiter, 1977, pp. 536-543.
- Tinsley, B.A. (2005), On the variability of the stratospheric column resistance in the global electric circuit, *Atmospheric Research* 76 (2005) 78–94.
- Tinsley, B.A., and Zhou, L. (2006), Initial results of a global circuit model with variable stratospheric and tropospheric aerosols, *J. Geophys. Res.*, 111, D16205, doi:10.1029/2005JD006988
- Tinsley B.A., Electric charge modulation of aerosol scavenging in clouds: Rate coefficients with Monte Carlo simulation of diffusion, *J. Geophys. Res.*, 115, (2010) D23211, doi:10.1029/2010JD014580
- Usoskin, I.G., G.A. Kovaltsov, etc. (2011), Ionization effect of solar particle GLE events in low and middle atmosphere, *Atmos. Chem. Phys.*, 11, 1979–1988, 2011.

Identification of features in solar ALMA images and comparison with solar atmospheric models

I. Skokić¹, R. Brajša², D. Sudar², M. Kuhar³, A.O. Benz³

¹ Astronomical Institute of the CAS, Ondřejov, Czech Republic

² Hvar Observatory, Faculty of Geodesy, University of Zagreb, Zagreb, Croatia

³ University of Applied Sciences and Arts Northwestern Switzerland, Windisch, Switzerland

E-mail: ivica.skokic@gmail.com

Abstract.

Various solar features were identified in the full-disc single-dish ALMA images taken at wavelength of 1.2 and 2.8 mm and compared with H α , Ca II K and EUV images and magnetograms. Assuming thermal bremsstrahlung as the dominant radiation mechanism, several models were constructed to calculate the brightness temperature of various solar features (quiet and active solar regions, filaments and coronal holes) in a wavelength range from 0.3 to 10 mm. It is found that model predictions are in a qualitative agreement with ALMA images where active regions appear brighter, while filaments and coronal holes are not discernible from the quiet Sun level. It is also found that in ALMA images regions around magnetic neutral lines appear darker than the quiet Sun. Models predict a critical frequency below which filaments should appear in absorption and above it in emission.

Introduction

With the recent commissioning of the solar observing mode, Atacama Large Millimeter/submillimeter Array (ALMA) is now capable of observing the Sun in two frequency bands centered around 100 GHz and 239 GHz, in both interferometric and single-dish (total power) mode [Shimojo M. *et al.*, 2017; White S.M. *et al.*, 2017]. It is expected that interferometric observations will provide new insight into the dynamics of the solar chromosphere [Wedemeyer S. *et al.*, 2016], but single-dish observations will also be essential to give the absolute flux information and for producing full-disc images of the Sun. Comparing full-disc images with theoretical models is an important step in constraining the properties of the solar plasma in various solar regions. In this paper, we construct models of several solar structures and compare their predicted visibility with ALMA full-disc images.

Data

We selected two full-disc single-dish ALMA images from the December 2015 CSV campaign, one in band 3 (107 GHz, 2.8 mm) and one in band 6 (248 GHz, 1.2 mm). The images were taken on 17 December 2015 using double-circle fast scan mapping with a total power ALMA antenna [Phillips N. *et al.*, 2014]. The beam size is ~60 arcsec and ~26 arcsec for bands 3 and 6, respectively.

In Figure 1, the selected full-disc ALMA images (top row) are compared with H α and Ca II K filtergrams (middle row), SDO/HMI magnetogram, and SDO/AIA EUV composite (bottom row). It can be seen that active regions appear as bright regions in the ALMA images, while regions around magnetic neutral lines appear darker than the surrounding quiet Sun level. Filaments, easily visible in H α image, do not have identifiable ALMA counterparts, as well as the coronal hole, which is visible in EUV image but not in the ALMA images.

Models

Millimeter radiation originating from the quiet Sun region (without strong magnetic fields) is predominantly generated by thermal bremsstrahlung at temperatures 10^4 - 10^7 K [Hurford, G., 1992; White, S.M., 2006]. The source function is in that case Planckian and the Rayleigh-Jeans approximation holds in the millimeter range:

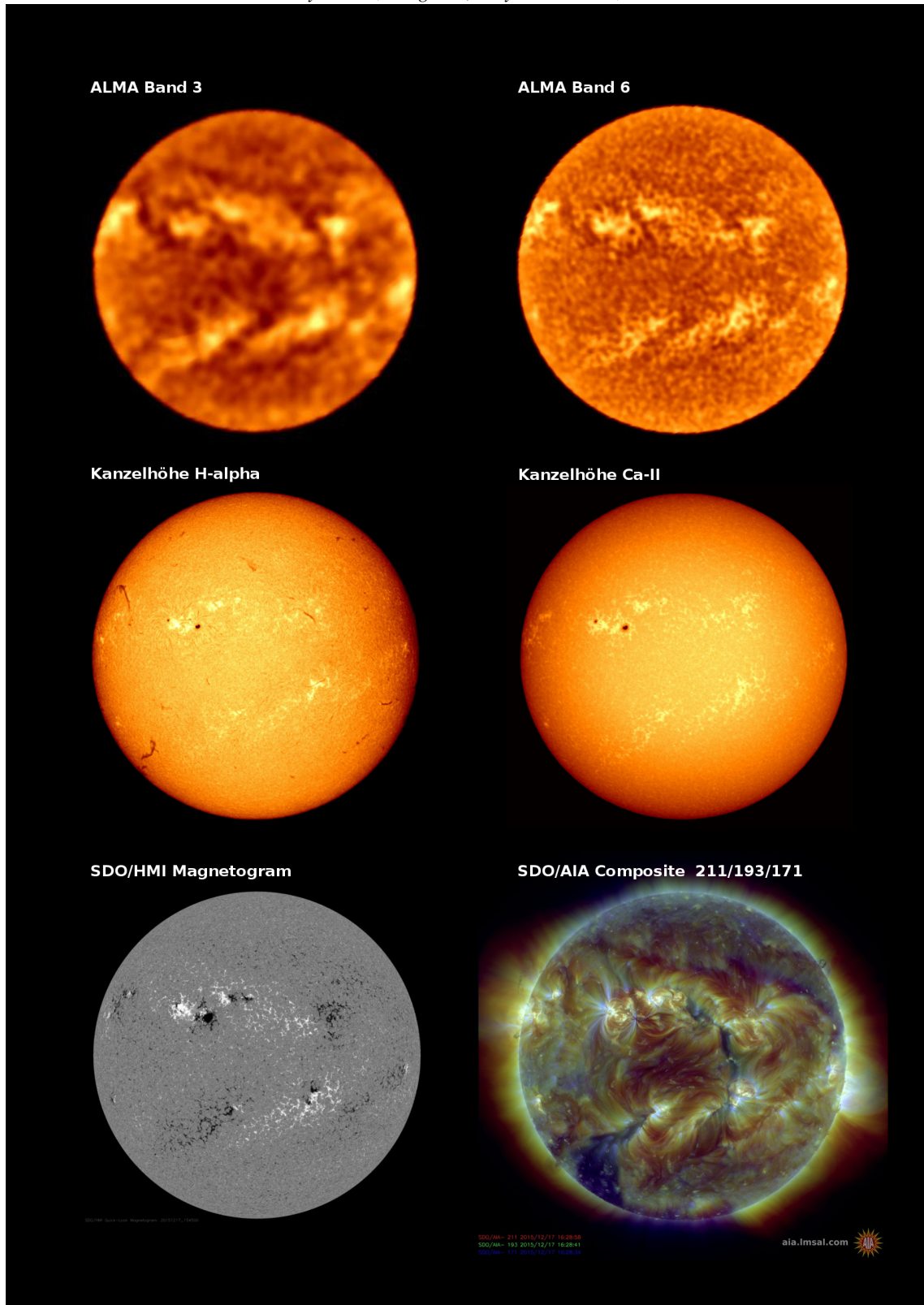


Fig. 1 Full-disc single-dish ALMA images of the Sun taken on 17 December 2015 at 107 GHz (top left) and 248 GHz (top right). H α and Ca II K filtergrams from the same date from Kanzelhöhe Observatory (middle). SDO HMI magnetogram (bottom left) and SDO/AIA composite of 171/193/211Å channels (bottom right).

$$B_\nu = \frac{2h\nu^3}{c^2 \left(e^{\frac{h\nu}{k_B T_e}} - 1 \right)} \approx \frac{2k_B \nu^2}{c^2} T_e \quad (1)$$

where B_ν is the spectral radiance, k_B is the Boltzmann constant, ν is the observing frequency, T_e is the electron temperature, and c the speed of light. Intensity can then be determined by integrating the source function over the optical depth τ :

$$I = \int_0^\infty B_\nu e^{-\tau} d\tau \quad (2)$$

In the millimeter range, intensity is usually expressed as brightness temperature T_b :

$$T_b = \frac{c^2 I}{2k_B \nu^2} \quad (3)$$

Combining equations (1), (2) and (3), we get:

$$T_b = \int_0^\infty T_e e^{-\tau} d\tau \quad (4)$$

where the optical depth is given by [Benz, A.O., 2002]:

$$d\tau = \frac{0.01146 \ln \Lambda n_e^2}{(1 - 8.06 \cdot 10^7 n_e / \nu^2)^{1/2} \nu^2 T_e^{3/2}} ds. \quad (5)$$

The optical depth expression assumes bremsstrahlung radiation and solar abundances without magnetic field. The Gaunt factor ($\ln \Lambda$) has a value of ~ 8 in the upper chromosphere and varies slowly with the electron density n_e and temperature [Benz A.O. et al., 1997].

We used atmospheric models of [Fontenla, J.M., et al., 1993] because they reasonably agree with radio observations [Bastian, T.S., et al., 1996]. FAL model A was used, which describes the coronal hole regions, supplemented with Baumbach-Allen model at higher latitudes with $T_e = 1.2 \cdot 10^6$ K [Benz, A.O. et al., 1997]. This average model was used as the starting quiet Sun model (QS model) which was then perturbed to describe conditions in other regions and structures. A program was written which calculates brightness temperature contributions for different heights in the solar atmosphere and integrates them for a given wavelength. The procedure is repeated for the whole wavelength range under consideration.

Results and discussion

a) Quiet Sun regions

A comparison between our QS model and previous measurements summarized by [Benz A.O. et al., 2009] is shown in Figure 2a. Calculated brightness temperatures are somewhat lower than the measured ones but are in a general qualitative agreement. Only at wavelengths larger than 1 m the model begins to deviate, mostly due to the increased refraction of radio waves. QS model prediction is also shown as a reference model in Figures 2b, 3a and 3b for the wavelength range covered by ALMA. The model predicts T_b values of around 4500 K and 6000 K for ALMA bands 3 and 6 (2.8 and 1.2 mm wavelength), while actual measurements on ALMA full-disc images give larger values, 5900 K and 7300 K, respectively [White S.M. et al., 2017]. A similar discrepancy was also found with the radiation hydrodynamics code CO5BOLD [Wedemeyer-Böhm S. et al., 2007]. An opposite disagreement (overestimated calculated intensity at cm and mm wavelengths) was found when older VAL models were used [Gary D., 1996].

b) Active regions

In active regions, the solar atmosphere has density and temperature values which are different from those above quiet Sun regions. Gyromagnetic emission contribution to the total radiation is small for the typical magnetic field values found in active regions and can be neglected [Brajša R. et al., 2009; Romštajn I. et al., 2009]. Assuming thermal bremsstrahlung

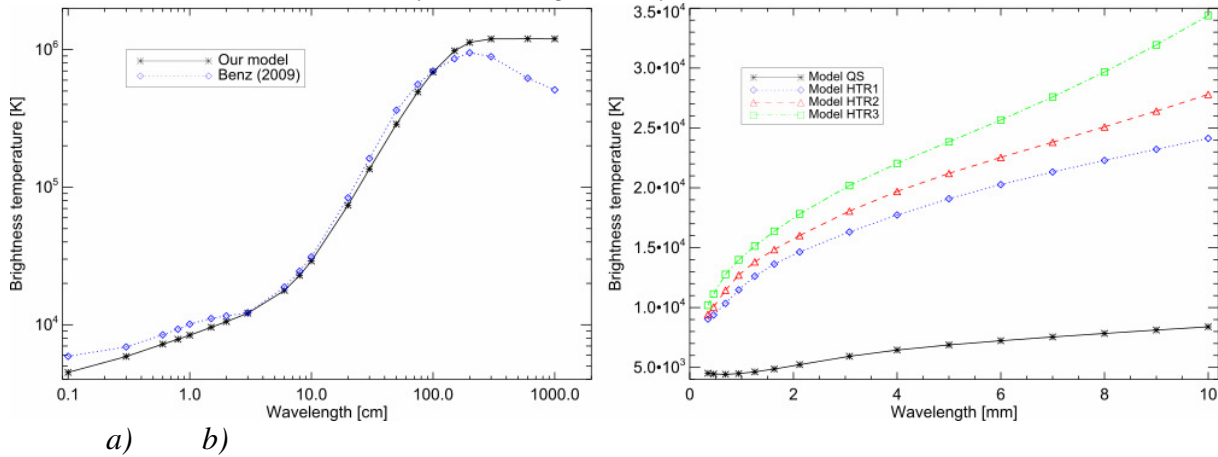


Fig. 2 Comparison of T_b between (a) measurements (blue) and quiet Sun (QS) model (black), and between (b) QS and 3 active region models (HTR1, HTR2, HTR3).

as the dominant radiation mechanism, higher brightness temperatures are a consequence of the enhanced density in the chromosphere above the temperature minimum and the corona.

We developed 3 models (HTR1, HTR2, HTR3) of active regions with temperatures 2 times higher than in the QS model and density increased by factor of 5, 7 and 10, respectively. The results are shown in Figure 2b. All three models predict significantly higher brightness temperatures than the QS model, which means that active regions should appear bright in ALMA images. This is in qualitative agreement with ALMA observations, however the predicted values seem to be overestimated.

c) Filaments

Prominences are denser and cooler structures in the solar atmosphere. When observed on the solar disc, typically in H α filtergrams, they are also called filaments. Taking into account the physical parameters of prominences [Engvold O. et al., 1990; Tandberg-Hanssen E., 1995], we developed six prominence models (PROM1, PROM2, PROM3, PROM4, PROM5, PROM6). At millimeter wavelengths there are also structures visible in absorption called coronal condensations [Kundu M.R. et al., 1978; Vršnak B. et al., 1992]. Therefore, we added one model of coronal condensations (CC model).

Prominence models assume hydrostatic equilibrium; so the pressure is conserved at a given altitude. Therefore, in our PROM models we increased the QS density by factors of 80, 120, 160, 200, 240 and 280 and decreased the temperatures by the same factor so that the product $n \cdot T$, which is proportional to the pressure, is conserved. This factor is applied at typical prominence heights of 40 000 – 50 000 km [Bastian T.S. et al., 1993a; Brajša R. et al., 2009]. For the CC model, we increased the density by factor of 50, and decreased the temperature by factor of 175.

Figure 3a shows the resulting brightness temperatures. CC model predicts levels quite close to the QS model at wavelengths shorter than 5 mm, while at longer wavelengths the level monotonically drops below the QS level. Interesting models are PROM3 and PROM4 which show two radiation regimes: absorption and emission. At some specific wavelength depending on the model the filaments become invisible against the background quiet Sun level and a transition from absorption to emission takes place. Filaments are not clearly visible either in absorption or in emission in the ALMA images in Figure 1 indicating that at the observed frequencies the difference between brightness temperature of filaments and the quiet Sun is below the noise level. Finding the critical frequency where filaments go from emission into absorption, using multi-band ALMA observations, would be a valuable constraint on the temperature and density of the filament.

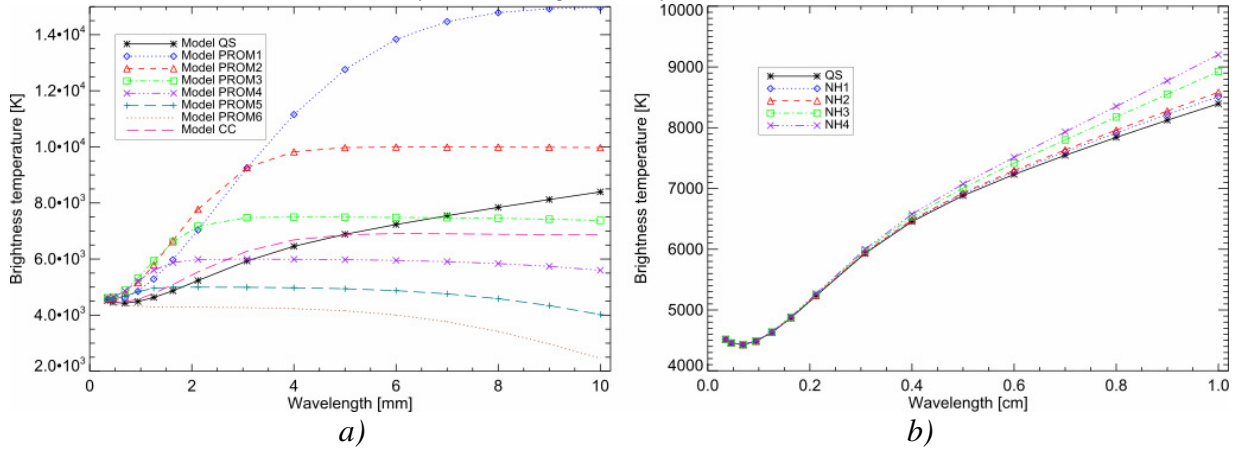


Fig. 3 Predictions of the T_b for 6 prominence and one coronal condensation model (a), and 4 non-hole models (b) in comparison with the QS model (black).

d) Coronal holes

Coronal holes are regions of lower temperature and density in the solar corona. Our starting quiet Sun model actually describes the conditions similar to the coronal hole atmosphere (QS model = CH model). To investigate the visibility of coronal holes against the QS background, we developed 4 non-hole (NH) models based on the hybrid network model of [Gabriel A., 1992]. Temperature and density parameters used for constructing these models are based on various studies [Stix M., 1989; Hara H. et al., 1994; Gabriel A., 1992; Doschek G.A. et al., 1997; Golub L. & Pasachoff J.M., 1997; Gallagher P.T. et al., 1999; Avrett E., 2000; Koutchmy S., 2000; Lang K.R., 2000; Aschwanden M.J., 2004].

The models are constructed by changing the values of the density and temperature from the coronal hole structure towards the structure of the quiet non-hole chromosphere and corona. In the hybrid network model of [Gabriel A., 1992] the temperature is slightly increased at higher altitudes (h) and the electron density (n) is multiplied by a factor (f) above a specific height. We assume that $T_{NH} > T_{CH}$, for $h > 28000$ km, with $n_{NH} = n_{CH} \cdot f$, where f is in the range from 1.7 to 3.6. The models deviate only in density at the transition region and at coronal heights below 28 000 km, consistent with the observed lack of temperature enhancements in the chromosphere and transition region. Since the coronal radiation is optically thin, a change in coronal temperature would not result in a significant change of brightness temperature. The main criterion which models should fulfill is that the pressure should be a monotonically decreasing function with the height.

In Figure 3b the resulting brightness temperatures for all models (QS = CH and 4 non-hole models) are shown. It can be seen that there is no difference in predicted intensity between the quiet Sun and coronal holes for the main ALMA wavelength range, in agreement with the ALMA images presented in Figure 1, where no coronal holes can be detected. However, at longer wavelengths (>4 mm), the predicted difference becomes more pronounced and coronal holes should be visible as areas of lower brightness temperature than the quiet Sun regions. This could be tested observationally representing a strong motivation for solar observations with ALMA bands 1 and 2 (the longest ALMA wavelengths).

Conclusions

In this paper we presented results of brightness temperature calculated for the quiet Sun, active regions, filaments and coronal holes, performed for the wavelength range from 0.3 mm to 10 mm, corresponding to ALMA bands. Various models were developed assuming thermal bremsstrahlung as the relevant radiation mechanism. The main aim was to make a quantitative prediction of the radiation intensity for various solar structures and to compare qualitatively the results with the solar ALMA images obtained at 1.2 and 2.8 mm (Figure 1).

Regular observations of the Sun with ALMA will be an important test for the described models helping to accept or reject some of them. Such observations will represent a significant improvement of our understanding of the solar chromosphere. A comparison between results of the calculations and measurements will also help to guide and refine future modeling efforts.

Acknowledgements.

Research leading to this work was performed within ESO Development Plan Study: Solar Research with ALMA (2014 - 2017). This work has been supported in part by Croatian Science Foundation under the project 6212 "Solar and Stellar Variability" and by the European Commission FP7 project SOLARNET (312495, 2013 - 2017), which is an Integrated Infrastructure Initiative (I3) supported by FP7 Capacities Programme. This paper makes use of the following ALMA data: ADS/JAO.ALMA#2011.0.00020.SV. ALMA is a partnership of ESO (representing its member states), NSF (USA) and NINS (Japan), together with NRC (Canada) and NSC and ASIAA (Taiwan), and KASI (Republic of Korea), in cooperation with the Republic of Chile. The Joint ALMA Observatory is operated by ESO, AUI/NRAO and NAOJ. The National Radio Astronomy Observatory is a facility of the National Science Foundation operated under cooperative agreement by Associated Universities, Inc. H α data / Ca II K data were provided by the Kanzelhöhe Observatory, University of Graz, Austria. SDO AIA/HMI images are courtesy of NASA/SDO and the AIA, EVE, and HMI science teams.

References

- Aschwanden, M. J. 2004, *Physics of the Solar Corona. An Introduction* (Praxis Publishing Ltd)
- Avrett, E. 2000, in *Allen's Astrophysical Quantities*, Springer, New York, ed. A. N. Cox, 348
- Bastian, T. S., Ewell, Jr., M. W., & Zirin, H. 1993a, *ApJ*, 418, 510
- Benz, A., ed. 2002, *Astrophysics and Space Science Library*, Vol. 279, *Plasma Astrophysics*, second edition
- Benz, A. O. 2009, *Landolt Börnstein*, 4116
- Benz, A. O., Krucker, S., Acton, L. W., & Bastian, T. S. 1997, *A&A*, 320, 993
- Brajša, R., Romštajn, I., Wöhl, H., et al. 2009, *A&A*, 493, 613
- Doschek, G. A., Warren, H. P., Laming, J. M., et al. 1997, *ApJ*, 482, L109
- Fontenla, J. M., Avrett, E. H., & Loeser, R. 1993, *ApJ*, 406, 319
- Gabriel, A. 1992, in *NATO Advanced Science Institutes (ASI) Series C*, Vol. 373, *NATO Advanced Science Institutes (ASI) Series C*, ed. J. T. Schmelz & J. C. Brown, 277
- Gallagher, P. T., Mathioudakis, M., Keenan, F. P., Phillips, K. J. H., & Tsinganos, K. 1999, *ApJ*, 524, L133
- Gary, D. E. 1996, in *Astronomical Society of the Pacific Conference Series*, Vol. 93, *Radio Emission from the Stars and the Sun*, ed. A. R. Taylor & J. M. Paredes, 387
- Golub, L. & Pasachoff, J. M. 1997, *The Solar Corona*, Cambridge University Press, Cambridge
- Hara, H., Tsuneta, S., Acton, L. W., et al. 1994, *PASJ*, 46, 493
- Hurford, G. 1992, in *NATO Advanced Science Institutes (ASI) Series C*, Vol. 373, *NATO Advanced Science Institutes (ASI) Series C*, ed. J. T. Schmelz & J. C. Brown, 297
- Koutchmy, S. 2000, in *Allen's Astrophysical Quantities*, Springer, New York, ed. A. N. Cox, 357
- Kundu, M. R., Fuerst, E., Hirth, W., & Butz, M. 1978, *A&A*, 62, 431
- Lang, K. R. 2000, *The sun from space*, Berlin, Heidelberg: Springer-Verlag
- Phillips, N., Hills, R., Bastian, T., et al. 2015, in *ASP Conf. Ser.*, Vol. 499, *Revolution in Astronomy with ALMA: The Third Year*, ed. D. Iono, K. Tatematsu, A. Wootten, & L. Testi, 347
- Romštajn, I., Brajša, R., Wöhl, H., et al. 2009, *Central European Astrophysical Bulletin*, 33, 79
- Shimojo, M., et al. 2017, *Sol. Phys.*, 292, 87
- Stix, M. 1989, *The Sun. An Introduction*, Springer-Verlag, Berlin, Heidelberg, New York
- Vršnak, B., Pohjolainen, S., Urpo, S., et al. 1992, *Sol. Phys.*, 137, 67
- Wedemeyer-Böhm, S., Ludwig, H. G., Steffen, M., Leenaarts, J., & Freytag, B. 2007, *A&A*, 471, 977
- Wedemeyer, S., Bastian, T., Brajša, R., et al. 2016, *Space Science Reviews*, 198
- White, S. M., Loukitcheva, M., & Solanki, S. K. 2006, *A&A*, 456, 697
- White, S. M. et al. 2017, *Sol. Phys.*, 292, 88

Solar research with ALMA: Czech node of European ARC as your user-support infrastructure

*M. Bárta*¹, *I. Skokič*¹, *R. Brajša*^{2,1} & *the Czech ARC Node Team*

¹ European ARC – Czech node, Astronomical Inst. CAS, Ondřejov, Czech Republic

² Faculty of Geodesy, University of Zagreb, Croatia

E-mail: barta@asu.cas.cz

Abstract.

ALMA (Atacama Large Millimeter/sub-millimeter Array) is by far the largest project of current ground-based observational facilities in astronomy and astrophysics. It is built and operated in the world-wide cooperation (ESO, NRAO, NAOJ) at altitude of 5000m in the desert of Atacama, Chile. Because of its unprecedented capabilities, ALMA is considered as a cutting-edge research device in astrophysics with potential for many breakthrough discoveries in the next decade and beyond. In spite it is not exclusively solar-research dedicated instrument, science observations of the Sun are now possible and has recently started in the observing Cycle 4 (2016-2017).

In order to facilitate user access to this top-class, but at the same moment very complicated device to researchers lacking technical expertise, a network of three ALMA Regional Centers (ARCs) has been formed in Europe, North America, and East Asia as a user-support infrastructure and interface between the observatory and users community. After short introduction to ALMA the roles of ARCs and hint how to utilize their services will be presented, with emphasis to the specific (and in Europe unique) mission of the Czech ARC node in solar research with ALMA. Finally, peculiarities of solar observations that demanded the development of the specific Solar ALMA Observing Modes will be discussed and the results of *Commissioning and Science Verification* observing campaigns (solar ALMA maps) will be shown.

Introduction

ALMA (Atacama Large Millimeter/sub-millimeter Array) is current cutting-edge observational facility in the astrophysical research constructed and operated in the world-wide international cooperation in Chile. Because of its unique parameters it brings potential for many break-through discoveries in space research and fundamental physics and represents a key ground-based device in the field for the next decade and beyond. Nevertheless, its utilization for regular users even with a high-quality background in astrophysics might become cumbersome because of lack of their expertise in the ALMA technology and ALMA service software. In order to increase scientific return and to support excellence in research, the main partners in the ALMA consortium – ESO (Europe), NRAO (U.S.) and NAOJ (Japan) – decided to form a user-support infrastructure – the network of three ALMA Regional Centers / ARCs, located at the respective organizations. The main goal of this infrastructure is direct support (on-line and face-to-face) to the ALMA user community at all stages of their ALMA oriented research projects. Furthermore, the ARCs contribute to the further development of ALMA helping with the ALMA SW and infrastructure tests and promoting new possible ALMA capabilities.

The European ARC is formed as a coordinated distributed network of seven nodes centered around ESO. One of the nodes is hosted at the Astronomical Institute of Academy of Sciences in Ondřejov, Czech Republic. The Czech node of the European ARC provides the standard user services to the local, European, as well as international ALMA users' community. In addition to that it contributes to the further development of ALMA observatory by definition and commissioning of a new observing mode targeted to solar research with ALMA.



Fig. 1: ALMA Observatory by night (<http://www.almaobservatory.org>).

ALMA Observatory

ALMA (Atacama Large Millimeter/sub-millimeter Array) is the far largest project of current ground-based observational facility in astronomy and astrophysics. It has been recently built in a literally world-wide international cooperation of European Southern Observatory (ESO), U.S. National Radio Astronomy Observatory (NRAO) and National Astronomical Observatories of Japan (NAOJ) in the altitude of 5000m in the desert of Atacama, Chile. Because of its unprecedented capabilities ALMA is considered as a top research device in astrophysics with potential to many breakthrough discoveries for the next decade and beyond.

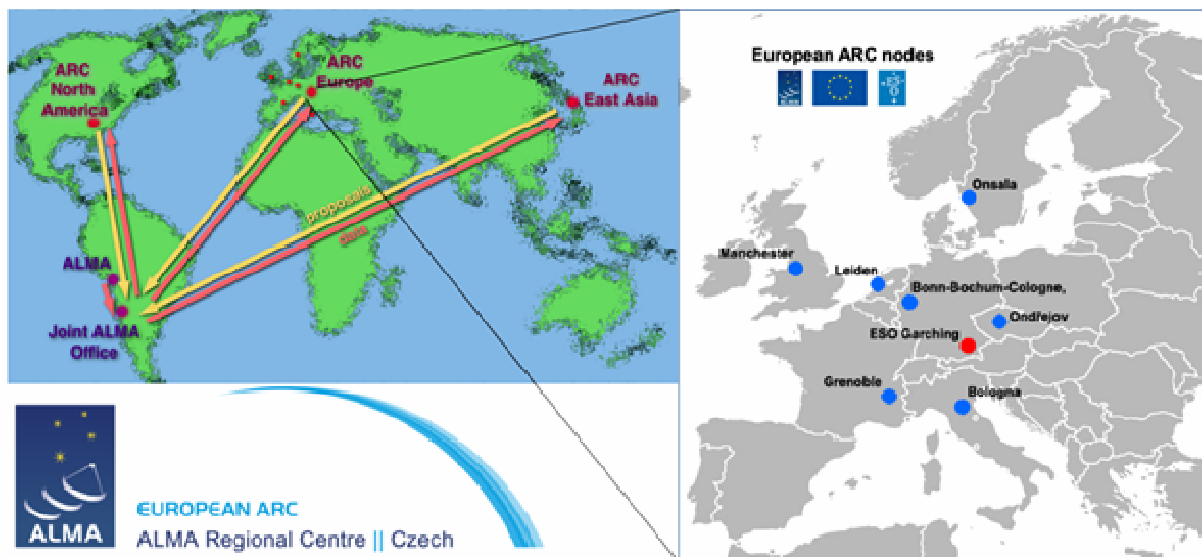


Fig. 2: Relations of JAO and ARCs and the structure of the European ALMA Regional Center.

ALMA is a complex system of more than sixty high-precision antennas connected as an interferometer (see Fig. 1). The main ALMA array, consisting of fifty 12m dishes, is supplemented by twelve 7m antennas for proper mapping of larger scales in the observed sources (known as Atacama Compact Array - ACA), and next four 12m Total Power (TP) dishes for scanning of the most extended sources. With this setup it can observe celestial objects with unprecedented spatial resolution as good as 5 milliarcseconds which is far too better than current (and planned) optical telescopes. Moreover, ALMA is observing in the range of millimeter and sub-millimeter wavelengths that has not been – because of technical difficulties – covered so far at all, and opens thus a completely new window to the Universe. And, in addition to that, ALMA provides multi-frequency images with an excellent spectral resolution down to 30 kHz in the broad range of frequencies of 30GHz – 1THz. These properties together with its high sensitivity make ALMA a unique tool for research in many

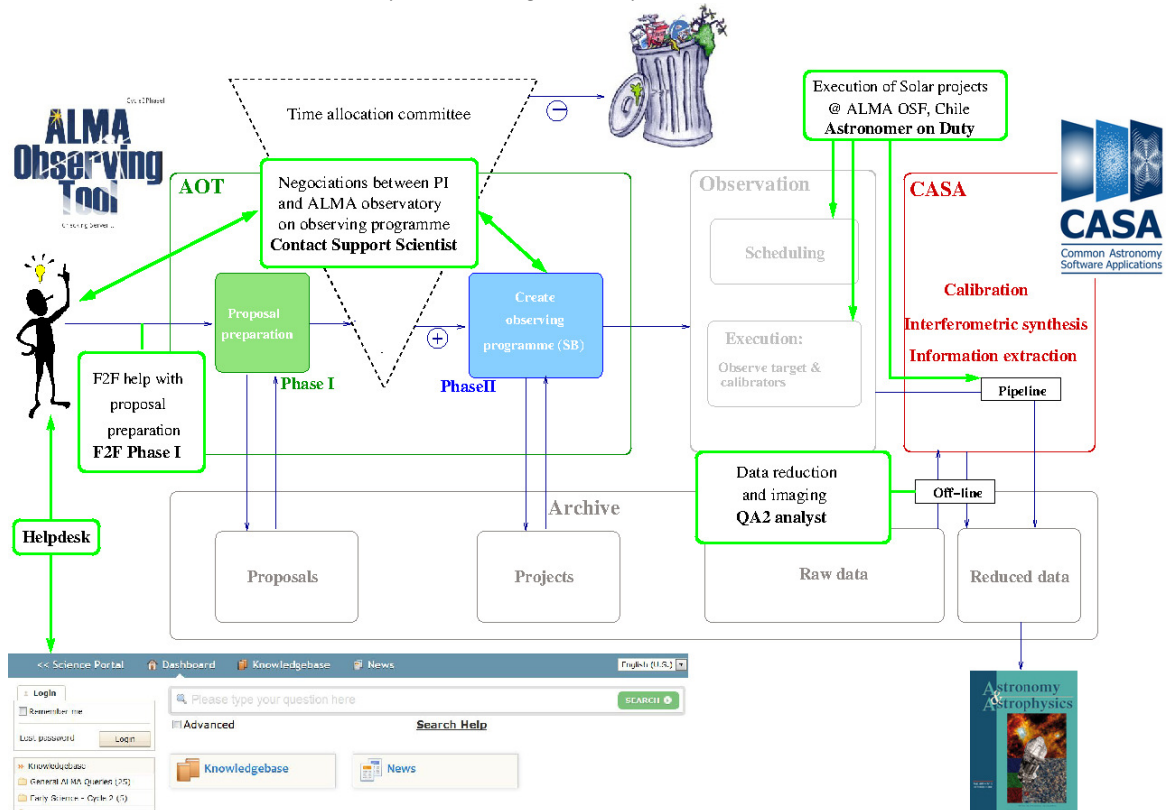


Fig. 3: ALMA infrastructure and the project flow with points of engagement (light-green frames) of the ARC-node staff into the project.

branches of astrophysics ranging from the physics of the Sun (Karlický et al., 2011; Wedemeyer et al., 2016) and solar system objects, through research of stars and their formation, interstellar matter, astrochemistry, exoplanets, and galaxies up to cosmology and the Universe as a whole

Role of ARCs and ARC nodes

In order to increase accessibility of ALMA to much broader scientific community and strengthen thus the scientific return, the Joint ALMA Observatory (JAO) created a support infrastructure – the network of ALMA Regional Centers (ARCs) – the European (EU ARC) operated by ESO, the North American (NA ARC) by the NRAO, and the East Asia (EA ARC) managed by NAOJ – the partner institutions that participated in the ALMA construction and development and that jointly operate the observatory (Fig. 2, left).

The main role of ARCs is to serve as an interface layer between the ALMA observatory and the research community. In accomplishing this task the ARCs and their nodes (see below) namely:

- Provide support (also personal – face-to-face/F2F) to the members of research community in proper usage of ALMA in all stages of their research projects (help with proposal submission, negotiations with the ALMA astronomers on technical details of the project, scientific data reduction and quality assurance, etc. – in the case of solar observations we even serve personally at ALMA/OSF as Astronomers on Duty / AoDs) – see Fig. 3.
- Spread the technical knowledge and awareness of ALMA among the research community (workshops/schools, training).
- Help the ALMA developers (e.g. tests of infrastructure and user SW, laboratory molecular spectroscopy – updates of spectral line catalogues).
- Promote and define user-community driven enhancements of ALMA (e.g. new observing modes – solar).

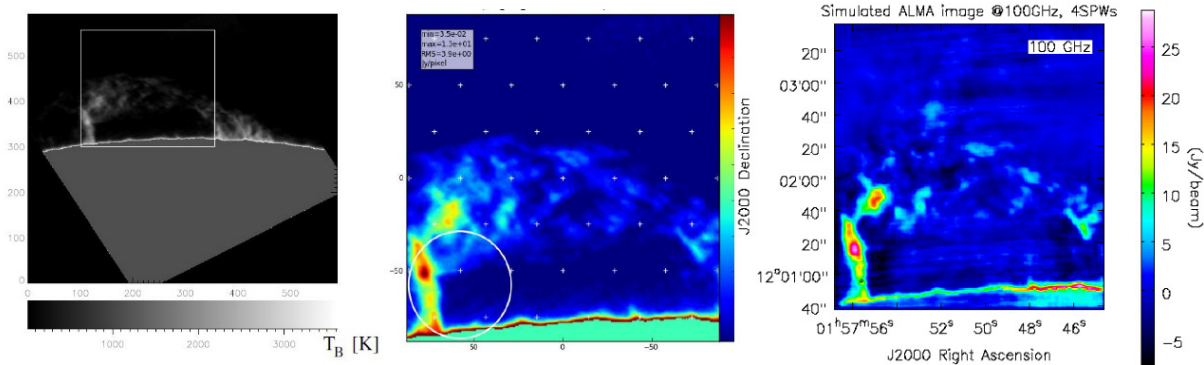


Fig. 4: Model brightness temperature (left), ALMA pointings at the background of ideal radio map (middle), and simulated ALMA image (right) of the prominence at 100GHz (ALMA Band 3; Heinzl et al., 2015).

Unlike the NA and EA ARCs, the European ARC is not a compact infrastructure but it has been formed as a distributed network of nodes centered around the ESO headquarters in Garching. One of the seven EU ARC nodes has been in 2009 established at the Astronomical Institute ASCR (AI ASCR) in Ondřejov (see Fig. 2, right), since 2016 being one of *National Research Infrastructures* listed in the European Roadmap of RIs.

EU ARC – Czech node: Specific Services for European solar-physics community

The node in Ondřejov is unique among the European ARC network because of its expertise in solar research with ALMA. The node has been established in 2009 and since then its staff is acquiring experience with technical details of ALMA observatory as well as user-level software and pre- and post-observing procedures. We have participated in many tests of ALMA Observing Tool (AOT), Helpdesk system, ALMA archive and CASA. Since Cycle 0 (2012) we are providing standard services to the community in non-solar research, namely, our staff members act as *Contact Support Scientists* (CSS) and work as *QA2 analysts* – the executive workers who make calibration and interferometric synthesis/imaging, whose final product is then delivered via ESO to the PI of respective projects. For solar-oriented projects we serve as *Astronomers on Duty* directly in Chile (Fig. 3).

Besides the expertise in ALMA technology the CZ-node staff is experienced in solar physics and solar radio research in dm and cm wavelength range, and the radiative transfer theory and computing – all the branches have decades long tradition at the Institute. Therefore, three members of the CZ node staff are part of international *ALMA Solar ObsMode Development Team* (Fig. 5) that takes part in the solar mode commissioning and testing.

This combined expertise makes the Czech node the primary access point of European solar-physics ALMA user community to the observatory. What can we do for you?

- Help with proposal preparation (so called Phase I). Both on-line (via Helpdesk tickets) and face-to-face (f2f) support is possible – we can support your stay at our node during consultations. It is advisable to use ALMA visibilities simulations in your proposal – we have expertise in that (Fig. 4)
- Help with converting your project into observing program in ALMA OT (Phase II) and its execution in Chile (AoD).
- In addition to standard calibration/imaging in frame of QA2 we can do this in a specific way customized to the science goals of your project.
- Help with science data interpretation.

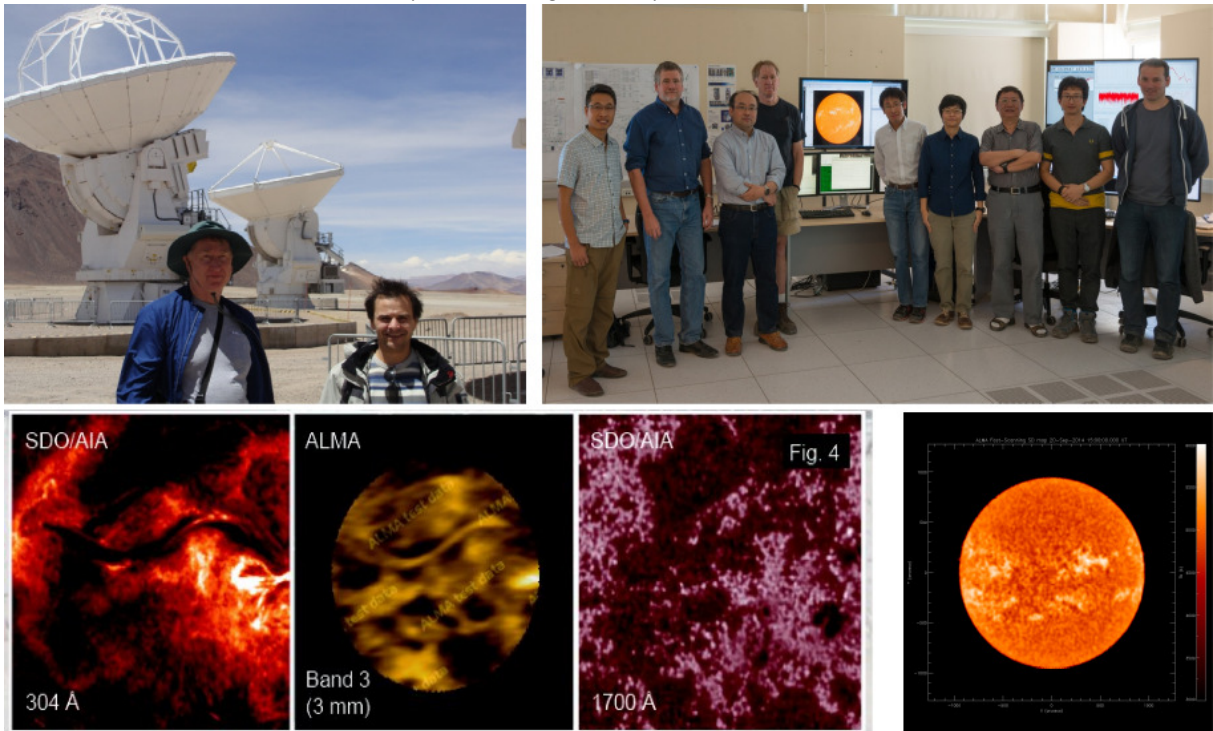


Fig. 5: Solar ALMA Observing Campaign (solar mode commissioning and science verification – CSV) 2014 and 2015: Part of Solar ALMA ObsMode Development Team (top) and sample of the CSV results: Interferometric image of filament at 100GHz compared with AIA observations (bottom left), single-dish image of the Sun at 100GHz (bottom right). Results of the campaign acquired by the team has been recently published in Shimojo et al (2017) and White et al. (2017)

Conclusions

ALMA is a recent cutting-edge ground-based astrophysical instrument for observations in the microwave and terahertz wavelength range. It is now ready to observe also the Sun and study its activity. In order to overcome difficulties with access to the ALMA observatory implying from the huge complexity of the ALMA systems (and lack of specific technical knowledge among general user community) ALMA has created three ALMA Regional Centers – ARCs in Europe, US, and East Asia, serving as a user support infrastructure and the link between the observatory and the community. The European ARC works as a distributed network of seven nodes coordinated by ESO. The node located in Ondřejov, Czech Republic, is specifically targeted at solar research with ALMA and it is ready to assist you with all aspects of your prospective solar-oriented ALMA science.

Acknowledgments

This study was supported by the project LM2015067: *EU-ARC.CZ – National Research Infrastructure* by Ministry of Education of the Czech Republic, ALMA/EoC project no. 59283/14/63437/HNE: *Solar Research with ALMA – Development Study* by ESO, and the project no. GACR 16-13277S by the Grant Agency of the Czech Republic.

References

- Karlický, M.; Bárta, M.; Dąbrowski, B. P.; Heinzel, P. (2011): Solar research with ALMA, Sol. Phys. 268, 165-173
- Heinzel, P.; Berlicki, A.; Bárta, M.; Karlický, M.; Rudawy, P. (2015): On the Visibility of Prominence Fine Structures at Radio Millimeter Wavelengths, Sol. Phys. 290, 1981-2000
- Wedemeyer, S. et al. (2016): Solar Science with the Atacama Large Millimeter/Submillimeter Array—A New View of Our Sun, SSR 200, 1-73
- Shimojo, M. and the Solar ALMA ObsMode Development Team (2017): Observing the Sun with the Atacama Large Millimeter/submillimeter Array (ALMA): High-Resolution Interferometric Imaging, Sol. Phys. 292, id. 87
- White, S.M. and the Solar ALMA ObsMode Development Team (2017): Observing the Sun with the Atacama Large Millimeter/submillimeter Array (ALMA): Fast-Scan Single-Dish Mapping, Sol. Phys. 292, id. 88

Author's Index

| | | | |
|------------------|----------|--------------------------|----------|
| Bárta M. | 127 | Odzimek A. | 109 |
| Belyaev G. | 58 | Olyak M. | 07 |
| Benz A.O. | 121 | Ovcharenko O. | 58 |
| Bershanskaya I. | 97 | Panchenko M. | 13 |
| Bojilova R. | 54 | Podgorny A.I. | 01 |
| Boychev B. | 58 | Podgorny I.M. | 01 |
| Brajša R. | 121, 127 | Popova E. | 34 |
| Brazhenko A | 40 | Romanchuk O. | 07 |
| Brazhenko A. | 07, 13 | Rozelot J.- P. | 70 |
| Bubnov I. | 07 | Rucker H. | 13, 40 |
| Canyilmaz M. | 83 | Ruzhin Yu. | 97 |
| Chernouss S. | 86 | Rycroft M. | 91 |
| Danov D. | 66 | Samwel S.W. | 19 |
| Despirak I. | 86 | Sergeeva N.A. | 46 |
| Dorovskyy V. | 13, 40 | Shagimuratov I. | 86 |
| Dremukhina L.A. | 103 | Shepherd S. | 34 |
| Efishov I. | 86 | Shevchuk M. | 13 |
| Filatov M. | 86 | Skokič I | 121, 127 |
| Frantsuzenko A. | 13 | Stanislavsky A.A. | 29 |
| Gromov S.V. | 103 | Sudar D. | 121 |
| Gromova L. | 91 | Tepenitsyna N. | 86 |
| Gromova L.I. | 103 | Tonev P. | 115 |
| Ishkov V.N. | 46 | Trushkina E.. | 58 |
| Ishkova L. | 97 | Turunen T. | 91 |
| Ivantishin O. | 07 | Veselovsky I. | 24 |
| Kalinichenko N. | 07 | Volvach Ya.S. | 29 |
| Kaportseva K. | 24 | Yankova Kr. | 77 |
| Kilcik A. | 70 | Yaşar M. | 83 |
| Kleimenova N. | 91, 109 | Yerin S. | 07 |
| Kleimenova N.G. | 103 | Zabarinskaya L.P. | 46 |
| Konovalenko A. | 07, 40 | Zharkov S. | 34 |
| Konovalenko A.A. | 29 | Zharkova V. | 34 |
| Kosovichev Al. | 70 | the Czech ARC Node Team. | 127 |
| Kostin V. | 58 | | |
| Koval A.A. | 29 | | |
| Krupar V. | 19 | | |
| Kubicki M. | 109 | | |
| Kuhai N. | 07 | | |
| Kuhar M. | 121 | | |
| Lukashenko A. | 24 | | |
| Lytvynenko O. | 07 | | |
| Manninen J. | 91 | | |
| Melnik V. | 13, 40 | | |
| Michnowski S. | 109 | | |
| Miteva R. | 19, 66 | | |
| Mukhtarov P. | 54 | | |

Proceedings of
Ninth Workshop “Solar Influences on the Magnetosphere, Ionosphere and Atmosphere”
Sunny Beach, Bulgaria, May 30 - June 3, 2017